Development of Surface Acoustic Wave Devices as Micro/Nano Actuators

by

Ricky Theodore Tjeung

Submitted in total fulfillment of the requirements of the degree of

Doctor of Philosophy

Department of Mechanical & Aerospace Engineering
Monash University

June 2012

Table of Contents

iii

Chapter 5. Conclusions and Recommendations for Future Work 161

Appendices

Publications

Journal Papers

1. **Tjeung, R. T.**, Hughes, M. S., Yeo, L. Y. & Friend, J. R., "Surface acoustic wave micromotor with arbitrary axis rotational capability", Applied Physics Letters 99, 214101 (2011).

2. Tan, M. K., **Tjeung, R.**, Ervin, H., Yeo, L. Y. & Friend, J., "Double aperture focusing transducer for controlling microparticle motions in trapezoidal microchannels with surface acoustic waves", Applied Physics Letters 95, 134101-134103 (2009).

3. Glass, N. R., **Tjeung, R.**, Chan, P., Yeo, L. Y. & Friend, J. R., "Organosilane deposition for microfluidic applications", Biomicrofluidics 5, 036501 (2011).

4. **Tjeung, R.T.**, Kandasamy, S., Maurya, D.K., Yeo, L.Y., and Friend, J.R., "Development of surface acoustic wave devices based on ZnO/Al2O3 hybrid material for microfluidic applications", (in preparation).

Conference Papers

5. **Tjeung, R. T.**, Hughes, M. S., Yeo, L. Y. & Friend, J. R., "Arbitrary axis rotating surface acoustic wave micro motor", in Proceeding of the 2011 6th IEEE International Conference on Nano/Micro Engineered and Molecular Systems (NEMS). 184-187 (2011).

6. **Tjeung, R. T.,** Maurya, D. K., Yeo, L. Y., Friend, J. R. & Kandasamy, S., "ZnO/sapphire based layered surface acoustic wave devices for microfluidic

applications", Proceeding of the 2011 6th IEEE International Conference on Nano/Micro Engineered and Molecular Systems (NEMS). 211-214 (2011).

Intellectual Properties

1. James R Friend, Leslie Yu-ming Yeo, **Ricky Theodore Tjeung**; Mark St.Clair Hughes, "Single and multi-axis surface acoustic wave motor", *Australian Provisional Patent*, 201090505, filling date: 16 November 2010

Abstract

Despite comprehensive reports on the utilization of SAW (surface acoustic wave) devices as micro/nano actuators, there are still unexplored potentials to be pursued. Most current SAW actuators utilize 128° Y-X cut lithium niobate (LiNbO$_3$) piezoelectric substrates due to the high electromechanical coupling coefficient in this crystal direction. However, these substrates have a major disadvantage of being highly anisotropic, the piezoelectric coupling is therefore exceptionally dependent on the propagation direction and cut.

Utilization of LiNbO$_3$-based SAW devices as linear microactuators has been extensively reported; however, work on extending the work to *rotate* a solid object has been limited. At the same time, SAW based microfluidics applications has been gaining interest in the past decade; however, extension of this work, using piezoelectric materials other than LiNbO$_3$ has rarely been reported. Hence, there is a need to advance this field further.

This thesis proposes the use of alternative—*isotropic*—piezoelectric materials for SAW actuators. The materials selected for this purpose are lead zirconate titanate (PZT) and a hybrid of zinc oxide (ZnO) and sapphire (Al$_2$O$_3$) material. PZT and ZnO are common piezoelectric materials, but have not been used widely as SAW actuators. They are selected due to their isotropic piezoelectric properties in the plane of the substrate, which is essential for generating multi-axis actuation on the plane of the substrate

The hybrid ZnO/Al$_2$O$_3$ material is selected to exploit the collective benefits of these materials for the development of a high performance SAW device. A higher order harmonic wave, the Sezawa wave, can be induced in a stratified material. This mode of SAW propagation is generally perceived to have superior performance compared to the Rayleigh mode.

The foremost aim of this thesis is to *develop SAW based actuators for both solid and liquid objects*: (1) the utilization of SAW generated on PZT material to drive a rotary

motor, and (2) the utilization of a hybrid ZnO/Al$_2$O$_3$ material for microfluidics applications.

The first aim of the thesis is to *develop* a *high speed* SAW actuated *motor* prototype with *the capability of rotating about an arbitrary axis*. The following work was performed to achieve this goal: the fabrication and characterization of SAW devices made on the PZT substrate (the stator), the development of the SAW rotary motor operating with and without an external preload, and performance analysis of the motor with two different hole size configurations, specifically 0.25 and 0.45 mm.

The main *contribution* of this work is an operational SAW actuated rotary motor with *an arbitrarily chosen* rotational axis. The motor has a simpler configuration and exhibits superior performance compared to SAW rotary motors reported in literature.

The second aim of the project is to *develop* a SAW device *exploiting* the beneficial properties of a *hybrid material* for *microfluidics applications*, specifically SAW devices made on a *ZnO/Al$_2$O$_3$* stratified material. The following work was performed to achieve this goal: the fabrication and characterization of the performances of SAW devices made on ZnO/Al$_2$O$_3$ hybrid material, verification and performance characterization of the generated Sezawa wave, and the utilization of the SAW device for microfluidics applications.

The *key finding* of this work is that the wave vibration speed is the *most influential parameter* for acoustic streaming. As generally perceived, the Sezawa mode demonstrates better performance (it induces higher acoustic streaming speed) because it has higher electromechanical coupling (validated by the network analyzer data) and hence higher vibration speed for a given input power (validated by the LDV data).

The main *contribution* of this work is the development of *SAW devices* based on a *ZnO/Al$_2$O$_3$ stratified material* for microfluidics application. The devices performances are

comparable to those based on the more common $LiNbO_3$ material; in addition, utilization of the Sezawa mode offers superior performances.

Author's Declaration

I hereby declare that this thesis contains no material which has been accepted for award of any other degree or diploma in any university; and to the best of my knowledge and belief contains no material previously published or written by another person, except where due reference is made.

_____

Signature of Author

_____

Date

Acknowledgement

First of all, I would like to express appreciation towards my supervisors, Dr. James Friend and Dr. Leslie Yeo for their advices, continuous support, constructive feedback and guidance throughout my candidature. Their enthusiast work ethics and encouragement inspire me to pursue this research toward completion.

I would also like express my sincere gratitude to a number of colleagues who has work untiringly with me. Their inputs and advices are invaluable for me in finishing this thesis; Dr. Sasikaran Kandasamy and Devendra Maurya for working determinedly with me in developing the ZnO/sapphire based material for SAW devices; Dr. Yuejun (Greg) Kang for the countless inputs and beneficial discussions on microfluidics research area; Dr. Christina Cortez-Jugo for sharing her insights in SAW devices applications for nano particles precipitation; and Dr. Jenny Ho for her assistance in scanning electron microscopy.

I would furthermore like to thank Dr. Ofer Manor for the helpful discussions during my preparation of this thesis; Dr. Cheol-ho Yun for his kind assistance, unvarying guidance and advices regarding ultrasonic motors development; and Mark Hughes who has been working diligently with me in the development of the SAW rotary motor.

I would like to take this opportunity to thank Dr. Kuang Chen (Daniel) Liu, David Collins, Anushi Rajapaksa and Dr. Debadi Chakraborty for all the beneficial discussions we had and for the kind support in proof reading this thesis. I would like to thank my MNRL colleagues for their companionships and the enjoyable atmosphere during my candidature. They are, in alphabetical order: Jeremy Blamey, Dr. Peggy Chan, Michael Dentry, Lydia Chong, Nick Glass, Dr. Sean Langelier, Dr. Aisha Qi, Rohan Raghavan, Amgad Rezk, Priscilla and Geoff Rogers, Richard Shilton, Dr. Ming Kwang Tan, Dr. Brett Watson, Catherine Wittman. I am especially thankful to the technical and

Lastly, I would like to express my greatest gratitude to my family who has always been there for me. To both my parents, sister and late brother, I am greatly fortunate for the comfort, hope and support whenever I needed it. No words or phrases can express what you all mean to me.

Abbreviations and Acronyms

SAW	Surface Acoustic Wave
IDT	Inter Digital Transducers
PZT	Lead Zirconate Titanate
k^2	Electromechanical Coupling Coefficient
LDV	Laser Doppler Vibrometer
ω	Rotational Velocity
h	Film Thickness
k	Wave Number
λ	Wavelength
$\boldsymbol{e_x}, \boldsymbol{e_y}, \boldsymbol{e_z}$	Unit Vector along X, Y and Z axis respectively
γ	Wave Amplitude
	Vertical Wave Velocity
ρ	Density
	Wave Velocity Vector
	In-plane Wave Velocity
T	Torque
J	Mass Moment of Inertia
τ_r	Time Constant, the time to reach 1-1/e (≈63.2%) of asymptotic value.
RF	Radio Frequency

SEM	Scanning Electron Microscope
AFM	Atomic Force Microscope
G_a	Radiation Conductance
f_0	Center Frequency
C_T	Total Electrode Capacitance
Re	Streaming Reynolds number
ρ_f	Density of the Fluid
μ	Dynamic viscosity
U_0	Fluid Streaming Speed
L	Characteristic Length Scale
$\propto_L$	Attenuation Coefficient
C_f	Speed of Sound in the Fluid
C_s	Speed of Sound in the Solid
X_p	Path length required for discontinuity formation
B/A	Non-linearity parameter in acoustic
u_i	Excitation Speed
M	Mach Number
F_{ar}	Acoustic Radiation Force.
F_D	Drag Force
PLGA	Poly(**D,L**-lactic acid-co-glycolic acid)
NPs	Nano Particles

List of Figures

xvii

List of Tables

Chapter 1

Introduction

1.1 Background

Surface acoustic waves (SAWs) are confined to travel along the surface of a material; most of the energy is confined to within one wavelength of the surface of the substrate. SAW is most commonly generated by utilizing interdigital transducers (IDTs); a series of interleaved metallic electrodes fabricated on top of a piezoelectric substrate material, used to both excite and detect SAWs [1]. The operating frequency of a SAW device is inversely proportional to the geometry of its IDT electrodes: high operating frequencies (MHz range) with sub-millimeter wavelengths suitable for microactuation require fabrications of electrodes with micron to sub-micron dimensions.

Continuous development of microfabrication technologies has extended the frequency range of surface acoustic wave (SAW) devices into the ultrasound region [2]. As higher frequency SAW device becomes easier to fabricate, many more applications other than their traditional use as filters, resonators and transformers are opened up. For tens of

1

MHz devices, the surface acceleration would be greater than 10^4 m/s^2, more than *ten thousand times* the *gravitational acceleration*; which is sufficient for them to be harnessed as microactuators [3]. Most existing applications utilize SAW devices constructed on a LiNbO$_3$ piezoelectric material due to the high efficiency (electromechanical coupling) of these devices in generating the Rayleigh SAW. However, working with LiNbO$_3$ substrate has one major intrinsic disadvantage: the substrate is highly anisotropic, and thus the piezoelectric coupling is exceptionally dependent on the SAW propagation and the cut orientation. As a result, the propagation directions of the generated SAW are limited.

Nevertheless, utilization of lithium niobate based SAW devices to actuate a solid object has been comprehensively reported. Kurosawa *et al.* have dedicated extensive work developing SAW actuated linear motors [4-16]. However, to date, work on utilizing the same principle to *rotate* an object has rarely been reported. Cheng et al [17, 18] has reported work on utilizing the same principle in rotating an object, yet the complexity of the device hinders its performance; the reported maximum rotational velocity is low and there is no report on the torque. Shilton et al [19] has reported rotary SAW motor with improved rotational velocity, albeit with the inconvenience of additional fluid coupling layer. Therefore, there is potential for a dry friction-coupled Rayleigh SAW-driven rotary motor with simple configuration and high performance.

Utilization of an alternative—*isotropic*—piezoelectric material to generate SAW should be advantageous for this purpose. Lead zirconate titanate (PZT) is a well-known piezoelectric ceramic with good electromechanical coupling [20, 21]. PZT ceramics are commonly used to generate bulk acoustic waves (BAWs); their usage to generate SAW, conversely, has been minimal. For these reasons, this thesis proposes the utilization of SAW generated on PZT material to drive the rotary motor.

Work on utilizing lithium niobate based SAW devices to actuate liquid has been gaining interest in the past decade; various microfluidics applications such as fluid mixing, transport, and atomization has been reported [22-42]. Utilization of SAW devices constructed on a thin film piezoelectric material should also prove to be valuable; however, such work has rarely been reported and there is a need to advance this field further.

Zinc oxide is a good candidate material for thin-film SAW devices as it retains moderate electromechanical coupling even in the thin film form. Additionally, its distinct form enables easy integration with other microsensors and microactuators. Furthermore, the isotropic nature of ZnO also addresses the intrinsic single axis actuation limitation associated with $LiNbO_3$ material. Sapphire (Al_2O_3) substrate possesses high acoustic velocities and low propagation loses, which compensate the associated drawbacks that of ZnO. A combination of these materials should give rise to collective benefits in the development of a high performance SAW device. Importantly, the higher order harmonic

wave, Sezawa wave, is known to occur in a stratified material. This mode of SAW propagation is generally perceived to have superior efficiency compared to the Rayleigh mode [43-46].

1.2   Research Aims

The foremost aim of this thesis is to *develop SAW based actuators for both solid and liquid objects*. This thesis aim comprises of two parts, the first part is to develop SAW devices to actuate a rotary motor, while the second part is to develop SAW devices based on zinc oxide/sapphire stratified material for microfluidics application.

1.2.1 SAW based actuators of solid objects (SAW actuated rotary motor)

The first part of the thesis aims to *develop* a *high speed* SAW actuated *motor* prototype with *an arbitrary rotational axis capability*. The stator is a group of SAW devices fabricated on the surface of a lead zirconate titanate (PZT) piezoelectric material. The rotor is a solid steel sphere placed on a blind hole drilled on the PZT substrate. The rotor would be limited to 1 mm diameter. The dimension is selected for proof-of-concept purpose; the aim is to demonstrate the ability of SAW to rotate a large and heavy object.

To achieve the aim, the work includes:

1. Fabrication and characterization of SAW devices made on the PZT substrate (the stator).

2. Development of the SAW rotary motor operating with and without an external preload.

3. Performance analysis of the motor with two different hole size configurations, specifically 0.25 and 0.45 mm.

1.2.2 SAW based actuators of liquid objects (SAW microfluidics using stratified structures)

The second part of the thesis aims to *develop* a SAW device *exploiting* the collective properties of a *hybrid material* for *microfluidics applications*, specifically SAW devices made on a *ZnO/Al_2O_3* stratified material. The result would be an essential contribution to the development of a practical platform for microfluidics actuations with sufficient flexibility to accommodate the needs of potential applications.

To achieve the main aim, the work includes:

1. Fabrication and characterization of the performances of SAW devices made on ZnO/Al_2O_3 hybrid material.

2. Verification and performance characterization of the generated Sezawa wave.

3. Utilization of the SAW device for microfluidics applications.

1.3 Thesis Structure

This thesis consists of six chapters to communicate the findings of the project and is presented as follows:

Chapter 1. Overview of the motivation, which leads to detailed descriptions of the objectives and scopes of the project. This chapter also outlines the structure of the thesis.

Chapter 2. Review of the current literature on SAW actuated motor and SAW actuated microfluidics devices. The research rationales justification is presented.

Chapter 3. Development a SAW actuated rotary motor. Motor configurations, device characterization and performance are presented and analyzed.

Chapter 4. Development of a SAW device based on zinc oxide/sapphire stratified material for microfluidics applications. Fabrication methods, material and device characterization, and applications are presented and analyzed.

Chapter 5. Conclusions and recommendations for future work.

References

1. White, R.M. and F.W. Voltmer, *Direct piezoelectric coupling to surface elastic waves.* Applied Physics Letters, 1965. **7**(12): p. 314-316.
2. Hickernell, F.S., *Surface acoustic wave technology, macrosuccess through microseisms.* Physical Acoustics, 1999. **24**: p. 135-207.
3. Wixforth, A., *Acoustically driven planar microfluidics.* Superlattices and Microstructures, 2003. **33**(5-6): p. 389-396.
4. Kurosawa, M., M. Takahashi, and T. Higuchi, *Ultrasonic linear motor using surface acoustic waves.* Ultrasonics, Ferroelectrics and Frequency Control, IEEE Transactions on, 1996. **43**(5): p. 901-906.
5. Kurosawa, M., M. Takahashi, and T. Higuchi, *Friction drive surface acoustic wave motor.* Ultrasonics, 1996. **34**(2-5): p. 243-246.
6. Kurosawa, M., N. Takahashi, and T. Higuchi. *An ultrasonic XY stage using 10 MHz surface acoustic waves.* 1994. IEEE.
7. Kurosawa, M., et al., *Surface acoustic wave atomizer.* Sensors and Actuators, A: Physical, 1995. **50**(1-2): p. 69-74.
8. Kurosawa, M.K., *State-of-the-art surface acoustic wave linear motor and its future applications.* Ultrasonics, 2000. **38**(1-8): p. 15-19.
9. Kurosawa, M.K., M. Chiba, and T. Higuchi, *Evaluation of a surface acoustic wave motor with a multi-contact-point slider.* Smart Materials and Structures, 1998. **7**(3): p. 305-311.
10. Kurosawa, M.K., H. Itoh, and K. Asai, *Elastic friction drive of surface acoustic wave motor* 1.* Ultrasonics, 2003. **41**(4): p. 271-275.
11. Kurosawa, M.K., et al. *Micro linear motor using surface acoustic wave device.* 2002. IEEE.
12. Kurosawa, M.K., et al. *Surface acoustic wave motor with feed back controller considering dead zone.* in *IECON Proceedings (Industrial Electronics Conference).* 2005. Raleigh, NC.
13. Sakano, K., M.K. Kurosawa, and T. Shigematsu, *Driving characteristics of a surface acoustic wave motor using a flat-plane slider.* Advanced Robotics, 2010. **24**(10): p. 1407-1421.
14. Shigematsu, T. and M.K. Kurosawa. *Miniaturized SAW motor with 100 MHz driving frequency.* in *Proceedings of the IEEE International Conference on Micro Electro Mechanical Systems (MEMS).* 2004. Maastricht.
15. Takahashi, M., M. Kurosawa, and T. Higuchi. *Direct frictional driven surface acoustic wave motor.* 1995. IEEE.
16. Takasaki, M., M. Kuribayashi Kurosawa, and T. Higuchi, *Optimum contact conditions for miniaturized surface acoustic wave linear motor.* Ultrasonics, 2000. **38**(1-8): p. 51-53.
17. Cheng, L.P., et al., *Miniaturization of surface acoustic waves rotary motor.* Ultrasonics, 2002. **39**(8): p. 591-594.
18. Zhang, G.M., et al., *Surface acoustic wave rotation motor.* Electronics Letters, 2000. **36**(16): p. 1437-1438.
19. Shilton, R.J., et al., *Rotational microfluidic motor for on-chip microcentrifugation.* Applied Physics Letters, 2011. **98**(25).
20. Hsiao, Y.-J., et al., *Surface acoustic wave characteristics and electromechanical coupling coefficient of lead zirconate titanate thin films.* Materials Letters, 2006. **60**(9-10): p. 1140-1143.

_____

21. Kirby, P.B., et al. *PZT thin film bulk acoustic wave resonators and filters*. in *Frequency Control Symposium and PDA Exhibition, 2001. Proceedings of the 2001 IEEE International*. 2001.

22. Beyssen, D., et al., *Microfluidic device based on surface acoustic wave.* Sensors and Actuators B: Chemical, 2006. **118**(1-2): p. 380- 385.

23. Yeo, L.Y. and J.R. Friend, *Ultrafast microfluidics using surface acoustic waves.* Biomicrofluidics, 2009. **3**(1).

24. Schneider, M.F., et al., *An acoustically driven microliter flow chamber on a chip (μFCC) for cell-cell and cell-surface interaction studies.* ChemPhysChem, 2008. **9**: p. 641-645.

25. Wacogne, B., et al., *Effective piezoelectric activity of zinc oxide films grown by radio-frequency planar magnetron sputtering.* Applied Physics Letters, 1995. **67**(12): p. 1674-1676.

26. Wixforth, A., et al., *Acoustic manipulation of small droplets.* Analytical and Bioanalytical Chemistry, 2004. **379**(7-8): p. 982-991.

27. Cecchini, M., et al., *Acoustic-counterflow microfluidics by surface acoustic waves.* Applied Physics Letters, 2008. **92**(10): p. 104103-3.

28. Friend, J.R., et al., *Evaporative self-assembly assisted synthesis of polymeric nanoparticles by surface acoustic wave atomization.* Nanotechnology, 2008. **19**(14).

29. Tan, M.K., *Microparticle collection and concentration via a miniature surface acoustic wave device.* Lab on a Chip, 2007. **7**(5): p. 618-625.

30. Tan, M.K., J.R. Friend, and L.Y. Yeo, *Direct visualization of surface acoustic waves along substrates using smoke particles.* Applied Physics Letters, 2007. **91**(22).

31. Tan, M.K., et al., *Double aperture focusing transducer for controlling microparticle motions in trapezoidal microchannels with surface acoustic waves.* Applied Physics Letters, 2009. **95**(13): p. 134101-3.

32. Sritharan, K., et al., *Acoustic mixing at low Reynold's numbers.* Applied Physics Letters, 2006. **88**(5).

33. Schneider, M.F., et al., *An acoustically driven microliter flow chamber on a chip (μFCC) for cell-cell and cell-surface interaction studies.* ChemPhysChem, 2008. **9**(4): p. 641-645.

34. Shilton, R., et al., *Particle concentration and mixing in microdrops driven by focused surface acoustic waves.* Journal of Applied Physics, 2008. **104**(1).

35. Rathgeber, A., M. Wassermeier, and A. Wixforth, *Acoustic'distributed source' mixing of smallest fluid volumes.* Journal of ASTM International, 2005. **2**(6): p. 259-266.

36. Renaudin, A., et al., *SAW nanopump for handling droplets in view of biological applications.* Sensors and Actuators, B: Chemical, 2006. **113**(1): p. 389-397.

37. Qi, A., J. Friend, and L. Yeo. *SAW atomization application on inhaled pulmonary drug delivery*. in *Biomedical Applications of Micro- and Nanoengineering IV and Complex Systems*. 2008. Melbourne, Australia: SPIE.

38. Qi, A., L.Y. Yeo, and J.R. Friend, *Interfacial destabilization and atomization driven by surface acoustic waves.* Physics of Fluids, 2008. **20**(7): p. 074103-14.

39. Li, H., J.R. Friend, and L.Y. Yeo, *Surface acoustic wave concentration of particle and bioparticle suspensions.* Biomedical Microdevices, 2007. **9**(5): p. 647.

40. Li, H., J.R. Friend, and L.Y. Yeo, *A scaffold cell seeding method driven by surface acoustic waves.* Biomaterials, 2007. **28**(28): p. 4098-4104.

41. Raghavan, R.V., J.R. Friend, and L.Y. Yeo, *Particle concentration via acoustically driven microcentrifugation: MicroPIV flow visualization and numerical modelling studies.* Microfluidics and Nanofluidics, 2009. **8**(1): p. 73-84.

42.   Friend, J. and L.Y. Yeo, *Microscale acoustofluidics: Microfluidics driven via acoustics and ultrasonics.* Reviews of Modern Physics, 2011. **83**(2): p. 647.

43.   Du, X.Y., et al., *Microfluidic pumps employing surface acoustic waves generated in ZnO thin films.* Journal of Applied Physics, 2009. **105**(2): p. 024508-7.

44.   Du, X.Y., et al., *ZnO film for application in surface acoustic wave device.* Journal of Physics: Conference Series, 2007. **76**: p. 012035.

45.   Emanetoglu, N.W., et al., *Epitaxial ZnO piezoelectric thin films for SAW filters.* Materials Science in Semiconductor Processing, 1999. **2**(3): p. 247-252.

46.   Winey, J.M., Y.M. Gupta, and D.E. Hare, *r-axis sound speed and elastic properties of sapphire single crystals.* Journal of Applied Physics, 2001. **90**: p. 3109.

Chapter 2

Literature Review

This review presents evaluation of two areas of study, namely surface acoustic wave (SAW) actuated microfluidics and micromotors. The review starts by introducing surface acoustics wave (SAW) and interdigital transducer (IDT). This is essential as this thesis project utilized SAW extensively as the actuation mechanism for both micromotors and microfluidics applications. This is presented in Section 2.1.

Section 2.2 focuses on micromotors. Development of micromotors based on various actuating mechanism is presented; leading to the SAW driven linear micromotors. This section concludes with our motivation for developing a SAW motor with an arbitrarily chosen axis of rotation.

Section 2.3 focuses on microfluidics. More common microfluidics actuation mechanism are discussed, i.e. pressure driven and electro kinetic flow. Drawbacks associated with these two actuating principles are presented; which leads to the benefits of utilizing SAW as actuation principle for microfluidics. Discussions of the mechanism of SAW and its

applications in microfluidics are subsequently presented. More importantly, the inherent drawbacks of using a more common SAW material, $LiNbO_3$ are presented; leading to the rationale of exploring other piezoelectric materials for SAW driven microfluidics.

2.1 Surface acoustic wave (SAW)

Surface acoustic waves (SAWs) are acoustic waves that are confined to travel along the surface of a material. They were discovered by Lord Rayleigh in 1885. The most commonly utilized wave, the Rayleigh wave, name after Lord Rayleigh, has displacement amplitude that decays exponentially into the depth of the substrate material; most of the energy is confined to within one wavelength of the surface of the substrate. These waves are assumed to have minimal gravitational dependence and depend only on the deformation for the material. Additionally, unlike bulk travelling wave in an elastic medium, the longitudinal and transverse modes of surface waves are coupled. Due to the asymmetry of the elastic forces at the surface, these two modes of propagation do not have the same magnitude, the surface particles therefore move in a retrograde elliptical fashion [1-5]. Figure 2-1(a) provides a schematic of the surface particles motion and depth dependence of SAW.

Although surface acoustics waves can be generated by various ways, the most common method, developed by White *et al*. [6] in the 1960s, is via the use of interdigital transducers (IDTs). The development of interdigital transducers (IDTs) had also extended

11

the range of frequency for the application of SAW into the ultrasound region. These small devices can be used both to excite and detect SAWs [6]. The IDT is a series of interleaved metallic electrodes fabricated on top of a piezoelectric substrate material. These IDTs transform electrical energy into acoustic energy along the surface in the following manner: an oscillating electric field electrical input is supplied to the IDT results in the generation of stress on the piezoelectric substrate material, which then creates acoustic waves that propagate along the surface of the substrate [7-9].

The size of the SAW device affects its operating frequency, as the electrode aperture size depends on the wavelength of the wave; $f = \frac{v_s}{\lambda}$ and $\lambda = 4 \times d$, in which f, v_s, λ, and d are operating frequency, speed on sound in the material, wavelength and the electrode width, respectively [10]. To generate properly propagating Rayleigh wave, an aperture size of twenty wavelength of more would be required [11]. Hence, for miniaturization of the device, higher operating frequencies (i.e. smaller IDTs sizes) are preferable. This challenge has been met due to advancements in micromachining technology, allowing structures of sub micron dimension to be produced with relative ease.

Rayleigh waves are non-dispersive; hence their phase velocity is independent of the frequency. This property coupled with the continuous development of microfabrication technologies enables smaller design (micron to sub-micron dimensions) of IDTs which further extend the frequency range of SAW devices (10-100 MHz). These SAW devices have found ubiquitous applications in delays lines, resonators and high-frequency filters

used in mobile phones [1, 4].As higher frequency SAW device becomes easier to fabricate, it opens up many more applications for SAW. With its deceptively low amplitude (10^{-11} to 10^{-9} m), SAW has extremely high acceleration due to its high frequency. For tens of MHz devices, the acceleration would be $\geq 10^4$ m/s^2, more than *ten thousand times* the gravitational acceleration, sufficient for usage as microactuators [12] .
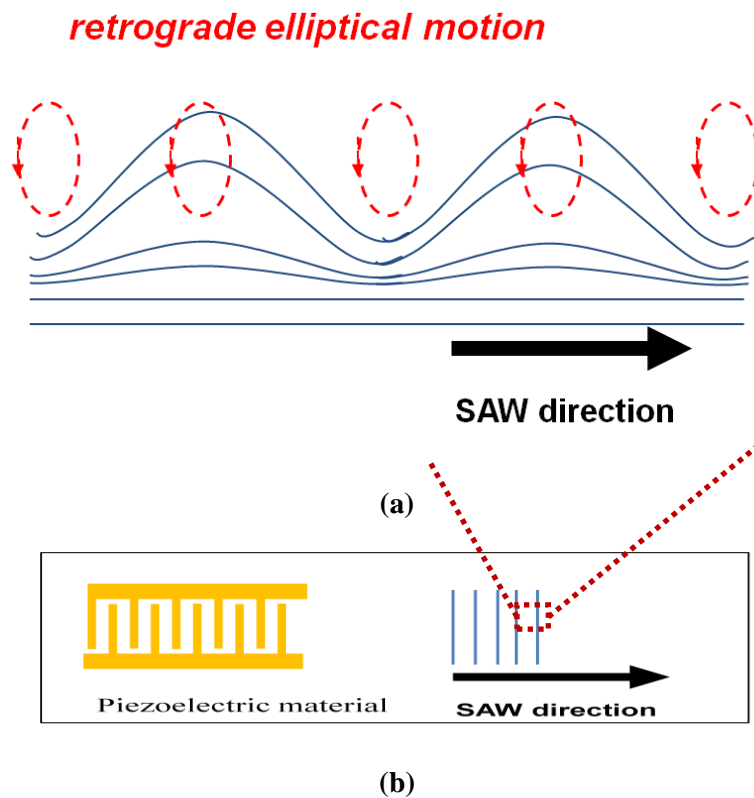
Figure 2-1. (a) Trajectory of substrate points during the propagation of surface acoustics waves (SAW) or Rayleigh waves. Each point in the substrate moves in retrograde elliptical fashion. Note the exponential decay with depth. (b) Schematics of a SAW device; the interdigital transducer (IDT) generates the wave which propagates away from it.

2.2 Microactuators/Motors

Researcher have investigated many different approaches to address the diverse needs and challenges of applications requiring micromotion [13]: including electrostatic, electromagnetic and piezoelectric actuation schemes [14]. One of the main challenges associated with microactuators is the inherent complexity of the fabrication process needed to achieve the required accuracy at this scale. They require extreme precision and creativity in design and machining techniques [15-20]. Among those schemes, ultrasonic motors, based on bulk flexural wave generated by piezoelectric material offer some flexible features and have demonstrated high output force/torque and power [21-23]. Yet, the problem of fabricating piezoelectric thick films with performance characteristics sufficient for actuation remains [24]. Surface acoustic wave (SAW), on the other hand, can be generated by devices with substantially simpler design and greater flexibility in fabrication.

SAW seems to be a poor selection for an actuator, with vibration amplitude in the order of nanometers or less. But in terms of power density, SAW device has an overwhelming advantage: the power density of SAW device is in the order of 100 W/cm^2, several orders of magnitude higher than low frequency PZT transducers. In addition, SAW motor has high thrust force, high velocity and precise positioning [25]. Moreover, SAW motors have the benefit of scalability.

14

Kurosawa *et al*. has successfully developed SAW actuated linear motors [11, 19, 26-42]. The driving mechanism behind linear SAW motor is the motion of the surface of a propagating Rayleigh wave. As discussed in Section 2.1, the substrate surface moves in a retrograde elliptical fashion due to the coupling between the transverse and longitudinal components of the Rayleigh wave. Note that a travelling wave is required for this actuation mechanism to work. The SAW device acts as the stator in this configuration. A slider is then brought into contact with the substrate surface using an external preload such as a beam-spring mechanism. The external preload is essential for a large thrust. RF electrical power is applied to the IDT, which generates Rayleigh waves, propagating away from the IDT. The Rayleigh wave propagates along the stator surface (the SAW device) a frictional force opposite to the wave propagation direction is exerted on the slider. Assuming a no-slip condition, the linear velocity of the slider should be the same as the tangential velocity of the SAW wave. The no-load velocity is observed to be proportional to the input voltage [35, 38, 43, 44]. The schematic and photographic image of a linear SAW motor is shown in Figure 2-3.

The development of linear SAW motors has been performed and reported extensively. The stator of Kurosawa *et al.* motor [11]] consisted of a 1-mm thick, 60×15 mm^2 rectangular plate of 128° y-rotated x-propagation LiNbO$_3$. The IDTs were fabricated at both ends of the stator using standard photolithographic process; utilizing vacuum vapor deposition chromium and aluminum as the electrode materials. The silicon slider was 5×5 mm^2 square with 4×4 mm^2 square contact region. The device was designed to operate

at a frequency of 9.8 MHz. For a friction drive, high pressure contact condition (10-100 MPa) is required [11]. Preload is essential to obtain higher output velocity of the SAW motor, extensive preload from 10 to 120 N was therefore utilized for the maximum driving voltage of 125 V_{peak} (V_p).
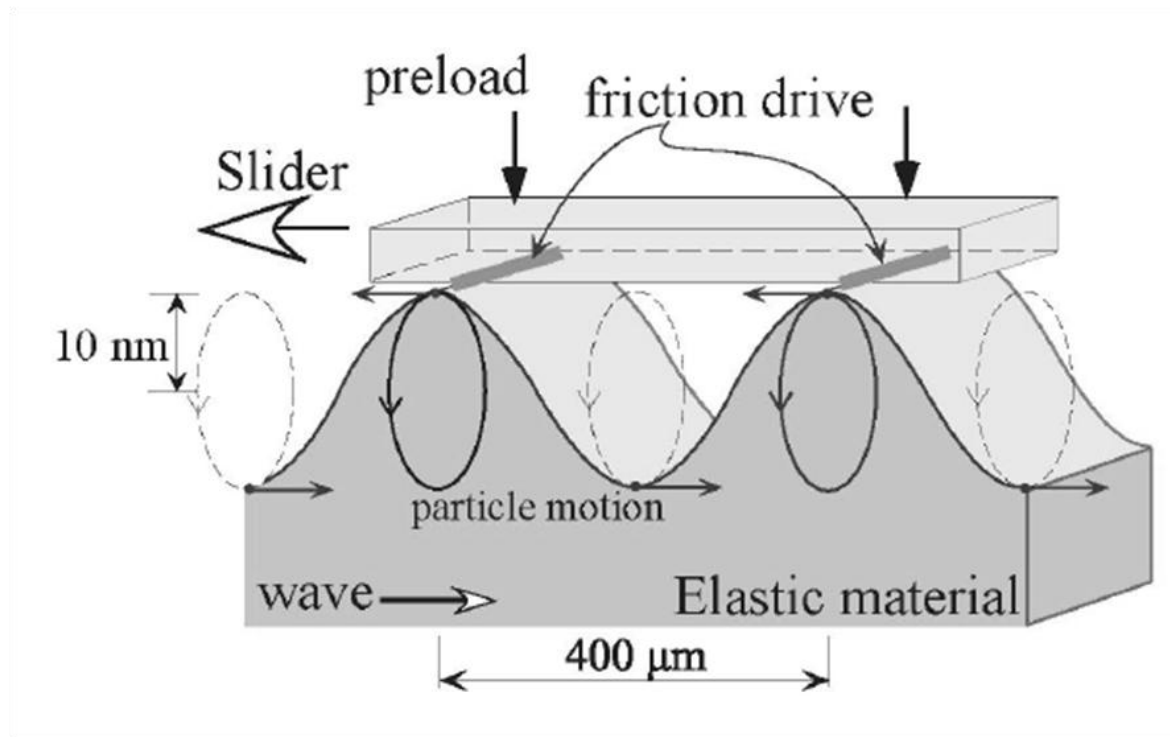
Figure 2-2. Working principle of the Linear SAW motor. As the Rayleigh wave propagates, from left to right in this figure, the particle of the surface of the piezoelectric material move in retrograde elliptical fashion. The frictional contact force between the substrate and slider pulls the slider towards the IDT. From Sakano *et al* (2008) [45]. Copyright 2008, IEEE.

The alternative designs explored include modifications of the stator-slider contact using: multiple steel balls [27], chemically etched projections/bumps[44] and chemically

reduced the stator material, LiNbO$_3$ [29]. The flat-plane slider using chemically reduced LiNbO$_3$ were able to deliver 18 N output force and no-load velocity of 0.9 m/s at a driving voltage of 125 V$_p$ with a 120 N preload. The stepper motor capability was also investigated, achieving a resolution of 2 nm [44].

Miniaturization of the SAW motor has also been reported with the operation of the SAW motor at a much higher frequency of 100 MHz. The stator size 3 x 12.5 x 0.5 mm^3, while the slider was 2 x 2 x 0.5 mm^3 with 25 μm diameter microlens-shaped projections on contact surface. As the size was significantly reduced, the preload was exerted using a neodymium magnet, giving approximately 200 mN of force. The configuration can be viewed in Figure 2-6. The miniaturized SAW motor was reported to achieve a high speed of up to 0.3 m/s and an output force of 13 mN over 4.3 mm long strokes [11].
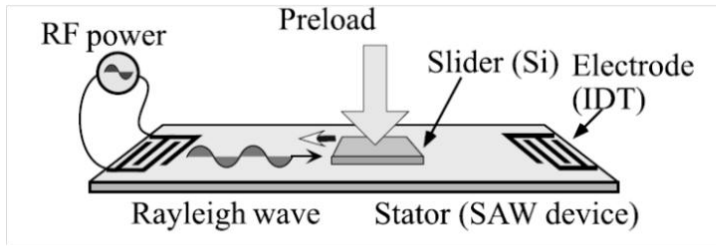
(a)
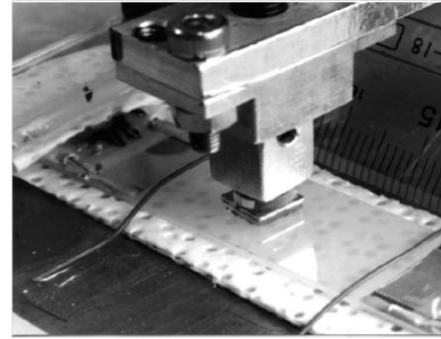
(b)
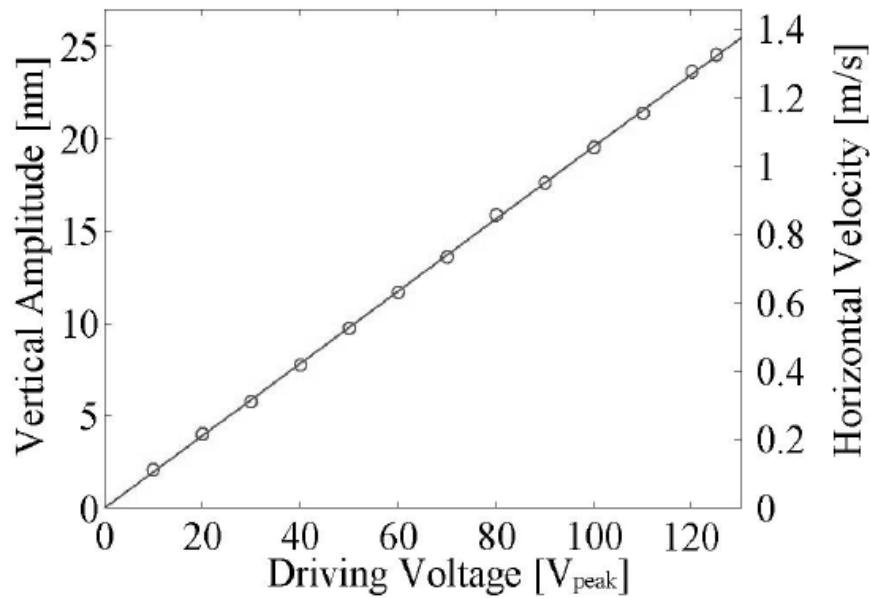
(c)

Figure 2-3. Images of a linear SAW motor: (a) schematic [29] and (b) photographic image. SAW amplitude with respect to the input voltage. The amplitude was observed to be linearly proportional to input voltage. Images are reprinted with permission from Kurosawa *et al*. (1998) [27]. Copyright 1998. IEEE. and from Sakano *et al* (2008) [45]. Copyright 2008, IEEE.
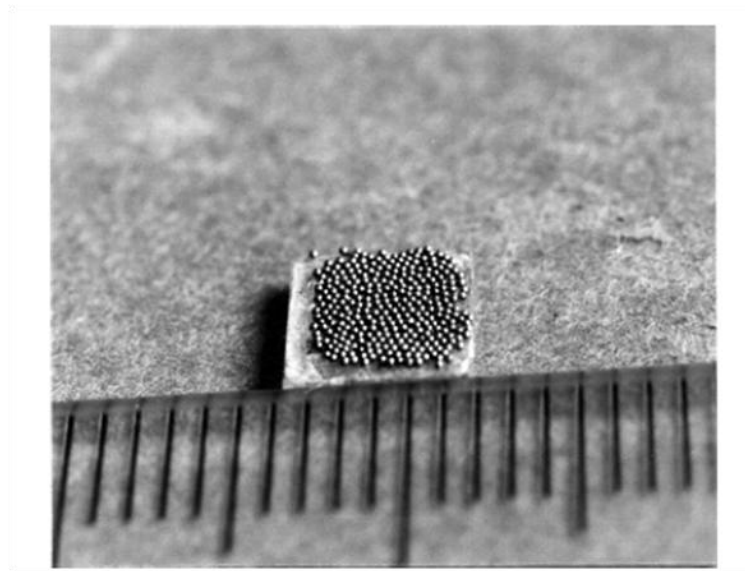
(a)
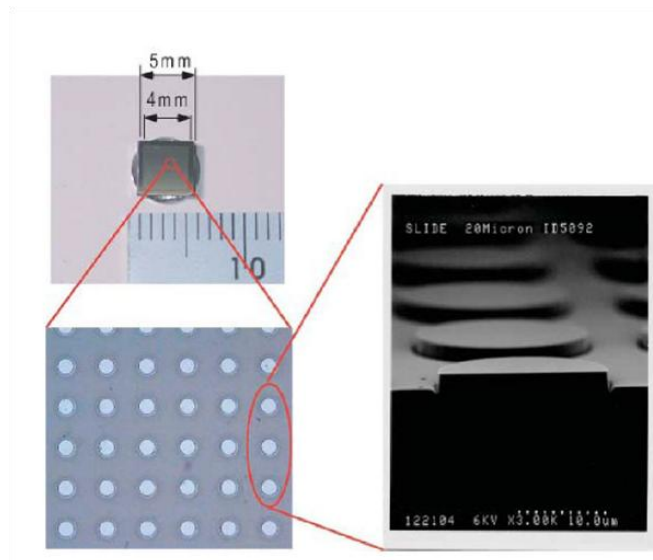
(b)

Figure 2-4. The contact surface between the slider and the stator. The development of the slider to improve motor performance using: (a) steel-ball projections (0.2mm diameter) and (b) chemically wet etched projection of 5 to 50 μm diameter. Images are reprinted with permission from Kurosawa *et al*. (1998) [27]. Copyright 1998. IEEE. and from Sakano *et al* (2008) [45]. Copyright 2008, IEEE.

(a)   **(b)**
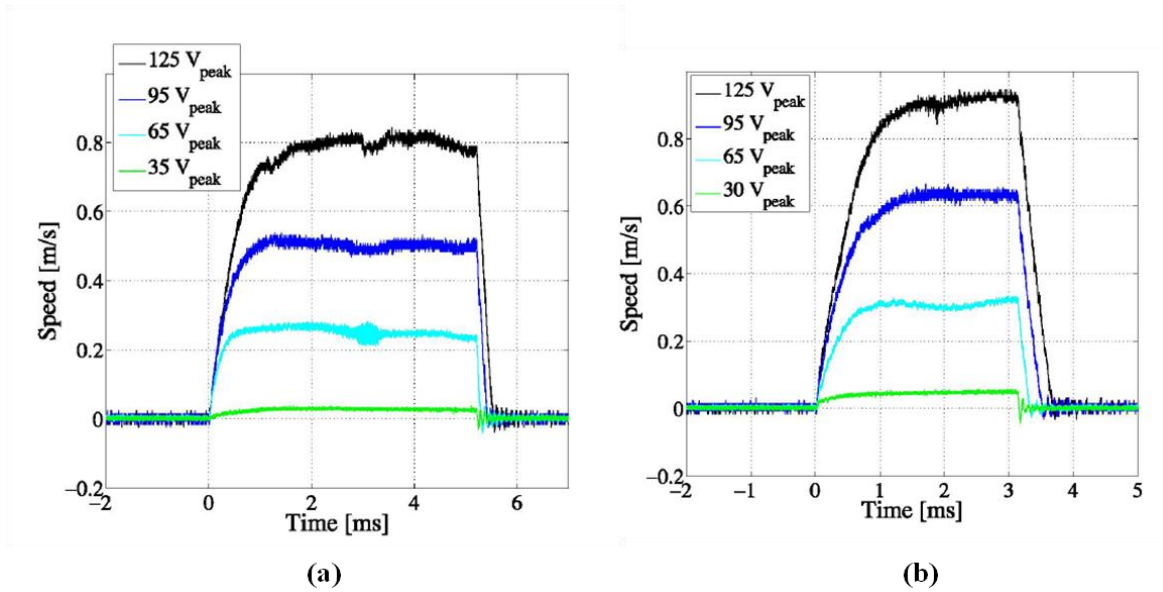
Figure 2-5. Comparison of the transient response of the motor with improved contact with preload of 20 N: (a) flat plane slider and (b) slider with projections. From Sakano *et al* (2008) [45]. Copyright 2008, IEEE.

(a)   **(b)**
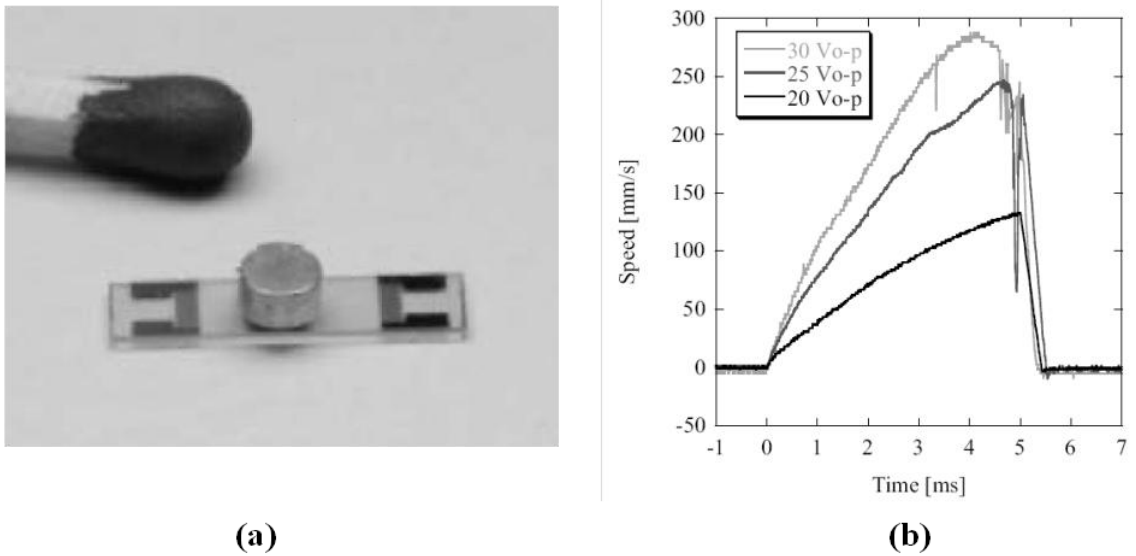
Figure 2-6. (a) Photographic images to the 100 MHz linear SAW motor with neodymium magnet as the preload, giving ~200 mN of force. (b) Transient response of the motor, exhibiting up to 0.3 mm/s linear velocity. From Shigematsu *et al.* (2004) [11]. Copyright 2004, IEEE.

20

A major limitation of most linear motors is that the stroke of the motor depends on the length of the SAW device. In other words, the stroke depends on the size and shape of the $LiNbO_3$ wafer in which the IDT was fabricated on. Altering the shape and size would be unfavorable, firstly, due to the cost of material, second and more importantly, the dependency of the piezoelectric property of $LiNbO_3$ on the cut. Kotani *et al*. [6] proposed a simpler solution to address this limitation. Instead of relying of the piezoelectric material, i.e. the LiNbO3 substrate, they proposed an 'indirect' excitation method (Figure 2-7). With this method, the stator is separated into two parts, the excitation and propagation medium of the SAW. SAW device made on LiNbO3 is again selected as to excite the SAW; however, a glass substrate was selected as the medium for the SAW to propagate. This method removes the complication of addressing the stroke limitation using a direct excitation approach. The glass substrate has the benefit of being cheaper and much easier to machine to the desired shape and size [6].

(a)

(b)
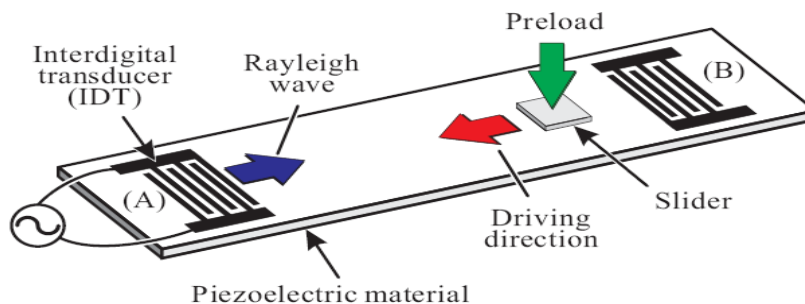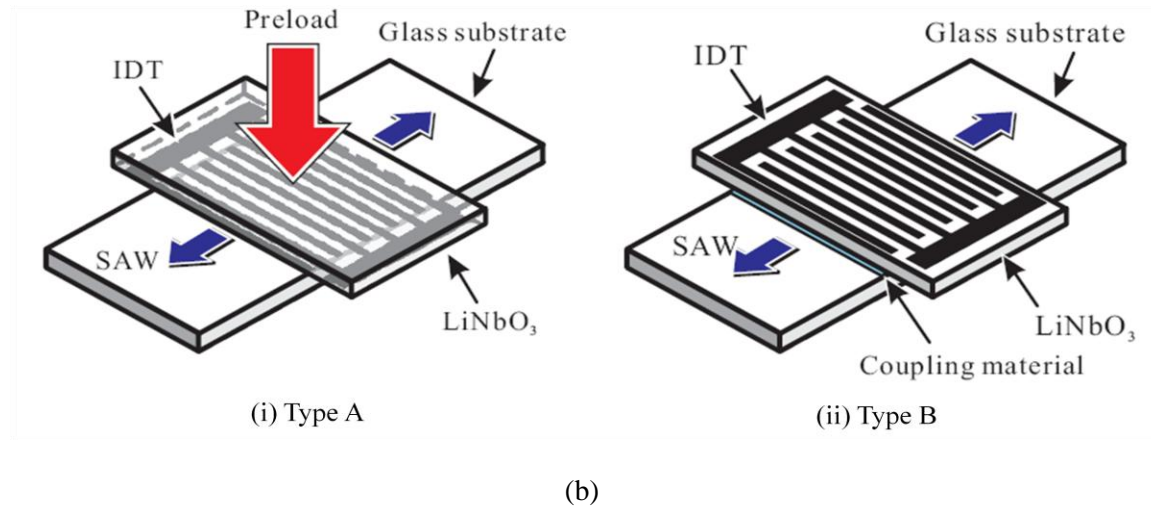
Figure 2-7. Comparison of the linear SAW motor configurations; the (a) 'direct' and (b) 'indirect' excitation. There are two types of 'indirect' methods: (I) the IDT is facing down and held in contact with the glass substrate by a preload and (ii) the IDT is facing up and a coupling material is utilized to transfer the vibration onto the glass substrate, no preload is required for this configuration. From Kotani *et al*. (2008) [6]. Copyright 2008, Springer.

The configuration of an indirectly excited SAW motor is shown in Figure 2-8. As in the normal configuration, the IDT was fabricated on a 128 ° Y-cut, *x*-propagating LiNbO$_3$ substrate using a standard photolithography process. The substrate was then cut to the same size of the IDT; the dimension of the excitation medium was 25 mm × 8 mm × 2 mm. The glass substrate was cut to a size corresponding to the IDT width, the dimension was 100 mm × 20 mm × 2 mm. The glass substrate was subsequently orientated to the propagation direction, perpendicular to the IDT fingers. The back side of the LiNbO$_3$ substrate (with the IDT facing up) was then put into contact with the glass via a coupling material (silicone oil in this case). The slider was then subjected to a preload exerted by a combination of a beam and coiled springs, providing a load of approximately 10 N [6].

The glass substrate linear SAW motor was designed to operate at a frequency of 4.768 MHz. The transient response was plotted for a preload of 10 N, and it was observed that the slider's maximum velocity increased with increasing current. A maximum velocity if 200 mm/s was achieved for input current of 0.5 A_p. The result was of the same order of magnitude as conventional linear SAW motors [6].
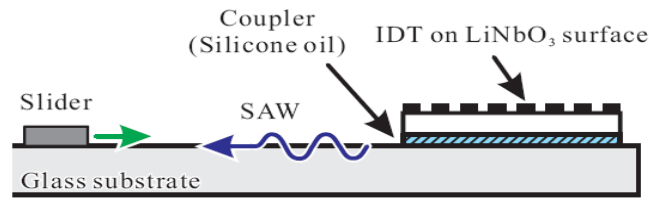
(a)
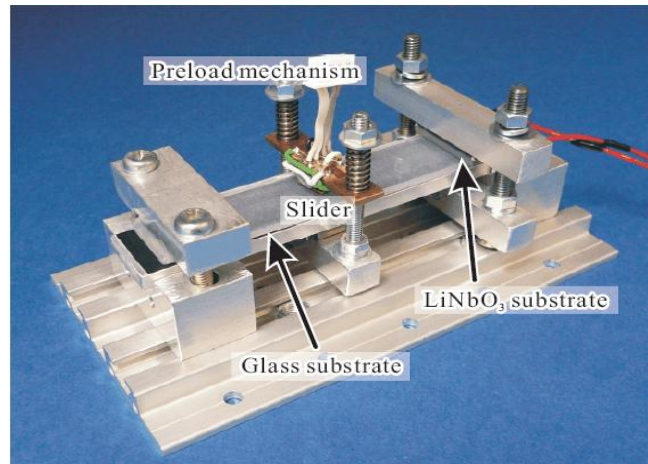
(b)

Figure 2-8. The configuration of a linear SAW motor using 'indirect' excitation as proposed by Kotani *et al*. (a) Cross-sectional schematic and photographic image. The IDT was fabricated on a LiNbO$_3$ substrate cut to the same size as the IDT; the glass substrate was also cut to the same width as the IDT, it was subsequently orientated to the propagation direction, perpendicular to the IDT fingers. The back side of the LiNbO$_3$ substrate (with the IDT facing up) was then put into contact with the glass via a coupling material, in this case silicone oil. From Kotani *et al*. (2008) [6]. Copyright 2008, Springer.
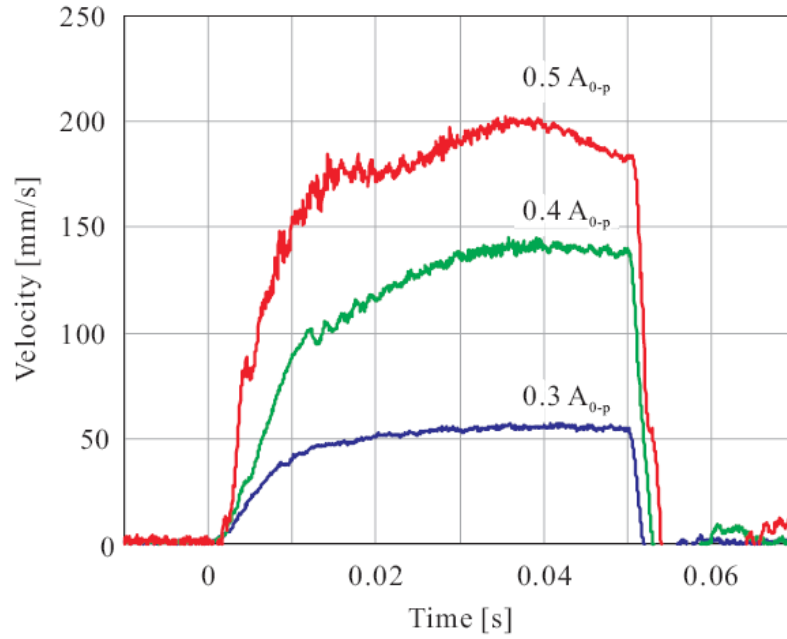
Figure 2-9. Transient response of the linear SAW motor using the 'indirect' excitation. The maximum linear velocity was shown to increase with increasing input current. From Kotani *et al*. (2008) [6]. Copyright 2008, Springer.

Research on using the SAW to drive rotary motion has been rare; Cheng *et al*.[46, 47] reported one of two known examples. The schematic of the motor design is presented in Figure 2-10. Counter-propagating SAWs generated by diagonally positioned IDTs were used to drive a contraption made of steel balls housed in a 9-mm diameter disc. The disc was driven to rotate in a similar fashion to a circus carousel. The maximum rotation speed reported with a driving voltage of 120 V_{pp} was 270 rpm while the torque was not reported. The motor performance is possibly hindered by the complexity of the device, bringing in substantial parasitic friction and standing wave SAWs.

25
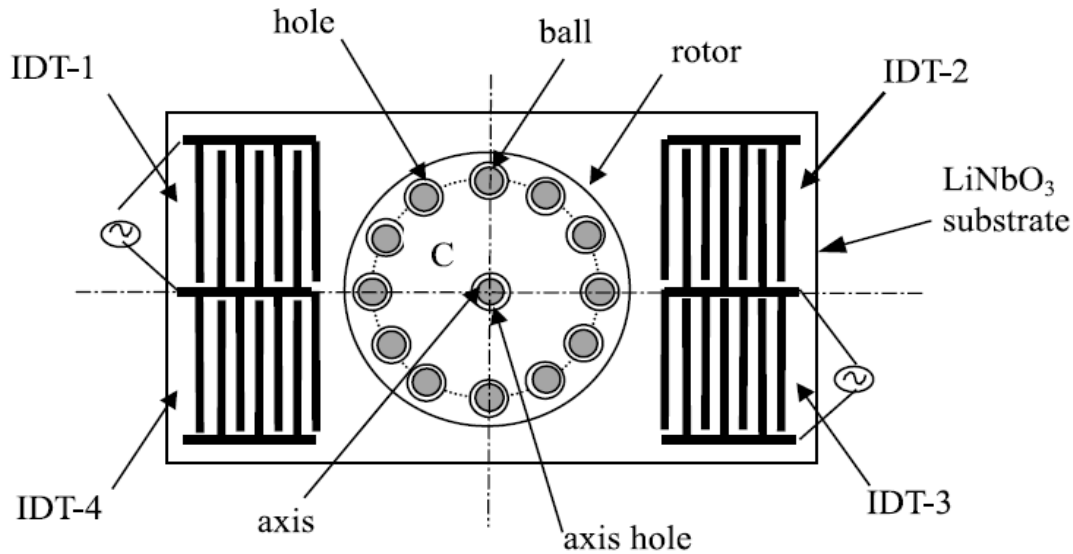
Figure 2-10. Schematic of the Cheng *et al.*'s rotary SAW motor; Rayleigh SAWs propagating in opposition from diagonally positioned IDTs are used to drive a collection of steel balls housed in a 9-mm diameter disc; the disc is allowed to rotate on a hub placed between the counter-propagating SAW. The maximum rotation speed reported was 270 rpm. From Cheng *et al*. (2002) [46]. Copyright 2002, Elsevier.

Another known example of rotary SAW motor was reported by Shilton *et al.*, in which a combination of counter-propagating focused SAWs with a liquid coupling layer was used. The rotor was a 5-mm diameter **Mylar** sheet, which was demonstrated to rotate with velocity and stall torque of up to 2250 rpm and 60 nN.m, respectively [48]. A schematic view of the motor is shown in Figure 2-11. The requirement of an additional fluid coupling layer was, however, a disadvantage; as it adds complexity and limits the applications.

The lack of reported work on SAW driven rotary motor maybe due to the difficulty of creating counter-propagating SAW waves on a single substrate. Utilizing an isotropic piezoelectric material to generate SAW may be a more straightforward way to address this challenge. Lead zirconate titanate (PZT) is a good candidate for this purpose, it is a well-known piezoelectric ceramic widely used in micro devices due its robustness and good electromechanical coupling (~ 20%) [49, 50]. The material property of PZT is well characterized; considerable amount of work has been performed using PZT with applications such as filters, transducers and resonators in micromotors and telecommunications. Particularly, PZT ceramics are commonly used to generate bulk acoustic waves (BAWs).

On the other hand, exploitation of PZT to generate SAW is still limited, most likely due to limitations in the operating frequency of PZT ceramics. A PZT ceramic normally performs well at low frequency (< 20 kHz); however, higher frequency SAW operations are currently achievable using a thin-film PZT, albeit with the drawback of reduced electromechanical coupling (~ 0.12%) [49]. Nevertheless, Tsai *et al.* (2009) have recently shown a PZT ceramic based SAW device that successfully operates at a MHz frequency range (27.45 MHz) [51], opening up a large number of potential applications. Utilization of PZT generated SAW to drive a rotary motor is therefore proposed for this thesis.
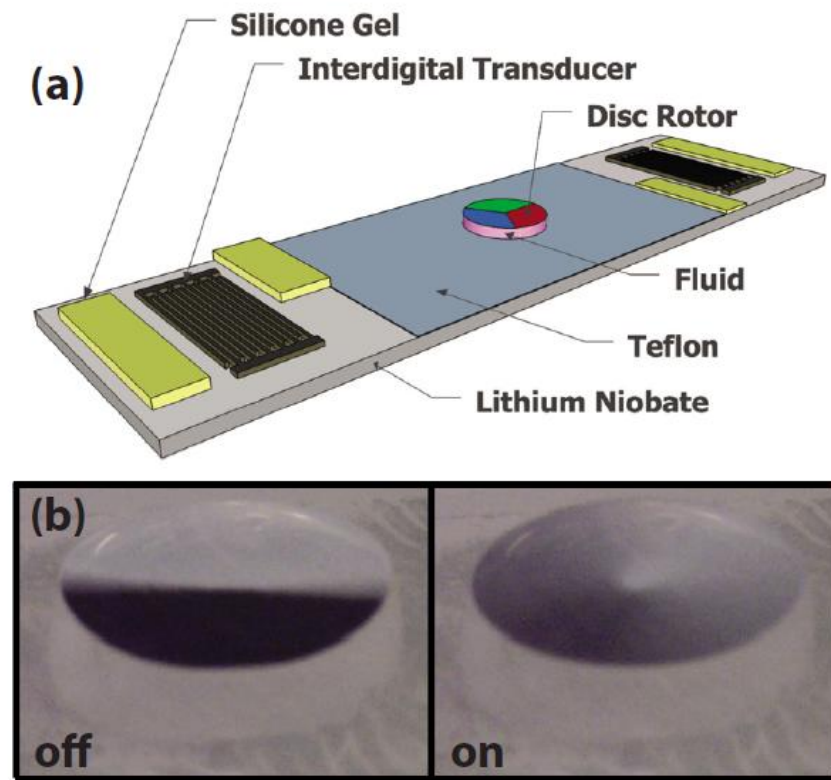
Figure 2-11. (a) Schematic of the motor in isometric view. Counter propagating SAWs were created by breaking the symmetry of the SAW propagating into the liquid drop. Silicone gels were used to blocked part of the SAWs from the two opposing IDTs, creating the counter propagating SAWs. The resulting liquid rotation on the drop then caused the rotor to spin. (b) Images of the rotor during the absence (static) and presence (rotating) of input voltage . From Shilton *et al*. (2011) [48]. Copyright 2011, American Institute of Physics.

2.2.1 Summary and Research Rationale

In summary, a lot of work has been performed on the development of SAW actuated linear motor. Since the early 1990s, research on linear SAW motors has lead to various improvements, from precision positioning as a stepper motor [40], increasing the driving frequency for miniaturization [11], to energy circulation method for saving the driving power [19]. Work on the development of SAW rotary motor, in contrast, have been limited. To date, only two examples such motors have been reported; the former, though, produced low rotational velocity and while the latter had higher rotational velocity, it added an extra complexity of a fluidic coupling [46, 48].

For this reason, the development of a dry friction-coupled Rayleigh SAW driven rotary motor is proposed. The rotary motor would have the capability to rotate about a arbitrarily chosen axis in high velocity. Lead zirconate titanate (PZT) is chosen as the substrate because its isotropy is essential for generating multi-axis actuation on the plane of the substrate. Detailed discussion is presented in chapter 3 of this thesis.

2.3 Microfluidics

Microfluidics can be defined as a field dedicated to the study and manipulation of liquids at the 10^{-9} to 10^{-18} liters scale. It generally deals with liquid in devices with lateral dimension of less than 1 mm, in the form of complex channels with dimensions of tens to hundreds of micrometers. The multidisciplinary field is of great interest to researchers due to the dramatic changes in physical behavior as size is decreased. One of the most critical aspects in microfluidics is the absence of turbulence flow. Flows are laminar at the micro scale because inertial forces are much less significant compare to the surface force, such as surface tension and viscosity. The main challenge is, therefore, to find suitable actuation mechanism to overcome such forces [52, 53].

SAW would be a suitable candidate for this purpose. The application of an acoustic force on a fluid gives rise to an acoustic radiation force as well as acoustic streaming (time-averaged bulk viscous fluid motion). In addition, SAW addresses the intrinsic drawbacks associated with low frequency ultrasonic bulk wave actuator (kHz order frequencies), namely long wavelength (at least one order of magnitude larger compare to microfluidics devices characteristic length scale) as well as design and mounting complexity at the scale required [54].

SAW actuated microfluidics

Figure 2-12 provides a schematic illustration of how the fluid-structural interaction that arises as the SAW propagating on the substrate comes into contact with a liquid droplet above it. This interaction constitutes the underlying mechanism of SAW microfluidic actuation. When a propagating SAW comes into contact with the liquid in its path, the energy and momentum of the SAW are transmitted into the liquid, inducing a strong fluid recirculation known as acoustic streaming. The SAW is diffracted into the liquid at the Rayleigh angle θ_R, which depends on the ratio between the SAW velocity in the fluid v_L and the solid substrate v_S by Snell's diffraction law [55-57].
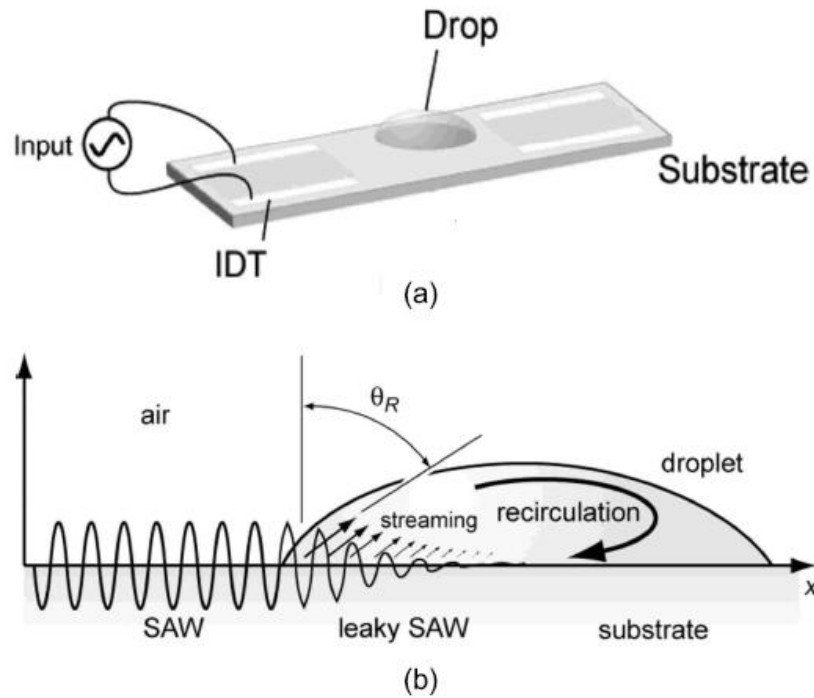
Figure 2-12. An illustration of SAW streaming. The Rayleigh angle θ_R is based on Snell's law of diffraction due to the difference in sound velocities in the liquid and the solid substrate. From Yeo *et al*. (2009) [54]. Copyright 2009, American Institute of Physics.

$$sin\ \theta_R = \frac{v_L}{v_S}$$

(1)

The fluid-acoustic energy interaction arising from SAW can be harnessed to generate various types of nano-liter scale fluid manipulation. Depending on the actuation power, the manipulation could be in form of mixing, transport or even atomization [54-74].

Most, if not all of the current SAW microfluidics devices utilize 127.68° Y-X cut lithium niobate (LiNbO$_3$) piezoelectric substrates because of the high electromechanical coupling coefficient of LiNbO$_3$ in this crystal direction (~5.3%) [8, 75, 76]. For piezoelectric materials, the electromechanical coupling coefficient, k^2, is a measure of its conversion efficiency between electrical and acoustic energy. For SAW devices, it is defined as twice the fractional change in the SAW velocity as it propagates from the metalized interdigital electrodes to the bare substrate surfaces [75],

$$k^2 = 2\frac{|\Delta v|}{v}.$$

(2)

Although LiNbO$_3$ is commonly employed in SAW devices, it has a major inherent disadvantage when used as a substrate for microfluidics: the substrate's piezoelectric effect is highly anisotropic, hence the piezoelectric coupling is therefore exceptionally dependent on the propagation direction and cut.

The use of an alternative piezoelectric material for SAW microfluidics is therefore proposed in this thesis. The material selected for this purpose is a thin film zinc oxide (ZnO). It is a common piezoelectric material widely used for SAW devices, yet its application for SAW driven microfluidics has been minimal. It has the advantage of being isotropic along the substrate plane with piezoelectric properties comparable to $LiNbO_3$ [77].

ZnO based Surface Acoustic Wave (SAW) Microfluidics

The use of ZnO for generating SAW has gained interest primarily due to its moderate electromechanical coupling coefficient even in the form of a thin film (~ 2%). Thin film ZnO can be easily grown on common microelectronics materials such as silicon, and thus provide great opportunities for integration with microsensors and microactuators. Another advantage of utilizing this material is the possibility for high frequency operation. Wang *et al.* (2008) has demonstrated the development of 1.6 GHz SAW devices using IDTs patterned on thin film ZnO [78]. ZnO is thus the material of choice in electronics and telecommunications for generating high frequency SAW. It is commonly used for both sensors and actuators [43, 58, 78-88].

An interesting phenomenon that occurs in SAW device based on material with multiple/stratified layer is the occurrence of the Sezawa wave, which appears in addition

to the more commonly observed Rayleigh wave. The Sezawa wave occurrence is very rare, limited by the properties of the materials of the surface and lower layers [88, 89].

The Sezawa waves have short wavelengths and their appearance is limited to multiple layers substrate and only if the acoustic velocity in the surface layer is lower than or equal to the acoustic velocity in the lower layer. It is essential to note, unlike that of Rayleigh waves, the Sezawa waves' surface particles move in a prograde elliptical motion, in the same sense as that of gravitational waves. Hence, it can be confirmed that the wave is not of the higher order of the Rayleigh wave. In addition, the amplitudes of Sezawa waves have been observed to be larger compare to that of the Rayleigh waves [90-98]. Figure 2-13 (a) provides a schematic of the surface particles motion and depth dependence of SAW.
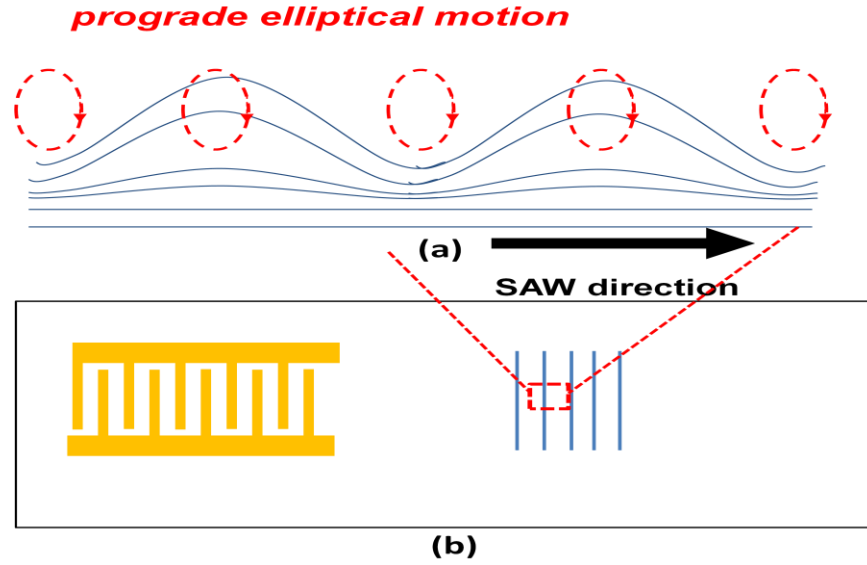
Figure 2-13. (a) Trajectory of substrate points during the propagation of the Sezawa waves. Each point in the substrate moves in prograde elliptical fashion. (b) Schematics of a SAW device; the interdigital transducer (IDT) generates the wave which propagates away from it.

As shown in Figure 2-14, the Sezawa wave normally has a higher phase velocity than the Rayleigh wave; this is attributed to the higher resonance frequency of this mode. For a thin film, a normalized thickness parameter, *kh*, is commonly used in the literature, where *h* is the thickness and *k* is wave number ($k = \dfrac{2\pi}{\lambda}$). Figure 2-15 shows that the electromechanical coupling coefficient (K^2) is highly dependent on the *kh* value of the film. It should be noted that the Sezawa mode has a higher K^2 value (maximum value of ~3.5%) compared to the Rayleigh mode (maximum of ~1%). Le Brizoual *et al.* have shown that the highest coupling coefficient corresponding to the Sezawa mode occurs with a *kh* value of 2.5 [88].

35
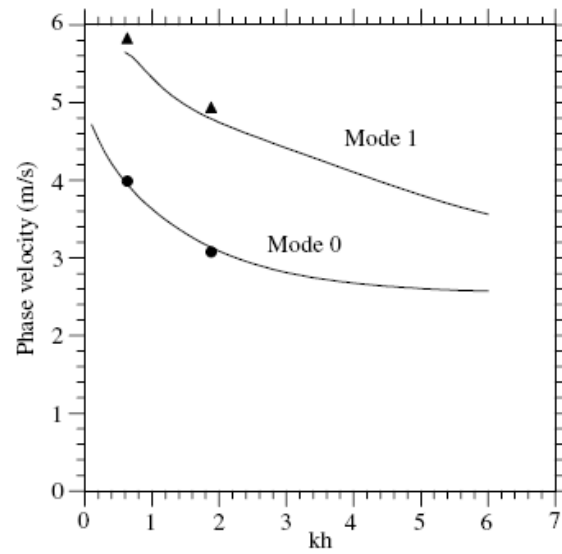
Figure 2-14 Phase velocity comparison of the Rayleigh (mode 0) and the Sezawa (mode 1). The variable *kh* is the normalized film thickness parameter. From Le Brizoual *et al*. (2006) [88]. Copyright 2006, Elsevier.
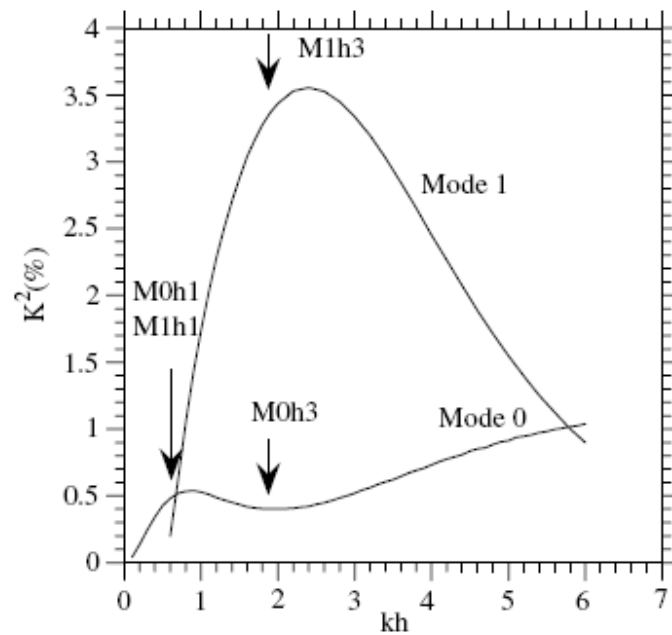
Figure 2-15 The film thickness effect on the electromechanical coupling coefficient for the Rayleigh (mode 0) and the Sezawa (mode 1) waves. The h value represents the harmonic order. From Le Brizoual *et al*. (2006) [88]. Copyright 2006, Elsevier.

Research on the use of ZnO for SAW microfluidic actuation has only recently commenced [91-93, 99], and has not yet been thoroughly explored. Initial results show that SAW streaming in water droplets can be induced by high frequency Rayleigh and Sezawa waves [91-93] Figure 2-15 and Figure 2-16 show the results obtained by Du *et al.* [93].
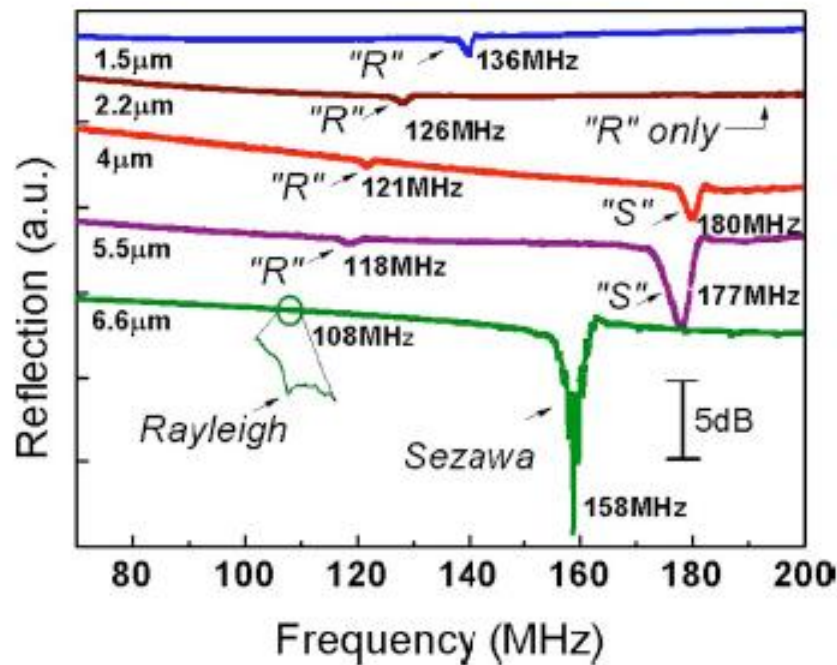
Figure 2-16 Reflection spectra of the Rayleigh (R) mode and the Sezawa (S) mode for different ZnO thickness parameters. From Du *et al*. (2008) [93]. Copyright 2008, American Institute of Physics.

Figure 2-16 shows the qualitative reflection spectra of the Rayleigh and Sezawa waves. Du *et al.* showed that the Sezawa wave is much more efficient than the Rayleigh wave for ZnO films with the same thickness. They also observed that the streaming velocity increases linearly with the input voltage and that below a threshold voltage, no acoustic streaming was observed; this result is shown in Figure 2-17 [71]. For film thicknesses

less than 4 µm, the Sezawa mode was not observed, consistent with the results shown by

Le Brizoual *et al*. [88]. It was also shown that the operating frequency is up to 130 MHz

for Rayleigh waves and 180 MHz for Sezawa waves. The resonance frequencies for both

of these modes decrease as film thickness is increased. We also note that the amplitudes

of the Sezawa modes are five to ten times larger than those of the Rayleigh modes; this

enhancement is stronger as the thickness of the film is increased.
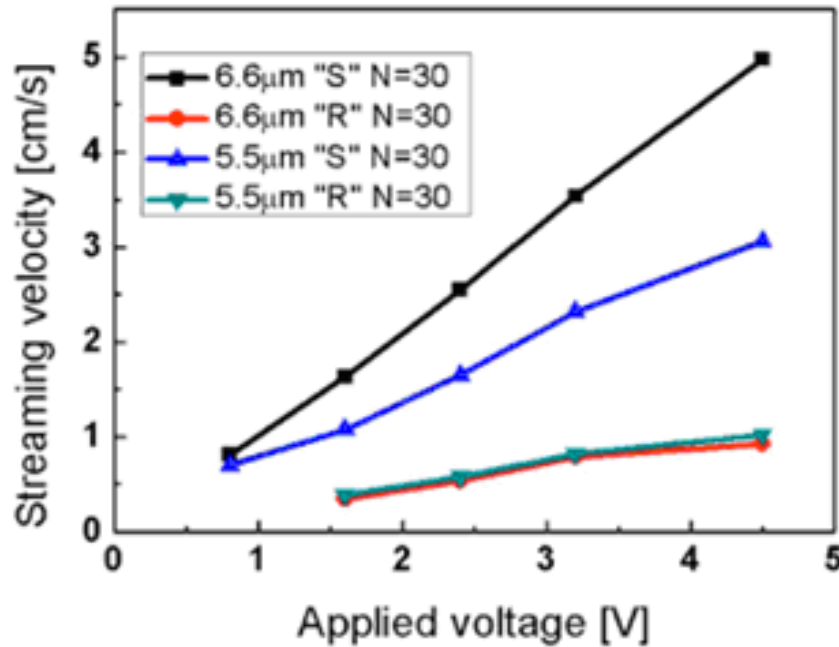
Figure 2-17. Relationship between streaming velocity and applied voltage. The streaming
velocities of the Sezawa (S) mode are larger than the Rayleigh (R) mode for SAW device using
ZnO thin film with two different thicknesses and same number of IDT finger pairs (N). From Du
et al. (2008) [93]. Copyright 2008, American Institute of Physics.

These results highlight the possibility for exploiting thin film ZnO for a wide range of

microfluidics applications. Initial observations show promising results for efficient and

effective microfluidic actuation [88, 100, 101]. An in-depth exploration of the acoustic

streaming phenomenon generated from thin film ZnO SAW could open up potential areas of research for various droplet microfluidic actuations from particle concentration[72], centrifugation[74] to atomization [71]. The higher frequency of operation also provides prospective integration capability with Radio Frequency (RF) systems to make remote-actuated microfluidic chips.

2.3.1 Summary and Research Rationale

While considerable amount of research has been dedicated to SAW driven microfluidics, the research to date is mainly limited to the use of 127.68° Y-X cut lithium niobate (LiNbO$_3$) piezoelectric substrate to generate the SAW. Despite the advantage of high electromechanical coupling, actuation in this material is restricted to a single axis. Therefore, there is a need to investigate the possibility of using alternative piezoelectric materials to address this limitation. Little research has been conducted in investigating ZnO as potential materials for SAW microfluidics. It is a common piezoelectric material widely used in many other areas and has vast potential for microfluidics utilization. Exploration of this material to generate SAW for microfluidics manipulation is therefore performed. The results are presented and discussed in chapter 4 of this thesis.

References

1.   Hess, P., *Surface acoustic waves in materials science.* Physics Today, 2002. **55**(3): p. 42-48.
2.   Asai, K., M.K. Kurosawa, and T. Higuchi. *Evaluation of the driving performance of a surface acoustic wave linear motor.* 2000. IEEE.
3.   Farnell, W., *Types and properties of surface.* Acoustic surface waves, 1978: p. 13-60.
4.   Cheeke, J.D.N., *Fundamentals and applications of ultrasonic waves*2002: CRC.
5.   Rudenko, O.V. and S.I. Soluyan, *Theoretical foundations of nonlinear acoustics*1977: Consultants Bureau.
6.   Kotani, H., M. Takasaki, and T. Mizuno, *Surface AcousticWave Linear Motor Using Glass Substrate.* Motion and Vibration Control, 2009: p. 211-219.
7.   Morgan, D.P., *Surface Acoustic Wave Devices and Applications - 1. Introductory Review.* Ultrasonics, 1973. **11**(3): p. 121-131.
8.   Hickernell, F.S., *Surface acoustic wave technology, macrosuccess through microseisms.* Physical Acoustics, 1999. **24**: p. 135-207.
9.   White, R.M., *Acoustic interactions from faraday's crispations to mems.* Faraday Discuss., 1997. **107**: p. 1-13.
10.   Tang, I.T., et al., *A novel integrable surface acoustic wave notch filter.* Solid-State Electronics, 2003. **47**(11): p. 2063-2066.
11.   Shigematsu, T. and M.K. Kurosawa. *Miniaturized SAW motor with 100 MHz driving frequency.* in *Proceedings of the IEEE International Conference on Micro Electro Mechanical Systems (MEMS).* 2004. Maastricht.
12.   Wixforth, A., *Acoustically driven planar microfluidics.* Superlattices and Microstructures, 2003. **33**(5-6): p. 389-396.
13.   Watson, B., J. Friend, and L. Yeo, *Piezoelectric ultrasonic micro/milli-scale actuators.* Sensors and Actuators A: Physical, 2009. **152**(2): p. 219-233.
14.   Liu, D.K.C., J. Friend, and L. Yeo, *A brief review of actuation at the micro-scale using electrostatics, electromagnetics and piezoelectric ultrasonics.* Acoustical Science and Technology, 2010. **31**(2): p. 115-123.
15.   Barbic, M., et al., *Electromagnetic micromotor for microfluidics applications.* Applied Physics Letters, 2001. **79**(9): p. 1399-1401.
16.   Friend, J., et al., *A simple bidirectional linear microactuator for nanopositioning - The "Baltan" microactuator.* IEEE Transactions on Ultrasonics, Ferroelectrics, and Frequency Control, 2006. **53**(6): p. 1160-1167.
17.   Friend, J., K. Nakamura, and S. Ueha, *A piezoelectric micromotor using in-plane shearing of PZT elements.* IEEE/ASME Transactions on Mechatronics, 2004. **9**(3): p. 467-473.
18.   Friend, J., K. Nakamura, and S. Ueha, *A traveling-wave, modified ring linear piezoelectric microactuator with enclosed piezoelectric elements - The "scream" actuator.* IEEE Transactions on Ultrasonics, Ferroelectrics, and Frequency Control, 2005. **52**(8): p. 1343-1353.
19.   Asai, K., M.K. Kurosawa, and T. Higuchi, *Energy circulation methods for surface acoustic wave motor.* Electronics and Communications in Japan (Part III: Fundamental Electronic Science), 2004. **87**(2): p. 10-19.

20.   Friend, J.R., *Analysis of the 0.668 inch traveling-wave piezoelectric motor.* Proceedings of the 37th AIAA/ASME/ASCE/AHS/ASC Structures, Structural Dynamics, and Materials Conference and Exhibit. , 1996. **96**(1452): p. 1-15.

21.   Biwersi, S., et al., *Production of a quasi-travelling wave in silicon membranes with a thin deposited layer of sol--gel PZT.* Sensors and Actuators A: Physical, 1998. **70**(3): p. 291-295.

22.   Flynn, A.M., et al., *Piezoelectric micromotors for microrobots.* Microelectromechanical Systems, Journal of, 1992. **1**(1): p. 44-51.

23.   Ueha, S., et al., *Ultrasonic motors: theory and applications*1993: Clarendon Press Oxford.

24.   Hong, E., et al., *Vibration of micromachined circular piezoelectric diaphragms.* IEEE Transactions on Ultrasonics, Ferroelectrics, and Frequency Control, 2006. **53**(4): p. 697-706.

25.   Kuribayashi Kurosawa, M., M. Takahashi, and T. Higuchi, *Elastic contact conditions to optimize friction drive of surface acoustic wave motor.* Ultrasonics, Ferroelectrics and Frequency Control, IEEE Transactions on, 1998. **45**(5): p. 1229-1237.

26.   Kurosawa, M., et al., *Surface acoustic wave atomizer.* Sensors and Actuators, A: Physical, 1995. **50**(1-2): p. 69-74.

27.   Kurosawa, M.K., M. Chiba, and T. Higuchi, *Evaluation of a surface acoustic wave motor with a multi-contact-point slider.* Smart Materials and Structures, 1998. **7**(3): p. 305-311.

28.   Kurosawa, M.K., et al. *Surface acoustic wave motor with feed back controller considering dead zone*. in *IECON Proceedings (Industrial Electronics Conference)*. 2005. Raleigh, NC.

29.   Sakano, K., M.K. Kurosawa, and T. Shigematsu, *Driving characteristics of a surface acoustic wave motor using a flat-plane slider.* Advanced Robotics, 2010. **24**(10): p. 1407-1421.

30.   Kurosawa, M.K., *State-of-the-art surface acoustic wave linear motor and its future applications.* Ultrasonics, 2000. **38**(1-8): p. 15-19.

31.   Morita, T., M.K. Kurosawa, and T. Higuchi, *Simulation of surface acoustic wave motor with spherical slider.* Ultrasonics, Ferroelectrics and Frequency Control, IEEE Transactions on, 1999. **46**(4): p. 929-934.

32.   Kurosawa, M.K., et al. *Micro linear motor using surface acoustic wave device*. 2002. IEEE.

33.   Nguyen, N.T. and Z. Wu, *Micromixers --- a review.* Journal of Micromechanics and Microengineering, 2005. **15**: p. R1.

34.   Kurosawa, M., M. Takahashi, and T. Higuchi, *Friction drive surface acoustic wave motor.* Ultrasonics, 1996. **34**(2-5): p. 243-246.

35.   Barbulovic-Nad, I., et al., *DC-dielectrophoretic separation of microparticles using an oil droplet obstacle.* Lab Chip, 2005. **6**(2): p. 274-279.

36.   Emanetoglu, N.W., et al. *MOCVD growth and SAW properties of epitaxial ZnO thin films*. 1998. IEEE.

37.   Tjeung, R.T., et al., *Surface acoustic wave micromotor with arbitrary axis rotational capability.* Applied Physics Letters, 2011. **99**(21): p. 214101.

38.   Alexis, F., et al., *Factors affecting the clearance and biodistribution of polymeric nanoparticles.* Molecular pharmaceutics, 2008. **5**(4): p. 505-515.

39.   Buxton, D.B., *Nanomedicine for the management of lung and blood diseases.* Nanomedicine, 2009. **4**(3): p. 331-339.

40.   Shigematsu, T. and M.K. Kurosawa, *XY surface acoustic wave motor with nanometer resolution.* Proceeding of the 21st Sensors Symposium, 2004., 2004: p. 237-240.

41.   Asai, K. and M.K. Kurosawa, *Simulation model of surface acoustic wave motor considering tangential rigidity.* Electronics and Communications in Japan (Part III: Fundamental Electronic Science), 2004. **87**(2): p. 54-66.

42.   Asai, K. and M.K. Kurosawa, *Performance estimation of surface acoustic wave motor using simulation model of friction drive.* Electronics and Communications in Japan (Part III: Fundamental Electronic Science), 2005. **88**(1): p. 37-47.

43.   Kadota, M., *Development of substrate structures and processes for practical applications of various surface acoustic wave devices.* Jpn. J. Appl. Phys, 2005. **44**(6 B): p. 4285-4291.

44.   Kurosawa, M., M. Takahashi, and T. Higuchi, *Ultrasonic linear motor using surface acoustic waves.* Ultrasonics, Ferroelectrics and Frequency Control, IEEE Transactions on, 1996. **43**(5): p. 901-906.

45.   Sakano, K., M.K. Kurosawa, and T. Shigematsu. *Surface Acoustic Wave Motor with Flat Plane Slider*. 2008. IEEE.

46.   Cheng, L.P., et al., *Miniaturization of surface acoustic waves rotary motor.* Ultrasonics, 2002. **39**(8): p. 591-594.

47.   Zhang, G.M., et al., *Surface acoustic wave rotation motor.* Electronics Letters, 2000. **36**(16): p. 1437-1438.

48.   Shilton, R.J., et al., *Rotational microfluidic motor for on-chip microcentrifugation.* Applied Physics Letters, 2011. **98**(25).

49.   Hsiao, Y.-J., et al., *Surface acoustic wave characteristics and electromechanical coupling coefficient of lead zirconate titanate thin films.* Materials Letters, 2006. **60**(9-10): p. 1140-1143.

50.   Kirby, P.B., et al. *PZT thin film bulk acoustic wave resonators and filters*. in *Frequency Control Symposium and PDA Exhibition, 2001. Proceedings of the 2001 IEEE International*. 2001.

51.   Tsai, C.C., S.Y. Chu, and C.H. Lu, *Doping Effects of CuO Additives on the Properties of Low-Temperature-Sintered PMnN-PZT-Based Piezoelectric Ceramics and Their Applications on Surface Acoustic Wave Devices.* Ieee Transactions on Ultrasonics Ferroelectrics and Frequency Control, 2009. **56**(3): p. 660-668.

52.   Squires, T.M. and S.R. Quake, *Microfluidics: Fluid physics at the nanoliter scale.* Reviews of Modern Physics, 2005. **77**(3): p. 977.

53.   Whitesides, G.M., *The origins and the future of microfluidics.* Nature, 2006. **442**(7101): p. 368-373.

54.   Yeo, L.Y. and J.R. Friend, *Ultrafast microfluidics using surface acoustic waves.* Biomicrofluidics, 2009. **3**(1).

55.   Beyssen, D., et al., *Microfluidic device based on surface acoustic wave.* Sensors and Actuators B: Chemical, 2006. **118**(1-2): p. 380- 385.

56.   Schneider, M.F., et al., *An acoustically driven microliter flow chamber on a chip (µFCC) for cell-cell and cell-surface interaction studies.* ChemPhysChem, 2008. **9**: p. 641-645.

57.   Friend, J. and L.Y. Yeo, *Microscale acoustofluidics: Microfluidics driven via acoustics and ultrasonics.* Reviews of Modern Physics, 2011. **83**(2): p. 647.

58.   Wacogne, B., et al., *Effective piezoelectric activity of zinc oxide films grown by radio-frequency planar magnetron sputtering.* Applied Physics Letters, 1995. **67**(12): p. 1674-1676.

59. Wixforth, A., et al., *Acoustic manipulation of small droplets.* Analytical and Bioanalytical Chemistry, 2004. **379**(7-8): p. 982-991.

60. Cecchini, M., et al., *Acoustic-counterflow microfluidics by surface acoustic waves.* Applied Physics Letters, 2008. **92**(10): p. 104103-3.

61. Friend, J.R., et al., *Evaporative self-assembly assisted synthesis of polymeric nanoparticles by surface acoustic wave atomization.* Nanotechnology, 2008. **19**(14).

62. Tan, M.K., *Microparticle collection and concentration via a miniature surface acoustic wave device.* Lab on a Chip, 2007. **7**(5): p. 618-625.

63. Tan, M.K., J.R. Friend, and L.Y. Yeo, *Direct visualization of surface acoustic waves along substrates using smoke particles.* Applied Physics Letters, 2007. **91**(22).

64. Tan, M.K., et al., *Double aperture focusing transducer for controlling microparticle motions in trapezoidal microchannels with surface acoustic waves.* Applied Physics Letters, 2009. **95**(13): p. 134101-3.

65. Sritharan, K., et al., *Acoustic mixing at low Reynold's numbers.* Applied Physics Letters, 2006. **88**(5).

66. Schneider, M.F., et al., *An acoustically driven microliter flow chamber on a chip (μFCC) for cell-cell and cell-surface interaction studies.* ChemPhysChem, 2008. **9**(4): p. 641-645.

67. Shilton, R., et al., *Particle concentration and mixing in microdrops driven by focused surface acoustic waves.* Journal of Applied Physics, 2008. **104**(1).

68. Rathgeber, A., M. Wassermeier, and A. Wixforth, *Acoustic'distributed source' mixing of smallest fluid volumes.* Journal of ASTM International, 2005. **2**(6): p. 259-266.

69. Renaudin, A., et al., *SAW nanopump for handling droplets in view of biological applications.* Sensors and Actuators, B: Chemical, 2006. **113**(1): p. 389-397.

70. Qi, A., J. Friend, and L. Yeo. *SAW atomization application on inhaled pulmonary drug delivery.* in *Biomedical Applications of Micro- and Nanoengineering IV and Complex Systems.* 2008. Melbourne, Australia: SPIE.

71. Qi, A., L.Y. Yeo, and J.R. Friend, *Interfacial destabilization and atomization driven by surface acoustic waves.* Physics of Fluids, 2008. **20**(7): p. 074103-14.

72. Li, H., J.R. Friend, and L.Y. Yeo, *Surface acoustic wave concentration of particle and bioparticle suspensions.* Biomedical Microdevices, 2007. **9**(5): p. 647.

73. Li, H., J.R. Friend, and L.Y. Yeo, *A scaffold cell seeding method driven by surface acoustic waves.* Biomaterials, 2007. **28**(28): p. 4098-4104.

74. Raghavan, R.V., J.R. Friend, and L.Y. Yeo, *Particle concentration via acoustically driven microcentrifugation: MicroPIV flow visualization and numerical modelling studies.* Microfluidics and Nanofluidics, 2009. **8**(1): p. 73-84.

75. Čiplys, D. and R. Rimeika, *Electromechanical coupling coefficient for surface acoustic waves in proton-exchanged 128Â°-rotated Y-cut lithium niobate.* Applied Physics Letters, 1998. **73**(17): p. 2417-2419.

76. Weis, R.S. and T.K. Gaylord, *Lithium niobate: Summary of physical properties and crystal structure.* Applied Physics A Solids and Surfaces, 1985. **37**(4): p. 191-203.

77. Jagadish, C. and S.J. Pearton, *Zinc Oxide Bulk, Thin Films and Nanostructures* 2006: Elsevier Science Ltd.

78. Wang, Q.J., et al., *Gigahertz surface acoustic wave generation on ZnO thin films deposited by radio frequency magnetron sputtering on III-V semiconductor substrates.* Journal of vacuum science & technology. B, Microelectronics and nanometer structures, 2008. **26**(6): p. 1848-1851.

79.   Dang, W.L., et al., *Deposition and characterization of sputtered ZnO films.* Superlattices and Microstructures, 2007. **42**(1-6): p. 89-93.

80.   Gorla, C.R., et al., *Structural, optical, and surface acoustic wave properties of epitaxial ZnO films grown on (011-bar 2) sapphire by metalorganic chemical vapor deposition.* Journal of Applied Physics, 1999. **85**(5): p. 2595-2602.

81.   Muthukumar, S., et al., *Control of morphology and orientation of ZnO thin films grown on SiO2/Si substrates.* Journal of Crystal Growth, 2001. **225**(2-4): p. 197-201.

82.   Nakahata, H., et al. *High frequency surface acoustic wave filter using ZnO/diamond/Si structure*. in *Ultrasonics Symposium, 1992. Proceedings., IEEE 1992*. 1992.

83.   Pearton, S.J., et al., *Recent progress in processing and properties of ZnO.* Superlattices and Microstructures, 2003. **34**(1-2): p. 3-32.

84.   Su, Q.X., et al., *Thin-film bulk acoustic resonators and filters using ZnO and lead-zirconium-titanate thin films.* Microwave Theory and Techniques, IEEE Transactions on, 2001. **49**(4): p. 769-778.

85.   Tay, K.-W., et al., *Characteristics of ZnO thin film for film bulk acoustic-wave resonators.* Journal of Electroceramics.

86.   Hickernell, F.S., *ZINC OXIDE FILMS FOR ACOUSTOELECTRIC DEVICE APPLICATIONS.* IEEE transactions on sonics and ultrasonics, 1985. **SU-32**(5): p. 621-629.

87.   Laude, V., et al., *Surface acoustic wave trapping in a periodic array of mechanical resonators.* Applied Physics Letters, 2006. **89**(8): p. 083515-3.

88.   Le Brizoual, L., et al., *High frequency SAW devices based on third harmonic generation.* Ultrasonics, 2006. **45**(1-4): p. 100-103.

89.   Yamaguchi, R. and Y. Sato, *Range of Possible Existence of Rayleigh-and Sezawa-Waves in a Stratified Medium.* 1955.

90.   Luo, J.K., et al., *Integrated ZnO Film Based Acoustic Wave Microfluidics and Biosensors.* Advances in Science and Technology. **67**: p. 49-58.

91.   Du, X.Y., et al., *Microfluidic pumps employing surface acoustic waves generated in ZnO thin films.* Journal of Applied Physics, 2009. **105**(2): p. 024508-7.

92.   Du, X.Y., et al., *ZnO film for application in surface acoustic wave device.* Journal of Physics: Conference Series, 2007. **76**: p. 012035.

93.   Du, X.Y., et al., *ZnO film thickness effect on surface acoustic wave modes and acoustic streaming.* Applied Physics Letters, 2008. **93**(9): p. 094105-3.

94.   Du, X.Y., et al., *Surface acoustic wave induced streaming and pumping in 128° Y-cut LiNbO3 for microfluidic applications.* Journal of Micromechanics and Microengineering, 2009(3): p. 035016.

95.   Kanai, K., *On Sezawa-waves (M2-waves).: Part II.* 1955.

96.   Sezawa, K. and K. Kanai, *The M2 seismic waves.* 1935.

97.   Kanai, K., *On the M2-waves (Sezawa-waves).* 1951.

98.   Sezawa, K. and K. Kanai, *1. The Range of Possible Existence of Stoneley-waves, and Some Related Problems.* 1939.

99.   Yaralioglu, G.G., et al., *Ultrasonic Mixing in Microfluidic Channels Using Integrated Transducers.* Analytical Chemistry, 2004. **76**(13): p. 3694-3698.

100.   Fu, Y.Q., et al., *Recent developments on ZnO films for acoustic wave based bio-sensing and microfluidic applications: a review.* Sensors and Actuators B: Chemical, 2009. **143**(2): p. 606-619.

101.   Luo, J.K., et al., *Moving-part-free microfluidic systems for lab-on-a-chip.* Journal of Micromechanics and Microengineering, 2009. **19**: p. 054001.

Chapter 3

SAW actuated rotary motor

3.1 Introduction

As discussed in Chapter 2, piezoelectric motors exhibit superior performance qualities compared to many other actuation principles. However, some difficulties associated with piezoelectric motor, especially fabrication challenges, greatly hinder the progress in this area. Using SAW as the piezoelectric actuation method is an inventive way to overcome this challenge.

3.2 SAW rotary motor (method and characterization)

Extensive work on SAW linear motors has been performed previously, however little has been reported regarding exploiting SAW to produce a rotational motor. To achieve rotation, counter propagating SAW must be created along the object. Cheng et al[1, 2] used a complex contraption to achieve rotation, and Shilton et al has reported rotation inside a liquid[3]. However, a motor in which a rotor rotates in its own center of rotation is yet to be reported. We report here such a motor. The stator is a SAW device; consisting

of IDTs fabricated on top of a piezoelectric material which produces travelling SAW waves called a Rayleigh wave. We can use the force generated by this travelling wave to actuate a solid object in a stick-slip mechanism. The rotor selected in this work is a 1 mm solid steel sphere. As stated in the introduction chapter, the dimension is selected for proof-of-concept purpose, for demonstrating the ability of SAW to rotate a large and heavy object.

3.2.1 Working principle

The working principle of the rotating SAW motor is similar to the linear SAW motor. The working principle is summarized in Figure 3.1. The IDTs are activated (provided with input RF signal) generating SAW which travels away from the IDT. As the SAW propagate away from the IDT, (left to right in Figure 3.1), the particle on the surface move elliptically in a retrograde fashion. These motions give rise to a resultant force in the opposite direction of the SAW propagation. Consequently, if a round shape solid object is placed on top of the surface --- at the point of contact--- the attractive force shall create a torque with respect to the center of the solid object. The torque produced shall give rise to rotational motion.
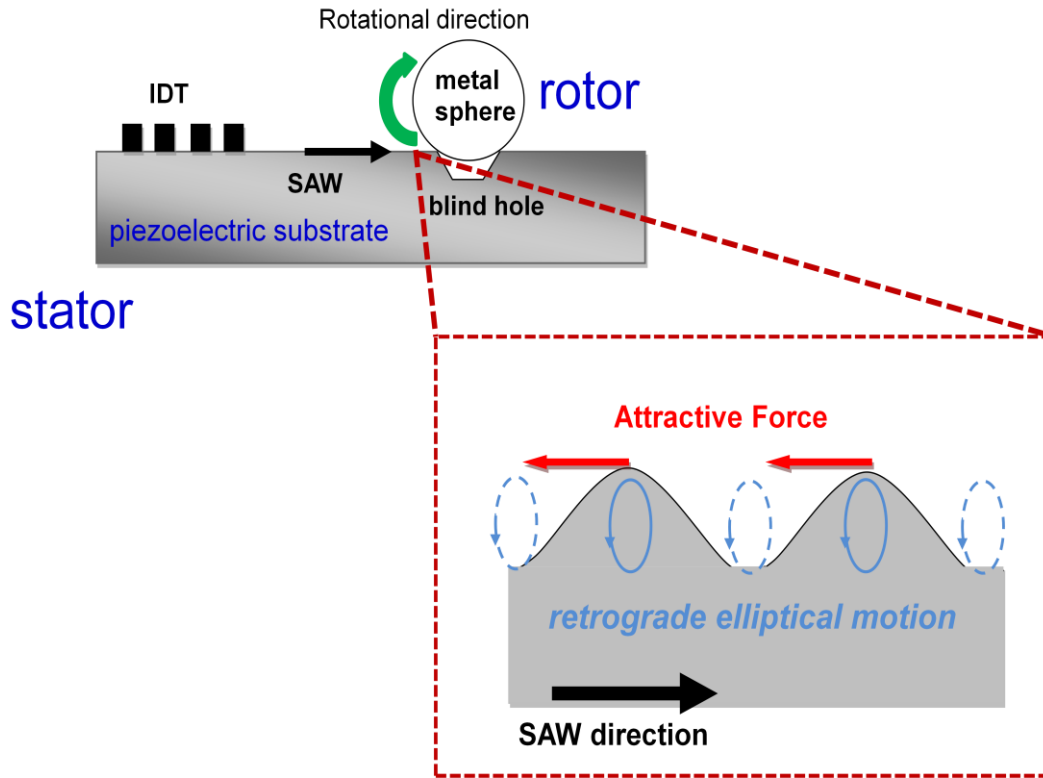
Figure 3.1. The working principle of the motor. The images are shown in cross-sectional views and are not to scale. The retrograde elliptical motion of the surface as the wave passes acts against the ball's inertia—which is small; its weight is hence *negligible*— that causes about the rotation. This is true due to the large SAW acceleration; which is up to *five orders of magnitude larger* than the gravitational acceleration. As SAW propagates parallel to the position of the IDT which generates it, the rotor rotates about an axis parallel to the substrate and perpendicular to the incident SAW propagation.

3.2.2 Method

Figure 3.2 shows the steps of the work performed on this project. The work started with designing the motor configuration, continued with the fabrication of the motor; which included SAW device fabrication and blind hole microdrilling. After the fabrication step had been completed, characterization of the travelling wave propagation around the hole was performed using a Laser Doppler Vibrometer (LDV; Polytec PI MSA-400,

47

Waldbrunn, Germany). The final step was then to operate the motor and measure the performances.

| Material selection | Design |

SAW device Fabrication

Blind hole microdrilling | Fabrication

Wave visualization around the hole | Characterization

Operation of the SAW motor

Without external preload / With external preload

transient response / transient response

torque speed curve model / torque speed curve model | Operation
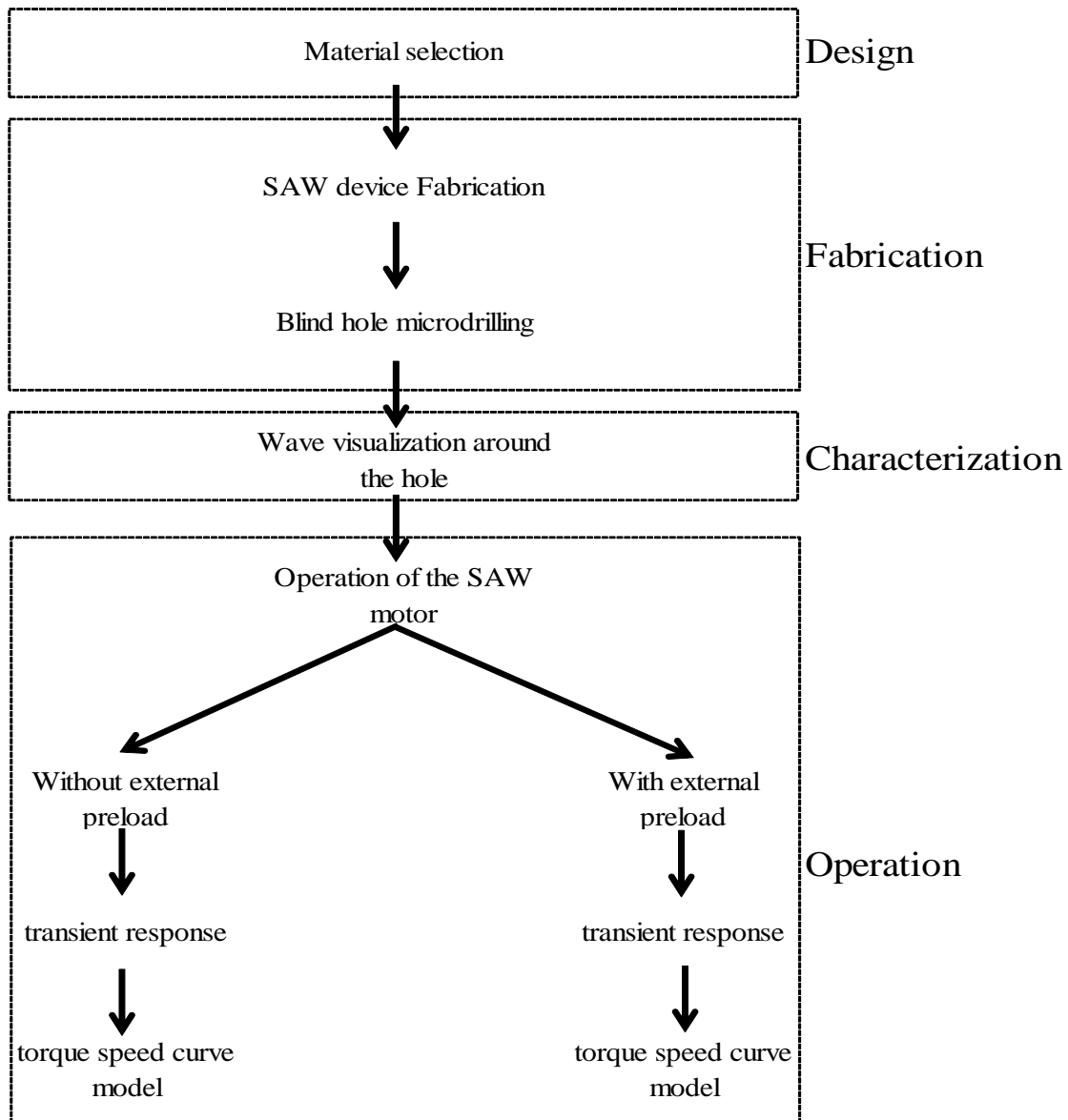
Figure 3.2. Work steps performed on this project. The work includes, firstly, the motor configuration design and fabrication; the wave propagation characterization; lastly, motor operation and performance analysis.

3.2.3 Motor configuration

A solid steel sphere of 1 mm diameter size was selected as the rotor. SAW device made on a on the surface of a lead zirconate titanate (PZT C-203, Fuji Ceramics Corporation, Tokyo, Japan) ceramic substrate was selected as the stator. PZT disk (40 mm diameter and 0.99 mm thick) was chosen due to its high electromechanical coupling (~20%) and isotropic piezoelectric properties, which are essential for high power actuation and multiple axis actuations, respectively [4-6].

The metal sphere (rotor) is placed onto a blind hole drilled on the PZT surface. The blind hole is used to confine the rotor from translating during operation. SAWs are then generated by applying a continuous sinusoidal electrical input into an interdigital transducer (IDT) patterned on a surface of the PZT ceramic substrate.

3.2.4 SAW device fabrication

The PZT ceramics purchased comes with 2 μm thick silver (Ag) layer deposited on its surface. Standard microfabrication techniques, employing photolithography and etching processes, were utilized to fabricate the IDTs. The devices were designed to work with a 3.2 MHz resonance frequency, resulting in a 700 μm wavelength. Photolithographic mask was designed using a versatile layout and design system for integrated circuits

(LAyout System for Individuals/LASI) and produced in a transparency materials (CAD/Art Services Inc.).

The IDT design was as follow:

- finger width and spacing was 150 μm,

- bus bar was 500 μm,

- aperture width was 3 mm,

- bond pad was 3 mm,

- number of IDT fingers was 7 finger-pair.

The fabrication steps can be viewed as Figure 3.3, and the fabricated devices can be viewed at Figure 3.4, shown with the mask design.

The fabrication steps were as follow (refer to Figure 3.3):

1. Photoresist coating

    a. The positive photoresist (AZ 4562, AZ Electronics Materials) was spread onto a spin coater (Delta 80RC, SUSS MicroTec AG).

    b. Maximum rotation velocity of 3000 rpm for 30 s.

    c. Soft bake at 90°C for 20 minute in a vacuum drying oven (Heraeus instrument vacutherm, Thermo Fisher Scientific Inc.).

    d. Thickness of the photoresist is ~ 5 μm

2. Ultraviolet (UV) exposure

a. Utilizing a photolithographic mask (CAD/Art Services Inc.)

b. The UV (365 nm wavelength) exposure was performed using a mask aligner (MA6, SUSS MicroTec AG)

c. Use hard contact vacuum exposure for a dose of 100 mJ/cm^2.

3. Developing and Etching

a. The photoresist was developed using a mixture of photoresist developer (AZ400K, AZ Electronics Materials) with de-ionized (DI) water for a total developing time of 70 seconds.

b. The sample was further baked in a vacuum oven (Heraeus instrument vacutherm, Thermo Fisher Scientific Inc.) at 110°C for 20 minute.

c. The Ag layer was etched using an etching solution, a mixture of 4 g Potassium Iodide (KI), 1 g Iodine (I_2), and 40 ml Water (H_2O).

4. Photoresist removal

a. The photoresist layer was finally removed by acetone ((CH_3)$_2$CO) to yield the interdigital transducers of the SAW devices.

1. Photoresist coating

Photoresist

Ag

PZT

UV Lamp

Photolithographic mask

Photoresist

Ag

PZT

2. UV Exposure

Photoresist

Ag

PZT

3. Developing and etching

Ag

PZT
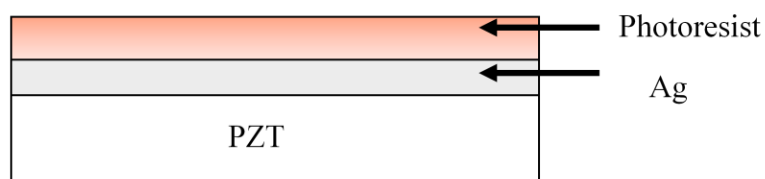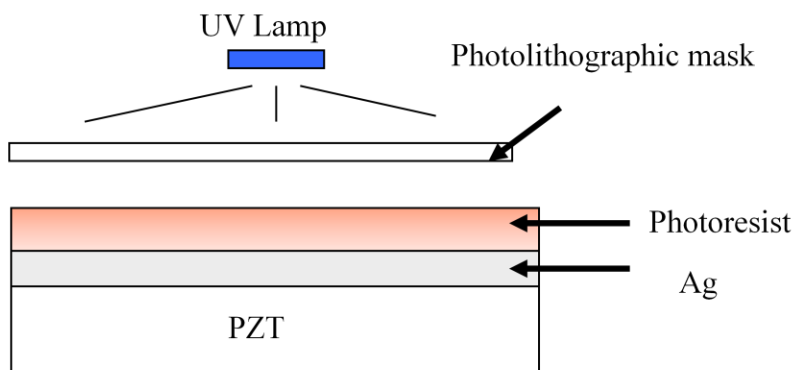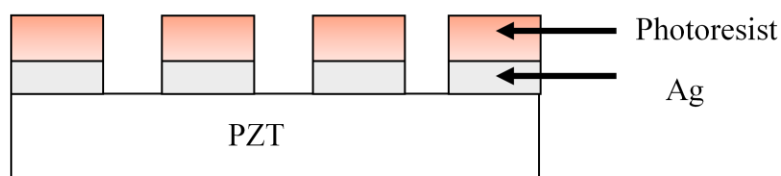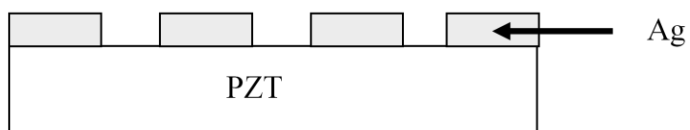
4. Photoresist Removal

Figure 3.3. The fabrication steps of the SAW devices, which include photoresist coating using a spin coater (Delta 80RC, SUSS MicroTec AG), ultraviolet (UV) exposure using a Mask Aligner (MA6, SUSS MicroTec AG), chemical wet etch using a solution of potassium iodide and iodine, and photoresist removal using acetone.

(a)   (b)
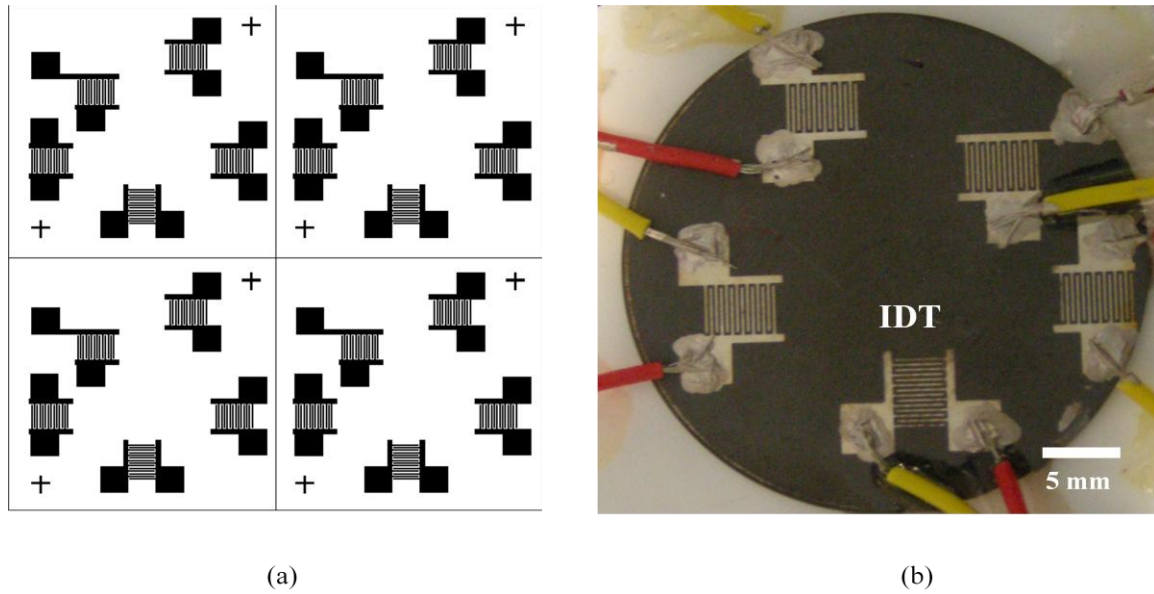
Figure 3.4. Images of the IDT design on the PZT substrate; (a) the photolithographic mask design and (b) the fabricated device with holes drilled.

3.2.5 Blind hole microdrilling

After the SAW devices were fabricated, the next step the stator construction was the hole on the surface of the substrate. Two sizes of holes were created, 0.25 mm and 0.45 mm diameter, using a precision table top drilling machine (SERIES 16 - 1/16 HP, Dumore Corporation). The depth of the hole was approximately one-third the thickness of the PZT disk, ~ *350 μm*. According to calculation discussed in subsequent subchapter, the hole does hinder the performance of the motor; hence they have to be as small as possible, yet comparable to the sphere and in the same order of magnitude with the SAW wavelength. The PZT surface was wetted by water during the drilling process. This was done for two reasons, namely, heat dissipation and lead containment.
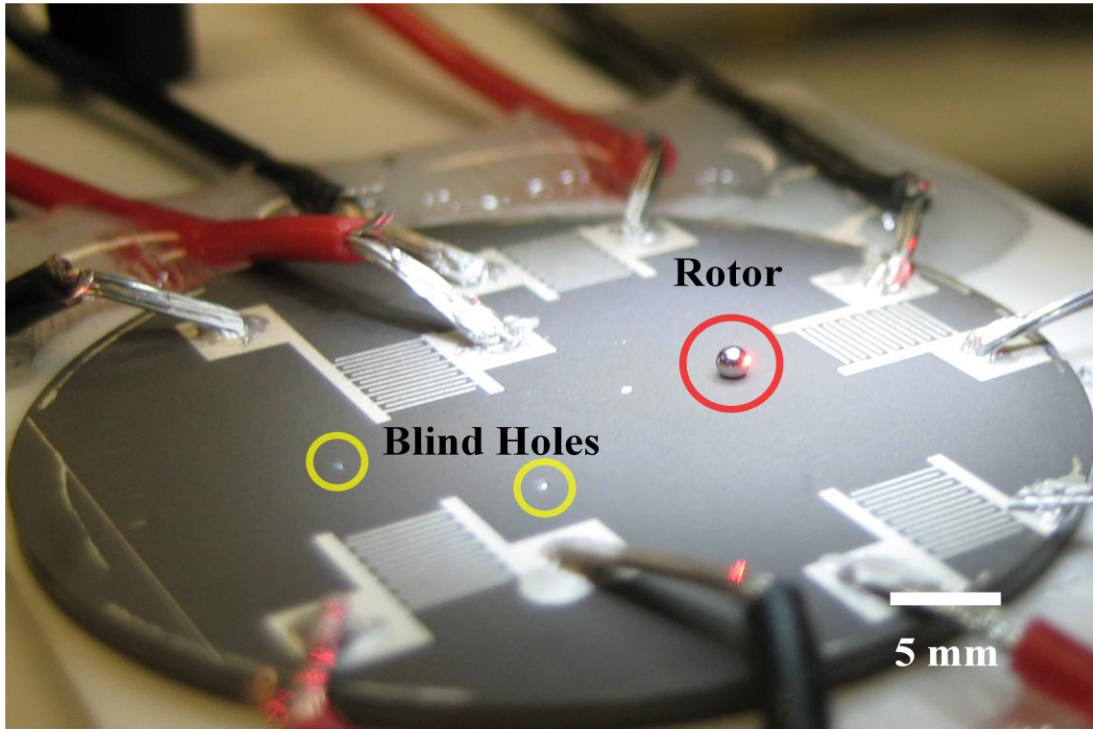
Figure 3.5. Image of the SAW motor; consists of multiple IDTs on top of a PZT substrate which act as the stator and 1 mm solid sphere on top of a blind hole (0.25 mm and 0.45 mm width) which acts as the rotor. The blind holes and rotor are positioned within 5 mm from the IDT. The IDT finger width and spacing was 150 μm, resulting in a 700 μm wavelength. The IDTs are connected to a set of RF power signal generator and amplifier, the red light on the sphere is the laser from the tachometer sensing the rotation of the sphere.

3.2.6 Wave measurement and visualization

The finished stator was examined using an impedance analyzer (4294A Precision Impedance Analyzer, Agilent) to measure the resonance frequencies of the device. The device resonance frequency was 3.2 MHz as per our design. We followed with amplitude measurement of the travelling SAW using a Laser Doppler Vibrometer with an amplitude resolution of 2 pm @ 4.88 kHz Resolution Band Width (LDV; Polytec PI MSA-400,

Waldbrunn, Germany). The measurement set up (schematic and photographic images) can be viewed at Figure 3.6. Input power was provided using a signal generator (NF Wave Factory, WF1946 2CH) coupled with an amplifier (NF High Velocity Bipolar Amplifier, HSA 4101). The LDV system (MSA-400, Polytec PI, Waldbrunn, Germany) inclusive of an RF junction box and an oscilloscope (LeCroy Corporation), was utilized to measure the vertical vibration amplitude of the SAW.

Figure 3.7 shows the measurement results. The amplitude is represented as $\boldsymbol{\gamma} = A \sin(\omega t)\, \boldsymbol{e}_z$. The vertical vibration velocity is then, $\dot{\boldsymbol{\gamma}} = \frac{d\gamma}{dt}\boldsymbol{e}_z = \omega A \cos(\omega t)\, \boldsymbol{e}_z$, in which the maximum is $\dot{\gamma}_{max} = \omega A = 2\pi f A$. The input voltage was observed to be proportional to both the amplitude and maximum vertical vibration velocity, which is in accordance to previous report [7, 8].
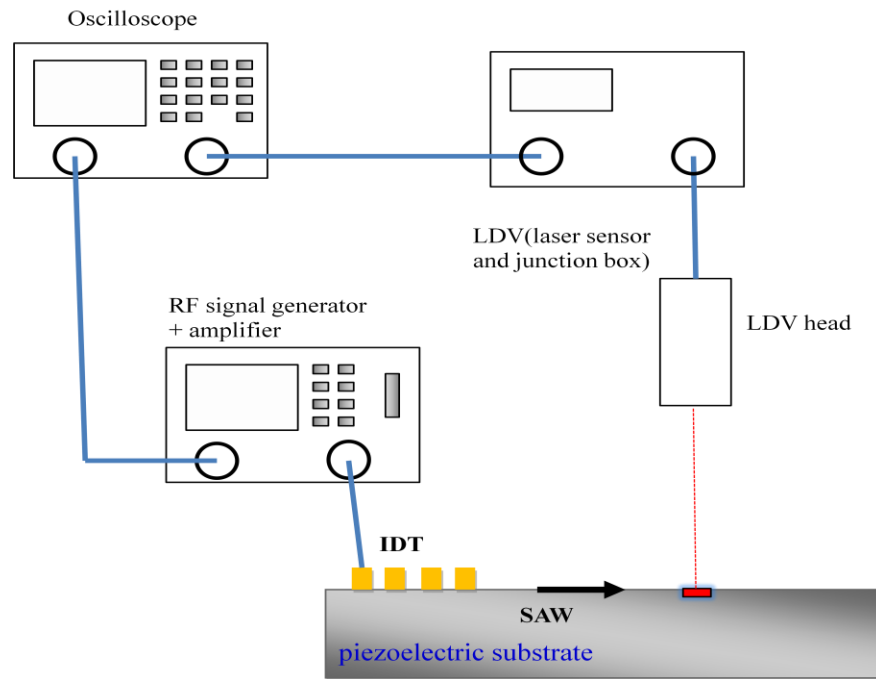
(a)
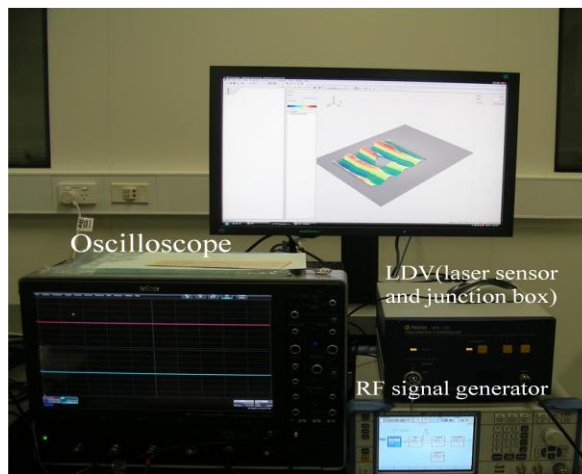
(b)

Figure 3.6. The LDV measurement set up (a) Schematic of the LDV measurement, and (b) photographic images
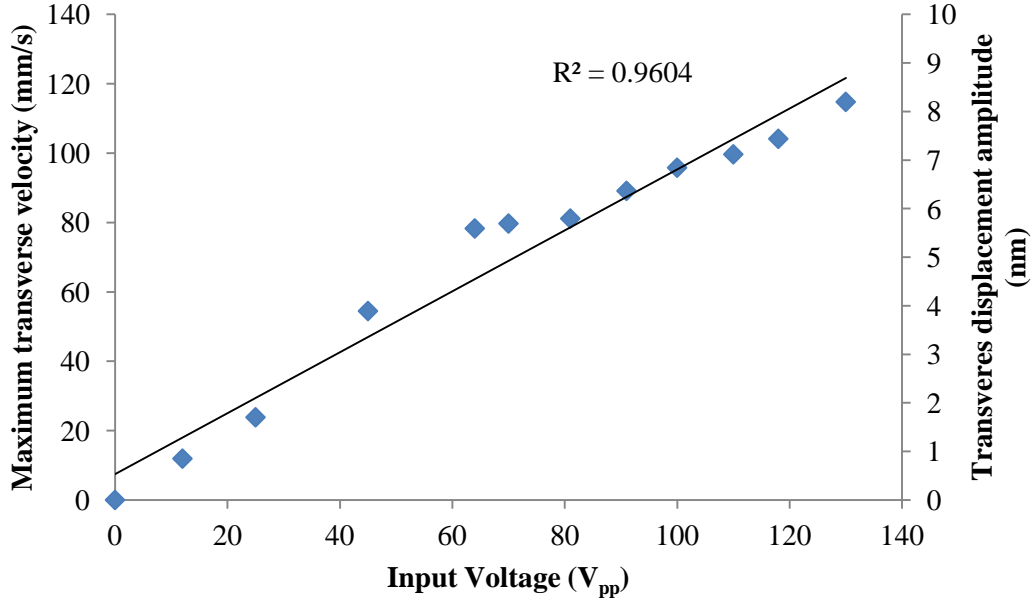
Figure 3.7. Surface acoustic wave measurement and visualization result, measure using an LDV. The maximum transverse displacement and velocity are proportional to the input voltage, which in our measurement up to 8 nm and 120 mm/s for a maximum input displacement of 130 V_{pp}.

We then continued with visualizing and measuring the displacement around the hole. The aim of this work was to observe if the presence of the hole along the SAW propagation pathway significantly affects the travelling wave propagation. The experiment was repeated for different IDTs and holes, and had shown the same results. The result can be viewed in Figure 3.8. In this experiment, the IDT was activated and the travelling wave was measured and visualized using the LDV as it propagates along the 0.25 mm hole. As we can see in Figure 3.8 (a) and subsequent successive images at Figure 3.8 (c), the presence of the hole does not significantly affect the travelling wave. Closer examination as shown in Figure 3.8 (b) shows that the traveling wave is essentially unaffected by the presence of the hole. It does, however, give rise to small discrepancies, expected due to localized reflection which give rise to small component of standing wave and also due to

57

stress release. The absence of data along path B-B in the hole is due to the slopes bottom preventing reflection of the laser in the LDV measurements.
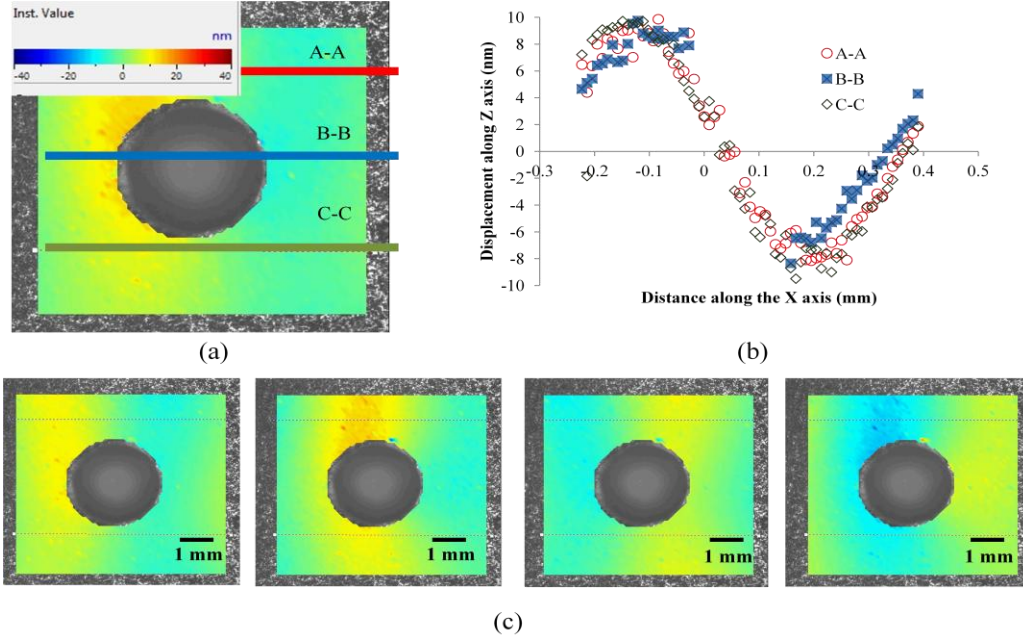
Figure 3.8. (a) SAW propagates left-to-right in the substrate, passing through the hole without substantial change as indicated by LDV measurement of the instantaneous z-polarized displacement, particularly in (b) comparison of the displacements along lines A-A, B-B, and C-C. (c) Progressive images of the displacement, separated in time by 70 ns intervals (representing ~0.22 of the wave period for 3.2 MHz).

It is important to note that as PZT has isotropic piezoelectric properties, SAW can be generated in any direction along the planar orientation of the IDTs. SAW generated on an IDT always propagates parallel and away from it. This motion can be used to generate rotation in any chosen axis along the plane of the wave by proper positioning the rotor with respect to IDT(s) locations. Multiple IDTs activation can, in addition, be used as another means to achieve arbitrary axis rotation. By controlling these, the rotor can be

58

made to rotate in any chosen angle along the planar direction of the wave. Figure 3.9 shows the LDV measurement result; the measured area is located in front of two IDTs, whose axes of wave propagation are perpendicular to each other. The activated IDTs are located below and to the right of the measured area. The SAW propagates from diagonally away from the IDTs, from bottom right to top left; the travelling wave is still a sinusoidal wave as shown in Figure 3.9(b).

(a)   (b)

(c)
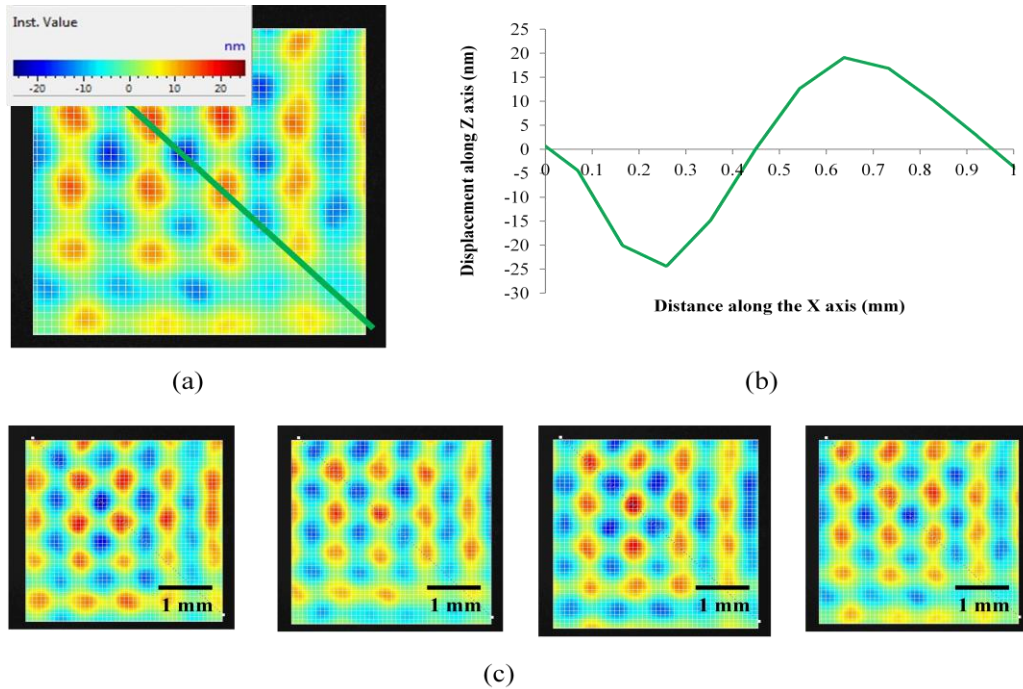
Figure 3.9. Laser Doppler Vibrometer (LDV) visualization of SAW generated by multiple IDTs actuations. The measured area is located in front of two IDTs, whose axes of wave propagation are perpendicular to each other. (a) SAW propagates from bottom right to top left as the activated IDTs were located below and to the right of the measured area; the solid line represents (b) the displacements as the SAW propagates diagonally away from the IDTs. (c) Progressive images of the displacement, separated in time by 70 ns intervals (representing ~0.22 of the wave period for 3.2 MHz).

3.3 SAW rotary motor operation without external preload

After the completion of the SAW visualization, the next step was to characterize the performances of the motor with various configurations during operations. The operation of the motor shall be discussed in two separate sections, with and without the addition of an external preload.

The configurations of the SAW motor can be viewed in Figure 3.10 and Figure 3.11. Input power was provided by a signal generator (NF Wave Factory, WF1946 2CH) coupled with an amplifier (NF High Velocity Bipolar Amplifier, HSA 4101). The signal generator was set to run in the "BURST" mode with 500,000 cycles output. The SAW device (stator) was held using high precision micromanipulators (MMJ manual micromanipulators, Märzhäuser Wetzlar GmbH & Co.). A laser tachometer (Canon, S-100Z) was utilized to measure the transient response of the motor. An oscilloscope (WaveJet 334A, LeCroy Corporation), set to capture data every *0.2 ms*, was connected to both the tachometer set (laser and junction box) and the signal generator. This was done for the purpose of synchronizing the measurement output recording with the signal generator trigger.

As no external preload is required for the motor to operate, the only preload is the weight $(\rho_s \times \frac{4}{3}\pi R^3 \times g$) of the steel sphere itself which is ≈ 40 μN. We have also validated the weight by measurement using analytical balances with an internal calibration mass (GR-

200, A&D Company Ltd.). In this thesis, two configurations of the motor were constructed, one with a 0.25 mm hole and another with a 0.45 mm hole.

In contrast to the linear SAW motor, the rotary motor does not have the requirement of an external preload to operate, likely because of the large interfacial stress present form the line contact. Analysis of the LDV result analysis suggests that the rotor should rotate with axis of rotation parallel to the surface and perpendicular to the SAW propagation path; the experimental results verified this closely.

The schematic of the motor operation is presented in Figure 3.11. As the SAW propagates about e_x (unit vector along the *X-axis*), the rotor always rotates along the same plane yet perpendicular to the SAW propagation path, about e_y. Hence, by placing the rotor along the propagation paths of multiple IDTs, the rotor rotational axis can be controlled by selective IDT activation.
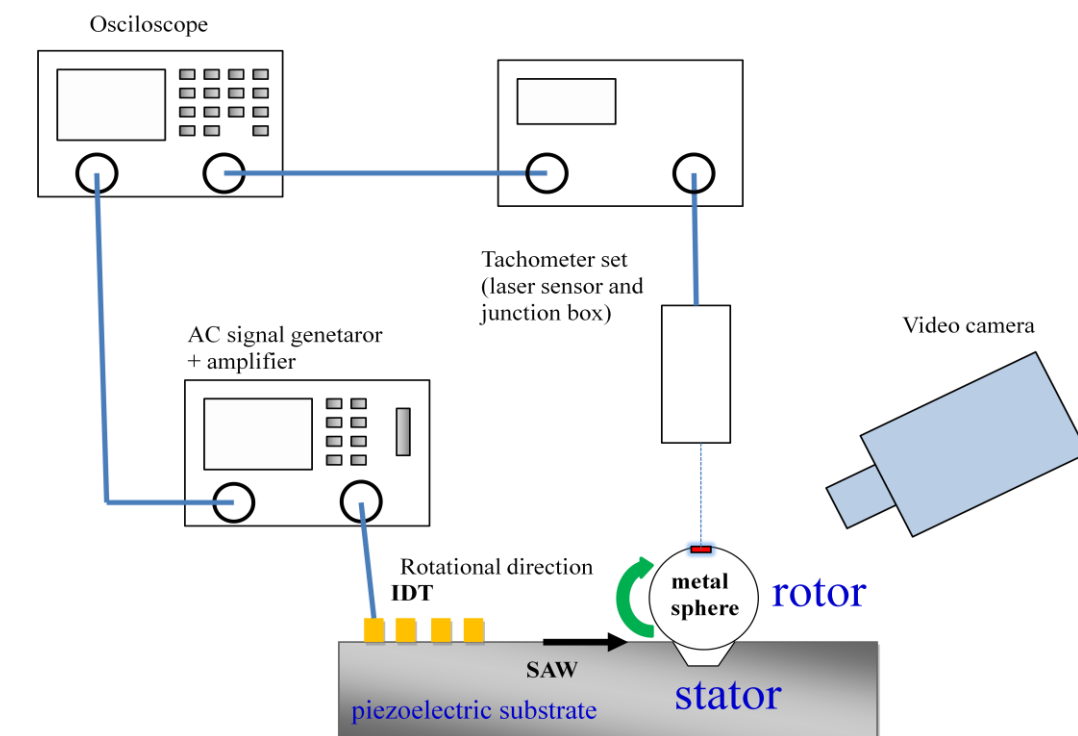
Figure 3.10. Schematic of the experimental set up. During operation the SAW device is connected to a set of signal generator and amplifier which provide RF signal onto the device. Laser tachometer was set up to measure the velocity of the motor, the set includes laser source and sensor and junction box. The junction box output was then connected to an oscilloscope. The oscilloscope was also triggered by the synchronized signal from the signal generator during operation. Video camera was also use to observe the rotation.
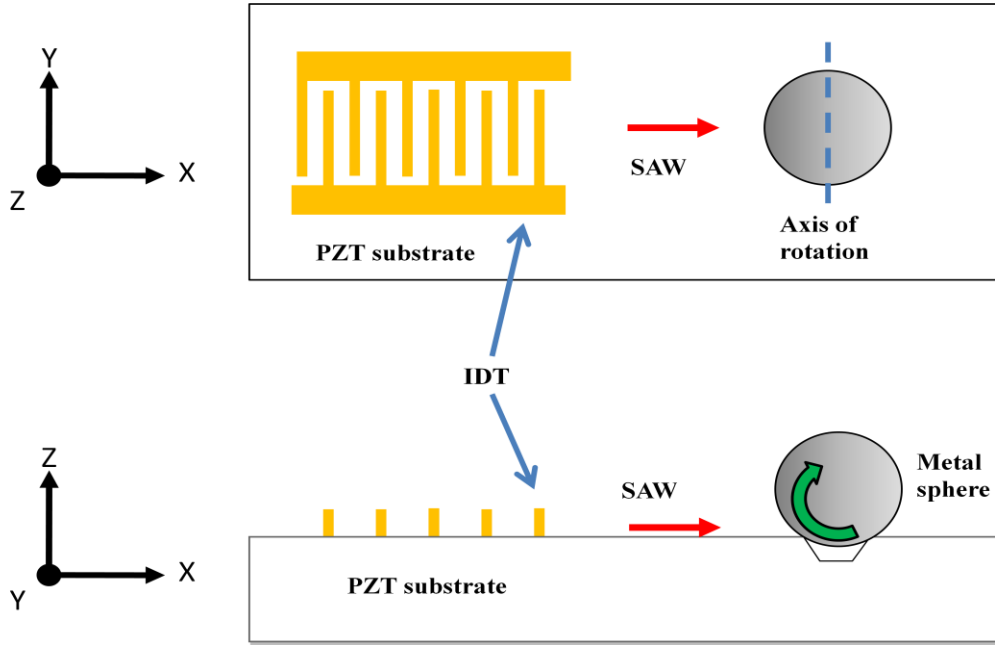
Figure 3.11. Schematic illustration of one mode of operation, i.e. without external pre-load; (a) top view and (b) cross-sectional view. The green arrow shows the rotor rotation direction (about e_y), the axis of rotation is perpendicular to the SAW propagation path (e_x).

3.3.1 Kinematics Estimation

We postulated an approximate estimation for the mechanism of the motor operation. Piezoelectric travelling wave ultrasonic motors use stick-slip mechanism to drive the motion [9-11]. The maximum rotor rotational velocity, ω_{max}, can therefore be estimated using the surface vibration velocity. We assumed, for each point of contact along the contact circle, the rotor is being driven to rotate such that the linear velocity of the rotor at that point, defined from the rotor center by r, in which $r = Re_r$ (refer to Figure 3.12) is equal to the velocity of the substrate at the point of contact, $\dot{\xi} = \dot{\eta} e_x + \dot{\gamma} e_z$. The in-plane rotational velocity component, $\dot{\eta} e_x$, cannot be measured using our LDV, yet it was

reported to be approximately 70% of the transverse component on a bare PZT surface [12]. The e_z component along the contact circle will add itself to zero hence we are left with $\dot{\xi} = \dot{\eta} e_x$. This implies the rotation of the rotor would be given by $\dot{\xi} = \omega \times r$, if the action was only at this point. To find the angular velocity, ω, we find $r \times \dot{\xi} = r \times \omega \times r$
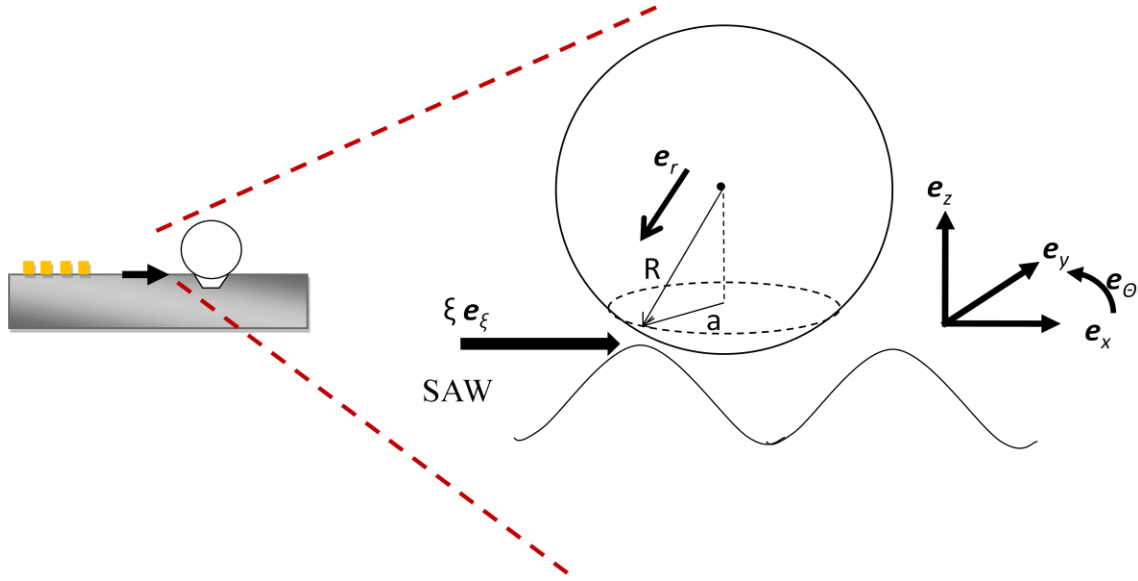
Figure 3.12. Schematic of the motor model, for this case, the SAW is travelling from left to right with ξ as the harmonic displacement, r is the radius of the rotor, and a is the radius of the blind hole.

Using the vector triple product yields, $r \times \dot{\xi} = |r \cdot r|\omega - |\omega \cdot r|r$. Recognizing that the only component of ω that can be generated from enforcing a displacement constraint between the substrate and the rotor at the point must be *perpendicular*, we are left with $r \times \dot{\xi} = |r \cdot r|\omega$, which can be solved for ω. Naturally, the angular velocity produced varies around the contact circle of radius a, violating the pointwise constraint, and so we

take the integral average of this pointwise velocity $\boldsymbol{\omega}$ over $\theta \in \{0,\ 2\pi\}$ for our estimate, as the rotor must do in response to the induced motion:

$$\omega_{max} = \frac{1}{2\pi} \int_0^{2\pi} \frac{\boldsymbol{r} \times \dot{\boldsymbol{\xi}}}{|\boldsymbol{r}.\boldsymbol{r}|} d\theta$$

(1)

In which (refer to Figure 3.12)

$$\boldsymbol{r} = a\left(\cos\theta\ \boldsymbol{e}_x + \sin\theta\ \boldsymbol{e}_y\right) - \left(\sqrt{R^2 - a^2}\right)\boldsymbol{e}_z$$

(2)

Substituting into equation (1), the result is:

$$\omega_{max} = \left(\frac{0.7\ \dot{\gamma}\sqrt{R^2 - a^2}}{R^2}\right)\boldsymbol{e}_y$$

(3)

As *validated* by the LDV result shown in Figure 3.8, the *spatial phase shift* over the contact circle can be *assumed* to be *negligible*$\left(\dot{\boldsymbol{\xi}} \neq \dot{\xi}(\theta)\right)$, due to the radius of the hole $a < \lambda_{SAW}$ where λ_{SAW} is the wavelength of the SAW. With this assumption, most of the integrand is harmonic on $\{0,\ 2\pi\}$, including the contribution from the z-axis motion $\dot{\boldsymbol{\xi}} = \dot{\gamma}\boldsymbol{e}_z$ and does not contribute to $\boldsymbol{\omega}_{max}$. The orientation of rotation is about the y-axis with the rotor in contact with the substrate moving *toward* the SAW source, indicating a means to control the rotation axis by defining the direction of SAW incident upon the contact circle. Several IDTs placed about and pointed towards the contact can be used to

65

change the rotation axis' orientation, as illustrated in Figure 3.8, though the axis will always remain parallel to the substrate surface. Figure 3.13 and Figure 3.14 show the estimated and experimental maximum rotation velocity for the motor with 0.25 mm and 0.45 mm hole, respectively.
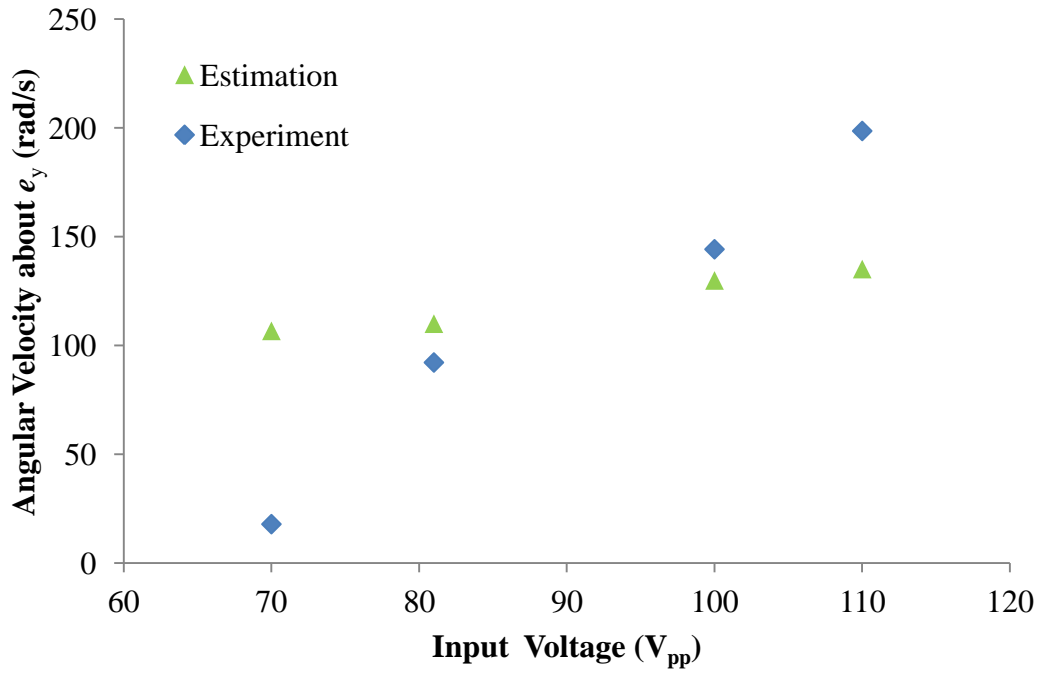
Figure 3.13. Comparison between model and experimental y-axis velocity values for 0.25 mm hole
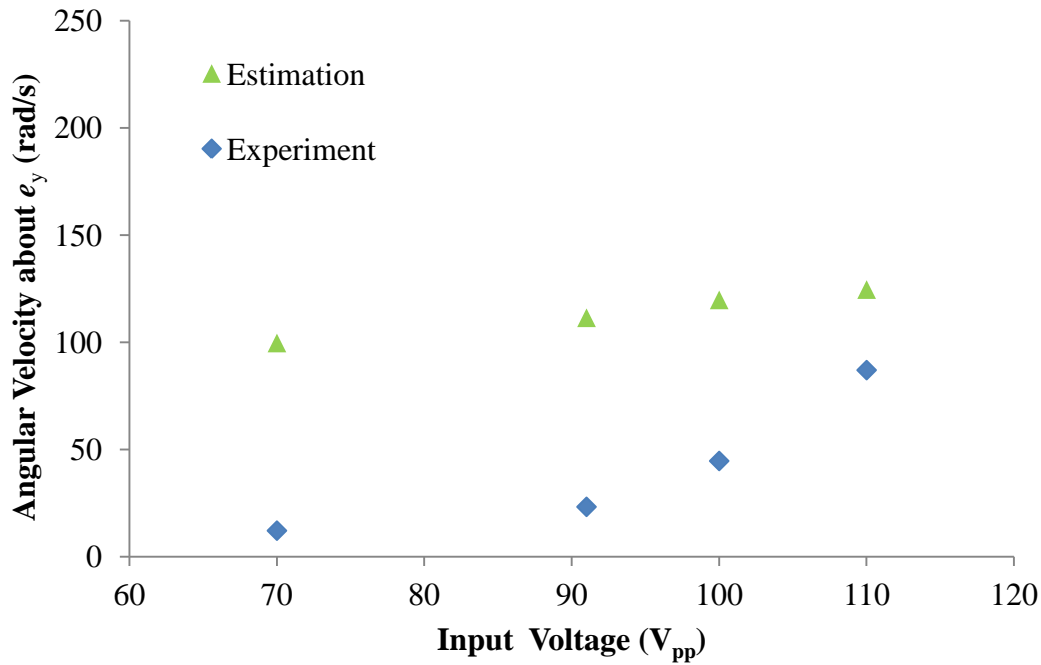
Figure 3.14. Comparison between model and experimental y-axis velocity values for 0.45 mm hole

Observation of Figure 3.13 showed that for the motor with 0.25 mm hole configuration, the experimental values were lower compare to the estimated values at lower input voltage. This could be explained by static friction during operation, the rotor needs high impulsive force to overcome static friction for it to start rotating. Once the static friction has been overcome, then the dynamic friction to be overcome is much lower in value. The estimated model does not take into account the static friction which would normally only found empirically. As the input voltage was increased, the experimental values also increased until at our highest input voltage, it overcomes the estimated values. This was also expected, since the estimation assumes a no-slip condition, which is never the case of any system. With input voltage supplied to the motor, the rotor rotates with the same

velocity at the point of contact, as the input voltage is increased; the rotor slips and rotates at a higher velocity. Moreover it was only recently established that during operation of a ultrasonic motor, the rotor bounce during operation, which would require a more complex analysis [13].

Observation of Figure 3.14 showed that for the motor with 0.45 mm hole configuration, the experimental values were lower compare to the estimated values at all the experimental input voltage. Similar to the result for the motor with 0.25 mm configuration, the estimated values does not take into account the static friction. As the input voltage was increased, the experimental values also increased to approach the estimated values. However unlike the previous configuration, up until the highest input voltage of our experiment, 120 V_{pp}, the experimental values has not able to overcome the estimated values. The trend however shows the experimental values would overcome the estimates one if the input voltage is kept increased, similar to the motor with 0.25 mm configuration. This could furthermore be explained by a more significant phase shift of the travelling wave around the hole during operation. The phase shift in this configuration is more significant because the size of the hole is approaching the wavelength of the travelling wave. The hole diameter, 0.45 mm, is more the half of the wavelength, 0.7 mm (700 μm), hence the phase shift is expected.

The model nevertheless is adequate to estimate the order of magnitudes. The model is in addition able to predict that the diameter of the hole has an inverse relationship with the rotor velocity, which was demonstrated by the experimental result.

3.3.2 Motor Characteristics

The report continues with the discussion of the characteristics of the motor, which were calculated based on the measured transient response. The transient response was measured, and the system was modeled as a first order lag approximation, validated by its coefficient of determination, R^2. After the validity of the approximation has been confirmed, it consequently shows a linearly inverse relationship between the torque and rotational velocity. Output power was in addition calculated and presented as a function of rotational velocity.

3.3.2.1 Transient Response

The transient responses of the motors are shown in Figure 3.15 and Figure 3.16.
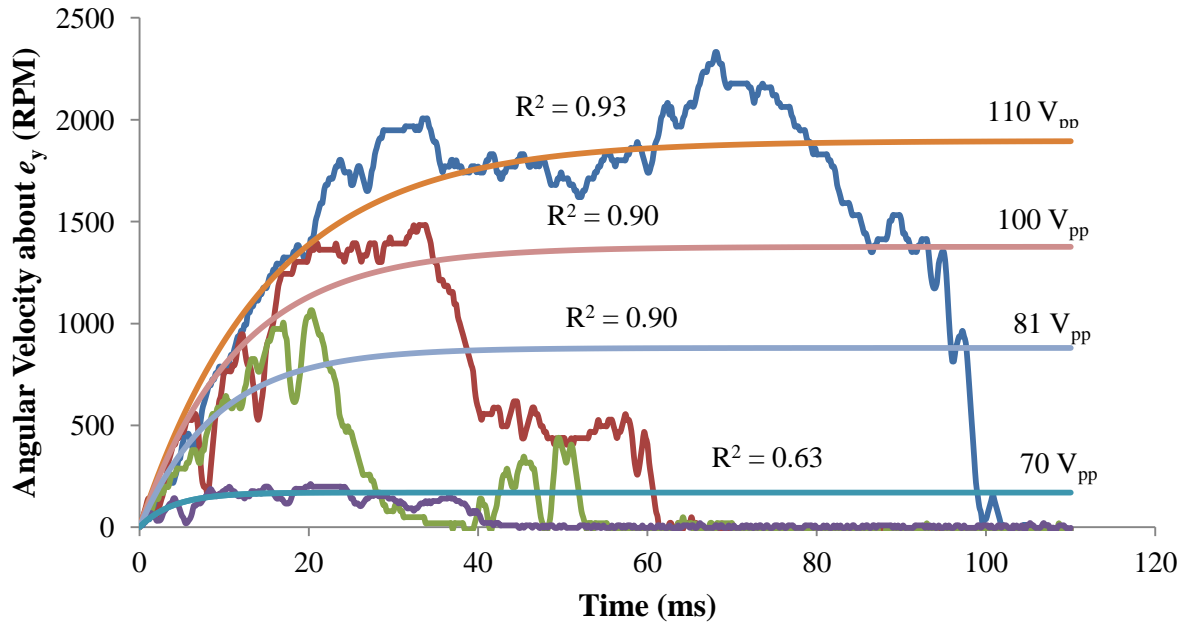
Figure 3.15. Transient response of the motor with 0.25 mm hole. The maximum rotational velocity achieved was approximately 2000 rpm with a rise time of ~15 ms at 110 V_{pp} input.
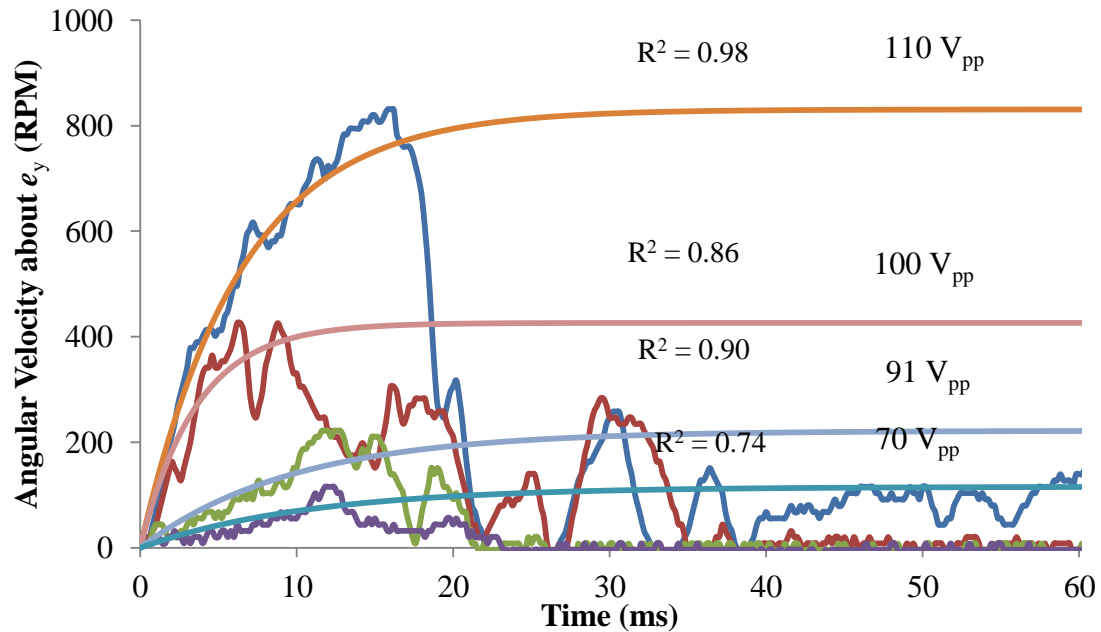
Figure 3.16. Transient response of the motor with 0.45 mm hole. The maximum rotational velocity achieved was approximately 900 rpm with a rise time of ~6 ms at 110 V_{pp} input.

The transient responses were not smooth, with fluctuations in rotational velocity observed during operation. This may be caused by insufficient frictional force to hold the rotor during operation, hence slip and more importantly significant bouncing can occur. The fluctuations were more prominent for the 0.45 hole configuration, leading to rotor instability at higher input voltage. At 110 V_{pp} input voltage, the rotor has the tendency to spring out of the hole during high speed rotation; this can be observed as the sudden drop in velocity shown in Figure 3.16.

The maximum rotational velocity achieved however, was high, achieved for 0.25 mm hole diameter configuration, close to *2000 rpm* at 110 V_{pp} input voltage. The rotational accelerations in this configuration, without any external preload, were very high. The rotor reaches its maximum velocity in less than 20 ms regardless of the input power. The rotational accelerations of the motor from rest to maximum were calculated and plotted as Figure 3.17. It can furthermore be observed that the acceleration of the motor increases with increasing input voltage, up to $\approx 8000\ rad/s^2$ for input voltage of 110 V_{pp}.
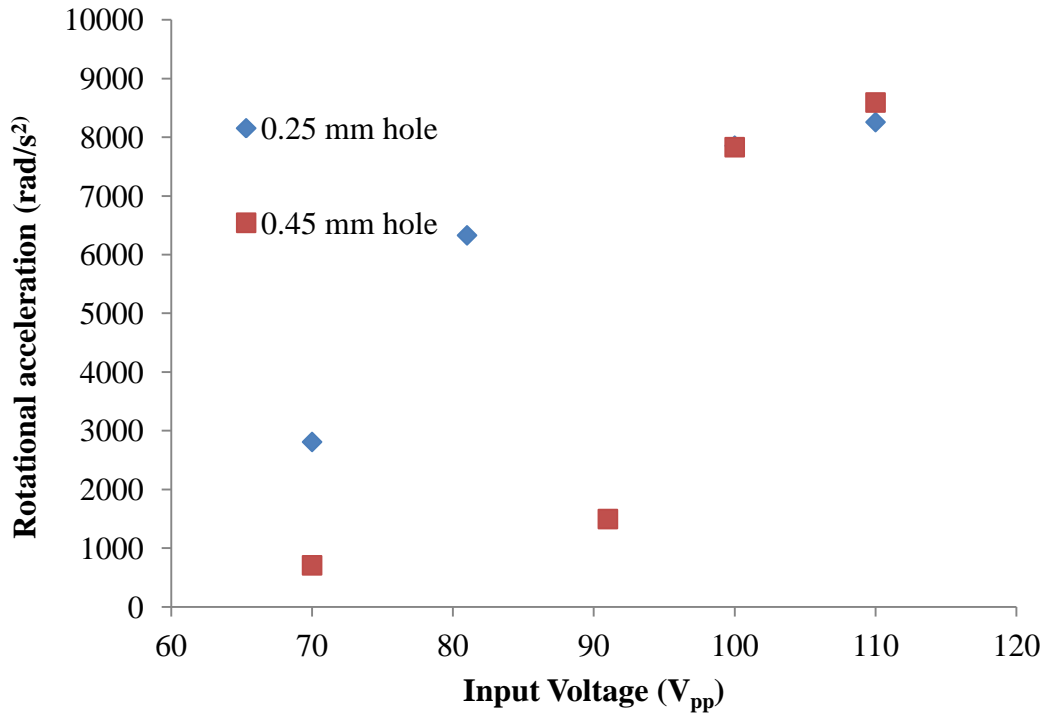
Figure 3.17. Rotational acceleration of the motor with respect to input voltage. The maximum acceleration achieved was close to 9000 rad/s for input voltage of 110 V_{pp} for both the motor with 0.25 mm and 0.45 mm holes configuration.

3.3.2.2 Load Characteristics

Utilizing the measured transient response, we tried to estimate the load characteristic of the motor. The motor transient response was modeled as first-order lag system similar to most ultrasonic motor response [14, 15]. The model was then validated with respect to the real response, in which the coefficient of determination, R^2, values between the experimental and the modeled transient responses are more than 60% (refer to Figure 3.15 and Figure 3.16). As the first order lag approximation is valid for the motor, it consequently shows a linearly inverse relationship between the torque and rotational

velocity. The torque was calculated and the torque-velocity curves were plotted; shown as Figure 3.18 and Figure 3.19 .

$$\omega = \omega_0 \left(1 - \frac{T}{T_0}\right)$$

(4)

And the torque is:

$$T = J \frac{d\omega}{dt}$$

(5)

Eliminating torque from equation (4) and (5),

$$\omega - \omega_0 = -J \frac{\omega_0}{T_0} \frac{d}{dt}(\omega - \omega_0)$$

(6)

$$\omega = \omega_0 \left[1 - exp\left(-\frac{t}{\tau_r}\right)\right]$$

(7)

$$\tau_r = J \frac{\omega_0}{T_0}$$

(8)

In the equations above, T is the torque, ω is the rotational velocity, J is the mass moment of inertia of the rotor, and t is the time; while T_o and ω_0 are the maximum torque (stall

torque) and rotational velocity (no-load velocity), respectively; τ_r is the time constant, the time to reach 1-1/e ($\approx$63.2%) of asymptotic value. Maximum torque achieved was ~5.5 µN.mm at 110 V_{pp} input power. Hence the force exerted by the stator to rotate the rotor is ~11 µN. With the preload (i.e. weight of the rotor) ~40 µN, the coefficient of static friction is therefore approximately *0.28*.
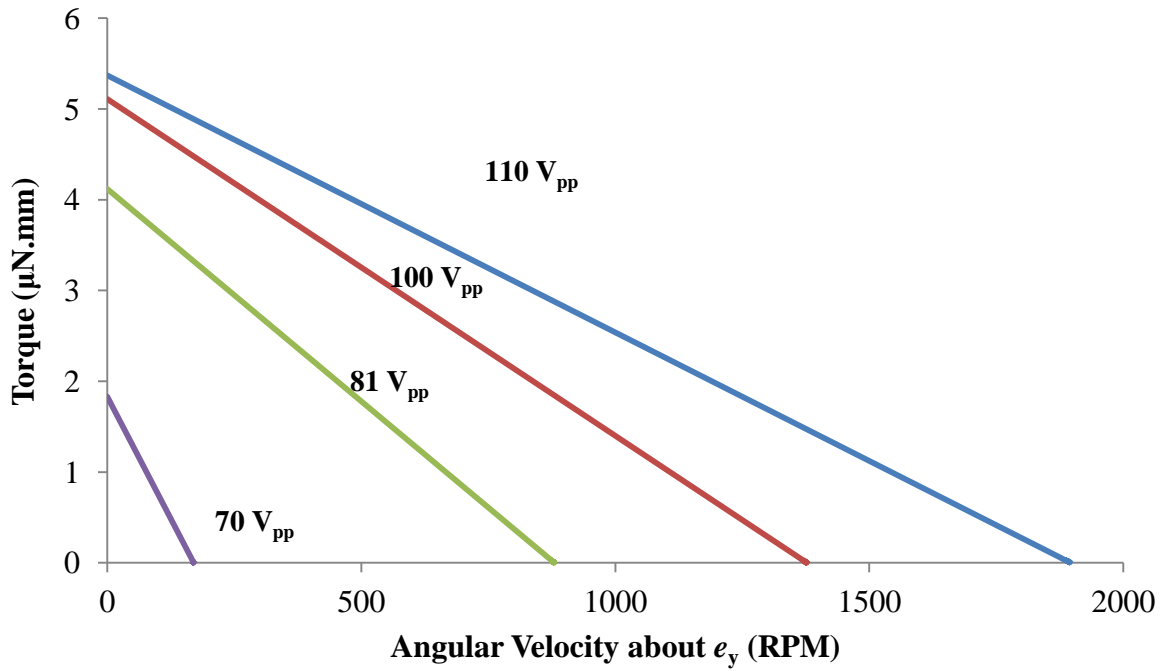
Figure 3.18. Torque velocity curves of the motor with 0.25 mm hole diameter obtained during operation. The maximum velocity achieved was close to 2000 rpm and the maximum torque achieved was approximately 5.3 µN.mm.
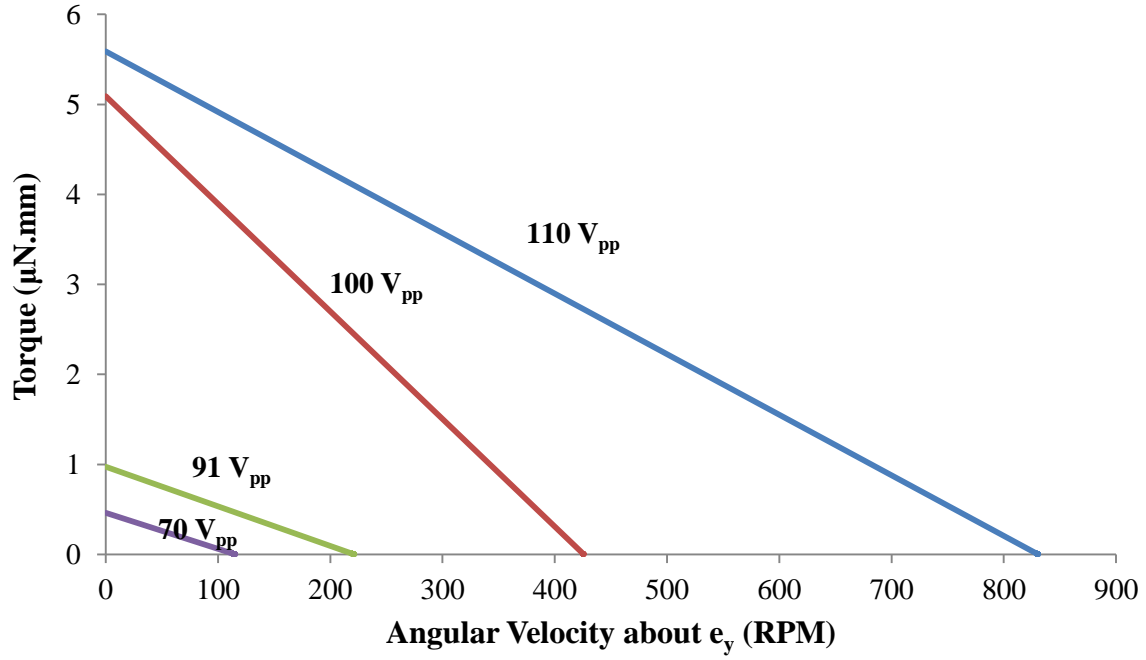
Figure 3.19. Torque velocity curves of the motor with 0.45 mm hole diameter obtained during operation. The maximum velocity achieved was close to 900 rpm and the maximum torque achieved was approximately 5.5 μN.mm.

3.3.2.3   Output Power

The output power of the motor can be calculated as the torque times the rotational velocity.

$$P_{output} = T \times \omega$$

(9)

Substituting equations (4):

$$P_{output}(\omega) = -\left(\frac{T_0}{\omega_0}\right)\omega^2 + T_0\omega$$

$$(10)$$

Similarly:

$$P_{output}(T) = -\left(\frac{\omega_0}{T_0}\right)T^2 + \omega_0 T$$

$$(11)$$

From equations (10) and (11), the maximum output power (P $_{max\ output}$) can be calculated to occur at $\tau = \frac{1}{2}\ \tau_0$ and $\omega = \frac{1}{2}\ \omega_0$. The power-angular velocity curves were plotted and shown in Figure 3.20 and Figure 3.21. The maximum output power produced was close to *270 nW* for the motor with 0.25 mm hole configuration at 110 V$_{pp}$ input power.
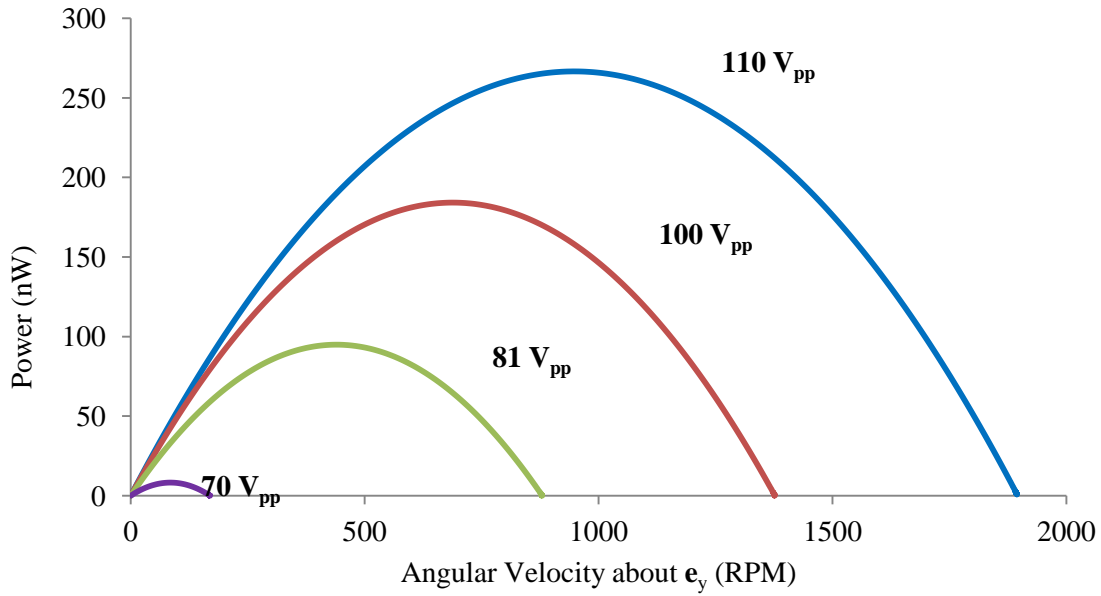
Figure 3.20. Power velocity curves of the motor with 0.25 mm hole diameter obtained during operation. The maximum velocity output power was close to 270 nW.
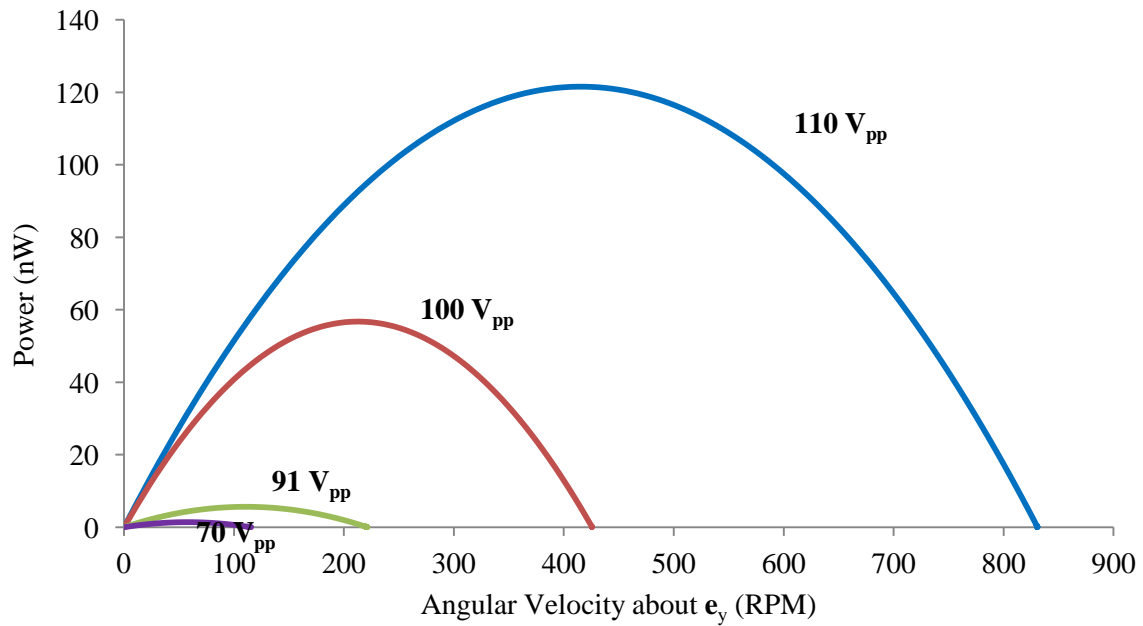
Figure 3.21. Power velocity curves of the motor with 0.45 mm hole diameter obtained during operation. The maximum velocity output power was more than 120 nW.

77

Table 3.1 Performance summary for the motor rotating about e_y.

Hole size	Input V_{pp}	Model	Experimental			Maximum (stall) Torque (nN.m)	Maximum Output Power (nW)
		Maximum (no-load) Rotation speed (rad/s)	Maximum (no-load) Rotational speed (rad/s)	Rise Time (ms)	Maximum Rotational acceleration (rad/s^2)		
0.25 mm	110	135.08	198.58	15.20	8256.75	5.37	266.59
	100	129.85	144.18	11.60	7855.32	5.11	184.19
	81	109.98	92.12	9.20	6328.24	4.12	94.88
	70	108.04	17.78	4.00	2809.24	1.83	8.13
0.45 mm	110	124.59	87.00	6.40	8591.25	5.59	121.58
	100	119.76	44.60	3.60	7829.78	5.09	56.75
	91	111.42	23.20	9.80	1496.16	0.97	5.63
	70	99.65	12.10	10.80	708.07	0.46	1.39

3.3.3 Summary

We have reported the development of a novel SAW actuated rotating motor with simple design and configuration. Two *novelties* are associated with the SAW actuated rotating motor. The first one is its *simplicity* and *effectiveness* to achieve a motor in which a rotor rotates in its own center of rotation. The second and *more important novelty* is its capability to operate in any *chosen yet arbitrary axis*. The rotor always rotates with an axis perpendicular to the SAW propagation direction in the same planar dimension; the axis of rotation can therefore be controlled by the IDTs-to-rotor placements. The motor is consequently able to rotate in arbitrary axis within the plane of the rotation (2D motor).

Two configurations were tested and reported in this section; i.e. with 0.25 mm and 0.45 mm hole diameter; in which the no-load velocities achieved were around 2000 and 900 rpm, respectively. An LDV was used to visualize the travelling wave on the stator, the result of which was able to confirm that the presence of the hole does not significantly affect the wave propagation. The LDV was additionally used to measure the SAW vibration velocity and amplitude, the results of which show linear proportionality to the input voltage.

We subsequently used the maximum vibration velocity as the basis to estimate the rotor maximum velocity. For lower input voltage, the estimations for both configurations generally showed higher rotational velocity values in comparison with the experimental

values. This would be expected as the rotor needs to overcome static friction to start the rotation. This static friction value was not taken into account in the model as it is normally measured empirically. As the input voltage was increased, the experimental values also increased approaching, or overcoming the estimated values, the later being the case of the 0.25 mm hole. This could be explained due to *slip*. As higher input voltage was supplied, the rotor rotates faster up to a point that slip start to occur and as a result its rotational velocity is higher than the SAW vibration velocity at the point of contact between the rotor and stator. The model nevertheless is sufficient to estimate the order of magnitudes; it is moreover able to predict the inverse relationship between the hole diameter and the rotor velocity, as empirically demonstrated by the experimental result.

We then modeled the motor transient response as first-order lag system similar to most ultrasonic motor response [14, 15]. The model was valid as the coefficients of determinations are of good values. We can use this model, which was proposed by Nakamura et al [14], to estimate the torque. The stall torques achieved for both configurations were around 5-6 μN.mm = 5-6 nN.m.

The maximum rise time for either configuration was found to be 15 ms; hence, the acceleration of the motor is very high. The maximum accelerations of the motor for both configurations were found to be more than 8000 rad/s^2. The output powers for both configurations were also plotted. The maximum output power occurs at half the no-load

velocity and half the stall torque. The values were calculated to be 260 nW and 120 nW for the 0.25 mm and 0.45 mm hole configuration, respectively.

The maximum velocity value achieved in this mode of operation is higher compare to reported SAW dry friction rotary motor [1], it is in the same order of magnitude and higher compare to common ultrasonic motor reported [16]. The stall torque and output power, however, are lower compare to common ultrasonic motor.

In the next section, we report the continuation of this project, the rotor rotation in the axis which is normal to the substrate, for achieving a three dimensional arbitrary axis rotating motor.

3.4 SAW rotary motor operation with external preload

As discussed in previous section, the SAW rotating motor does not require any external pre load to operate. Interestingly, further experiments by introducing a pre-load showed that the axis of rotation can be altered. The pre-load in our case was a magnet with 0.088±0.002T of strength. The axis of rotation is altered from parallel to normal to the surface of the substrate (*z-axis*). Combination of the IDTs-to-rotor placements with a pre-load could therefore be exploited to achieve the three dimensional arbitrary axis rotation. Figure 3.22 shows the two modes of operation (with and without pre-load).

Two similar configurations of the motor were constructed for this part of the project, the motor with 0.25 mm and 0.45 mm hole. The motors were operated and characterized using the same method as previous section. The operation of the motor can be viewed in the multimedia files attached to this report. Successive images of the rotor rotation during operation can also be viewed Figure 3.23. The images were captured using a high velocity camera (Motion BLITZ, Mikroton GmbH) at 1000 frames per seconds. The operation was with pre-load hence the axis of rotation is normal to the plane of the SAW.
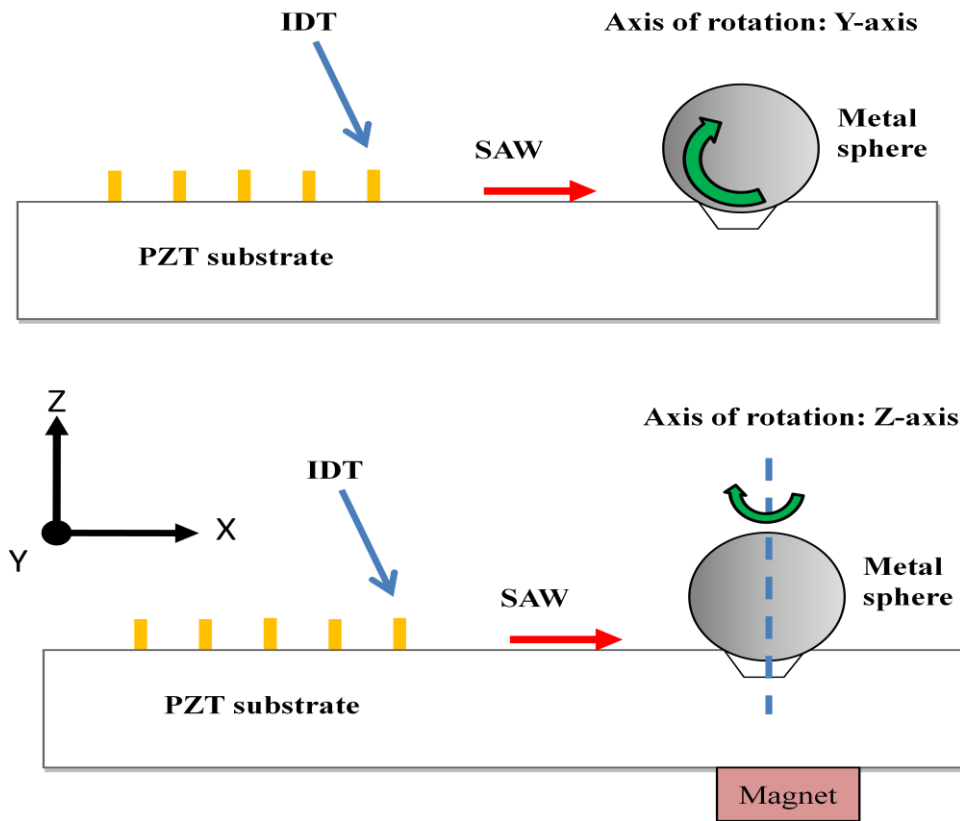
Figure 3.22. Schematic illustrations of two modes of operation. The blue arrow shows the rotor rotation directions. The axis of rotation can be altered with introduction of a magnetic pre-load (0.088±0.002T) from (a) perpendicular to the SAW propagation path to (b) normal to the substrates surface. This could be used as a mechanism to achieve the arbitrary axis rotation.
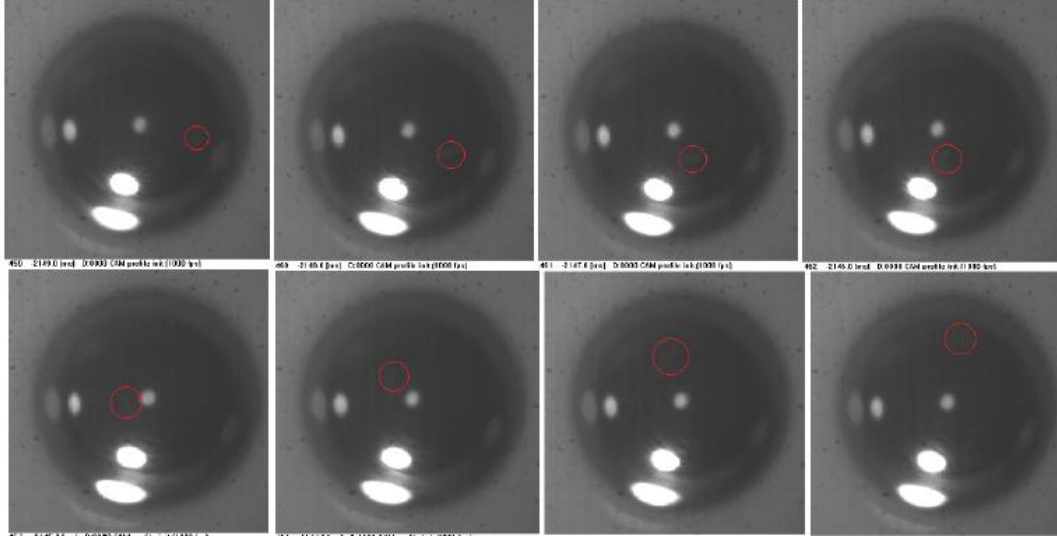
Figure 3.23. Successive images of the motor during one mode of operation. The motor was running with the magnetic pre-load, hence the axis of rotation is normal to the substrates surface. The images were captured using a high velocity camera (Motion BLITZ, Mikroton GmbH) at 1000 frames per seconds.

3.4.1 Kinematics Estimation

Using the previous estimation, assuming the spatial phase shift over the contact circle is negligible$\left(\dot{\boldsymbol{\xi}} \neq \dot{\xi}(\theta), validated\right.$ in Figure 3.8$\left.\right)$, and the maximum rotational velocity of the rotor can be estimated based on the vibration velocity of the SAW. Similarly, the $\boldsymbol{e}_z$ component along the contact circle will add itself to zero hence the equation is left with $\dot{\boldsymbol{\xi}} = \dot{\eta}\boldsymbol{e}_x \approx 0.7\,\dot{\gamma}\boldsymbol{e}_x$. In this case, the rotation is about $\boldsymbol{e}_z$, hence the $\boldsymbol{r}$ is represented by (refer to Figure 3.12):

$$\boldsymbol{r} = a\big(\cos\theta\ \boldsymbol{e}_x + sin\theta\ \boldsymbol{e}_y\big)$$

(12)

83

Substituting into equation ((1) and integrating,

$$\boldsymbol{\omega}_{max} = \frac{1}{2\pi} \int_0^{2\pi} \frac{\boldsymbol{r} \times \dot{\boldsymbol{\xi}}}{|\boldsymbol{r}.\boldsymbol{r}|} d\theta$$

$$= \frac{-1}{2\pi a} \int_0^{2\pi} 0.7 \, \dot{\gamma} \sin\theta \, d\theta \, \boldsymbol{e}_z = 0$$

(13)

The result is *zero* rotational velocity. The rotor, as a consequence, will not rotate about $\boldsymbol{e}_z$ during propagation of a travelling wave. Yet, rotations about $\boldsymbol{e}_z$ were observed. We hypothesized that the rotation is the result of the rotor tilting to one side of the hole periphery during operation. Since it is very difficult to perfectly align the magnet with respect to the rotor and the hole, the rotor would most probably tilt to one side of the hole. If this in reality is the case, then the maximum rotational velocity would not be zero. The rotational velocity would be inversely proportional to the length of the contact line, with the maximum value reached when the rotor sits on a certain contact point ($\theta = \pi/2 \text{ or } 3\pi/2$).

$$\boldsymbol{\omega}_{max} = \frac{0.7 \, \dot{\gamma}}{2\pi a} \boldsymbol{e}_z$$

(14)

To prove this hypothesis, an experiment was performed, in which the magnet position was shifted about $\boldsymbol{e}_x$ direction, as shown in schematic in
Figure 3.24. We observed that shifting the magnet altered the sphere z-axis rotation from positive to negative direction. The result, as shown in Figure 3.25, validates the hypothesis; the rotor does indeed tilt to one side of the hole during operation. The transient responses of the rotor with opposite rotational directions were almost identical

with some discrepancies due to the poor roughness uniformity along the periphery of the hole. Worth to note however, up until now, it is very difficult to control the exact position of the permanent magnet to fully controlled rotational direction, hence this also add to the discrepancies, because the resultant forces are not equal to each other.
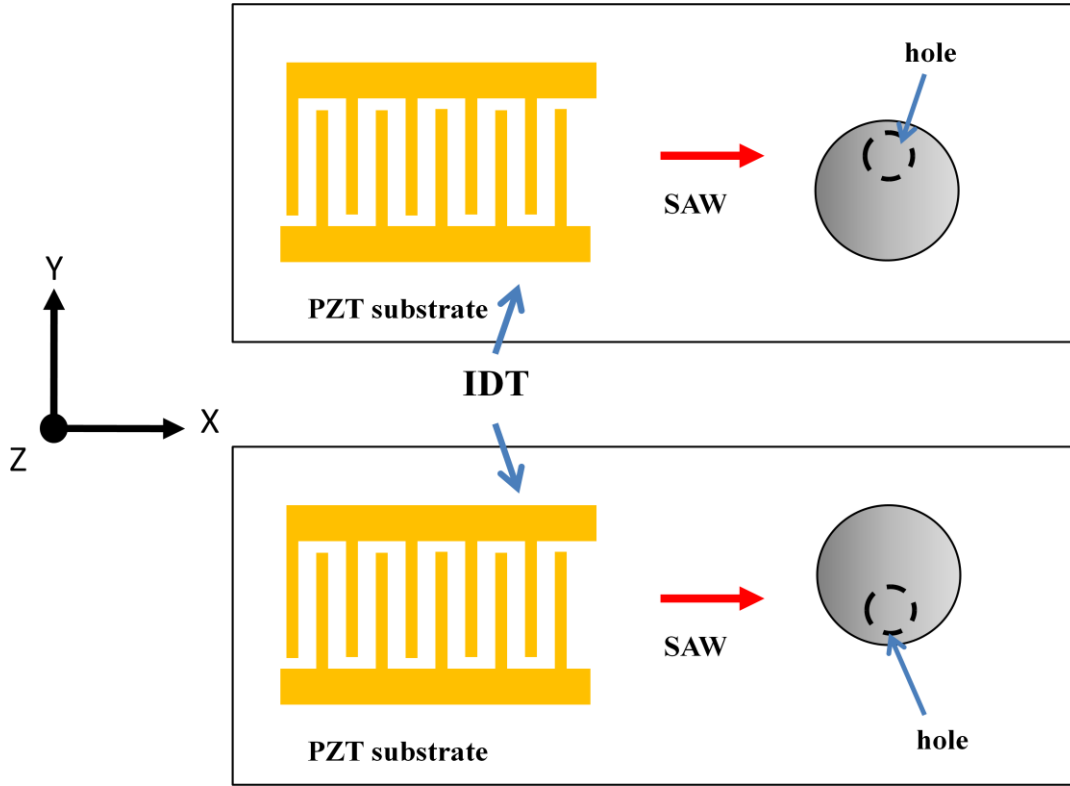
Figure 3.24. Schematic of the motor (top view), the rotor tilts to one side of the hole as the magnet is shifted about e_x direction.
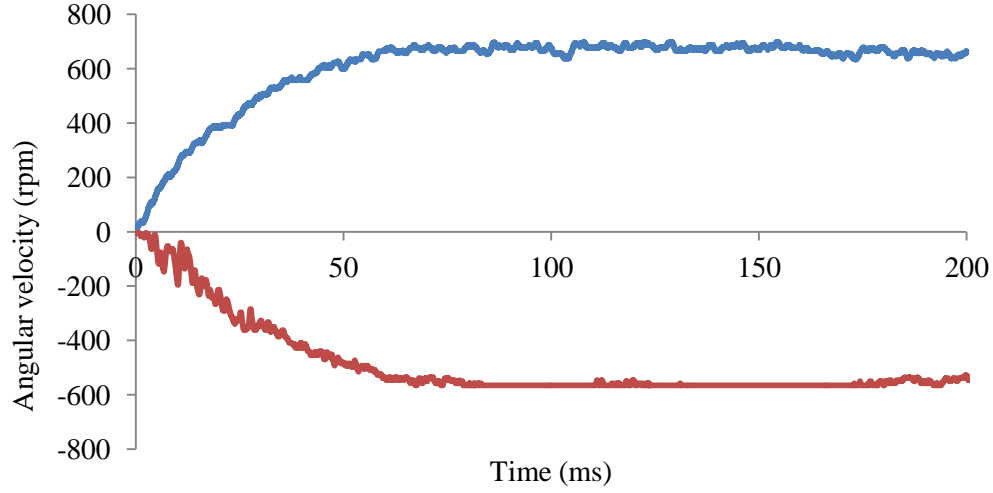
Figure 3.25. Positive and negative rotational z-axis direction with magnet shifting, both were run with input power of 100 V_{pp}. The maximum velocity is almost a mirror image; however the surface roughness uniformity of the hole hinders the attainable maximum velocity.

After our hypothesis had been proven, we continued estimating the maximum rotational velocity, which was calculated using equation (7). The results were plotted and compared with the experimental results as shown in fFigure 3.26 and Figure 3.27. The estimated model again shows an inverse relationship between the hole diameter and the maximum velocity. Analyzing equation (14), we notice that as the $a \rightarrow 0, \omega_{max} \rightarrow \infty$, hence, the smaller hole configuration was expected to give higher maximum rotational velocity.

The results in both Figure 3.26 and Figure 3.27 showed similar trend; the experimental values were lower than the estimated ones for lower input power but increasing in a higher slope as increasing input voltage. Similar to the result for the motor configuration without external preload (subchapter 4.3), these trends could be attributed to static friction and slip. Initially, for lower input voltage, the rotor needs to overcome static

friction to start rotating; hence its velocity would be lower than that of the travelling wave. As higher input voltage supplied increases the rotor would have enough power to overcome the static friction; hence the velocity is approaching that of the travelling wave.

Extrapolation of the graphs would show that with higher input voltage, the experimental velocity would overcome those of the estimated ones, which would be caused by slip. Due to the external preload holding the rotor normally toward the stator, the input voltage required for this to happen is expected to higher compare to those of the motor without external preload configuration.

Moreover, the estimated values are calculated for a rotor which sits on a contact point, while in reality, the rotor almost certainly sits on a contact sector; hence the lower experimental values and extra power requirements. As the input voltage was increased (which result in higher rotational velocity), the rotor polishes the contact sector as it rotates, hence reducing the line of contact between the rotor and the substrate. In other word, the contact sector between the rotor and substrate approaches contact point during high velocity operation. The rotor velocity therefore approaches the travelling wave velocity.
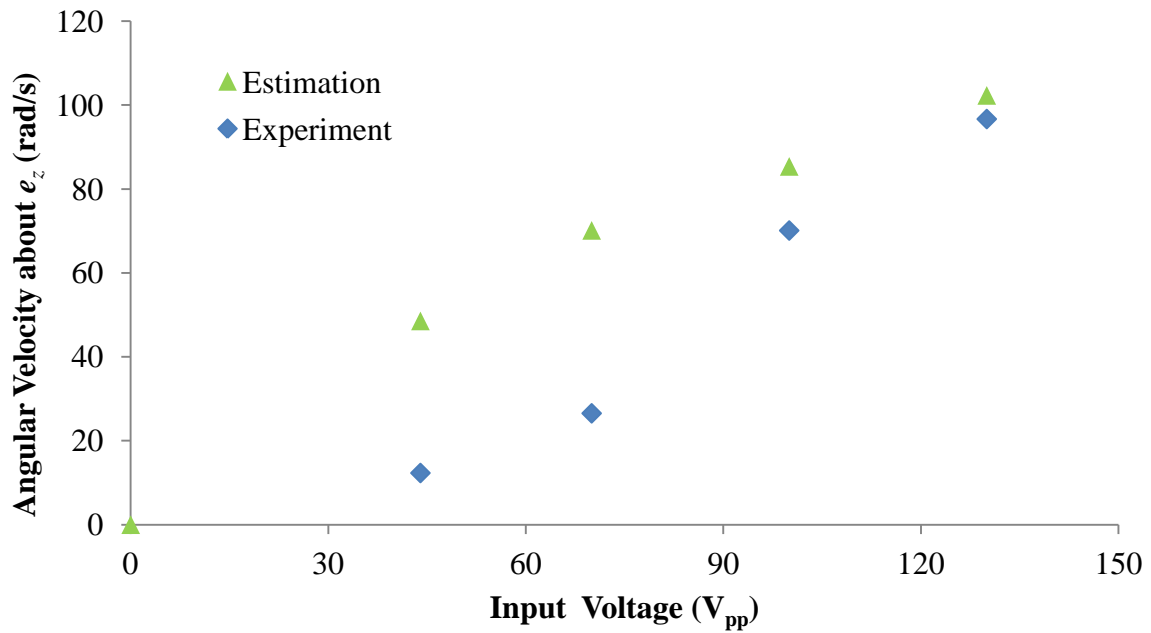
Figure 3.26. Comparison between model and experimental z-axis velocity values for 0.25 mm hole.
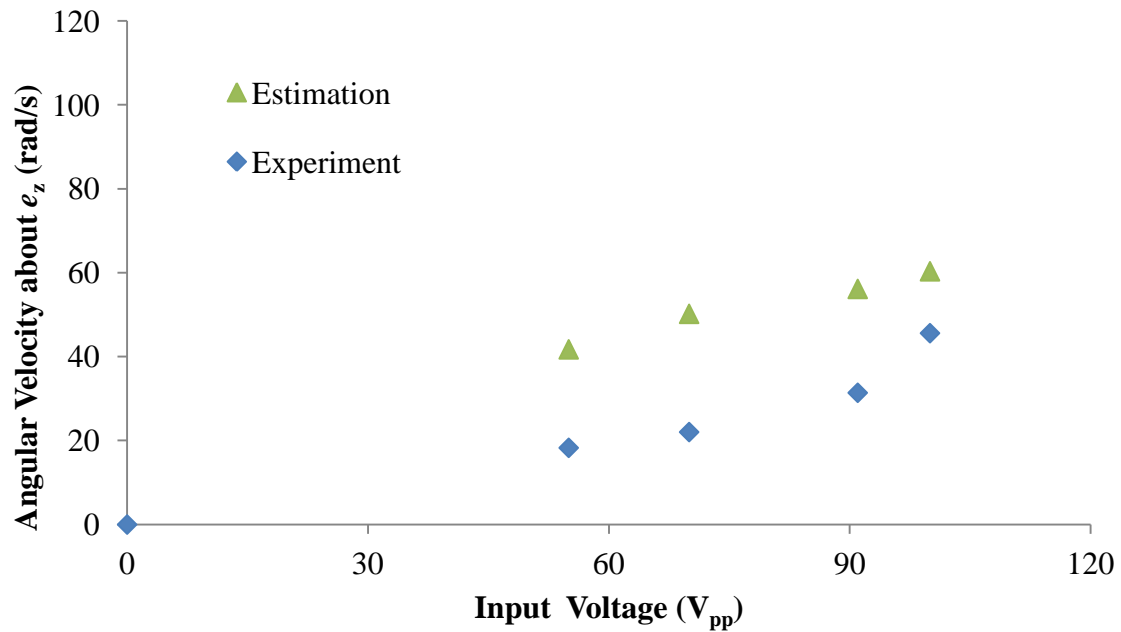
Figure 3.27. Comparison between model and experimental z-axis velocity values for 0.45 mm hole

3.4.2 Motor Characteristics

Similar to previous sub-chapter, the report continues with the discussion of the characteristics of the motor. The transient response was measured, and the system model as a first order lag approximation was also valid. The torque and output power were calculated and presented as a function of rotational velocity.

3.4.2.1 Transient Response

The transient responses can be viewed on Figure 3.28 and Figure 3.29.
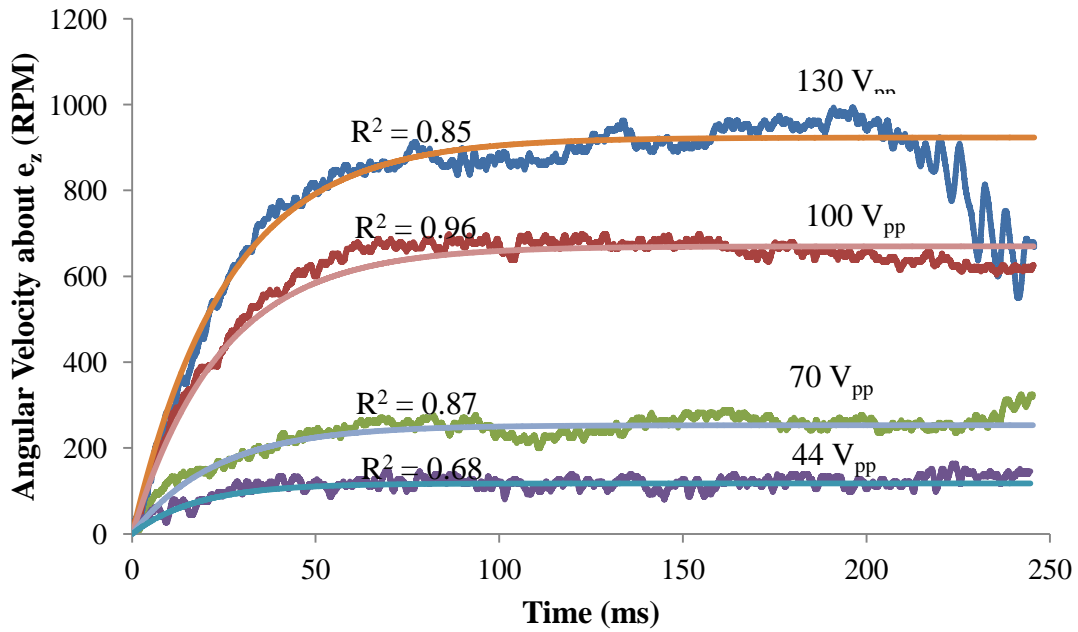
Figure 3.28. The transient response of the motor with the 0.25 mm hole configuration during operation with the magnetic pre-load. The maximum rotational velocity achieved was approximately 1000 rpm with a rise time of ~26 ms at 130 V_{pp} input.
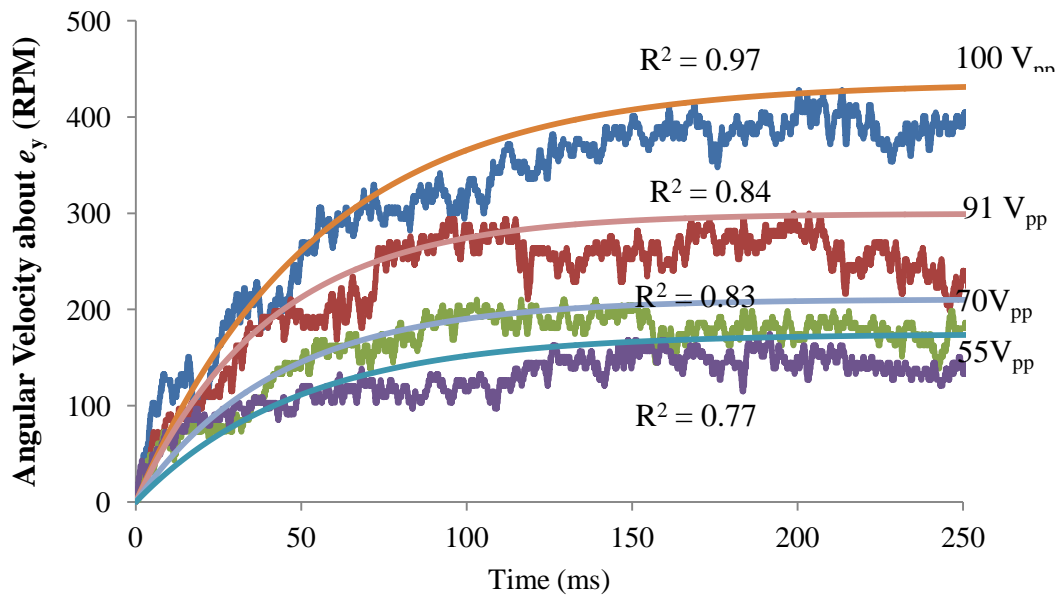
Figure 3.29. The transient response of the motor with the 0.45 mm hole configuration during operation with the magnetic pre-load. The maximum rotational velocity achieved was approximately 450 rpm with a rise time of ~60 ms at 100 V_{pp} input.

The additional pre-load however hinders the performance of the motor. The maximum velocity achieved was ~1*000 rpm* for a 110 V_{pp} input voltage on the 0.25 hole diameter configuration, approximately half of the maximum velocity achieved by the no external preload mode. The rotor now reaches its maximum velocity in approximately 40 ms and 80 ms for the 0.25 mm and 0.45 mm holes configuration, respectively. The rotational accelerations in this configuration were observed to be are significantly less than that of motor without external preload. These were particularly true for the motor with 0.45 m hole configuration. Up to input power of 100 V_{pp}, the maximum rotational acceleration achieved was approximately *500 rad/s²*, an order of magnitude less. The highest value recorded was close to *2000 rad/s²* for the 0.25 mm hole configuration at an input voltage of 130 V_{pp}, less the a quarter of the previous value.
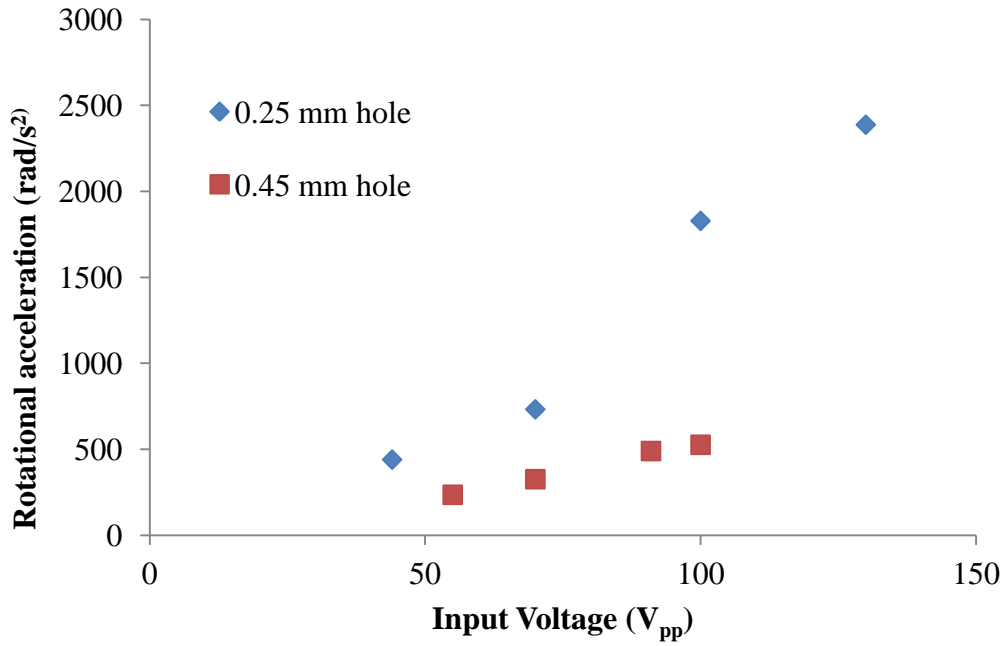
Figure 3.30. Rotational acceleration of the motor with respect to input voltage. The maximum acceleration achieved was approximately 2500 rad/s for input voltage of 130 V_{pp} for both the motor with 0.25 mm hole configuration.

3.4.2.2 Load Characteristics

The coefficient of determination, R^2, values between the experimental and the modeled transient responses are again more than 60% (refer to Figure 3.28 and Figure 3.29); the first order lag approximation is therefore valid for the motor. The torque was calculated and the torque-velocity curves were plotted; shown as Figure 3.31 and Figure 3.32. Maximum torque achieved was ~1.5 µN.mm at 130 V_{pp} input power for the motor with 0.25 mm hole configuration. In spite of higher input voltage, the maximum torque value is still less than that of the motor without pre-load.
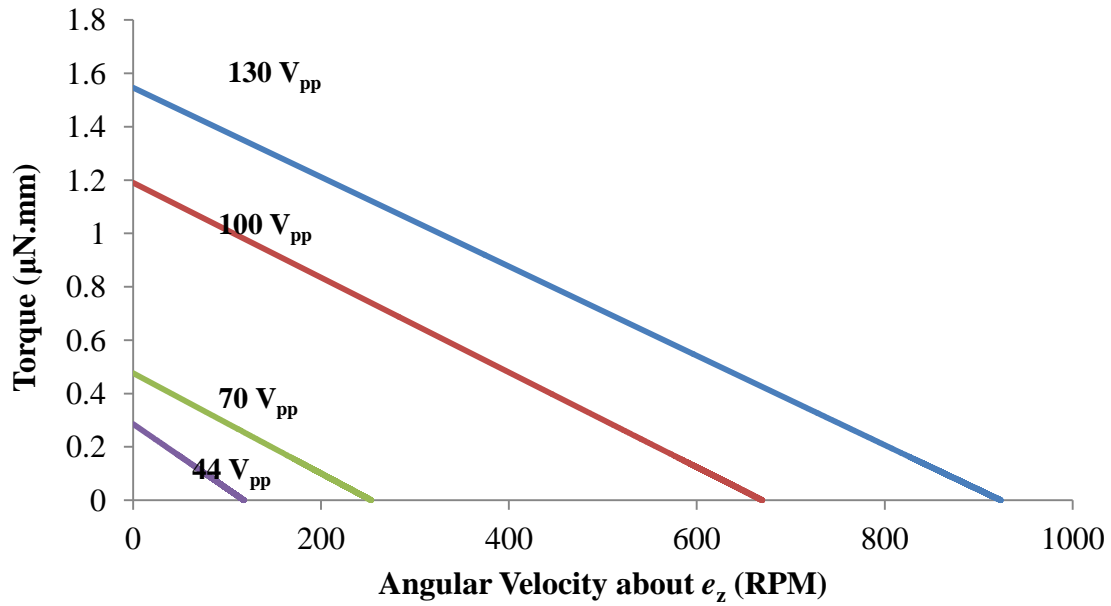
Figure 3.31. The torque velocity characteristic of the motor (with 0.25 mm hole) during operation with the magnetic pre-load. The torque was calculated using the method proposed by Nakamura et al [14]. The maximum torque achieved was over 1.5 μN.mm.
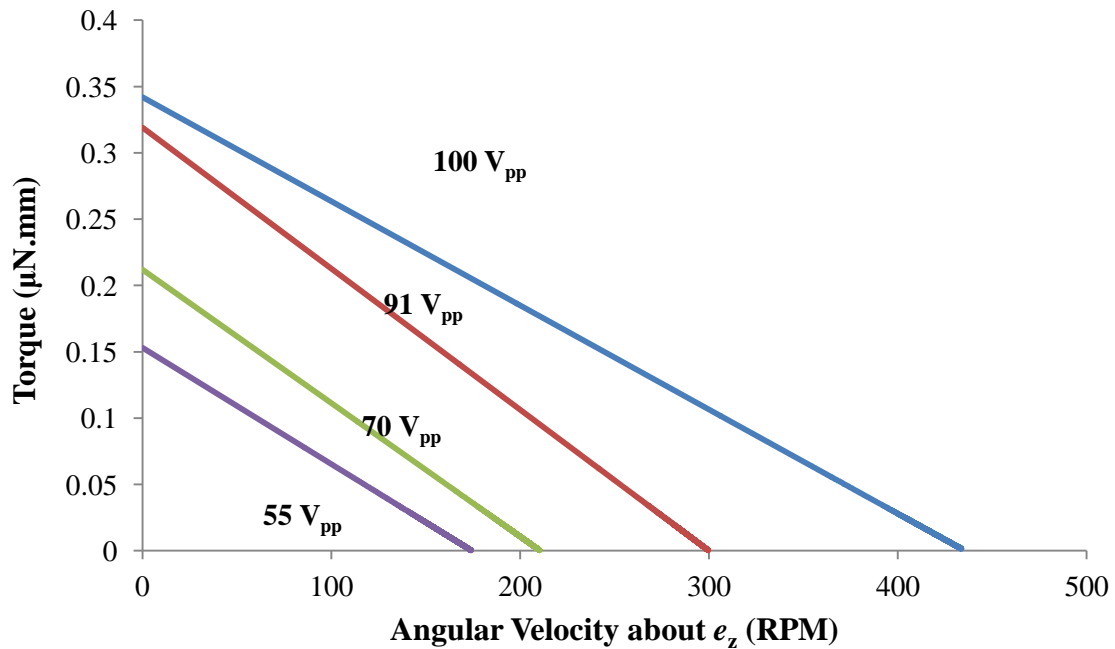
Figure 3.32. The torque velocity characteristic of the motor (with 0.45 mm hole) during operation with the magnetic pre-load. The torque was calculated using the method proposed by Nakamura et al [14]. The maximum torque achieved was over 0.35 μN.mm.

3.4.2.3 Output Power

The output power (P_{output}) can be calculated in the same way as previous subchapter, using equation (10). The power-angular velocity curves were plotted and shown in Figure 3.33 and Figure 3.34. The maximum output power produced was close to 40 nW for the motor with 0.25 mm hole configuration at 130 V_{pp} input power.
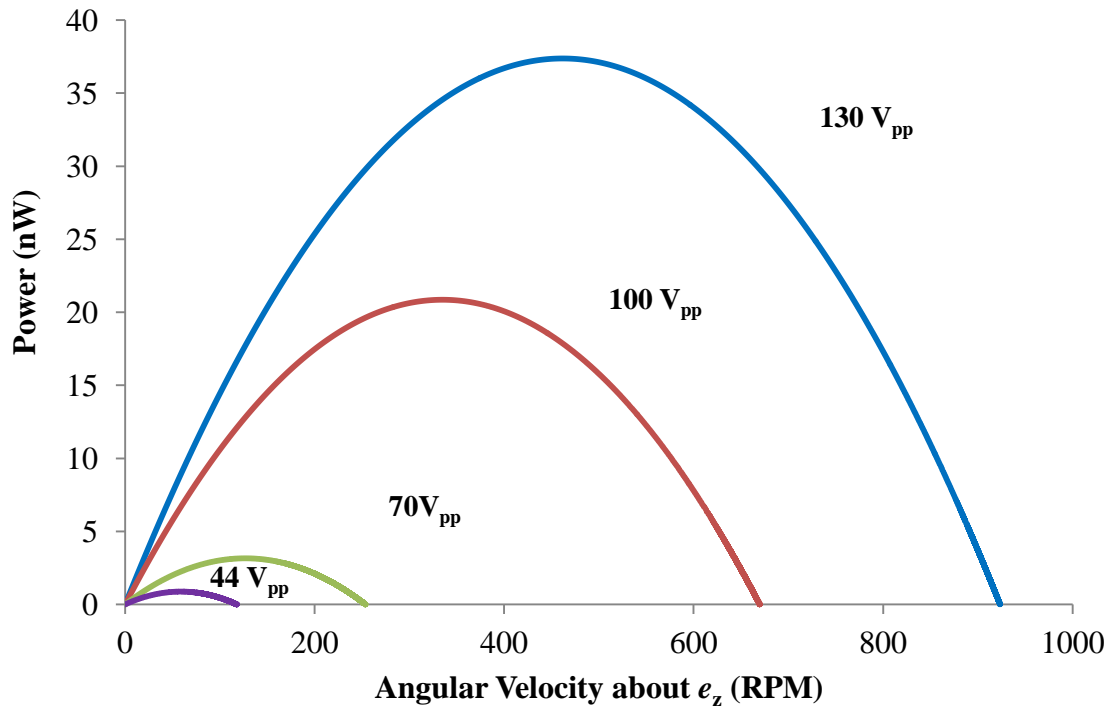
Figure 3.33. Power velocity curves of the motor with 0.25 mm hole diameter obtained during operation. The maximum velocity output power was close to 40 nW.
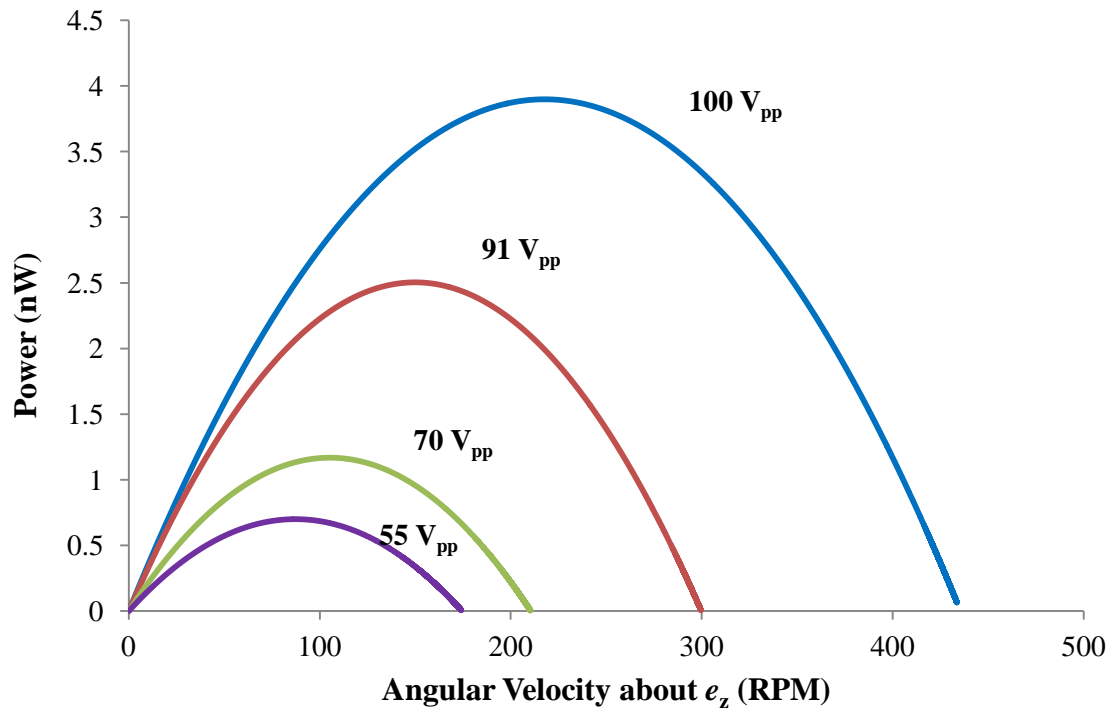
Figure 3.34. Power velocity curves of the motor with 0.45 mm hole diameter obtained during operation. The maximum velocity output power was more than 4 nW.

The summary or performance can be viewed in Table 3.2.

Table 3.2 Performance summary of the motor rotating about e_z.

Hole size	Input V_{pp}	Model	Experimental			Maximum Torque (nN.m)	Maximum Output Power (nW)
		Maximum Rotation speed (rad/s)	Maximum Rotation speed (rad/s)	Rise Time (ms)	Maximum Rotational acceleration (rad/s^2)		
0.25 mm	130	102.29	96.71	25.60	2387.53	1.55	37.48
	100	85.37	70.13	24.24	1828.47	1.19	20.86
	70	71.04	26.54	22.90	732.46	0.48	3.18
	44	48.55	12.32	17.70	439.90	0.29	0.89
0.45 mm	100	47.43	45.60	54.75	526.38	0.34	3.88
	91	44.13	31.40	40.50	490.00	0.32	2.51
	70	39.47	22.04	42.70	326.21	0.21	1.16
	55	32.37	18.28	49.05	235.53	0.15	0.69

3.4.3 Summary

The maximum rotational velocity and torque was achieved for the motor with 0.25 reported at 130 V_{pp} were ~1000 rpm and ~1.5 μN.mm, respectively. Arbitrary motions have also been demonstrated utilizing a magnetic pre-load and multiple IDTs activation. We have also observed that the rotor tilts to one side during operation.

We have reported the continuation of the development of a novel SAW actuated rotating motor with simple design and configuration. By adding an external pre-load to the system, the motor is able to rotate freely in three-dimensional space in a chosen yet arbitrary axis. Two similar configurations were tested and reported in this section; i.e. with 0.25 mm and 0.45 mm hole diameter.

We again used the maximum vibration velocity as the based to estimate the motor maximum velocity, with the only difference is the representation of the radius of rotation, *r*, value.   The estimation agrees with the experimental result in term of maximum vibration velocity against the hole diameter. In both cases, the motor with smaller hole diameter configuration shows higher maximum rotational velocity.

The experimental values were lower for lower input voltage and approaching the estimated ones as the input voltage was increased. The trends of the estimated and experimental values were similar to those of the motor without external preload.

Similarly, these could be attributed to static friction and slip occurring during the motor operation.

Another distinct findings associated with the operation with an external preload is the tilting of the rotor during operation. This was confirmed by changing the magnet position with respect to the rotor; as the result, the rotor rotational direction for altered oppositely in the same axis, for positive to negative e_z. This would also attribute to the discrepancies between the estimated and experimental rotor velocity. The estimation assumes that as the rotor tilt during operation, it sits in a contact point, however a more realistic situation is that the rotor sits in a contact sector, hence the lower rotor velocity. As higher input voltage is supplied and the motor rotates faster, it rotates and polishes the contact sector it sits on, and as a result the contact sector approach a contact point. Therefore, the rotor velocity approaches the estimated (travelling wave) velocity at higher input voltage.

We then similarly modeled the motor transient response as first-order lag system similar to most ultrasonic motor response [14, 15]. The model was valid as the coefficients of determinations are of good values. The maximum torques achieved for both configurations were around $0.3 - 1.5$ µN.mm.

The rise times for the two configurations were found to be different, around 30 ms and 50 ms for the 0.25 mm and 0.45 mm hole, respectively. Hence, at the same input voltage of 100 V_{pp}, both the acceleration and output power values were also different. The

acceleration values were ≈ 1800 rad/s^2 for the 0.25 mm hole configuration in comparison to ≈ 500 rad/s^2 for the 0.45 mm hole configuration; while the output power values were calculated to be around 20 nW and 2.5 nW for the 0.25 mm and 0.45 mm hole configuration, respectively.

3.5 Chapter summary and conclusion

Table 3.3 Performance summaries for motor with and without preload.

Hole size		Input V_{pp}	Significant Rotor bounce	Maximum Rotation speed (rpm)	Maximum Torque (nN.m)	Rise Time (ms)	Maximum Rotational acceleration (rad/s^2)
0.25 mm	Y-axis (no magnet)	100	Y	1376	5.11	11.6	7855.32
		70	Y	169.8	1.83	4	2809.24
	Z-axis (magnet)	100	N	669.73	1.19	24.24	1828.47
		70	N	253.49	0.48	22.9	732.46
0.45 mm	Y-axis (no magnet)	100	Y	425.9	5.09	3.6	7829.78
		70	Y	115.5	0.46	10.8	708.07
	Z-axis (magnet)	100	N	435.45	0.34	54.75	526.38
		70	N	210.47	0.21	42.7	326.22

We have developed a high performance SAW activated rotary motor. The *research contribution* of this work is a SAW actuated rotary motor which can operate in *a chosen yet arbitrary* axis. The stator is a SAW device made from PZT piezoelectric material,

while the rotor is 1 mm solid steel sphere. Two modes of operation were developed; with and without an external preload.

PZT is an isotropic piezoelectric material; hence IDTs can be designed in any direction on the plane of the substrate surface. The SAW generated would always propagate away from the generating IDT. This was confirmed with the travelling wave visualization using the LDV. Based on the working principle of a SAW motor, the rotor would always rotate about an axis which is perpendicular to the SAW propagation path. This is a very beneficial phenomenon to be exploited. By designing multiple IDTs, with relative positions with respect to the rotor, the rotor can be controlled to rotate in any chosen axis along the plane of the SAW propagation path. This was the hypothesis formed which has driven the project motivation. The hypothesis was proven to be true. As a result, we have successfully developed a SAW actuated rotary motor able to rotate in any planar axis chosen.

Contrary to current SAW linear motor developed, the rotating motor can operate without any external preload. Its maximum rotational capability is up to *2000 rpm* at 110 V_{pp} input voltage. If an external preload is provided, in our case a permanent magnet positioned under the PZT substrate, the rotor interestingly alters its rotational axis to the z-axis (normal to the surface). Hence, by adding the external preload, the 3rd degree of freedom was achieved. Another benefit associated with this mode is rotor stability during operation; the transient response shows significant reduction in fluctuations. The

maximum rotational capability is however, less, approximately up to *1000 rpm* even at a higher input voltage of 130 V_{pp}.

Combining the planar arbitrary axis capability with the external preload, a complete three dimensional rotating motor was developed. It is worth to note, however, with current precision tools, it was very difficult to control the z-axis rotational direction. Nevertheless, the capability of the motor to rotate in any chosen axis in x-y-z space has been demonstrated in this project.

The research aim of the project has been achieved. A SAW rotary motor has been developed with ***a chosen yet arbitrary*** rotational axis capability. The motor superior performance in comparison to SAW rotary motor reported on literature [1, 2] has been extensively demonstrated. Its configuration is far less complex and its maximum rotational velocities (either with or without external preload) are significantly higher.

A major potential application for the 3D rotary motor is for 3D micro-mirrors MEMS devices [17, 18]. The rotary motor would be a perfect candidate as the actuator for the mirrors motions. By constructing/attaching the micro-size mirrors to the rotors, *arbitrary but chosen* light reflections can be achieved. This will be highly beneficial for display devices, such as liquid crystal devices (LCDs) and high definitions projectors.

This study has also opened up many topics for further investigation and developments. Further work to give better understanding on the motor mechanism and further developments in scaling down the motor size would distinctly prove to be beneficial. These shall be discussed in more details in the recommendation chapter of this report.

References

1.	Cheng, L.P., et al., *Miniaturization of surface acoustic waves rotary motor.* Ultrasonics, 2002. **39**(8): p. 591-594.
2.	Zhang, G.M., et al., *Surface acoustic wave rotation motor.* Electronics Letters, 2000. **36**(16): p. 1437-1438.
3.	Shilton, R.J., et al., *Rotational microfluidic motor for on-chip microcentrifugation.* Applied Physics Letters, 2011. **98**(25).
4.	Hsiao, Y.-J., et al., *Surface acoustic wave characteristics and electromechanical coupling coefficient of lead zirconate titanate thin films.* Materials Letters, 2006. **60**(9-10): p. 1140-1143.
5.	Kirby, P.B., et al. *PZT thin film bulk acoustic wave resonators and filters*. in *Frequency Control Symposium and PDA Exhibition, 2001. Proceedings of the 2001 IEEE International*. 2001.
6.	Cho, J., et al., *Optimization of electromechanical coupling for a thin-film PZT membrane: II. Experiment.* Journal of Micromechanics and Microengineering, 2005. **15**(10): p. 1804-1809.
7.	Sakano, K., M.K. Kurosawa, and T. Shigematsu, *Driving characteristics of a surface acoustic wave motor using a flat-plane slider.* Advanced Robotics, 2010. **24**(10): p. 1407-1421.
8.	Sakano, K., M.K. Kurosawa, and T. Shigematsu. *Surface Acoustic Wave Motor with Flat Plane Slider*. 2008. IEEE.
9.	Wallaschek, J., *Contact mechanics of piezoelectric ultrasonic motors.* Smart materials and structures, 1998. **7**: p. 369.
10.	Ueha, S., et al., *Ultrasonic motors: theory and applications*1993: Clarendon Press Oxford.
11.	Friend, J.R., *Analysis of the 0.668 inch traveling-wave piezoelectric motor.* Proceedings of the 37th AIAA/ASME/ASCE/AHS/ASC Structures, Structural Dynamics, and Materials Conference and Exhibit. , 1996. **96**(1452): p. 1-15.
12.	Tseng, C.C., *Elastic Surface Waves on Free Surface and Metallized Surface of CdS, ZnO, and PZT 4.* Journal of Applied Physics, 1967. **38**(11): p. 4281-4284.
13.	Liu, K.C., J. Friend, and L. Yeo, *Rotating bouncing disks, tossing pizza dough, and the behavior of ultrasonic motors.* Physical Review E, 2009. **80**(4): p. 046201.
14.	Nakamura, K., et al., *An estimation of load characteristics of an ultrasonic motor by measuring transient responses.* IEEE Transactions on Ultrasonics, Ferroelectrics, and Frequency Control, 1991. **38**(5): p. 481-485.
15.	Friend, J., K. Nakamura, and S. Ueha, *A traveling-wave, modified ring linear piezoelectric microactuator with enclosed piezoelectric elements - The "scream" actuator.* IEEE Transactions on Ultrasonics, Ferroelectrics, and Frequency Control, 2005. **52**(8): p. 1343-1353.
16.	Liu, D.K.C., J. Friend, and L. Yeo, *A brief review of actuation at the micro-scale using electrostatics, electromagnetics and piezoelectric ultrasonics.* Acoustical Science and Technology, 2010. **31**(2): p. 115-123.
17.	Dudley, D., W. Duncan, and J. Slaughter. *Emerging digital micromirror device (DMD) applications*. 2003.
18.	Dechev, N., et al. *Microassembly of 3d micromirrors as building elements for optical mems switching*. 2006.

Chapter 4

SAW device development on stratified material for microfluidics applications

4.1 Introduction

The hybrid approach of developing a SAW device is desirable as it opens up much potential. As discussed in the literature review chapter (chapter 2), combination of piezoelectric thin film material on a commonly used substrate is highly desirable. With proper selection, materials with collective beneficial properties can be exploited. Du et al [1-3] have demonstrated some work on microfluidics applications using SAW devices fabricated on zinc oxide (ZnO) thin film deposited on a silicon substrate. In this thesis, the use of sapphire (Al_2O_3) as the substrate is proposed due to its higher acoustic velocities and low propagation loss [4].

4.2 SAW devices based on ZnO/Al_2O_3 stratified material (method + characterization)

_____

This project aimed to investigate SAW devices fabricated on a ZnO/Al$_2$O$_3$ stratified material for microfluidics applications. The combined properties of these two material was envisioned to result in a superior device performance. As the Rayleigh mode of SAW on ZnO device is known to have inferior electromechanical coupling [2, 5, 6], the Sezawa mode was to be explored for this purpose. Comparison of these devices based on different film thickness would be examined. In addition, similar device fabricated on lithium niobate (LiNbO$_3$) substrate would be compared. The wavelength of the devices was fixed at 32 μm. Throughout this report, LN represent the SAW device made on LiNbO$_3$ substrate, Z1 and Z2 represent the SAW device made on 1 μm and 11 μm thick ZnO/Al$_2$O$_3$ stratified material, respectively. The experimental process flow can be viewed in Figure 4.1; each step shall be discussed.

4.2.1 Materials Selection

The material use for this study was *c-axis* zinc oxide (ZnO) material grown on R-Plane (1 1 0 2) sapphire (Al$_2$O$_3$) substrate. The ZnO was deposited from an undoped ZnO ceramic sputtering target with 99.99% purity target, 3" diameter, 0.125", bonded to Cu plate (Plasmaterials, Inc.). Al$_2$O$_3$ substrate was selected due to its high acoustic velocity (~10,000 m/s) and very low propagation loss [4]. The high acoustic velocity of the substrate material is attractive for higher frequency SAW application as it avoids the needs of sub-micron IDT patterning. The Al$_2$O$_3$ wafer (UniversityWafer) selected specification was as follows: diameter of 50.8±0.1mm, thickness of: 400±15um, micro-roughness: Ra ≤ 0.3nm, with front surface epi-polished finish and back surface ground finish.

Material Selection   **Design**

↓

Material Deposition

Characterization

↓

Material Characterization
(XRD and SEM)

↓

SAW Device Fabrication   **Fabrication**

↓

Electrical Characterization
(Frequency Response and
Wave Visualization)

↓

The Operation of the SAW
Microfluidics

Applications

Acoustic
Streaming

PLGA
Nanoparticles
Precipitation
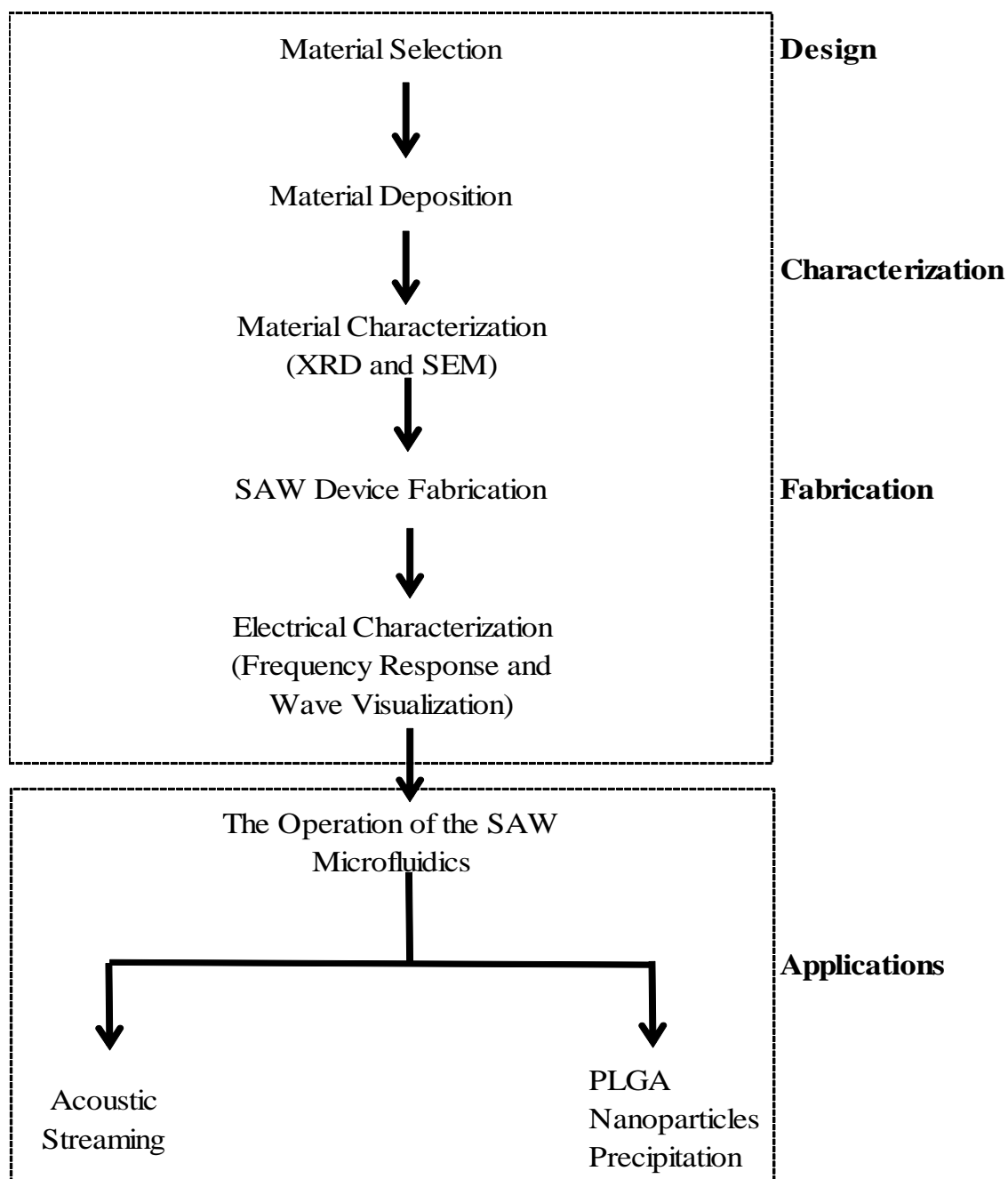
Figure 4.1. Experimental process flow

4.2.2 Material Deposition

Wafer cleaning

_____

Prior to sputter deposition, the Al_2O_3 wafers was cleaned in acetone for 5 minute to remove any organic impurities, followed by sequential cleaning with isopropanol and DI water, respectively. The wafers were then blown dried using nitrogen at room temperature. The next step was cleaning the wafers with oxygen plasma, in plasma cleaner (PDC-32G-2, Harrick Plasma). Following the cleaning processes, the wafers were loaded into the sputtering system.

ZnO thin films were deposited on sapphire substrate by RF magnetron sputtering (Hummer BC-20 DC/RF Sputter system, Anatech, USA). The deposition parameters highly affect the ZnO film quality; hence optimization was performed to achieve the deposition rate and desired film crystalline structure (c-axis). Utilizing the optimized deposition parameters, the sputtering rate was approximately *0.25 μm/hour*.

The optimized deposition parameters were as follow:

- Target-substrate distance: ~12cm

- Base pressure: 5×10^{-7} Torr.

- Sputtering gas: 60% Ar + 40% O_2

- Deposition pressure: 8×10^{-3} Torr.

- RF power: 150 W

- Substrate temperature: 150°C

After deposition, a subsequent post-annealing treatment was carried out at 500ºC for 5 hrs in ambient air; this aimed at providing sufficient energy to rearrange the atoms in the crystal sites interface and to eliminate the intrinsic stress induced by sputtering [7,

_____

8]. Three different thickness of ZnO film was deposited; they are 1 μm, 6 μm and 11 μm. Two thickness configurations, 1 μm and 11 μm were to be used for further experiments, due to the extreme difference in film thickness to wavelength ratio, h/λ, which would approximately be 0.031 and 0.34, respectively for a 32 μm wavelength SAW. Emanetoglu et al [5, 9] reported a critical value of h/λ, a ratio of greater than 0.15 to induce the Sezawa mode. Using these films with two thicknesses, below and over the critical ratio, the existence of the Sezawa mode could be established. After deposition, the materials and SAW devices were characterized with various methods similar to the ones proposed by Hickernell [10, 11].

4.2.3 Material Characterization

The deposited ZnO film was required to be c-axis oriented, due to its high electromechanical coupling coefficient [3, 5, 6, 9, 12-16]. The crystalline structure of ZnO on sapphire was examined by X-ray diffraction spectroscopy (XRD) with Cu Kα, λ of 0.1542 nm (Phillips X-ray Diffractometer); and the surface morphologies were observed with atomic force microscopy (AFM). The XRD data plotted in Figure 4.2 show the high *2θ* intensity at *34.4º*. This angle, representing (002) diffraction peak, indicates that the ZnO deposited on sapphire is c-axis oriented. The subsequent scanning electron microscopy (SEM) cross-sectional view validated the columnar structure growth of the ZnO film. The c-axis orientation and smooth surface are critical parameters of a SAW device.

_____
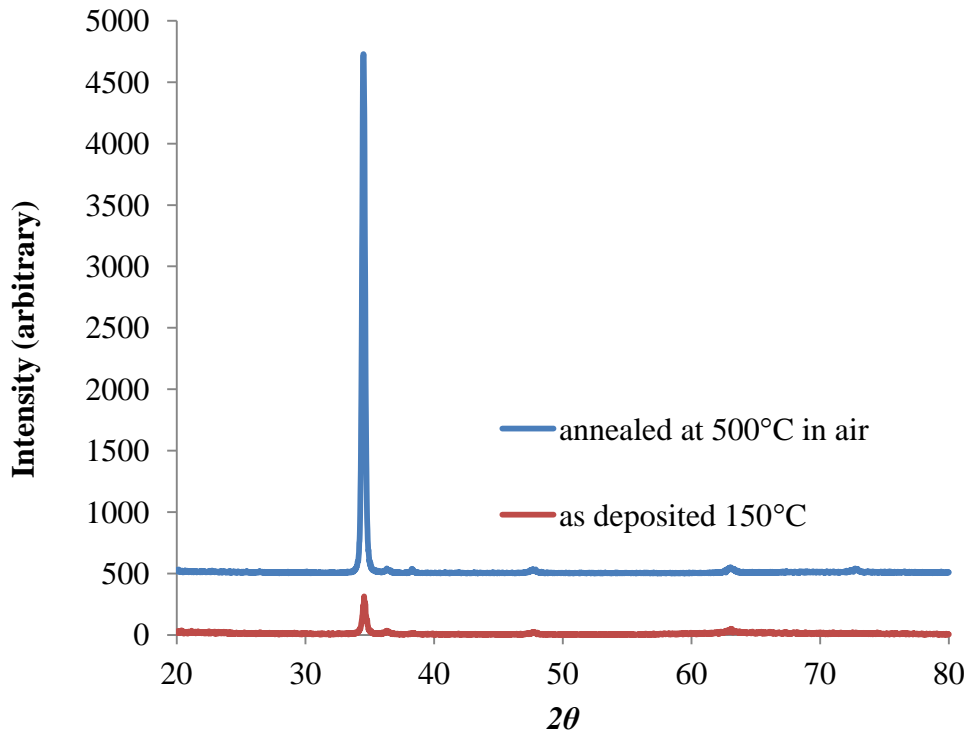
Figure 4.2. XRD spectra of the sputtered ZnO on sapphire substrate. The spectra shows the preferential *(002)* wurtzite c-axis orientation perpendicular to the surface of the substrate. The diffraction peak is observed at *2θ* of *34.4º*, which indicates the (002) crystallographic orientation

Scanning Electron Microscopy (SEM) with EDX

After XRD characterization, the work was followed by microscopy of the film using a Scanning Electron Microscope (SEM) (JSM-7001F, JEOL, Ltd.). The purpose was for further validation that the film growth was normal to the substrate material. The SEM results confirmed that the ZnO films were c-axis oriented, even in thick film (~6 µm) the film was still c-axis oriented, similar to SEM results found in previous reports (Figure 4.3) [8, 17]. Energy-dispersive X-ray spectroscopy (EDX) was performed

_____

concurrently with the scanning electron microscopy. The result confirmed the

majority existence of zinc and oxygen elements on the film.
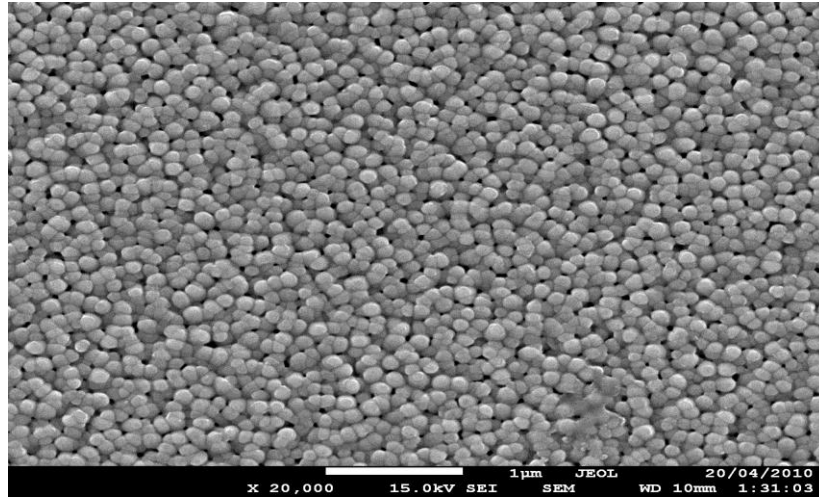
(a)
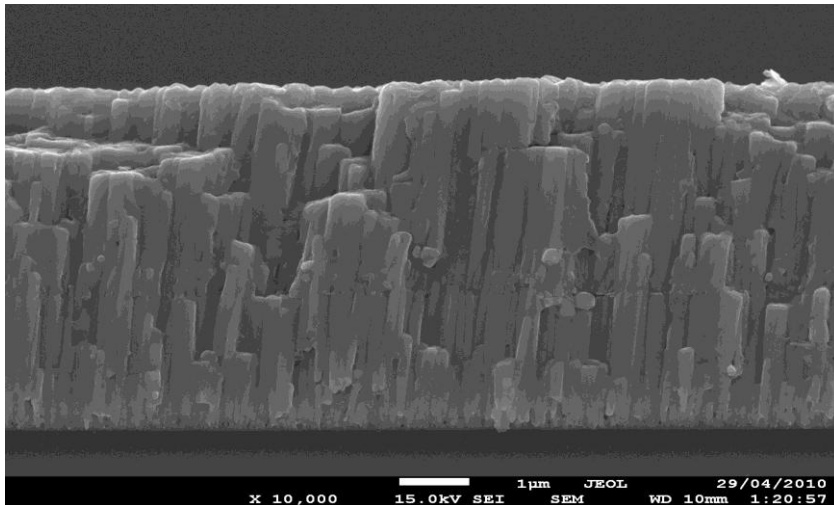
(b)

Figure 4.3. SEM micrographs of the ZnO films, (a) top and (b) cross-sectional view, sputter deposited at 150°C showing columnar growth of the ZnO films with average grain size of ~75 nm.

_____
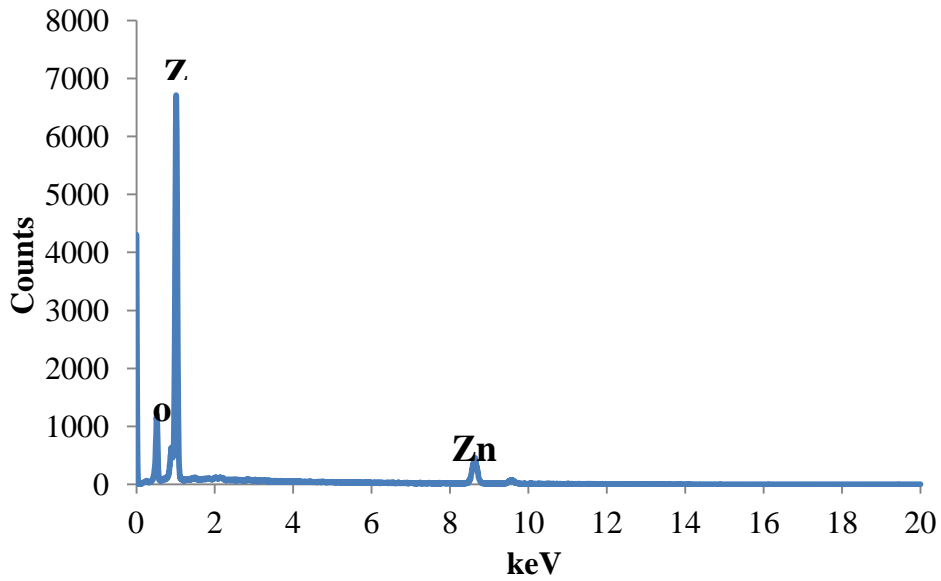
Figure 4.4. Energy-dispersive X-ray spectroscopy (EDX) result of the ZnO film deposited.

4.2.4 SAW Device Fabrication

After the required film quality has been evaluated, SAW devices were fabricated on the ZnO thin films. ZnO is very reactive to common metal etchants, as shown in empirical result and references [18-20]. Consequently, standard microfabrication technique which includes wet etching cannot be performed; as the film can be easily etched. The interdigital transducer (IDT) patterns were instead transferred on to the ZnO surface using a lift-off process.

The IDT consists of an adhesion layer of 10nm Cr and 200nm of Au, which were thermally evaporated. The IDT was designed to have 60 numbers of finger-pair with 8 μm dimension for both the width and the spacing, which corresponds to a wavelength of 32μm. The bus bar and aperture were 1 mm and 3 mm, respectively. The

111

_____

fabrication process steps are presented in Figure 4.5. An optical image of the fabricated device and the mask are shown in Figure 4.6 IDTs with similar design were also fabricated on a $LiNbO_3$ substrate.

The fabrication steps were as follow:

1. Photoresist coating

   - The positive photoresist (AZ 1512 HS, AZ Electronics Materials) was spread onto a spin coater (Delta 80RC, SUSS MicroTec AG).

   - Maximum rotation speed of 3000 rpm for 30 s.

   - Soft bake at 90°C for 20 minute in a vacuum drying oven (Heraeus instrument vacutherm, Thermo Fisher Scientific Inc.).

   - Thickness of the photoresist is ~ 1.1 μm

2. Ultraviolet (UV) exposure

   - Utilizing a photolithographic mask (CAD/Art Services Inc.)

   - The UV (365 nm wavelength) exposure was performed using a mask aligner (MA6, SUSS MicroTec AG)

   - Use hard contact vacuum exposure for a dosage of 100 mJ/cm^2.

3. Developing

   - The photoresist was developed using a mixture of photoresist developer (AZ726 MIF, AZ Electronics Materials) with de-ionized (DI) water for a total developing time of 55 seconds.

_____

- The sample surface was then cleaned using a plasma system (PDC-002, Harrick Plasma)

4. Metal Deposition

- E-beam evaporation process (Intlvac) was utilized to deposit 10 nm or Cr and 300 nm of gold.

5. Lift-off/ Photoresist removal

- The photoresist layer was finally removed by lift-off process. The sample is submerged in acetone $((CH_3)_2CO)$ solution in a glass beaker (Schott Duran), the beaker was then put into an ultrasonic cleaner (8890, Cole-Parmer). The ultrasonic vibration would assist the photoresist removal process to yield the interdigital transducers of the SAW devices.

Wafer Dicing

The fabricated wafer was subsequently cut using a diamond tip wafer scriber system (DTX-200-AB, Dynatex International). The 2 inch wafer was placed onto a scribing set, consisting of a hoop and adhesive tape (Dynatex International). The wafer was then carefully mounted onto the scriber system, and subsequently scribed onto individual devices with 8×20 mm^2 planar dimensions.

1. Photoresist coating

2. UV Exposure

3. Developing

4. Metal Evaporation
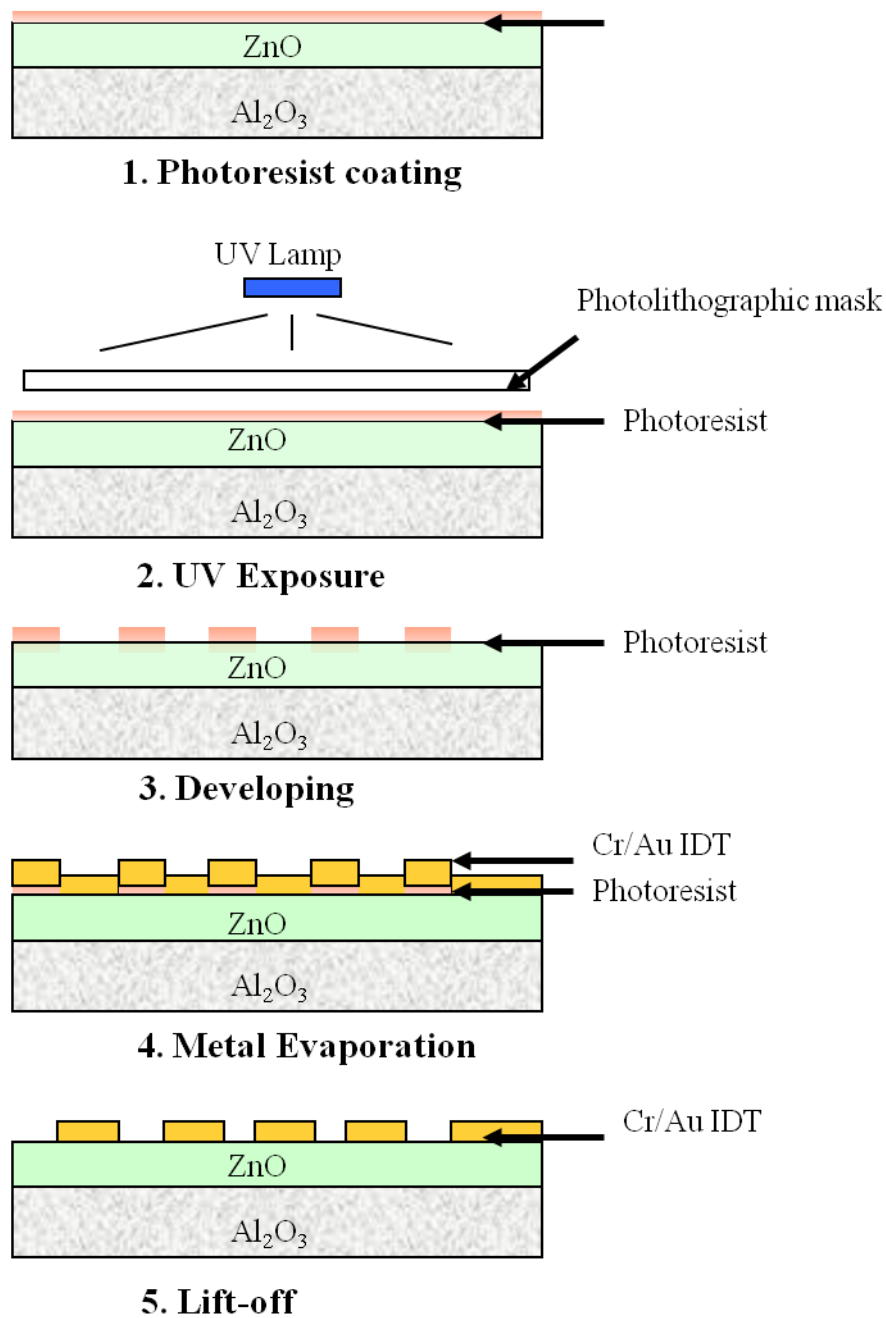
5. Lift-off

Figure 4.5. The fabrication steps of the SAW devices, using a lift-off process; which includes photoresist coating using a spin coater (Delta 80RC, SUSS MicroTec AG), ultraviolet (UV) exposure using a Mask Aligner (MA6, SUSS MicroTec AG), metal deposition, and finally photoresist removal to yield the IDTs.
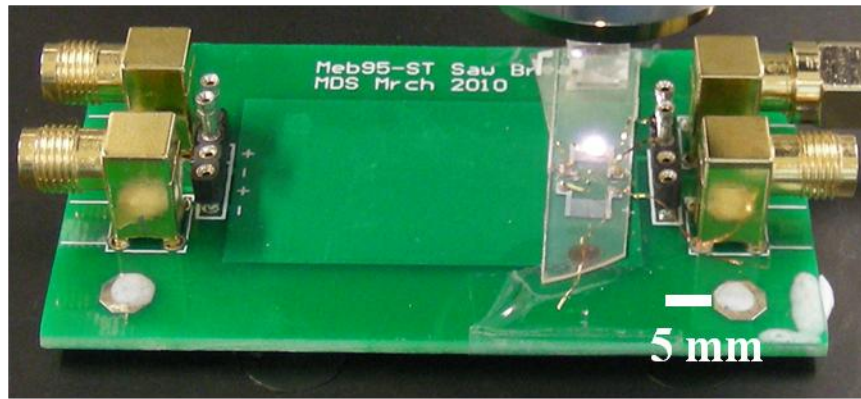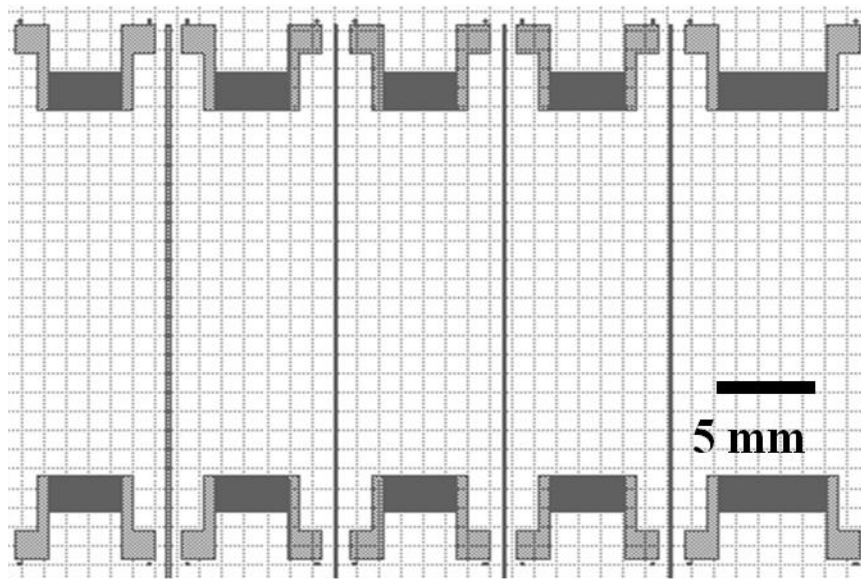
Figure 4.6. (a) An optical image of the fabricated SAW device attached to a jig with SMA connector, shown side-by-side with the (b) photolithographic mask design. The width and spacing are designed to be 8 μm, which correspond to 32 μm wavelength.

4.2.5 Electrical Characterization (Frequency Response and Wave Visualization)

Frequency Response

After the fabrication of the SAW devices, their electrical response was characterized using a network analyzer (Agilent E5062A). This step is essential to check that resonance frequency matches with the design. The wavelength for all the devices is set to 32 μm (pitch width of 8 μm). They are fabricated onto two different ZnO thicknesses, 1 μm and 11 μm. The two film thicknesses were selected as their h/λ (thickness over wavelength) ratios were lower and higher than the critical h/λ (0.15), respectively. This critical ratio is required to induce the Sezawa mode; a Rayleigh-like SAW mode with higher phase velocity trapped in the stratified structured as the frequencies in increase/wavelength is decreased. It is limited to occur in stratified medium and only if the acoustic velocity in the surface layer is lower than or equal to the acoustic velocity in the lower layer [21-24].

The frequency spectrums of all the devices are shown in Figure 4.7. The Rayleigh waves on both SAW devices made on 1 μm thick ZnO/Al_2O_3 film (indicated by Z1) demonstrated a high insertion loss. The minimum S_{11} values for the 1 μm thick ZnO/Al_2O_3 was approximately -2.62 dB for resonance frequency of 165 MHz, and for the 11 μm ZnO/Al_2O_3 (indicated by Z2-R), it was approximately -1.49 dB for resonance frequency of 96.1 MHz Both values were significantly less than that of the same mode of the device made on $LiNbO_3$ substrate (LN), which shows S_{11} of

_____

approximately -8.98 dB. The Sezawa mode of the SAW device made on 11 μm thick ZnO/Al$_2$O$_3$ (Z2-S) however demonstrated the lowest insertion loss, -22.14 dB for resonance frequency of 127.85MHz, indicating the highest electromechanical coupling coefficient. The Rayleigh mode resonance frequencies of the device on ZnO/Al$_2$O$_3$ were also observed to decrease as the film thickness increases. This is in accordance to observation reported in literatures [2, 5, 9].

_____
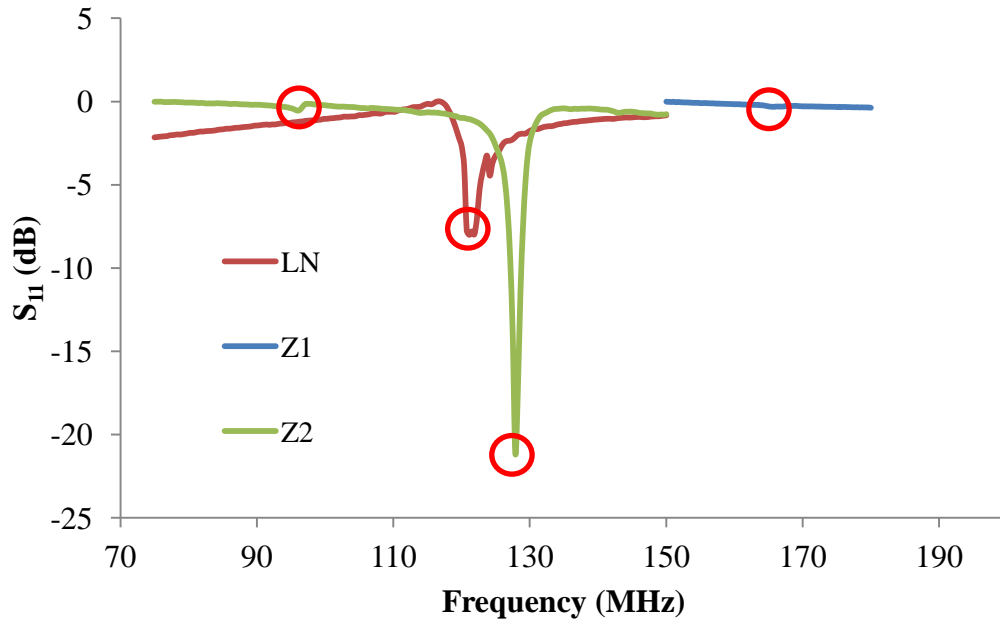
(a)
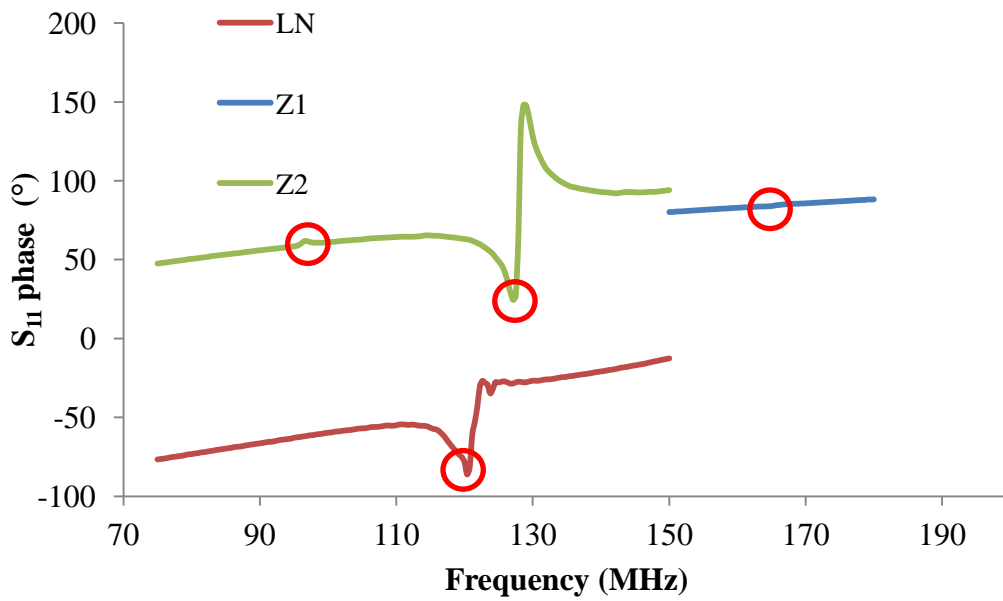
(b)

Figure 4.7. Frequency Spectrum, showing the (a) logarithmic of the magnitude and (b) phase of the S_{11} (reflection) parameter; of the SAW device, which were made on LiNbO3 substrate, 1 μm and 11 μm ZnO/Al$_2$O$_3$ stratified material. The red circles indicate the resonance frequencies; 121 MHz for LN, 165 MHz for Z1 and 96.1 MHz for Z2 on their Rayleigh mode; furthermore 127.85 MHz for Z2 on its Sezawa mode.

_____

The electromechanical coupling values can be calculated using the admittance values of the measured devices [25-27].

$$k^2 = \frac{G_a}{8 f_0 C_T N^2}$$

(1)

Where G_a is the radiation conductance, f_0 is the centre frequency, C_T is the total electrode capacitance of the IDT, and N is the number of IDT finger pairs. The admittance values $Y = G_a + jB = G_a + j2\pi f_0 C_T$ can be calculated based on S_{11} log magnitude and phase value.

Table 4.1 shows the measurement result of the devices resonance frequencies, frequency spectra and electromechanical coupling coefficient. Observation of the result shows that as the thickness of the ZnO increases, the resonance frequencies of the SAW devices decrease.

Furthermore, the Sezawa mode of the SAW device made on 11 μm thick ZnO/Al$_2$O$_3$, as indicated by the lowest insertion loss value, demonstrates the highest electromechanical coupling coefficient of 2.35%. It can be deduced that the Sezawa mode gives the most efficient amplitude to power ratio compared to the other.

_____

Table 4.1 SAW properties of the devices

Substrate	Lithium Niobate 128° Y-X cut	ZnO/Al$_2$O$_3$	ZnO/Al$_2$O$_3$	
Thickness (μm)	bulk (~500)	1	11	
Wave type	Rayleigh	Rayleigh	Rayleigh	Sezawa
Frequency (MHz)	121	165	96.1	127.85
S$_{11}$ (dB)	-8.00	-0.37	-0.54	-21.14
Phase Velocity (m/s)	3872	5280	3075.2	4091.2
k^2 (%)	0.16	0.02	0.02	2.35

Wave visualization results

The maximum vibration displacement (amplitude) and speed of the travelling wave on the fabricated devices were measured using a Laser Doppler Vibrometer (LDV; Polytec PI MSA-400, Waldbrunn, Germany). The wave amplitude measurement results were shown in Figure 4.8 and Figure 4.9. The amplitude is represented as $\boldsymbol{\gamma} = A\sin(\omega t)\,\boldsymbol{e}_z$. The vertical vibration velocity is then, $\dot{\boldsymbol{\gamma}} = \frac{d\gamma}{dt}\boldsymbol{e}_z = \omega A\cos(\omega t)\,\boldsymbol{e}_z$, in which the maximum is $\dot{\gamma}_{max} = \omega A = 2\pi f A$. Hence, the curves for amplitude and the maximum vibration speed should demonstrate the same trend. SAWs were generated by applying a continuous sinusoidal electrical input into an

_____

interdigital transducer (IDT, Au 60-finger pair electrode) patterned on the surface of the ZnO/ Al_2O_3 and $LiNbO_3$. The input power was observed to be proportional to the square of the amplitude or maximum vertical vibration speed (Figure 4.8 and Figure 4.9), which was in accordance to previous report [28]. The maximum standard deviation of the data was less than 10%.
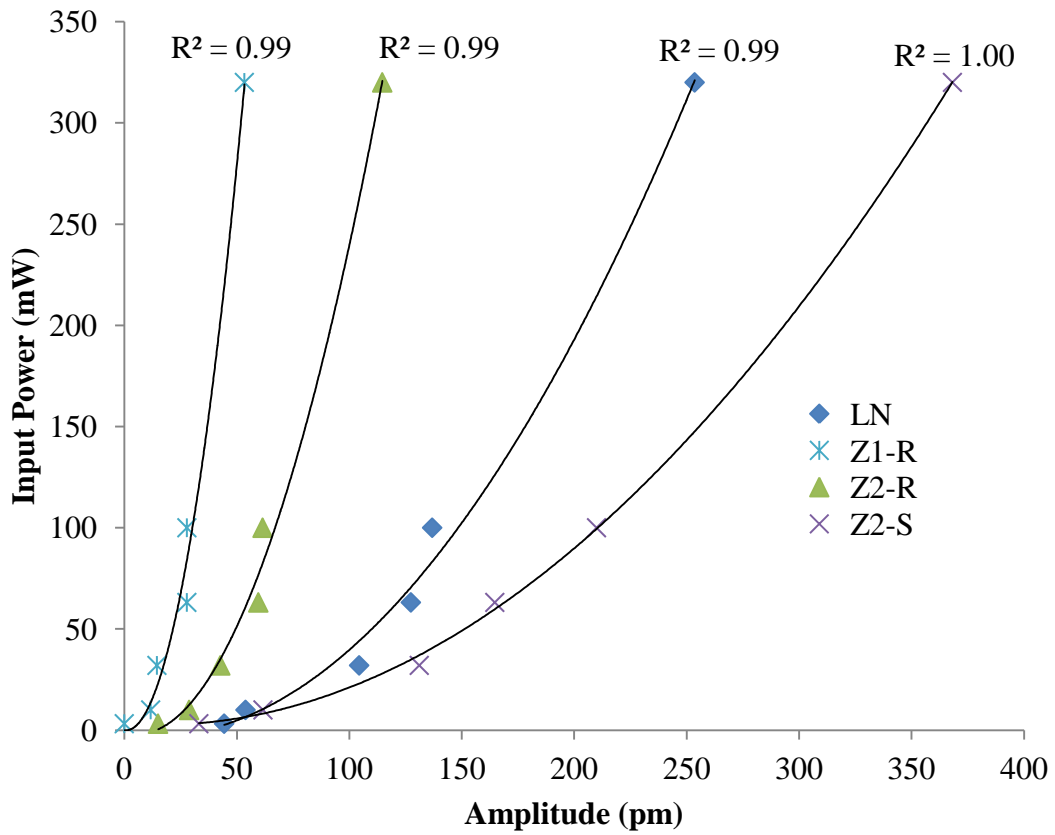
Figure 4.8. Wave amplitude for different input power for various devices operated at different mode. The LN device operated at Rayleigh mode shows high power to amplitude ratio, the Z2-S however showed the highest ratio. On the other end, Z1-R showed the lowest ratio.

_____
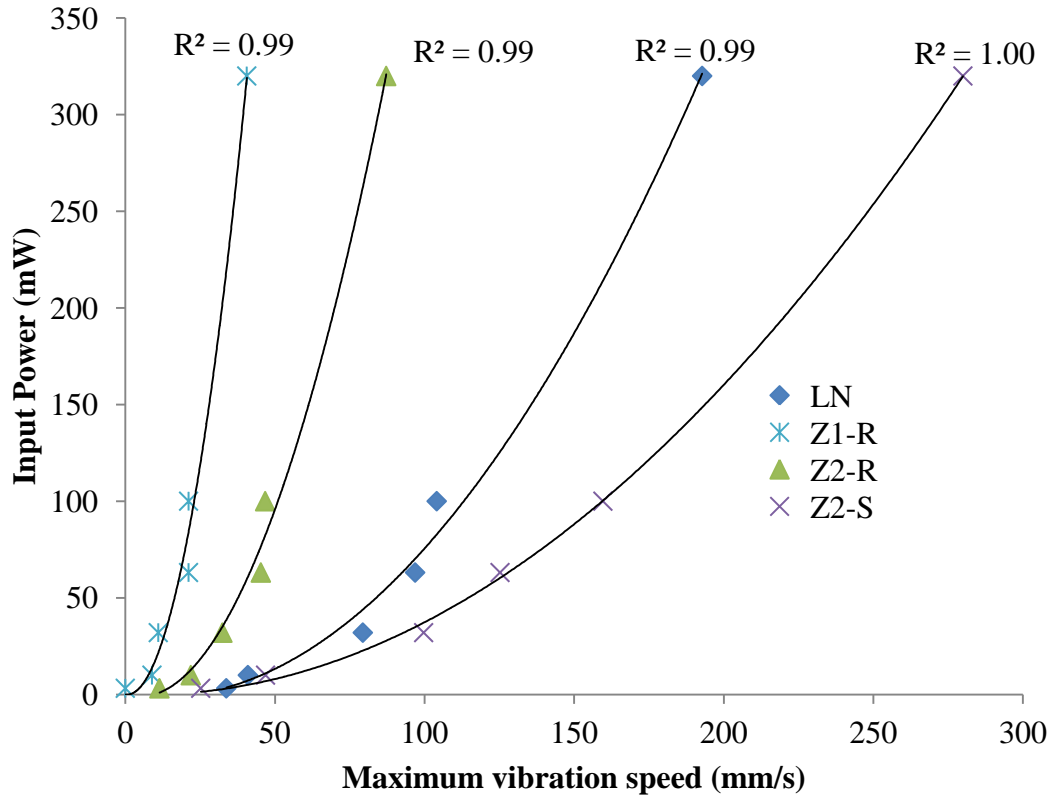
Figure 4.9. Maximum wave vertical/vibration speeds for different input power for various devices operated at different mode. The LN device operated at Rayleigh mode showed high power to vertical speed ratio, the Z2-S however showed the highest ratio. On the other end, Z1-R showed the lowest ratio.

Figure 4.8 shows the surface acoustic wave amplitudes of three SAW devices; they are two devices constructed on ZnO/Al_2O_3 and one device constructed on $LiNbO_3$ substrate. The amplitude to power ratio of the Rayleigh wave generated on 1 μm ZnO/Al_2O_3 (Z1-R) was the lowest among the others. As the thickness of the ZnO layer increased, the amplitude also increased. For 11 μm ZnO film, the Rayleigh wave (Z2-R) amplitude to power ratio was higher than the one generated on 1 μm thick film; this ratio however was still less compare to the amplitude of the SAW generated on $LiNbO_3$ substrate. The Sezawa mode wave generated on thick ZnO/Al_2O_3 (Z2-S)

_____

had nevertheless the highest ratio. This result was in accordance to previously reported findings [5, 13, 15].

In summary, the SAW devices made on ZnO/Al_2O_3 material generally gives poorer performances compare to more commonly use $LiNbO_3$ substrate. This is particularly true for the Rayleigh waves generated. Another phenomenon only occurring in layered/stratified medium is the occurrence of higher order SAW called the Sezawa wave. A Sezawa waves is a Rayleigh-like SAW mode which is trapped in the layered structured as the frequencies in increase/wavelength is decreased [21]. This Sezawa wave was able to be generated on an 11 μm thick ZnO film (h/λ value of ~ 0.3). This wave shows much higher amplitude to power ratio compares to its Rayleigh counterparts. The amplitude to power ratio of this wave is even higher than that of Rayleigh wave generated on $LiNbO_3$ substrate. The superiority in amplitude to power ratio indicates high electromechanical coupling coefficient, which is supported by the frequency response measurement result.

After the device performances analysis was completed, the devices, particularly in the Sezawa mode were utilized for various microfluidics applications.

4.3 Application of SAW devices based on ZnO/Al2O3 stratified material to induce acoustic streaming

_____

After completion of the characterization, the fabricated ZnO/Al_2O_3 based SAW devices were utilized to induce acoustic streaming in a sessile droplet. Acoustic streaming experiments utilizing $LiNbO_3$ based SAW device were also performed, and their maximum streaming speeds were compared.

4.3.1 Method

Water droplets with a volume of 0.5 to 2.5 µL seeded with 4.8 µm size fluorescent polystyrene microspheres (Duke Scientific Corporation, USA) were placed onto the surface of ZnO, in the propagation pathway of the SAW for flow visualization. The input power was provided using a signal generator (Agilent N9310A) coupled with an amplifier (Model 10W 1000C, Amplifier Research). The power input to the IDT was monitored using a digital source oscilloscope (Wave Jet 332, LeCroy). Visualization of the particle and fluid motion was carried out using a high speed video camera (Motion BLITZ, Mikroton GmbH) connected to a fluorescence stereomicroscope (Olympus BXFM) under reflected wideband blue light with its emission centered at 462 nm. The schematic experimental set-up was shown in Figure 4.10.

_____
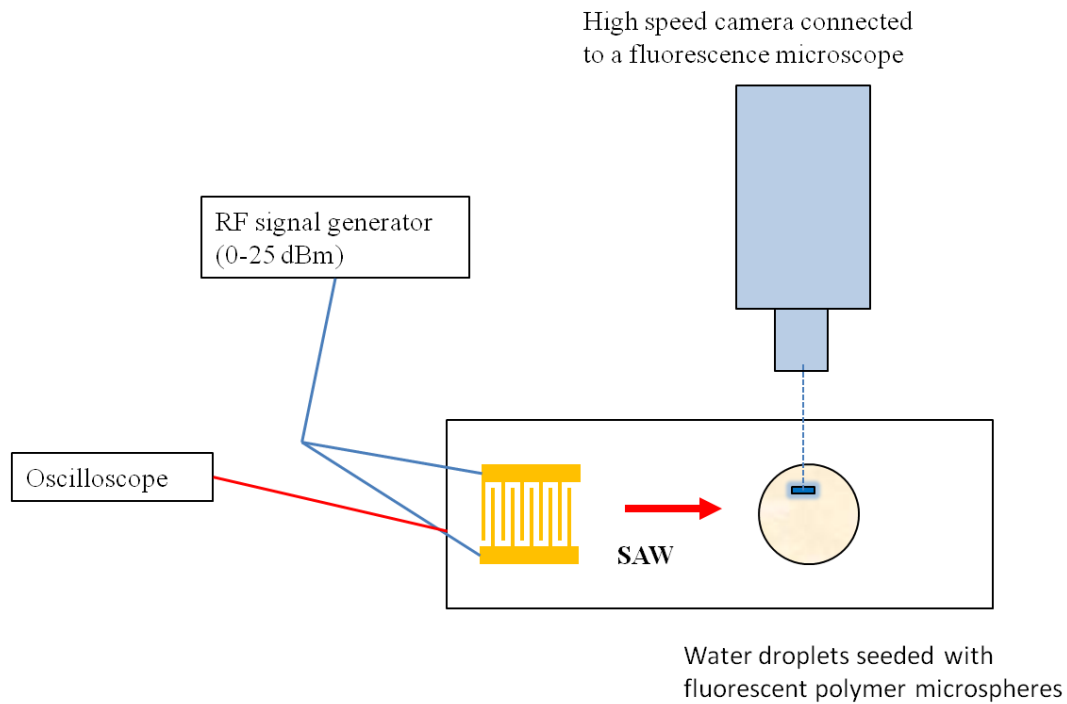
Figure 4.10. Schematic representation of the acoustics streaming visualization and speed measurement experiment. The IDT width and spacing are designed to be 8 μm, which correspond to 32 μm wavelength. Water droplets with various volumes (diameter of 0.7 mm to 1.5 mm) seeded with 4.8 μm size fluorescent polymer microspheres (Duke Scientific Corporation, USA) were placed in the propagation pathway of the SAW. The input power was provided using a signal generator (Agilent N9310A) coupled with an amplifier (Model 10W 1000C, Amplifier Research); and was monitored using a digital source oscilloscope (Wave Jet 332, LeCroy). Visualization of the particle and fluid motion was carried out using a high speed video camera (Motion BLITZ, Mikroton GmbH) connected to a fluorescence stereomicroscope (Olympus BXFM).

4.3.2 Result and Discussion

Acoustic streaming is a steady fluid motion resulted from the propagation of acoustic waves through a dissipative fluid medium. As the acoustic waves attenuated in the fluid medium, it generates a gradient in the momentum flux. This induces a Reynolds stress, which causes the steady fluid velocity [29].

_____

Acoustic streaming experiments were performed employing the fabricated SAW devices established and characterized earlier. The performances of these devices were compared with respect to maximum acoustic streaming speed generated. The acoustic streaming speed results of each modes and device should correlate to it wave speed amplitude, which acts as the excitation source.
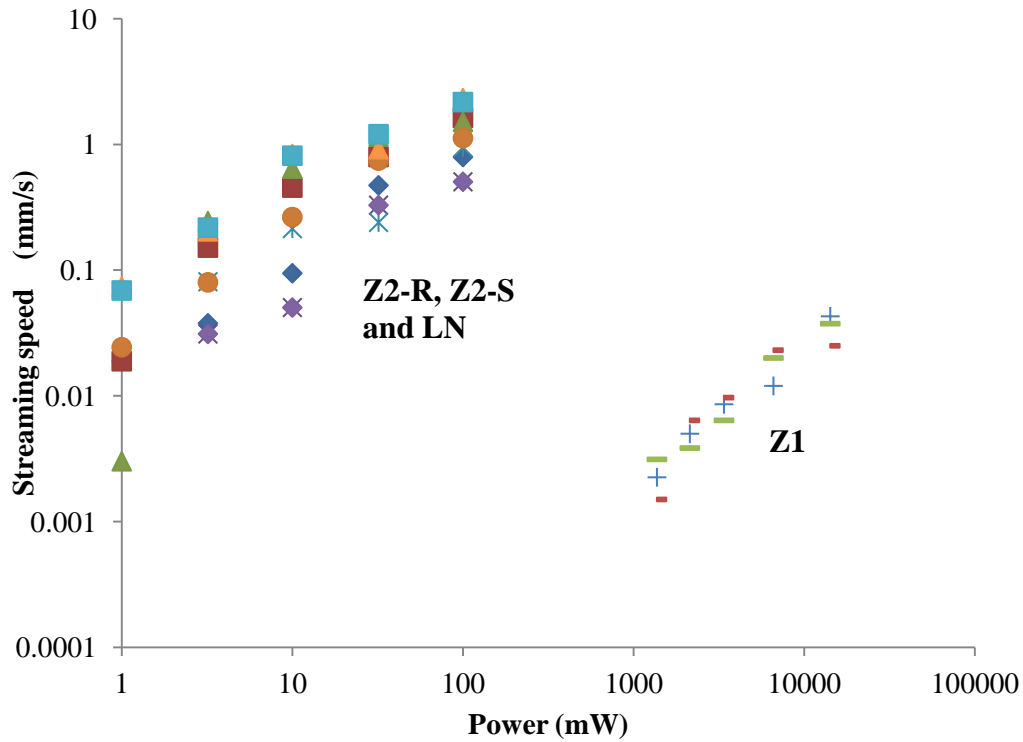
Figure 4.11. Acoustic streaming speed for various input power of three SAW devices; they are two devices constructed on ZnO/Al_2O_3 (Z1 and Z2) and one device constructed on $LiNbO_3$ substrate (LN). The water droplets volume utilized in the experiment were 0.5, 1 and 2 μL. Note that both the axes are in logarithmic scale. Note that LN represent the SAW device made on LiNbO3 substrate, Z1 and Z2 represent the SAW device made on 1 μm and 11 μm thick ZnO/Al_2O_3 stratified material, respectively.

The acoustic streaming speed measurement results are summarized in Figure 4.11. Maximum acoustic streaming speeds of *~25 mm/s* and of *~11 mm/s* were observed on the *11 μm* ZnO/Al_2O_3 SAW device during the Sezawa (Z2-S) and Rayleigh (Z2-R) mode operations respectively. These acoustic streaming speeds are *two orders of*

126

_____

magnitude higher than the maximum speed observed on the *1 μm* one during its
Rayleigh (Z1-R) mode operation. Furthermore, the input powers required to actuate
fast acoustic streaming in the *11 μm* ZnO/Al_2O_3 SAW device (1-100 mW) are *two
orders of magnitude lower* compare to those of *1 μm* ZnO/Al_2O_3 SAW device (> 1
W).
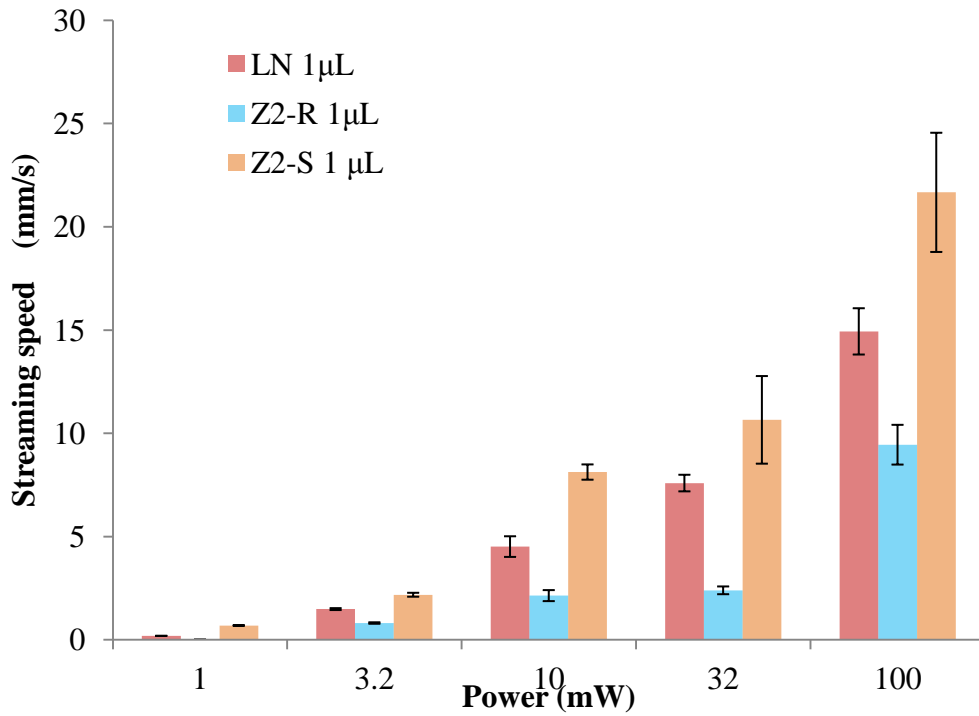
Figure 4.12. Acoustic streaming speed comparison of SAW devices fabricated on 11 μm thick
ZnO and Al_2O_3 substrate (Rayleigh and Sezawa wave) with those of fabricated on a $LiNbO_3$
substrate. The liquid used for the experiment was 1 μL water. Each error bar represents the
standard deviation of the data.

The acoustic streaming speed results of the 11 μm ZnO/Al_2O_3 SAW device were then
compared with that of $LiNbO_3$. The acoustics streaming speed data showed in Figure
4.11 demonstrate similar trends for various droplet volumes. As a representation, the
acoustics streaming speed of 1 μL sessile water droplet induced by the SAW
generated on the 11 μm ZnO/Al_2O_3 SAW device and on $LiNbO_3$ are plotted as
columns in Figure 4.12.

_____

The SAW generated by the Rayleigh mode (Z2-R) of the ZnO/Al$_2$O$_3$ device induced weaker acoustics streaming; the streaming speeds were less than those of induced by the Rayleigh mode of the LiNbO$_3$ substrate, albeit at the same order of magnitude. The acoustic streaming induced by the Sezawa mode (Z2-S) on the contrary, demonstrated the strongest acoustics steaming. This result demonstrated that thick film of ZnO piezoelectric material can be used as an alternative material for SAW induced microfluidics streaming.

In continuation of our study of the acoustics streaming speed values are now plotted with respect to the maximum vibration speed, *the excitation speed*, of each mode, shown in Figure 4.13. For ease of observation, the plots were separated to three figures for each of the sample respectively (Figure 4.14 - Figure 4.16). The results of 1 μm thick ZnO/Al$_2$O$_3$ (Z1) were omitted as the values were orders of magnitudes lower; hence would not be significant as a comparison. It should be *noted* that the maximum vibration (*excitation)* speed for each mode is *different*. As shown by the LDV measurement results, for the same input power, the Sezawa mode (Z2-S) has the highest excitation speed, followed by the Rayleigh mode on LiNbO$_3$ (LN) and Rayleigh mode (Z2-R) of the ZnO/Al$_2$O$_3$ device. This is why the acoustic streaming speeds induced by the Sezawa mode (Z2-S) has the highest value, followed by the Rayleigh mode on LiNbO$_3$ (LN) and Rayleigh mode (Z2-R) of the ZnO/Al$_2$O$_3$ device.

This is the *key finding* of the work, the *surface displacement (amplitude) or* the *vibration speed* was found to be the *most influential parameter* for acoustic streaming.

_____

The acoustic streaming speed results further validate the frequency response and wave visualization measurement.

Additionally, for low excitation speed, the streaming speed was found to be on the same order of magnitude with the excitation speed. Yet, as the excitation speed increases to tens of cm/s order of magnitude, the streaming speed increases much more conservatively, peaked at tens of mm/s order of magnitude (shown in Figure 4.17).
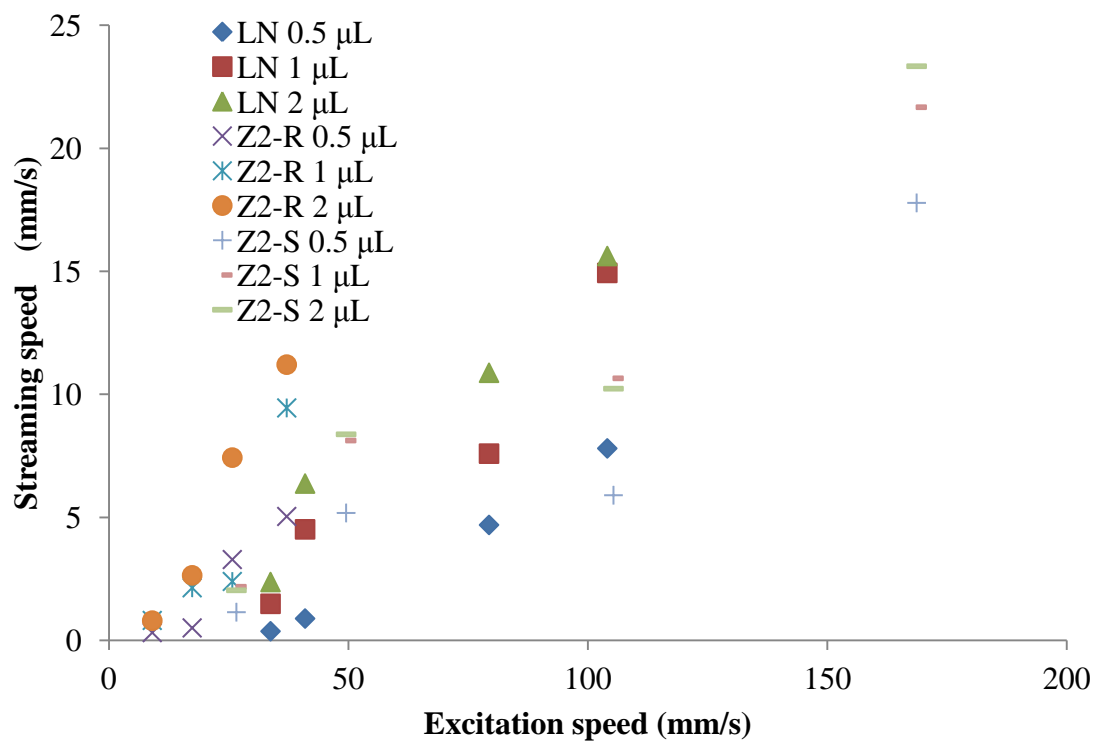
Figure 4.13. Acoustic streaming speed with respect to excitation speed of the SAW device fabricated on 11 μm ZnO/Al_2O_3 and $LiNbO_3$ substrate.
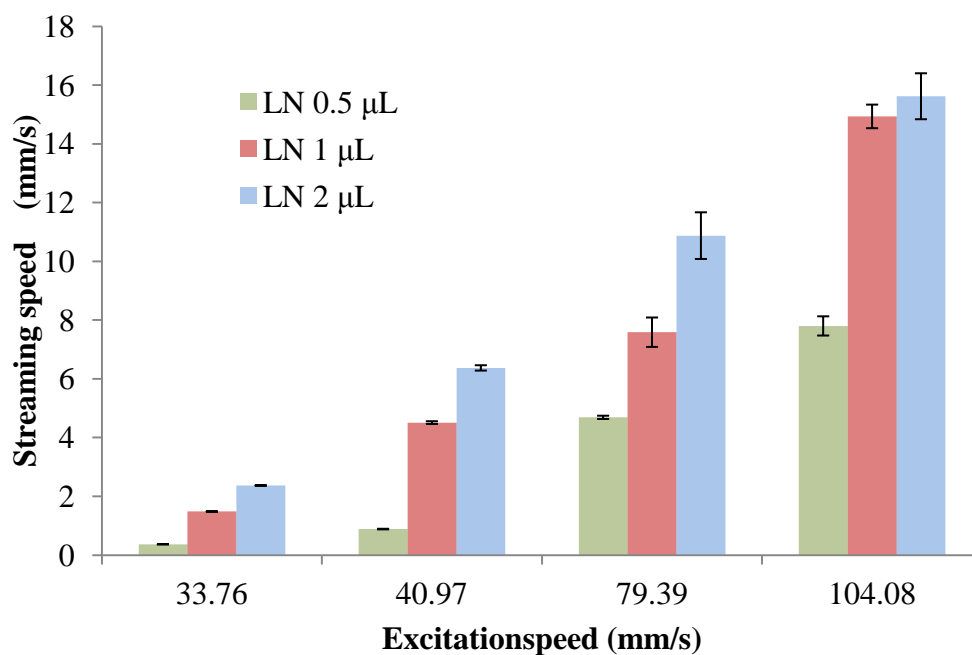
Figure 4.14. Acoustic streaming speed with respect to maximum vibration (excitation) speed of the SAW device fabricated on $LiNbO_3$ substrate. Each error bar represents the standard deviation of the data.
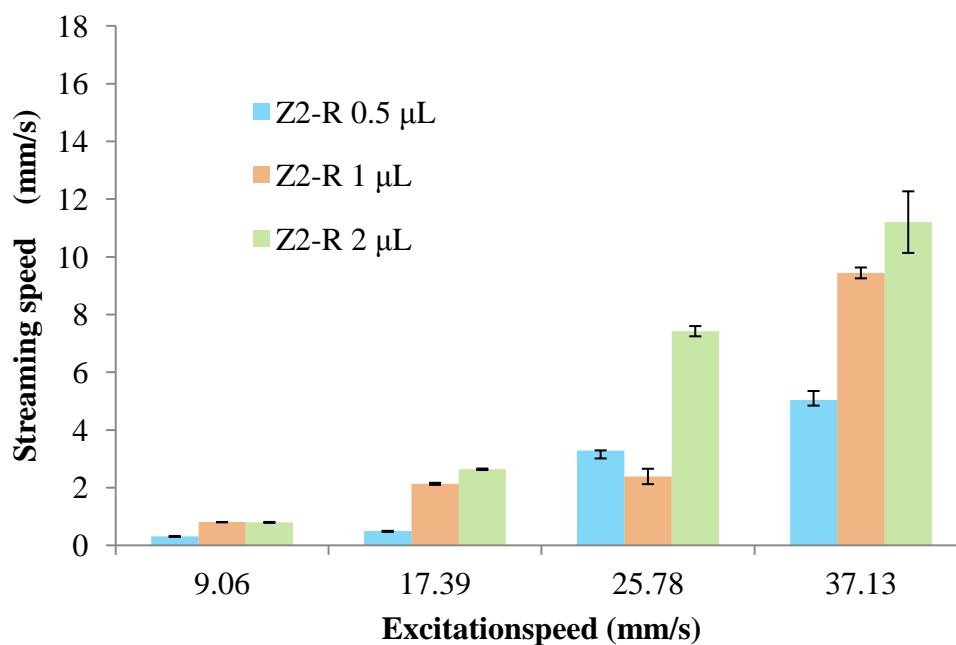
Figure 4.15. Acoustic streaming speed with respect to the maximum vibration (excitation) speed of the Rayleigh mode (Z2-R) the SAW device fabricated on 11 micron thick ZnO on Al_2O_3 substrate. Each error bar represents the standard deviation of the data.
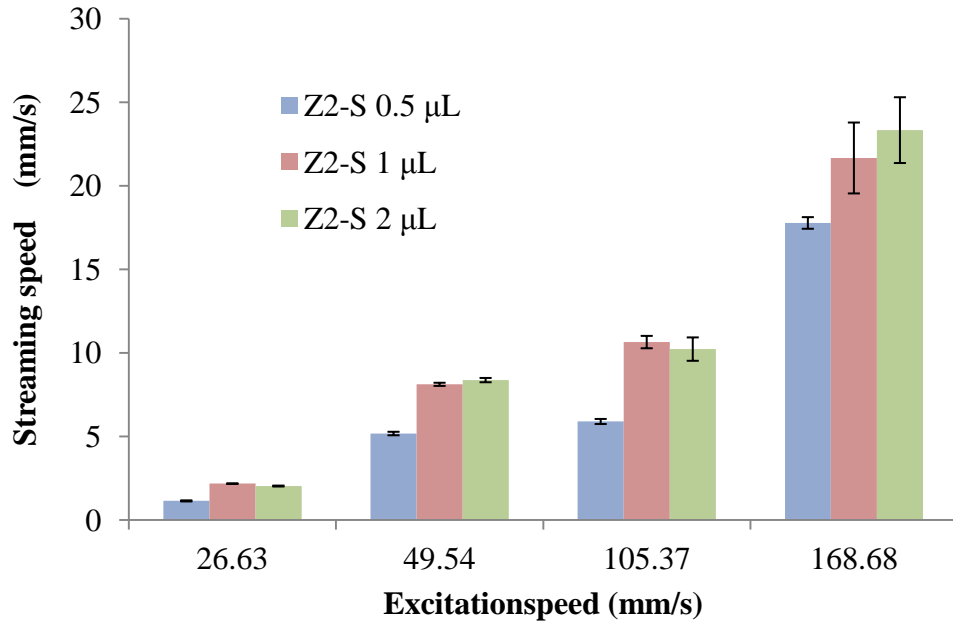
Figure 4.16. Acoustic streaming speed with respect to the maximum vibration (excitation) speed of the Sezawa mode (Z2-S) the SAW device fabricated on 11 micron thick ZnO on Al_2O_3 substrate. Each error bar represents the standard deviation of the data.
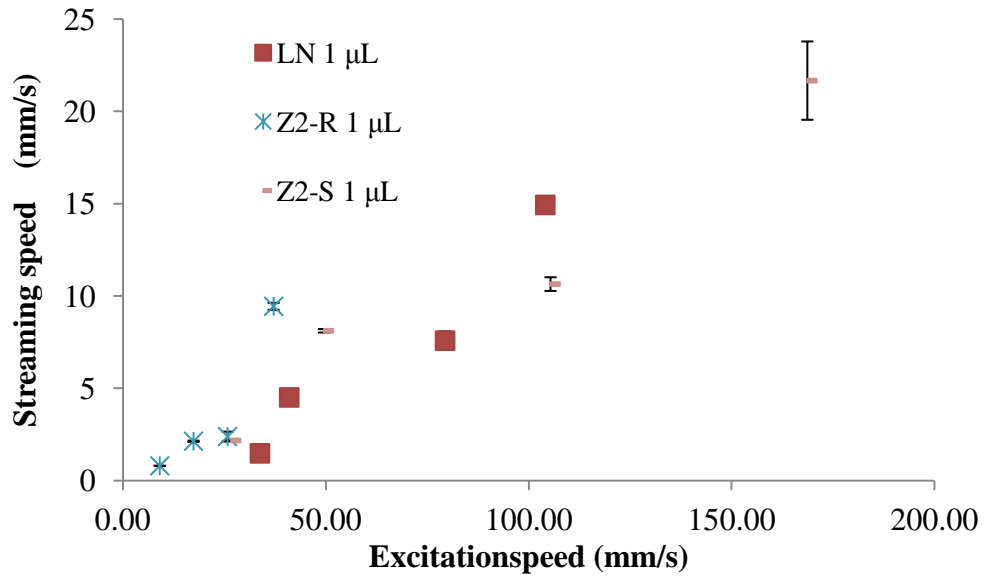
Figure 4.17. The comparison of acoustic streaming speed for 1 μL liquid volume of three of the SAW configurations; (i) Rayleigh mode of the SAW device fabricated on $LiNbO_3$ substrate, (ii) Rayleigh mode and (iii) Sezawa mode of the SAW device fabricated on 11 micron thick ZnO on Al_2O_3 substrate. Each error bar represents the standard deviation of the data.

Table 4.2 Acoustic streaming performance summary of all the SAW modes.

Power (mW)	Droplet volume (µL)	Lithium Niobate 128° Y-X cut (LN)		ZnO/Al$_2$O$_3$ - Rayleigh mode (Z2-R)		ZnO/Al$_2$O$_3$ - Sezawa mode (Z2-R)	
		SAW vibration (excitation) speed (mm/s)	Streaming speed (mm/s)	SAW vibration (excitation) speed (mm/s)	Streaming speed (mm/s)	SAW vibration (excitation) speed (mm/s)	Streaming speed (mm/s)
3.2	0.5	33.76	0.37	9.06	0.31	26.63	1.14
10		40.97	0.88	17.39	0.50	49.54	5.18
32		79.39	4.69	25.78	3.28	105.37	5.90
100		104.08	7.80	37.13	5.03	168.68	17.78
3.2	1	33.76	1.48	9.06	0.81	26.63	2.18
10		40.97	4.51	17.39	2.14	49.54	8.12
32		79.39	7.59	25.78	2.39	105.37	10.65
100		104.08	14.93	37.13	9.44	168.68	21.67
3.2	2	33.76	2.37	9.06	0.80	26.63	2.03
10		40.97	6.37	17.39	2.64	49.54	8.37
32		79.39	10.87	25.78	7.43	105.37	10.23
100		104.08	15.62	37.13	11.20	168.68	23.33

The thesis then proceeds with postulating the mechanism of the acoustics streaming observed in the experiment. As acoustic wave propagates through a fluid medium, two types of Reynolds (Re) numbers are significant in analyzing its behavior, namely: *streaming* and *acoustic* Reynolds numbers. The common Re occurs in ordinary hydrodynamics problems, which can be called the hydrodynamics Re, defines whether the present of convective acceleration is significant to affect the flow speed. However, as an acoustic wave propagates through a fluid medium, the appropriate velocity to be used in the Re is not simply the apparent velocity of the fluid (Eulerian fluid velocity or streaming velocity), instead the *Lagrangian* fluid velocity which incorporates both the Eulerian fluid velocity and the particle velocity of the fluid due to the acoustic energy propagating through it. The ubiquitous Re in fluid dynamics problems with significant acoustic fields in them is called *streaming* Reynolds number [30, 31].

$$Re = \rho_f U_0 L/\mu$$

(2)

Where:

ρ_f = density = 1000 kg/m^3 for water

μ = dynamic viscosity $\approx 10^{-2}$ N.s/m^2 for water at 25 °C

Uo = fluid streaming speed $\approx$ 2-20 mm/s

L = characteristic length scale = the droplet diameter = 0.7 to 1.5 mm $\approx$ 1 mm

Substituting the values in the equation, the Re ≈ 1 for our streaming case. As Re for our case is close to 1, we should be observing a fast streaming [30]. Furthermore, characteristic length of the SAW and the discontinuity path length were also calculated for a clearer understanding.

Attenuation coefficient is represented as [31, 32]:

$$\alpha_L = \frac{\rho_f C_f}{\rho_s C_s \lambda_s}$$

(3)

While the characteristic SAW attenuation length:

$$L_{SAW} = \frac{1}{\alpha_L}$$

(4)

Where:

α_L = attenuation coefficient

ρ_f = density of the fluid = $1000 kg/m^3$ for water

C_f = speed of sound in the fluid ≈ 1500 m/s for water

ρ_s = density of the solid material ≈ 4650 kg/m^3 for LiNiO$_3$, 5606 kg/m^3 for ZnO

C_s = speed of sound in the solid material ≈ 3992 m/s for LiNiO$_3$, 2690 m/s for ZnO

λ_s = wavelength of the SAW ≈ 32 μm

Substituting the values above, the characteristic length, L$_{SAW}$ was calculated to be approximately 0.40 mm for the LiNbO$_3$ substrate, and approximately 0.32 mm for the ZnO substrate. The length scale of the fluid/liquid; i.e. the diameters of the droplets used were between 0.7 and 1.5 mm width, *double* than that of the *L$_{SAW}$*. The droplets were consequently subjected to significant SAW radiation.

The path length required for the formation of discontinuity is represented as [31]

$$X_p = \frac{1}{\left(\dfrac{\varepsilon}{C_f^2}\omega u_i\right)} = \frac{\lambda}{2\pi\varepsilon M} = \left(\frac{1}{2\pi\varepsilon M}\right)\lambda$$

(5)

and:

$$\varepsilon = \frac{B}{2A} + 1$$

(6)

Where:

X_p = path lenght required for formation of discontinuity

$\frac{B}{A}$ = non linearity parameter in acoustics ≈ 5.2 for water

$\omega = 2\pi f$ = angular velocity of the SAW

C_f = speed of sound in the fluid ≈ 1500 m/s in water

u_i = excitation speed = transverse speed of the SAW $\approx$30-200 mm/s

$M =$ Mach Number $= \dfrac{u_i}{C_f} = 2 \times 10^{-5} - 1.33 \times 10^{-4}$

Using the values stated above the path length required for the formation of discontinuity is: $X_p \approx 0.01 - 0.07\ m\ \approx 10 - 70$ mm; $330 - 2210$ times the wavelength (λ)

Substituting the values above, the path lengths required for the SAW to show discontinuity were calculated to be *one order of magnitude higher* than the droplet diameter; hence the acoustic streaming exciting the droplets would still be continuous SAWs.

Analyzing all the results, we could deduce that the vibration speed is the main actuating mechanism to induce fluid streaming. For the same input power, depending of the material used and which mode the SAW in generated upon, the maximum vibration speed would vary. The mode with the highest vertical speed to power ratio, i.e. Z2-S shall induce the strongest streaming, followed by LN and Z2-R. This deduction is also validated by the network analyzer and LDV results, demonstrating that the vibration speed depend on the efficiency of the device in converting electrical to mechanical energy.
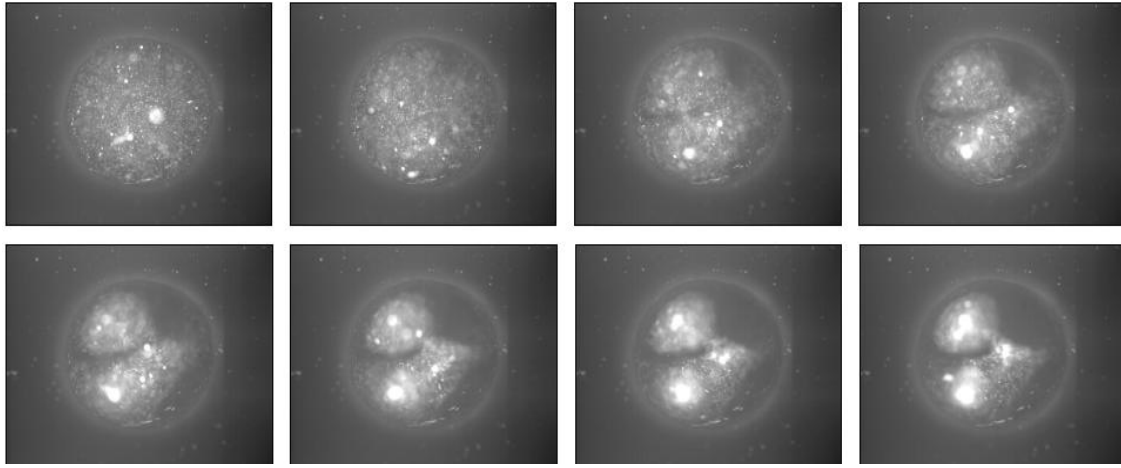
Figure 4.18. Successive images of the SAW streaming inside a 1 µL water droplet seeded with 4.8 µm fluorescent particles. The IDT is located to the right of the droplet. The particles are concentrated in the center of the two vortices.

Particles concentration was also observed that during the acoustic streaming. Micro particles were interestingly concentrated in the vortices within 500 milliseconds of device activation. Furthermore, the particles predominantly concentrated in the center of the two vortices. The reason for this phenomenon can be explained by the two competing forces subjected to the particles during the acoustic streaming.

A suspended solid particle during acoustic streaming is subjected to forces which are due to direct irradiation from the acoustic field and indirect irradiation from scattering of the acoustic field from other objects. If the indirect irradiation is negligible; in addition to neglecting the compressibility and viscous effect; a simple form of the acoustic radiation force can be derived, firstly by King [33]; which is valid for a particle much smaller

compare to the radiation wavelength. The acoustic radiation force, F_{ar}, can then be represented as [30]:

$$F_{ar} = 2\pi\rho_f A^2 \left(\frac{kD}{2}\right)^6 \left[\frac{1 + \frac{2}{9}\left(1 - \frac{\rho_f}{\rho_p}\right)^2}{\left(2 + \frac{\rho_f}{\rho_0}\right)^2}\right]$$

(7)

Where:

F_{ar} = acoustic radiation force.

D = diameter of the particle

ρ_f = density of the fluid = 1000 kg/m^3 for water

ρ_0 = density of the particle $\approx$ 1050 kg/m^3 for polystyrene.

A = amplitude of the SAW

k = wave number = $2\pi/\lambda$

Moreover, the suspended solid particle would also be subjected to a steady Stokes drag force. For microfluidics application, in which the Reynolds number is typically of order one or less, the appropriate drag force, F_D, can be represented as [30]:

$$F_D = 3\pi\mu U_0 D$$

(8)

Where:

F_D = drag force.

μ = dynamic viscosity $\approx 10^{-2}$ N.s/m^2 for water at 25 °C

U_o = fluid streaming speed $\approx$ 2-20 mm/s

L = characteristic length scale = the droplet diameter = 0.7 to 1.5 mm $\approx$ 1 mm

These two dominant forces compete with each other during acoustic streaming [30]; with the acoustic streaming force, F_{ar}, induces the particle to the center of the vortices and the Stokes drag force, F_D, induces the particle to the periphery of the vortices [34]. Shear induced migration effect in this case would be negligible as it only significantly affects solution with high concentration (> 25%); while the particle concentration used for this experiment was less than 1 %.

Analysis of equations (7) and (8) shows that the Stokes drag force increases modestly with D, while the acoustic streaming force increases rapidly with the D^6 and f^6. The drag force is therefore the dominant force on smaller particles, in which the acoustic streaming force is negligible.

Figure 4.19 shows the comparative force analysis for our configuration, in which the amplitude of the SAW was approximately 250 pm; the vibration speed was approximately 0.2 m/s. The result indicated that the acoustic streaming force, which draws the particle to the periphery of the droplet only become significant at particle diameter of more the 300 nm. In conclusion, the 4.8 μm particles would concentrate on

the center of the vortices, because of the dominance of the drag force, which is a few

orders of magnitude larger than the acoustic streaming force.
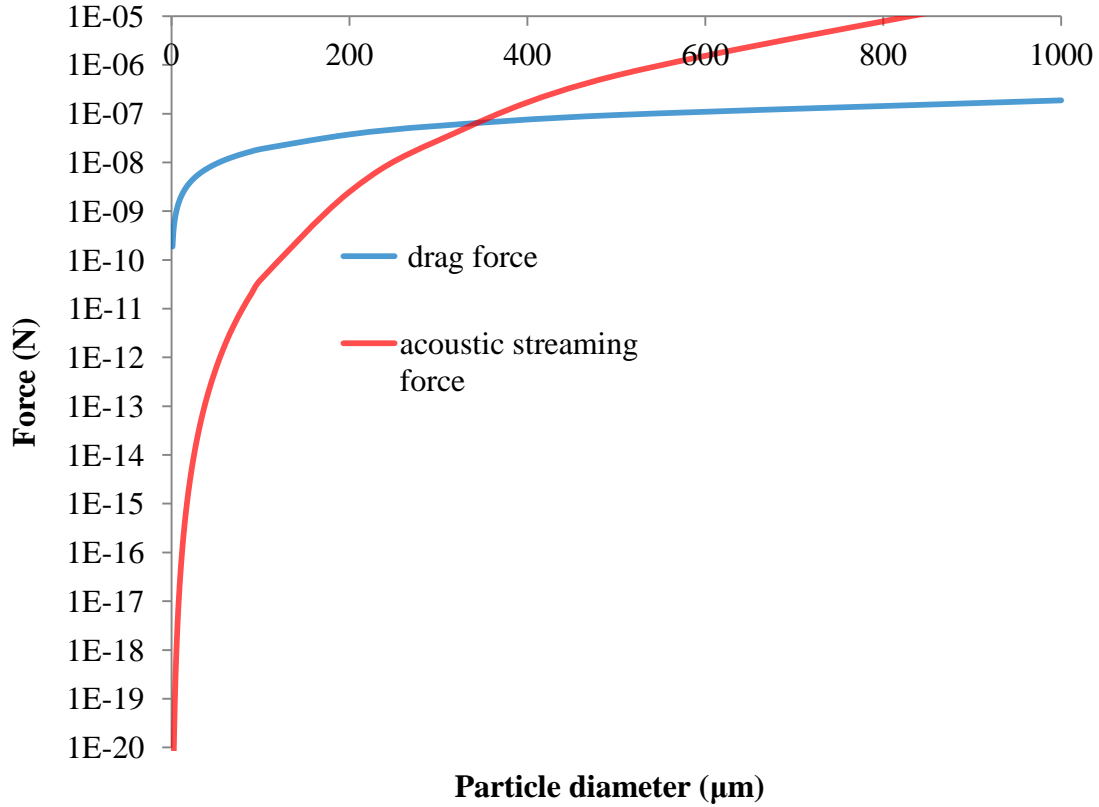
Figure 4.19. Comparative analysis of the acoustic radiation force F_{AR} and the drag force F_D acting on the particle as a function of particle size. The acoustic radiation force, which pulls the particles to the periphery of the droplet only become significant for particles with diameter of more than 300 μm

4.3.3 Summary

In summary, the results reported on this subchapter further validated the characterization

results. The Rayleigh SAW mode of the ZnO/Al_2O_3 hybrid material induced weaker

acoustic streaming compare to that of $LiNbO_3$ substrate, demonstrated by the maximum

streaming speed values achieved. The Sezawa mode of the ZnO/Al_2O_3 hybrid material on the other hand induced the strongest streaming compare to the others. These results followed their respective electromechanical coupling values closely.

It can be deduced that for microfluidics purpose, i.e. acoustic streaming, large *excitation speed* is essential. Utilization of Sezawa mode in thick ZnO film gives superior performance due to its efficiency in converting electrical to mechanical energy, hence the high excitation (SAW vibration) speed.

In addition, particle concentration was observed during the acoustic streaming experiment. The 4.8 μm polystyrene particles were observed to concentrate in the center of the vortices during operation. This is due to the dominance of the drag force over the acoustic streaming force on small particles (<< 300 μm) inside a sessile drop.

4.4 Application of SAW devices based on ZnO/Al_2O_3 stratified layers for PLGA nanoparticles precipitation

Targeted pharmacologically active agents (e.g. drugs and proteins) deliveries to specific areas are highly desirable; as they increase the effectiveness of the therapy and minimize the detrimental side effects. For this reason, biocompatible/biodegradable polymeric nanoparticles (NPs) have been exploited as carriers for such agents. Their inherent ability

in increasing the stability and control release (CR) of the drugs/proteins to be delivered is highly advantageous. The drugs/protein is encapsulated or attached to the polymeric matrix and only released to specific targets and times. Poly(**D,L**-lactic acid-*co*-glycolic acid) (PLGA) is one example of such polymers which has been highly explored. They experience hydrolysis, producing the original monomer, lactic and glycolic acid, making them effectively biocompatible/biodegradable. Furthermore, they can be administered easily and posses extended controlled release (up to days or weeks) [35-37].

Polymeric NPs are normally classified to be between 10 and 1000 nm in sizes. NPs with smaller sizes are favored, as they are more effective; they have been shown to remain longer in bloodstream, essential for temporal controlled release. Hence, work on developing PLGA NPs with size less than or equal to 100 nm has been gaining interest. The NPs normally prepared in a process called nanoprecipitation. In this method, the polymer is dissolved in an organic solvent (e.g. acetone) and put into mixture with water; the spontaneous diffusion of the water-soluble solvent creates an interfacial turbulence leading to the precipitation of the NPs. This method is also known as the solvent-displacement method [36, 38, 39].

It has also been reported that rapid mixing is essential in NPs nanoprecipitation [40, 41]. Valencia et al [41] have demonstrated that slow mixing, in which the PLGA-acetone solution was brought into mixture with lipid-PEG (poly(ethylene glycol)-water without any external heating or sonication, resulted in an non-homogeneous size distribution.

Multiple peaks ranging between 400 nm and 10 μm were observed in the normal size distribution. In contrast; rapid mixing, in which the PLGA-acetone solution was brought into mixture with lipid-PEG (poly(ethylene glycol)-water in a meander-type microfluidics channel (which acts as a passive mixer), resulted in smaller particles sizes and a more homogeneous size distribution (30-60 nm) [41].

Following the results, an active mixer would prove to be advantageous in inducing an even more rapid mixing for the NPs precipitation. For this reason, the utilization of the SAW devices developed as the candidate for the process was explored. Rapid mixing was induced by propagating SAW. The work encompassed the utilization of both the Rayleigh and Sezawa waves. The resultant NPs were subsequently compared with the control samples, produced by a more conventional rapid mixing method (repeat-pumping using a pipette).

4.4.1 Method

Materials utilized in this project:

- 0.05% poly(**D,L**-lactic acid-*co*-glycolic acid) (PLGA) diluted in acetone)

- 0.2 mg/mL Fluorescein in ETOH

- De-Ionized (DI) water

- Phosphate buffered saline (PBS)
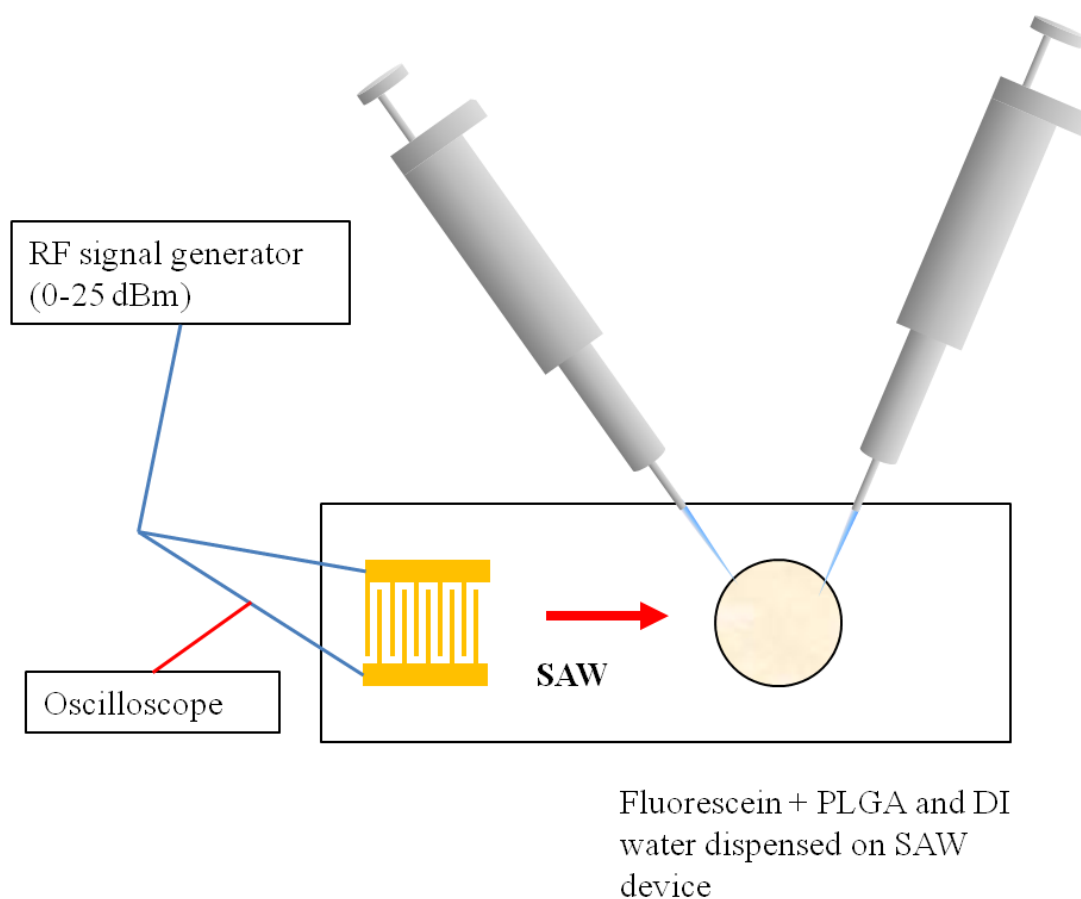
Figure 4.20. The schematic of the experiment. Two droplets (10 µL volume each) of DI water and a mixture of fluorescein + PLGA were dispensed onto the surface of the ZnO/Al_2O_3 material, along the SAW propagation path. Acoustics streaming was induced with the activation of the IDT (in both the Rayleigh and Sezawa modes), which caused rapid mixing and PLGA nanoparticles precipitation.

Precipitation steps:

1. The fluorescein was mixed with PLGA, 1:1 mixture.

2. 10 µL DI water was dispensed onto the SAW device using pipette (Eppendorf AG).

3. 10 µL PLGA/Fluorescein mix was dispensed onto the DI water droplet using pipettes (Eppendorf AG).

4. A Signal Generator (Agilent N9310A, Agilent Technologies, USA) provide the power to the SAW device.

5. The signal generator was set to operate in the Rayleigh wave resonance frequency of the SAW device, which is 96.1 MHz, and 20 dBm of power.

6. The RF power was activated for 10 second.

7. Use the pipette to collect the liquid mixture from the device and store it into a test tube.

8. Steps 6 and 7 were repeated until solution of 100 µL (0.1 mL) could be collected.

9. Steps 5-7 were repeated for different exposure times; 20, 30, 40, and 60 seconds.

10. The signal generator was subsequently set to operate in the Sezawa wave resonance frequencies of the SAW device, which is 127.85 MHz, and 20 dBm of power.

11. Steps 6-7 were repeated for these settings.

12. For the control sample, 50 µL of PLGA/fluorescein mix and 50 µL of DI water were put into a test tube and were mixed using a pipette.

After the nanoparticles precipitation steps were completed, the samples were prepared for size measurement. Size measurement steps:

1. The sample was mixed with 3 mL of dispersant (DI water and PBS) using a pipette in a disposable cuvette (SARSTEDT AG & Co).

2. The nanoparticles samples were subsequently measured using Zetasizer Nano ZS (Malvern Instruments Ltd). The measurements were performed in triplicates and

were repeated at least three times for each sample. The values plotted in the result section were the average of all the experimental values.

The results were then further confirmed by atomic force microscopy.

1. The sample was diluted with DI water, 1:5, and then was left to air-dry for 20 minute.

2. Tapping mode was use during operation of a Biological AFM (NanoWizard® BioScience AFM, JPK Instruments AG).

4.4.2 Result and Discussion

The experimental results can be viewed in Figure 4.21, Figure 4.22 and Figure 4.23, in which the size distributions of the nanoparticles precipitated using SAW in water dispersant were presented. The nanoparticles produced utilizing the Rayleigh wave (R) and the Sezawa wave (S) for various exposure times (10 and 60 seconds) were presented as broken lines and dotted lines, respectively. Control samples result, mixed using a pipette was plotted as comparison, presented as solid lines.
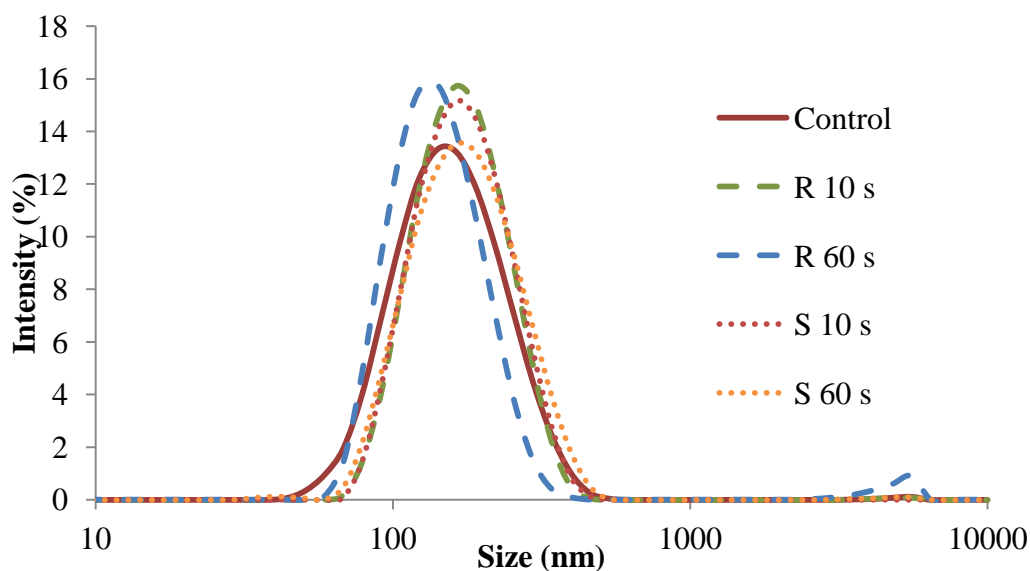
Figure 4.21. Size distribution of the nanoparticles precipitated using SAW in water dispersant; both for Rayleigh (R) (broken lines) and Sezawa (S) mode (dotted lines) for various exposure times. Control samples result, mixed using a pipette was plotted as comparison.
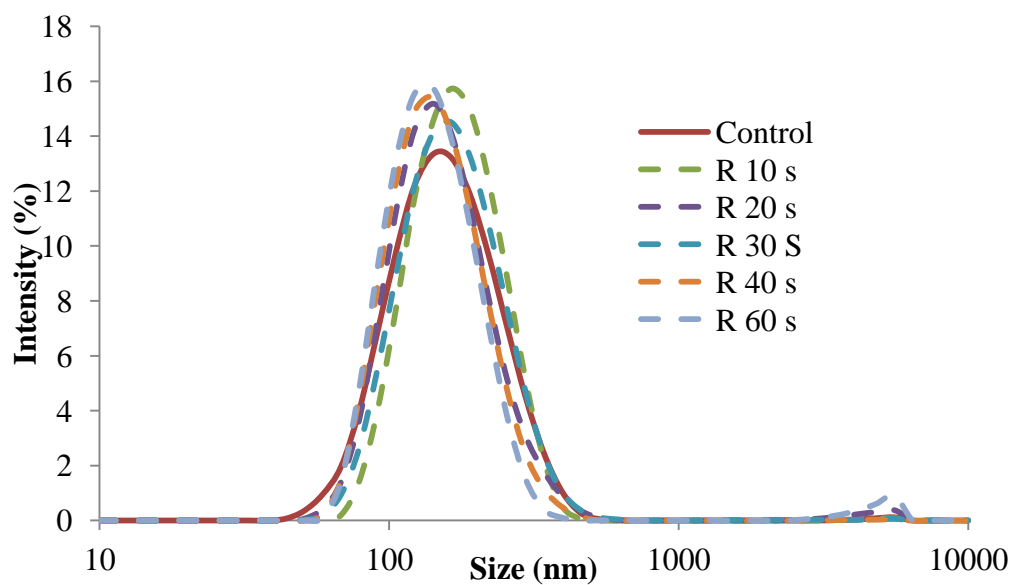
Figure 4.22. Size distribution of the nanoparticles precipitated using Rayleigh (R) mode SAW (broken lines) in water dispersant for various exposure times. Control samples result, mixed using a pipette was plotted as comparison.
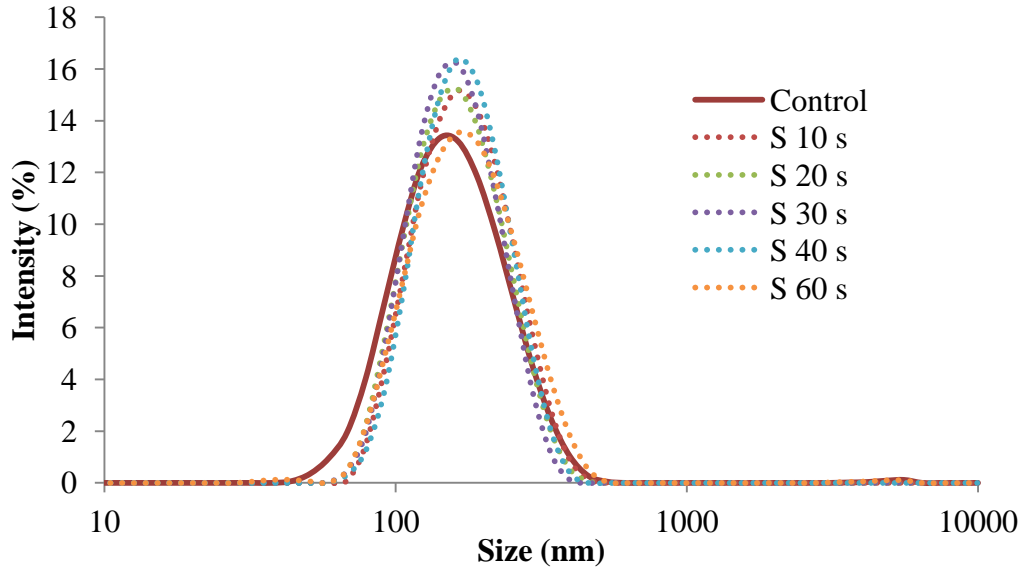
Figure 4.23. Size distribution of the nanoparticles precipitated using Sezawa (S) mode SAW (dotted lines) in water dispersant for various exposure times. Control samples result, mixed using a pipette was plotted as comparison.

For an easier observation, more detailed graphs for Rayleigh mode and Sezawa mode are presented separately as Figure 4.22 and Figure 4.23. Observation of the three figures showed the most important finding with respect to the aim of this project, that the nanoparticles size distributions are comparable with mixing using a pipette in water dispersant. The rapid mixing using SAW can then be use as an alternate method for nanoparticles precipitation.

Figure 4.22 showed the result of the rapid mixing done with the Rayleigh input frequency (96.1 MHz) and input power (20 dBm) with varying the exposure time; the control sample result was also plotted as comparison. The rapid mixing and encapsulation

using the SAW devices resulted in narrower distribution curves width and higher peak concentration intensity compare to the control sample, which is highly desirable for secondary benefits of producing smaller size nanoparticles, yet they were not to an order of significance. Further observation of the results would show that the effect of SAW exposure time (from 10 to 60 seconds) to the size distribution is minimal.

Similar result was observed for the rapid mixing done with the Sezawa input frequency (127.85 MHz) and input power (20 dBm) as shown in Figure 4.23. The exposure time however showed a moderate effect. Longer exposure time from 10 to 40 seconds resulted in narrower distribution width and peak intensity increase; interestingly SAW exposure time of 60 seconds showed reverse effect, and the size distribution curve was again almost the same as the curve of the control sample.

The acoustics streaming speed moreover also does not significantly affect the nanoparticles size distribution. Nano precipitation exploiting SAW generated at the Rayleigh and Sezawa modes showed similar result, although the streaming speed of the former is larger. To further analyze the results, the results of Rayleigh mode and Sezawa mode for 30 seconds are presented as Figure 4.24. It can be observed that both the Rayleigh and Sezawa mode size distribution curves showed narrower width and higher peak than the control sample, with the Sezawa mode showed more apparent effect. These effects however were again not order of magnitude significant.
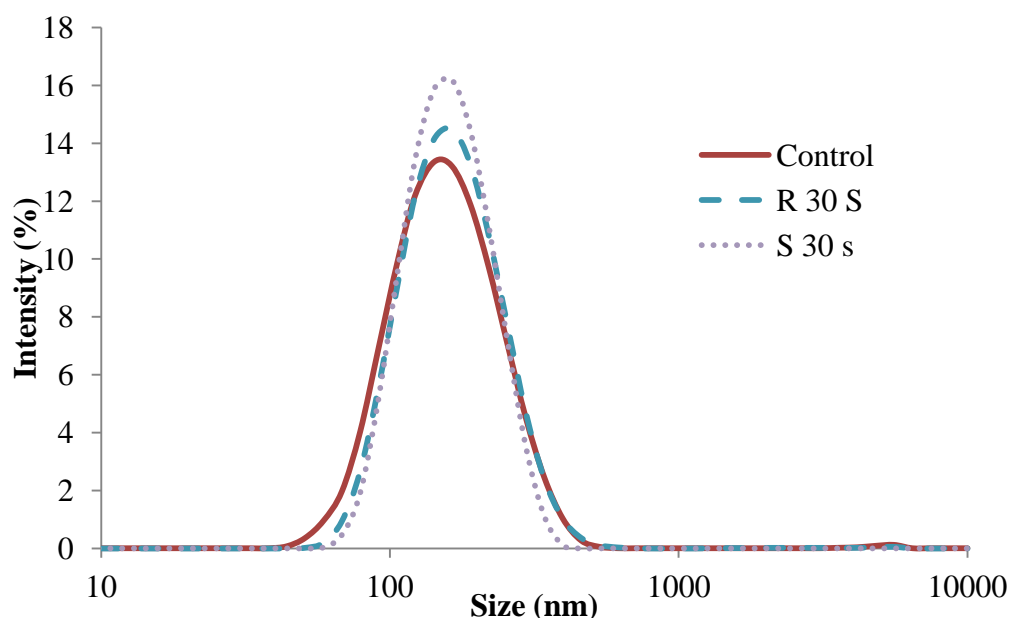
Figure 4.24. Size distribution of the nanoparticles precipitated using SAW in water dispersant. Both for Rayleigh (R) and Sezawa (S) mode for 30 seconds exposure time. Control samples result, mixed using a pipette was plotted as comparison.

The experiment was continued by measuring these particles sizes in PBS. These experiments were done to mimic realistic condition for biological purposes. PBS acts as better replica of biological fluids [42]. The samples were precipitated on 30 second exposure times were chosen for both Rayleigh mode (R) and Sezawa mode (S). Figure 4.25 shows the result, which again demonstrated that the nanoparticles sizes were comparable to the control sample.
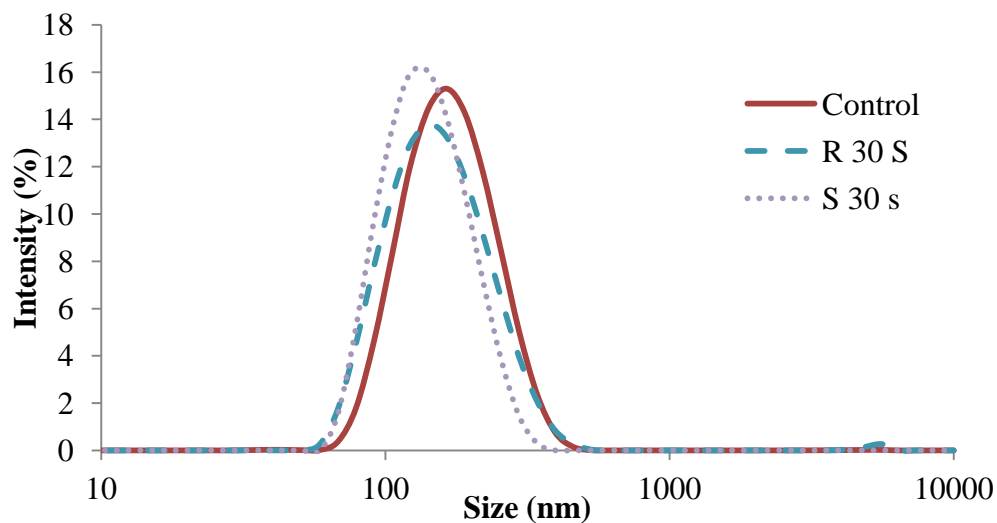
Figure 4.25. Size distribution of the nanoparticles precipitated using SAW in PBS dispersant. Both for Rayleigh mode and Sezawa mode for 30 seconds exposure time. Control samples result, mixed using a pipette was plotted as comparison.

The next step was to confirm the result by visualizing the nanoparticles using an Atomic

Force Microscope (AFM).

(a)

(b)
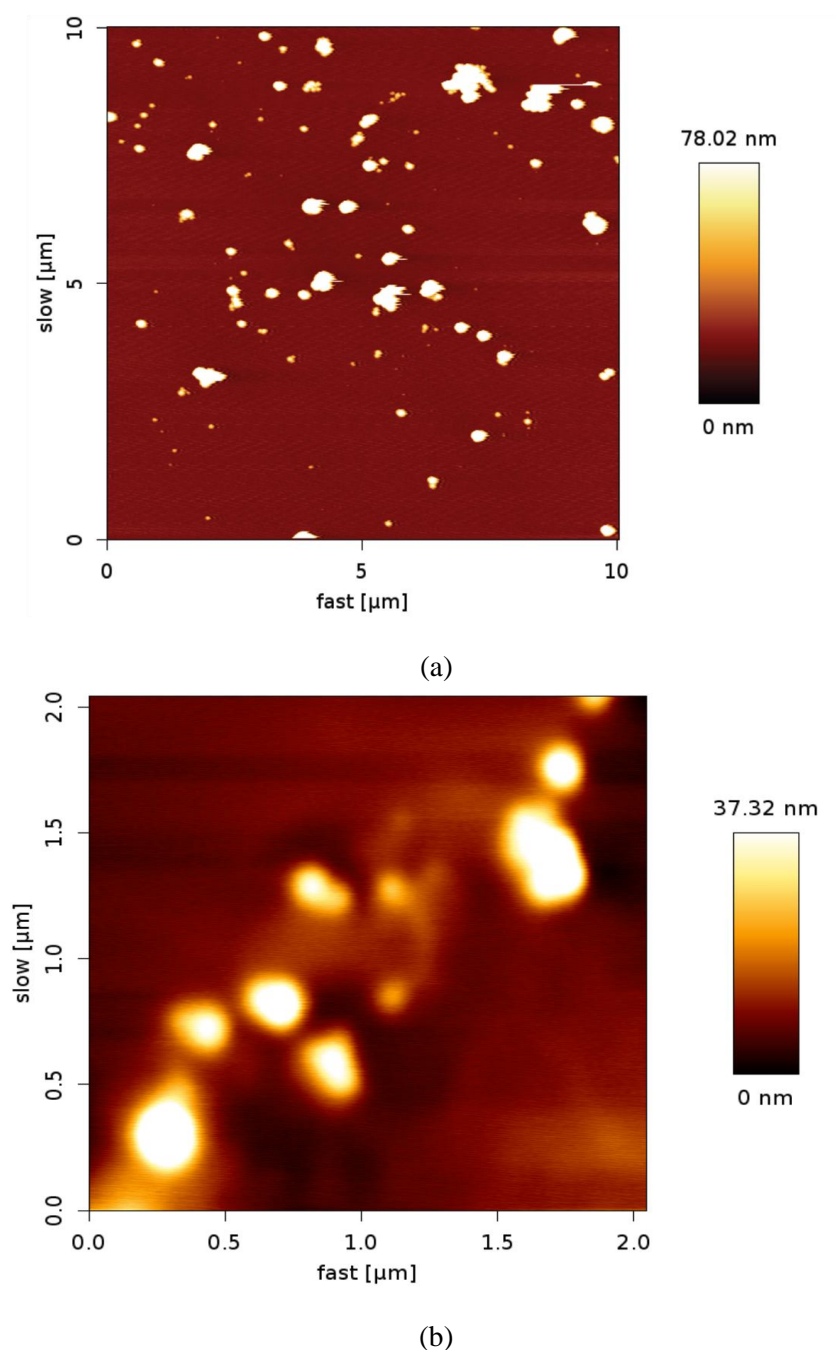
Figure 4.26. Atomic force microscopy (AFM) measurement result of the PLGA nanoparticles precipitated using a conventional manual mixing method; (a) shows aggregated nanoparticles on a 2 μm x 2 μm measurement area; and (b) a higher magnification image showing the nanoparticles with sizes approximately 100 nm.
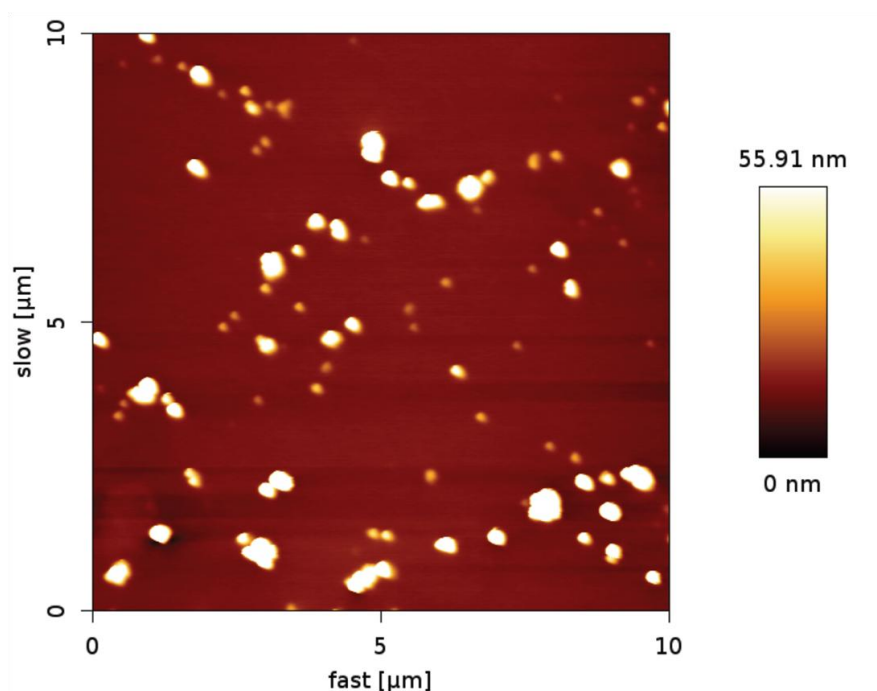
(a)
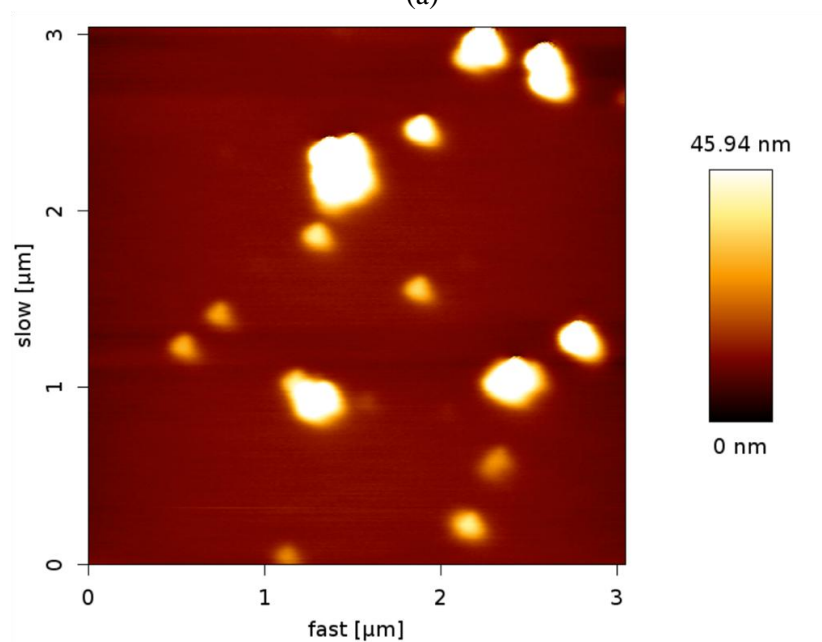
(b)

Figure 4.27. Atomic force microscopy (AFM) measurement result of the PLGA nanoparticles precipitated using a SAW rapid mixing method; the sample was subjected to SAW in Sezawa mode with 20 dBm input RF power and 30 seconds of exposure time. (a) The aggregated nanoparticles on a 2 μm x 2 μm measurement area and (b) a higher magnification image showing the nanoparticles with sizes approximately 100 nm.

4.4.3 Summary

In summary, nanoparticles precipitation using surface acoustic wave is reported. The benefit of using SAW would include smaller samples volume and the potential for an automated process. SAW devices based on ZnO/Al_2O_3 stratified layer has been explored as an alternative to produce PLGA nanoparticles. The nanoparticles size distributions are comparable with the ones produced using a more conventional manual mixing. The sizes are within the same order of magnitude with the nanoparticles produced using the reported micromixing method [39, 41]. In addition, it was found out that the acoustics streaming speed has non-significant effect on the size distribution, as shown for rapid mixing using SAW on Rayleigh and Sezawa modes. It was moreover found out that the SAW exposure time from 10 seconds up to 1 minute has also negligible effect on the nanoparticles size distributions. Atomic force microscopy was performed on the samples to further prove the size order of magnitudes of these nanoparticles. The SAW mixing hence has been demonstrated to be a good candidate for this process.

4.5 Chapter summary and conclusion

In this thesis, a hybrid approach in developing a SAW device for microfluidics purposes has been explored. ZnO film was selected as the piezoelectric material due to its good

electromechanical coupling; while sapphire (Al_2O_3) was chosen as the substrate due to its superior acoustic velocities and propagation loss.

The ZnO film was deposited using a sputtering process; two ZnO thickness configurations were explored, 1 μm and 11 μm. The purpose was to compare the performance of the devices based on different film thickness. Furthermore, the thick film was required to induce the higher order mode of SAW called the Sezawa wave, which should give superior performance. C-axis oriented ZnO films are essential for good piezoelectric properties and the orientation for both thick and thin film, consequently were verified by XRD and SEM characterization processes.

After the material characterization had been performed, the work continued with the SAW devices fabrication. The IDTs were made out 300 nm of gold (Au) with 10 nm of Chromium (Cr) as the adhesive layer. As ZnO film is very reactive to acid, wet etch process was unfeasible, hence, the IDTs were fabricated using a lift-off process. Three types of piezoelectric materials were utilized, namely 1 μm ZnO, 11 μm ZnO and on a bulk Lithium Niobate (Li_2NbO_3) wafer for comparison. The IDTs were designed to have 8 μm finger widths, resulted in 32 μm wavelength.

Subsequent step was the SAW device characterization. The SAW device was characterized using a network analyzer to measure its efficiency which then further

validated by a Laser Doppler Vibrometer (LDV). Furthermore, the LDV result showed the comparison of the vibration speed of all the configurations.

The characterization step using the network analyzer showed that Rayleigh waves generated on ZnO/Al_2O_3 material gives better performances as the thickness is increased. Yet, they still give poorer performances in comparison to those generated on a $LiNbO_3$ substrate. The Sezawa wave on the 11 μm thick ZnO film (h/λ value of ~ 0.3), on the other hand, gives the highest performance. Its electromechanical coupling coefficient is the highest. The results were further validated by its high vibration speed to input power ratio measured using the LDV.

The SAW devices were then utilized to induce streaming in a sessile drop of water seeded with polystyrene microparticles. The induced streaming speeds were analyzed using images captured by a high speed camera. The Sezawa mode of the ZnO/Al_2O_3 hybrid material induced the strongest streaming followed by the Rayleigh mode of the $LiNbO_3$ and ZnO/Al_2O_3 hybrid material, consecutively. This acoustic streaming results further verified the LDV measurement results. In addition, the 4.8 μm polystyrene particles were observed to concentrate in the center of the vortices during operation. This is due to the dominance of the drag force over the acoustic streaming force.

The *key finding* and *contribution* of the work is that *surface displacement (amplitude) or the vibration speed* was found to be the *most influential parameter* for acoustic

streaming. The ZnO thickness and the SAW mode resulted in different efficiency in their electromechanical coupling. Streaming induced by the Sezawa mode gives the highest speed because it has the highest electromechanical coupling (validated by the network analyzer data) and hence the highest vibration speed for a given input power (validated by the LDV data).

The work was continued with utilization of the devices for producing PLGA nanoparticles. The SAW device was shown to be a good alternative to a more conventional rapid mixing technique as it doesn't affect the size distribution of the produced nanoparticles. The success of using the SAW device as a rapid mixer for nanoparticles precipitation can be further extended to a hybrid pump-mixer device to further reduce the nanoparticles sizes.

References

1. Du, X.Y., et al., *Microfluidic pumps employing surface acoustic waves generated in ZnO thin films.* Journal of Applied Physics, 2009. **105**(2): p. 024508-7.
2. Du, X.Y., et al., *ZnO film thickness effect on surface acoustic wave modes and acoustic streaming.* Applied Physics Letters, 2008. **93**(9): p. 094105-3.
3. Fu, Y.Q., et al., *Recent developments on ZnO films for acoustic wave based bio-sensing and microfluidic applications: a review.* Sensors and Actuators B: Chemical, 2009. **143**(2): p. 606-619.
4. Winey, J.M., Y.M. Gupta, and D.E. Hare, *r-axis sound speed and elastic properties of sapphire single crystals.* Journal of Applied Physics, 2001. **90**: p. 3109.
5. Emanetoglu, N.W., et al., *Epitaxial ZnO piezoelectric thin films for SAW filters.* Materials Science in Semiconductor Processing, 1999. **2**(3): p. 247-252.
6. Du, X.Y., et al., *ZnO film for application in surface acoustic wave device.* Journal of Physics: Conference Series, 2007. **76**: p. 012035.
7. Dang, W.L., et al., *Deposition and characterization of sputtered ZnO films.* Superlattices and Microstructures, 2007. **42**(1-6): p. 89-93.
8. Schuler, L.P., et al., *Comparison of DC and RF sputtered zinc oxide films with post-annealing and dry etching and effect on crystal composition.* JAPANESE JOURNAL OF APPLIED PHYSICS PART 1 REGULAR PAPERS SHORT NOTES AND REVIEW PAPERS, 2005. **44**(10): p. 7555.
9. Emanetoglu, N.W., et al. *MOCVD growth and SAW properties of epitaxial ZnO thin films*. 1998. IEEE.
10. Hickernell, F.S., *ZINC OXIDE FILMS FOR ACOUSTOELECTRIC DEVICE APPLICATIONS.* IEEE transactions on sonics and ultrasonics, 1985. **SU-32**(5): p. 621-629.
11. Hickernell, F.S. *Measurement techniques for evaluating piezoelectric thin films*. 1996. IEEE.
12. Emanetoglu, N.W., et al. *Epitaxial growth and characterization of high quality ZnO films for surface acoustic wave applications*. 1997. IEEE.
13. Emanetoglu, N.W., et al., *Analysis of SAW properties of epitaxial ZnO films grown on R-Al$_2$O$_3$ substrates.* Ultrasonics, Ferroelectrics and Frequency Control, IEEE Transactions on, 2001. **48**(5): p. 1389-1394.
14. Emanetoglu, N.W., et al., *Surface acoustic wave ultraviolet photodetectors using epitaxial ZnO multilayers grown on r-plane sapphire.* Applied physics letters, 2004. **85**(17): p. 3702-3704.
15. Le Brizoual, L., et al., *High frequency SAW devices based on third harmonic generation.* Ultrasonics, 2006. **45**(1-4): p. 100-103.

16. Weber, A.H., G. Weiss, and S. Hunklinger. *Comparison of Rayleigh and Sezawa wave modes in ZnO-SiO2-Si structures*. in *Ultrasonics Symposium, 1991. Proceedings., IEEE 1991*. 1991.

17. Khuri Yakub, B.T., J.G. Smits, and T. Barbee, *Reactive magnetron sputtering of ZnO.* Journal of Applied Physics, 1981. **52**(7): p. 4772-4774.

18. Pearton, S.J., et al., *Recent progress in processing and properties of ZnO.* Superlattices and Microstructures, 2003. **34**(1-2): p. 3-32.

19. Sun, J., et al., *Realization of controllable etching for ZnO film by NH4Cl aqueous solution and its influence on optical and electrical properties.* Applied surface science, 2007. **253**(11): p. 5161-5165.

20. Kwon, J.W. and E.S. Kim, *Fine ZnO patterning with controlled sidewall-etch front slope.* Microelectromechanical Systems, Journal of, 2005. **14**(3): p. 603-609.

21. Jagadish, C. and S.J. Pearton, *Zinc Oxide Bulk, Thin Films and Nanostructures*2006: Elsevier Science Ltd.

22. Oliver, J. and M. Ewing, *Higher modes of continental Rayleigh waves.* Bulletin of the Seismological Society of America, 1957. **47**(3): p. 187.

23. Kanai, K., *On Sezawa-waves (M2-waves).: Part II.* 1955.

24. Sezawa, K. and K. Kanai, *The M2 seismic waves.* 1935.

25. Smith, W.R., et al., *Analysis of interdigital surface wave transducers by use of an equivalent circuit model.* Microwave Theory and Techniques, IEEE Transactions on, 1969. **17**(11): p. 856-864.

26. Wu, T.T. and W.S. Wang, *An experimental study on the ZnO/sapphire layered surface acoustic wave device.* Journal of applied physics, 2004. **96**: p. 5249.

27. Kalantar-Zadeh, K., et al. *Study of novel Love mode surface acoustic wave filters*. 2002. IEEE.

28. Franke, K., et al., *The highly sensitive optical measurement of absolute SAW amplitudes for power flow analysis.* Ultrasonics, Ferroelectrics and Frequency Control, IEEE Transactions on, 2003. **50**(1): p. 77-80.

29. Frampton, K.D., S.E. Martin, and K. Minor, *The scaling of acoustic streaming for application in micro-fluidic devices.* Applied Acoustics, 2003. **64**(7): p. 681-692.

30. Friend, J. and L.Y. Yeo, *Microscale acoustofluidics: Microfluidics driven via acoustics and ultrasonics.* Reviews of Modern Physics, 2011. **83**(2): p. 647.

31. Rudenko, O.V. and S.I. Soluyan, *Theoretical foundations of nonlinear acoustics*1977: Consultants Bureau.

32. Cheeke, J.D.N., *Fundamentals and applications of ultrasonic waves*2002: CRC.

33. King, L.V., *On the acoustic radiation pressure on spheres.* Proceedings of the Royal Society of London. Series A-Mathematical and Physical Sciences, 1934. **147**(861): p. 212.

34. Rogers, P.R., J.R. Friend, and L.Y. Yeo, *Exploitation of surface acoustic waves to drive size-dependent microparticle concentration within a droplet.* Lab Chip, 2010. **10**(21): p. 2979-2985.

35. Buxton, D.B., *Nanomedicine for the management of lung and blood diseases.* Nanomedicine, 2009. **4**(3): p. 331-339.

36.   Mundargi, R.C., et al., *Nano/micro technologies for delivering macromolecular therapeutics using poly (D, L-lactide-co-glycolide) and its derivatives.* Journal of Controlled Release, 2008. **125**(3): p. 193-209.

37.   Soppimath, K.S., et al., *Biodegradable polymeric nanoparticles as drug delivery devices.* Journal of controlled release, 2001. **70**(1-2): p. 1-20.

38.   Alexis, F., et al., *Factors affecting the clearance and biodistribution of polymeric nanoparticles.* Molecular pharmaceutics, 2008. **5**(4): p. 505-515.

39.   Kolishetti, N., et al., *Engineering of self-assembled nanoparticle platform for precisely controlled combination drug therapy.* Proceedings of the National Academy of Sciences, 2010. **107**(42): p. 17939.

40.   Johnson, B.K. and R.K. Prud'homme, *Mechanism for rapid self-assembly of block copolymer nanoparticles.* Physical review letters, 2003. **91**(11): p. 118302.

41.   Valencia, P.M., et al., *Single-Step Assembly of Homogenous Lipid- Polymeric and Lipid- Quantum Dot Nanoparticles Enabled by Microfluidic Rapid Mixing.* ACS nano, 2010. **4**(3): p. 1671-1679.

42.   John, S.E., et al., *An automated system for rapid evaluation of high-density electrode arrays in neural prostheses.* Journal of Neural Engineering, 2011. **8**: p. 036011.

Chapter 5

Conclusions and Recommendations for Future Work

5.1 SAW actuated rotary motor

5.1.1   Conclusions and contributions

The aim of this part of the thesis is to *develop* a *high speed* SAW actuated *motor* prototype with *an arbitrary rotational axis capability*. To achieve this, the work includes:

1. Fabrication and characterization of SAW devices made on a PZT substrate (the stator).

2. Development of the SAW rotary motor operating with and without an external preload.

3. Performance analysis of the motor with two different hole size configurations, specifically 0.25 and 0.45 mm.

The conclusion of each part is presented.

1. The stator is a SAW device made from PZT piezoelectric material with IDTs designed to work with a 3.2 MHz resonance frequency, resulting in a 700 µm wavelength, while the rotor is 1 mm solid steel sphere positioned on a blind hole drilled on the substrate. As PZT is an isotropic piezoelectric material; the IDTs can be designed in any direction on the plane of the substrate surface. The SAW generated would always propagate away from the generating IDT. This was confirmed with the travelling wave visualization using the LDV. The LDV measurements also experimentally verify that although the hole size is in the same order of magnitude with the wavelength, the presence of the smaller hole should not significantly affect the wave propagation; this is particularly true for the device with a hole size less than half of the wavelength.

2. The rotor always rotates on the same plane and about an axis perpendicular to the SAW propagation path; it can, consequently, be controlled to rotate in any chosen axis by activation of various IDTs fabricated around it. As a result, the motor ability to rotate in any planar axis chosen has been demonstrated. The SAW rotary motor is able to operate without any external preload. Its maximum rotational capability is up to *2000 rpm* at 110 V_{pp} input voltage. Addition of an external preload, in our case a permanent magnet positioned under the PZT substrate, alters the rotational axis to the z-axis (normal to the surface). This mode of operation also gives rise to rotor stability; the transient response shows significant

162

reduction in fluctuations. The maximum rotational capability is however, significantly less, approximately up to *1000 rpm* even at a higher input voltage of 130 V_{pp}. Combination of the planar arbitrary axis capability with the external preload would yield a complete three dimensional rotary motor. It is worth to note, however, it was very difficult to control the z-axis rotational direction. Nevertheless, the capability of the motor to rotate in any chosen axis in x-y-z space has been demonstrated.

3. For both with and without preload cases, the rotational speed increases as the hole size reduces. The motor with larger hole configuration, i.e. 0.45 mm, shows inferior performances. The results are predicted by the kinematic estimation, in addition can be further explained by the wave's phase delay and distortion as the hole size approaches the wavelength.

The main *contribution* of this work is an *operational prototype* of SAW actuated *rotary* motor which met the requirement. The SAW rotary motor has been developed with *a chosen yet arbitrary* rotational axis capability. The motor exhibits superior performance, in addition to require far less complex configurations, in comparison to SAW rotary motors reported on literature.

5.1.2 Recommendations

Several key areas of interest are indentified for further developments of the motor. Firstly, evaluation of the frictional characteristics of the motor is recommended. The motor performance in this thesis is estimated using the transient response, measured based on the ability of the stator. Another way of measuring the motor performance would be a more direct approach to the system; in which the motor performance is measured by varying the externally supplied torque onto the rotor in order to evaluate the frictional characteristic between the stator and the rotor. This direct measurement, however, is, at the time being, not possible. The complexity arises due to the small size of the device, particularly the rotor. Nevertheless, as the motor performance is essentially dependent on the frictional contact between the stator and rotor; the author believe that further work on this direct measurement method would prove to be beneficial.

Secondly, utilization of an electromagnet as the preload is recommended; this shall yield better control of the magnitude and direction of the preload force. Lastly, miniaturization is recommended. Smaller rotor coupled with higher operating frequencies, resulted in higher SAW acceleration, shall immensely increase the motor performances. With higher SAW frequencies being accessible with improve fabrication techniques for IDT patterning with smaller features, further development of motors at 10 to 100 micron dimensions should be performed.

5.2 SAW device development on stratified material for microfluidics applications

5.2.1 Conclusions and contributions

The aim of this part of the thesis is to *develop* a SAW device *exploiting* the beneficial properties of a *hybrid material* for *microfluidics applications*, specifically SAW devices made on a *ZnO/Al$_2$O$_3$* stratified material. To achieve this, the work includes:

1. Fabrication and characterization of the performances of SAW devices made on ZnO/Al$_2$O$_3$ hybrid material.

2. Verification and performance characterization of the Sezawa wave generated.

3. Utilization of the SAW device for microfluidics applications.

The conclusion of each part is presented.

1. The ZnO films with two different thicknesses, 1 μm and 11 μm, were deposited using a sputtering process, their c-axis orientations were verified by XRD and SEM. The SAW devices were fabricated using a lift-off process; the IDTs were designed to result in 32 μm wavelength and consisted of 300 nm of gold (Au) with 10 nm of Chromium (Cr) as the adhesive layer. Similar devices were also fabricated on a bulk Lithium Niobate (Li$_2$NbO$_3$) wafer for performance comparison. Subsequent performance characterization steps using a network

analyzer and an LDV demonstrated that Rayleigh waves generated on ZnO/Al_2O_3 material gives better performances as the thickness increases; yet, still inferior to that on $LiNbO_3$ substrate.

2. The Sezawa wave can be generated on stratified material with the thick piezoelectric material. For our case, the wave was induced on the 11 μm ZnO/Al_2O_3 substrate, h/λ ratio ≈ 0.3. Its electromechanical coupling coefficient was measured to be the highest among other samples, verified by its high vibration speed to input power ratio as measured by the LDV.

3. The SAW devices were then utilized for two microfluidics applications, inducing acoustic streaming in a sessile drop and PLGA nanoparticles precipitation. The Sezawa mode of the ZnO/Al_2O_3 hybrid material induced the fastest streaming speed followed by the Rayleigh mode of the $LiNbO_3$ and ZnO/Al_2O_3 hybrid material, consecutively. The acoustic streaming results follow the characterization results closely. In addition, the 4.8 μm polystyrene particles were observed to concentrate in the center of the vortices during operation. This is due to the dominance of the drag force over the acoustic streaming force on small particles (<< 300 μm) inside a sessile drop. The SAW device was then demonstrated to be a good alternative to precipitate PLGA nanoparticles. The size distributions of the nanoparticles produced by SAW are similar to those produced by to a more conventional rapid mixing technique.

The *key finding* of the work is that the surface displacement (amplitude) or the vibration speed is the most important factor for acoustic streaming. Whether it is the Sezawa or Rayleigh mode, or different thickness or material, surface displacement (amplitude) or the vibration velocity is the most important factor for acoustic streaming. The thickness and SAW mode factors give rise to different efficiencies in their electrical to mechanical energy conversion. Streaming induced by the Sezawa mode demonstrates the highest speed because it has the highest electromechanical coupling (validated by the network analyzer data) and hence highest vibration speed for a given input power (validated by the LDV data).

The main *contribution* of this work is the development of *SAW devices* based on a *ZnO/Al$_2$O$_3$ stratified material* as an *alternative* for microfluidics application. The devices performances are comparable to those based on a more common LiNbO$_3$ material; in addition, utilization of the Sezawa mode offers superior performances. The thin film form, furthermore, makes it more attractive for further integration as a practical platform for potential microfluidics applications.

5.2.2   Recommendations

Several key areas of interest are indentified for further work. Utilization of the ZnO/Al$_2$O$_3$ based SAW devices for various microfluidics applications from droplet translation, jetting to atomization is recommended. Explotiation of the Sezawa mode

should prove to be favorable. Secondly, as reviewed in the literature, ZnO is suitable material for up high frequencies (GHz) operation, development of such devices for microfluidics application should give rise to stronger streaming, therefore, is recommended.

Appendix A

Surface acoustic wave micromotor with arbitrary axis rotational capability

Tjeung, R. T., Hughes, M. S., Yeo, L. Y. & Friend, J. R.

Surface acoustic wave micromotor with arbitrary axis rotational capability

Ricky T. Tjeung, Mark S. Hughes, Leslie Y. Yeo, and James R. Friend[a)]

Micro/Nanophysics Research Laboratory, Melbourne Centre for Nanofabrication and the Department of Mechanical Engineering, Monash University, Clayton, Victoria, Australia

A surface acoustic wave (SAW) actuated rotary motor is reported here, consisting of a millimeter-sized spherical metal rotor placed on the surface of a lead zirconate titanate piezoelectric substrate upon which the SAW is made to propagate. At the design frequency of 3.2 MHz and with a fixed preload of 41.1 μN, the maximum rotational speed and torque achieved were approximately 1900 rpm and 5.37 μN-mm, respectively, producing a maximum output power of 1.19 μW. The surface vibrations were visualized using laser Doppler vibrometry and indicate that the rotational motion arises due to retrograde elliptical motions of the piezoelectric surface elements. Rotation about orthogonal axes in the plane of the substrate has been obtained by using orthogonally placed interdigital electrodes on the substrate to generate SAW impinging on the rotor, offering a means to generate rotation about an arbitrary axis in the plane of the substrate. © *2011 American Institute of Physics*. [doi:10.1063/1.3662931]

Despite many applications in microrobotics and microsurgery[1] and the schemes proposed to generate micromotion, including electrostatic, electromagnetic, and piezoelectric,[2] few practical motors exist at appropriate scales to enable them. The main challenges are the inherent complexity of the final device and the accuracy necessary in fabrication, requiring design simplicity and creativity in machining techniques.[3–7] While the use of bulk flexural waves at small scales has been proposed in the past for ultrasonic piezoelectric micromotors,[8,9] the problem of fabricating piezoelectric thick films with performance characteristics sufficient for actuation[10] has never really been overcome. Surface acoustic waves (SAW), on the other hand, may be generated in thick substrates and offer substantially greater flexibility in mounting and materials choices, not to mention the extraordinary power densities that may be achieved and the benefit that may be drawn from the decades-long effort in using SAW for telecommunications.[11,12]

Most SAW actuators to date have been millimeter-scale, *linear* actuators that use Rayleigh waves traveling across the surface of a piezoelectric material,[5,13,14] usually 127.68° Y-cut x-propagating (see Fig. 1 for coordinates) lithium niobate (LN).[15] Rayleigh waves possess in-plane, longitudinal (x-axis) motion leading, temporally by one-quarter of a period, transverse (z-axis) motions of approximately the same amplitude as they propagate along the x-axis. Points of the surface move in retrograde ellipses in the x–z plane, and an object placed upon the surface will move toward the source of acoustic radiation along the x-axis. The maximum speed is determined by the particle or vibration velocity of the wave, around 1 m/s:[5,14] a motor 60 × 15 mm in size generated up to 18 N force and a speed of 0.9 m/s with 250 V_{p-p} input,[14] but required a preload force of 120 N between the chemically reduced[16] LN substrate and Si slider, unfortunately causing wear that limits the motor's use to a few tens of cycles at most.

SAW motors, where the object in motion rotates about an axis, are far more rare; Cheng *et al.*[17] reports one of two known examples. Rayleigh SAW propagating in opposition from adjacent interdigital electrodes (IDTs) is used to drive a collection of steel balls housed in a 9-mm diameter disc; the disc is allowed to rotate on a hub placed between the counter-propagating SAW, altogether resembling a circus carousel. Probably due to substantial parasitic friction and standing wave SAW at the overlap region between the counter-propagating SAWs, the maximum rotation speed is only 270 rpm and there is no reported torque value, despite a driving voltage of 120 V_{p-p}. A more recent work[18] also makes use of counter-propagating Rayleigh SAW, but with a fluid coupling layer[19] to rotate a 5-mm disc at up to 2250 rpm and with 60 N-m torque. The inconvenience of the fluid common to fluid bearing-driven and acoustic levitation[20] motors is a drawback, however.

Here, we report the development of a dry friction-coupled Rayleigh SAW-driven motor capable of rotating the rotor, a 1 mm solid steel sphere, about a chosen yet arbitrary axis that lies within the plane of the piezoelectric substrate, lead zirconate titanate (PZT, C–203, Fuji Ceramics Corporation, Japan) as illustrated in Fig. 1. PZT was selected due to outright convenience in testing the concept of the motor, its isotropic piezoelectric properties along the substrate plane, and its large electromechanical coupling coefficient,[21] though the concept does work with other, lead-free materials like LN.

Rayleigh SAW of $f = 3.2$ MHz is generated from straight, unapodized 700 μm pitch IDTs patterned along orthogonal axes in 2-μm-thick Ag on the PZT substrate using standard photolithography, as illustrated in Fig. 1(a). Polydimethylsiloxane was cast in place around the periphery of the 40-mm diameter substrate to prevent acoustic interference from edge reflections. A blind hole with 250 μm diameter was drilled approximately 350 μm deep into the substrate along the SAW propagation pathway (see Figs. 1(b) and 1(c)), upon which the rotor is placed, preventing it from sliding across the substrate and forming a circular contact line. Here, the roughness of PZT can be a factor—the finished surface of the PZT has a roughness of about 1 μm, and so we polished the contact line using a spare rotor to sub-nm
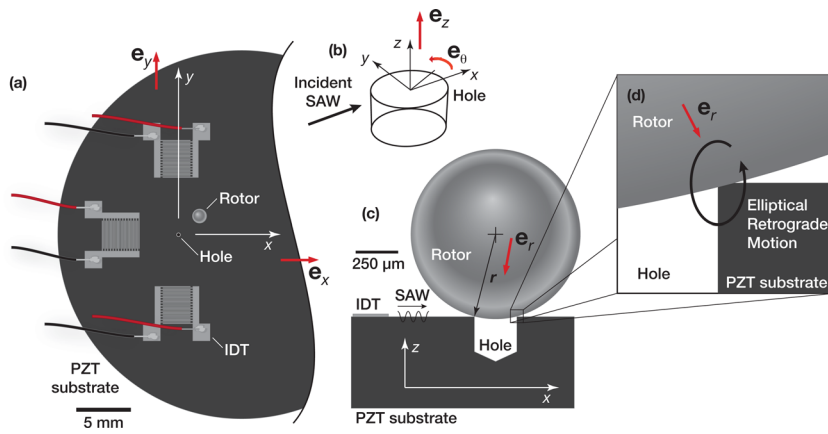
a)Electronic mail: ▮▮▮▮▮▮▮▮▮

FIG. 1. (Color online) (a) Top view of SAW micromotor, a 1 mm solid steel sphere placed atop a retaining hole in PZT patterned with orthogonally placed IDTs. Upon generation of a Rayleigh SAW from an IDT, the SAW propagates (b) past the hole and (c) the contact line formed with the rotor placed upon it. The particle motion is everywhere retrograde with respect to the propagation direction of the SAW, including all points (d) along the contact line. This motion acts against the ball's inertia and generates rotation through stick-slip motion.

roughness before testing. Friction along this contact circle, as the SAW passes, gives rise to rotation.

A laser Doppler vibrometer (LDV; Polytec PI MSA–400, Waldbrunn, Germany) was utilized to visualize the SAW propagation, essentially unaffected by the presence of the hole as shown in Fig. 2, save for a small phase delay of less than 10° and localized amplification of the motion due to stress release of about 15%. These results are expected since the hole diameter and depth are less than the SAW wavelength. The absence of data along path B–B in the hole is due to its sloped bottom preventing reflection of the laser used in LDV measurements.

In contrast to linear SAW motors, rotation can be obtained in this arrangement even with a very small preload force between the rotor and stator only due to gravity—the weight of the rotor, approximately 41.1 μN in our system—because of the large interfacial stress present from the line contact.

The measured z-axis vibration velocity, $\dot{\gamma} = 2\pi f \gamma$, can be used to estimate the maximum rotor velocity, ω_{max}, generated without placing a load on the rotor. The x-axis, in-plane component of the wave vibration velocity, $\dot{\eta}$, cannot be measured using our LDV but is known to be approximately 70% of the transverse component on the bare surface of hard PZT.[22] Piezoelectric traveling-wave ultrasonic motors rely upon stick-slip mechanisms to generate motion,[23–25] with the local relative motion transverse to the contact locally modulating the friction between the substrate

and rotor. Only recently has it become apparent that bouncing of the rotor can contribute to the dynamics in fascinatingly complex ways,[26] but here, we use an approximate model to estimate its maximum speed. We assume, for each point of contact along the contact circle, the rotor is being driven to rotate such that the linear velocity of the rotor at that point, defined from the rotor center by $\boldsymbol{r} = R\boldsymbol{e}_r$ (see Fig. 1(c)), is equal to the velocity of the substrate at the point of contact, $\dot{\boldsymbol{\xi}} = \dot{\eta}\boldsymbol{e}_x + \dot{\gamma}\boldsymbol{e}_z$. This implies the rotation of the rotor would be given by $\boldsymbol{\omega} \times \boldsymbol{r} = \dot{\boldsymbol{\xi}}$ if the action was only at this point. To find the angular velocity $\boldsymbol{\omega}$, we find $\boldsymbol{r} \times \dot{\boldsymbol{\xi}} = r^2\boldsymbol{\omega} - (\boldsymbol{\omega} \cdot \boldsymbol{r})\boldsymbol{r}$. Recognising that the only component of $\boldsymbol{\omega}$ that can be generated from enforcing a displacement constraint between the substrate and the rotor at the point must be perpendicular to $\boldsymbol{r}$, we are left with $\boldsymbol{r} \times \dot{\boldsymbol{\xi}} = |\boldsymbol{r} \cdot \boldsymbol{r}|\boldsymbol{\omega}$, easily solved for $\boldsymbol{\omega}$. Naturally, the angular velocity so produced varies around the contact circle of radius a, violating the pointwise constraint, and so we take the integral average of this pointwise velocity ω over $\theta \in \{0, 2\pi\}$ for our estimate, as the rotor must do in response to the induced motion,

$$\omega_{\text{max}} = \frac{1}{2\pi} \int_0^{2\pi} \frac{\boldsymbol{r} \times \dot{\boldsymbol{\xi}}}{|\boldsymbol{r} \cdot \boldsymbol{r}|} d\theta = \left(\frac{0.7\dot{\boldsymbol{\xi}}\sqrt{R^2 - a^2}}{R^2} \right) \boldsymbol{e}_y; \quad (1)$$

the latter result as a consequence of assuming the spatial phase shift over the contact circle is negligible in which the radius of the hole $a < \lambda_{\text{SAW}}$ where λ_{SAW} is the wavelength of
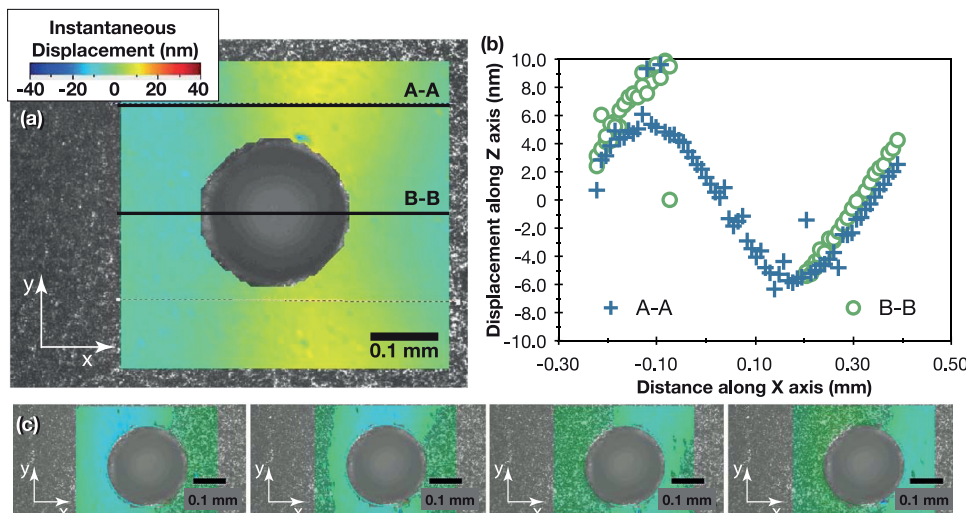
FIG. 2. (Color online) (a) SAW propagates left-to-right in the substrate, passing through the hole without substantial change as indicated by LDV measurement of the instantaneous z-polarized displacement, particularly in (b) comparison of the displacements along lines A–A and B–B, and (c) progressive images of the displacement, separated in time by 39 ns intervals (representing 1/8 of the wave period for 3.2 MHz) (enhanced online, along with demonstration of motor operation). [URL: http://dx.doi.org/10.1063/1.3662931.1]
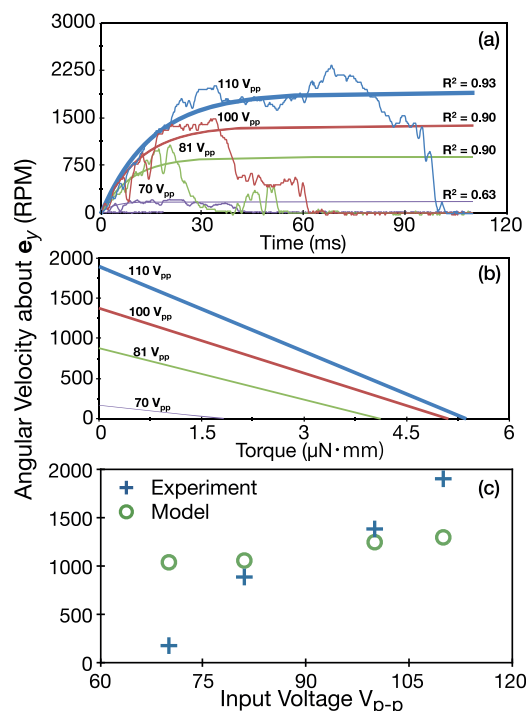
FIG. 3. (Color online) Angular velocity of the rotor with respect to (a) time and (b) torque of the motor obtained during operation with magnetic preload. The maximum speed achieved was approximately 1900 rpm, and the maximum torque achieved was 5.37 μN·mm using the weight of the rotor, approximately 41.1 μN, as the loading on the contact interface. Note the coefficient of determination, R^2, values is well above 0.5, permitting the use of Nakamura's method for estimating the torque-speed behaviour in (b). (c) Maximum model-predicted and experimentally measured rotor speeds in the system. The relatively poor comparison at low and high voltages is due to the complete absence of friction or stick-slip modelling in the very simple contact model, but the model does give an indication of the motor's output rotor speed without requiring substantial computations.

the SAW. Otherwise $\dot{\xi} = \dot{\xi}(\theta)$ and the integration may be more complex. With this assumption, most of the integrand is harmonic on $(0,2\pi)$, including the contribution from the z-axis motion $\dot{\gamma}e_z$, and does not contribute to $\omega_{\max}$. The orientation of rotation is about the y axis with the rotor in contact with the substrate moving toward the SAW source, indicating a means to control the rotation axis by defining the direction of SAW incident upon the contact circle. Several IDTs placed about and pointed towards the contact can be used to change the rotation axis' orientation, as illustrated in the multimedia content provided with Fig. 2, though the axis will always remain parallel to the substrate surface.

The motor performance was measured using a laser tachometer (S-100 Z, Canon, Tokyo, Japan) and signal generator and amplifier (WF1946 and HSA4101, NF Corporation, Japan) as shown in Fig. 3. The comparison in this figure between the modeled and measured maximum rotor speed over a range of input voltages is provided; the weight of the rotor, approximately 41.1 μN in our system, was used as a very light preload, permitting rotor bouncing[26] in this early

trial. The very simple theory offers a reasonable estimate for the rotor speed at intermediate voltages; considering the many assumptions underlying the very simple model, particularly in ignoring slip along the contact line, the rotor speed equation would be useful as a crude estimate. We modelled the motor's transient response as first-order lag system with good fit quality per Nakamura's method[27,28] to determine its torque and speed capabilities as shown in Fig. 3.

[1]B. Watson, J. Friend, and L. Yeo, Sens. Actuators, A **152**, 219 (2009).
[2]D. K.-C. Liu, J. Friend, and L. Yeo, Acoust. Sci. & Tech. **31**, 115 (2010).
[3]L. S. Fan, Y. C. Tai, and R. Muller, Sens. Actuators **20**, 41 (1989).
[4]J. Friend, L. Yeo, and M. Hogg, Appl. Phys. Lett. **92**, 014107 (2008).
[5]K. Asai and M. K. Kurosawa, Electron. Commun. Jpn. **88**(1), 37 (2005).
[6]M. Barbic, J. J. Mock, A. P. Gray, and S. Schultz, Appl. Phys. Lett. **79**, 1399 (2001).
[7]T. Kanda, A. Makino, T. Ono, K. Suzumori, T. Morita, and M. Kurosawa, Sens. Actuators A **127**, 131 (2006).
[8]A. Flynn, L. Tavrow, S. Bart, R. Brooks, D. Ehrlich, K. Udayakumar, and L. Cross, J. Microelectromech. Syst. **1**, 44 (1992).
[9]S. Biwersi, P. Gaucher, J. Hector, J. Manceau, and F. Bastien, Sens. Actuators, A **70**, 291 (1998).
[10]E. Hong, S. Trolier-McKinstry, R. Smith, S. Krishnaswamy, and C. Freidhoff, IEEE Trans. Ultrason. Ferroelectr. Freq. Control **53**, 697 (2006).
[11]K. Hashimoto, *Surface Acoustic Wave Devices in Telecommunications: Modelling and Simulation* (Springer, Berlin, Germany, 2000).
[12]R. White and F. Voltmer, Appl. Phys. Lett. **7**, 314 (1965).
[13]M. K. Kurosawa, M. Takahashi, and T. Higuchi, IEEE Trans. Ultrason. Ferroelectr. Freq. Control **43**, 901 (1996).
[14]K. Sakano, M. K. Kurosawa, and T. Shigematsu, Adv. Rob. **24**, 1407 (2010).
[15]J. Campbell and W. Jones, IEEE Transactions on Sonics Ultrason. **15**, 209 (1968).
[16]P. F. Bordui, D. H. Jundt, E. M. Standifer, R. G. Norwood, R. L. Sawin, and J. D. Galipeau, J. Appl. Phys. **85**, 3766 (1999).
[17]L. Cheng, G. Zhang, S. Zhang, J. Yu, and X. Shui, Ultrasonics **39**, 591 (2002).
[18]R. Shilton, N. Glass, P. Chan, L. Yeo, and J. Friend, Appl. Phys. Lett. **98**, 254103 (2011).
[19]R. P. Hodgson, M. Tan, L. Yeo, and J. Friend, Appl. Phys. Lett. **94**, 024102 (2009).
[20]J. Saito, J. Friend, K. Nakamura, and S. Ueha, Jpn. J. Appl. Phys. **44**, 4666 (2005).
[21]Y. J. Hsiao, T. H. Fang, Y. H. Chang, Y. S. Chang, and S. Wu, Mater. Lett. **60**, 1140 (2006).
[22]C. Tseng, J. Appl. Phys. **38**, 4281 (1967).
[23]S. Ueha and Y. Tomikawa, *Ultrasonic Motors—Theory and Applications*, Monographs in Electrical and Electronic Engineering Vol. 29 (Clarendon, Oxford, 1993).
[24]J. R. Friend, in *Proceedings of the 37th AIAA/ASME/ASCE/AHS/ASC Structures, Structural Dynamics, and Materials Conference and Exhibition* (American Institute of Aeronautics and Astronautics, 1996), Vol. 96, Paper No. 1452, pp. 1–15.
[25]J. Wallaschek, Smart Mater. Struct. **7**, 369 (1998).
[26]K.-C. Liu, J. Friend, and L. Yeo, Phys. Rev. E **80**, 046201 (2009).
[27]K. Nakamura, M. K. Kurosawa, H. Kurebayashi, and S. Ueha, IEEE Trans. Ultrason. Ferroelectr. Freq. Control **38**, 481 (1991).
[28]J. Friend, K. Nakamura, and S. Ueha, IEEE Trans. Ultrason. Ferroelectr. Freq. Control **52**, 1343 (2005).

Appendix B

Arbitrary axis rotating surface acoustic wave micro motor

Tjeung, R. T., Hughes, M. S., Yeo, L. Y. & Friend, J. R.

Proceedings of the 2011 6th IEEE International
Conference on Nano/Micro Engineered and Molecular Systems
February 20-23, 2011, Kaohsiung, Taiwan

Arbitrary Axis Rotating Surface Acoustic Wave Micro Motor

Ricky T. Tjeung, Mark S. Hughes, Leslie Y. Yeo, and James R. Friend*

Micro/Nanophysics Research Laboratory, Monash University, Clayton 3800, Victoria, Australia

* E-mail: ████████████████

Abstract- **We present a surface acoustic wave (SAW) actuated rotating micro motor. The rotors are 1 millimeter metal spheres which are placed on the surface of a Lead Zirconate Titanate (PZT) substrate with IDTs designed to generate SAW with ~ 700 μm wavelength. A Laser Doppler Vibrometer (LDV) was used to visualize the travelling SAW and the result was compared with the rotation of the rotor. The motor transient responses are presented, along with its torque-speed curve. The maximum rotational speed and torque reported were ~1000 rpm and ~14 μN.mm, respectively. Arbitrary motions have also been demonstrated utilizing a magnetic pre-load and multiple IDTs activation.**

Keywords: rotational micro motor, surface acoustic wave, ultrasonics motor, piezoelectric

I.   BACKGROUND

A surface acoustic wave (SAW) motor is a millimeter size motor actuated by travelling waves. Most applications utilize the Rayleigh wave, a type of acoustic wave which is confined to travel along the surface of a piezoelectric material [1-8].

Work on developing various linear SAW micro motors have been performed by Kurosawa et al [1-3] and Xing et al [4]. The systems consist of a rotor preloaded with magnet, set to linearly move along a slider. The maximum speed and force achieved were 0.9 m/s and 18 N respectively for a 125 V_p input voltage [3].

We present another type of SAW micro motor. Utilizing a metal sphere as the rotor, we developed a rotating micro motor, instead of a linear motor. The substrate material selected for this purpose was lead zirconate titanate (PZT) rather than the more common 127.68° Y-X cut Lithium Niobate (LiNbO$_3$) due to the anisotropic nature of the material. Using PZT as the piezoelectric substrate, arbitrary rotating motion can be achieved.

II.   CURRENT RESULT

SAWs were generated by applying a continuous sinusoidal electrical input into an interdigital transducer (IDT, Ag 7-finger pair electrode) patterned on a surface of the PZT ceramic substrate. The devices were designed to work with a 3.2 MHz resonance frequency, which results in a 700 µm wavelength.

Fig. 1 and 2 show the configuration of the rotating micro motor. A metal sphere (1 mm diameter) as the rotor was placed onto a blind hole drilled on the PZT surface. A permanent magnet, with strength of 0.088±0.002T was used as the pre-load. The blind hole (0.25 mm) was used to confine the rotor from translating during operation.
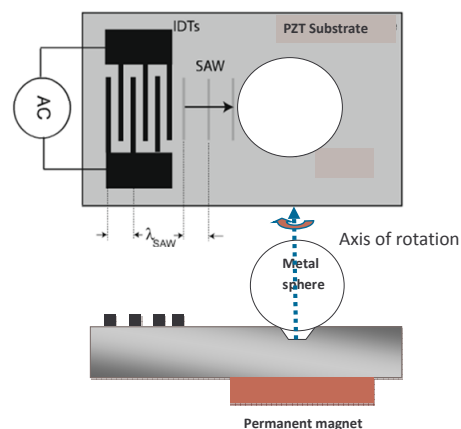
Fig. 1. Schematic representation of the rotating micro motor.
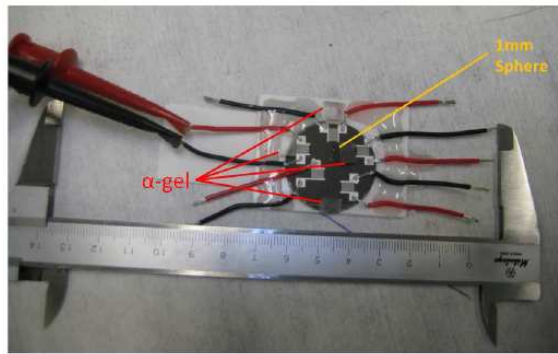
(a)
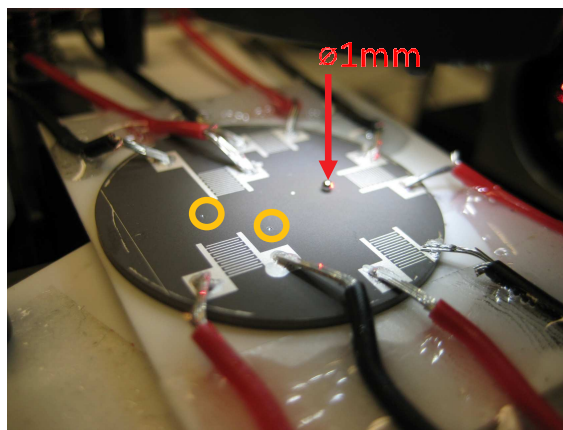
(b)

Fig. 2. The arbitrary axis SAW micro motor with 1mm diameter steel rotor on PZT substrate with 3.2MHz IDTs. An Alpha GEL (Taica Corporation, Japan) is used to absorb reflected SAWs from substrate boundaries, mitigating standing waves; (**b**) the yellow circles indicate the blind holes.

Visualization of the travelling SAW along the PZT surface with the hole was done using a Laser Doppler Vibrometer (LDV; Polytec PI MSA-400, Waldbrunn, Germany). The result is presented as fig.3. It was also observed that the SAW continues to travel along the blind hole.
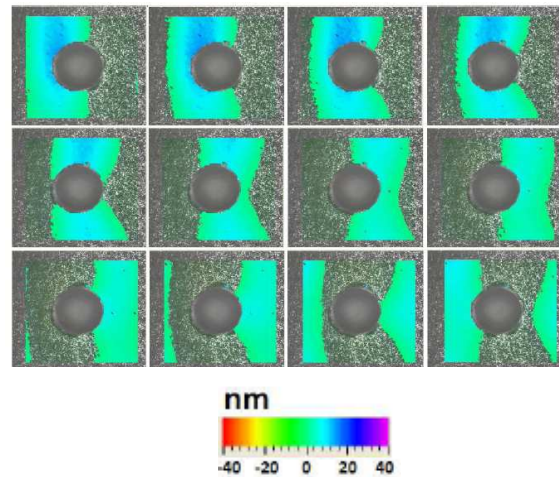
Fig. 3. Consecutive images of Laser Doppler Vibrometer data of a 700 μm SAW travelling along a 250 μm blind hole in PZT. The propagation direction of the SAW is from left to right.

After the completion of the SAW visualization, the next step was to characterize the performances of the motor during operation. Hypothesis formed after the LDV result analysis shows that the rotor should rotate with axis of rotation parallel to the surface and perpendicular to the SAW propagation path; experimental results prove this hypothesis closely. The schematic of this operation can be viewed in fig. 4.

Further experiments showed that the axis of rotation can be altered by introduction of a pre-load. The axis of rotation with magnetic pre-load is normal to the surface of the substrate. Fig. 5 shows the two modes of operation (with and without pre-load).
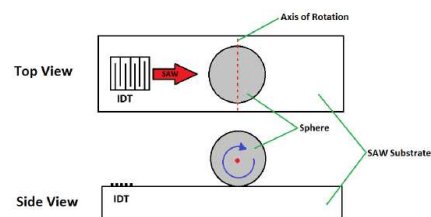
Fig. 4. Schematic illustration of one mode of operation, i.e. without any pre-load. The blue arrow shows the rotor rotation direction, the axis of rotation is perpendicular to the SAW propagation path.

185

(a)   **(b)**
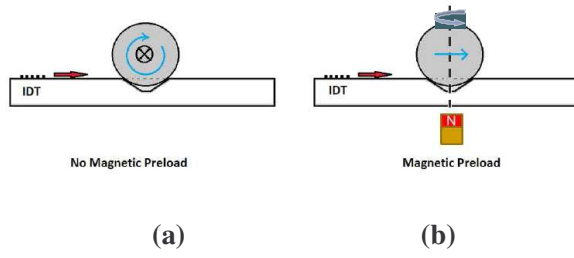
Fig. 5. Schematic illustrations of two modes of operation. The blue arrow shows the rotor rotation directions. The axis of rotation can be altered with introduction of a magnetic pre-load (0.088±0.002T) from (a) perpendicular to the SAW propagation path to (b) normal to the substrates surface. This could be used as a mechanism to achieve the arbitrary axis rotation.

Successive images of the rotor rotation during operation are shown in fig. 6. The images were captured using a high speed camera (Motion BLITZ, Mikroton GMBH) at 1000 frames per seconds. The operation was with pre-load hence the normal axis of rotation.
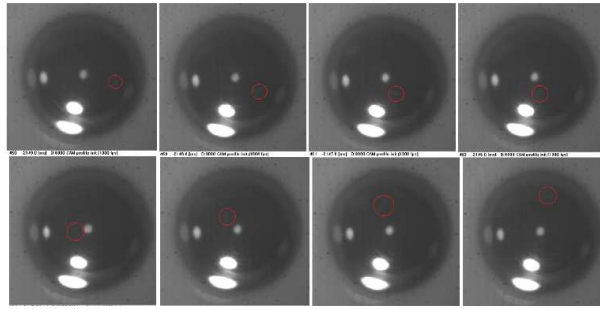
Fig. 6. Successive images of the motor during one mode of operation. The motor was running with the magnetic pre-load, hence the axis of rotation is normal to the substrates surface. The images were captured using a high speed camera (Motion BLITZ, Mikroton GMBH) at 1000 frames per seconds.

The motor start-up speeds were measured using a Laser Tachometer (Canon, S-100Z). Input power was provided using a signal generator (NF Wave Factory, WF1946 2CH) coupled with an amplifier (NF High Speed Bipolar Amplifier, HSA 4101). The transient response is shown in fig. 7. The torque is calculated using the method proposed by Nakamura et al [5] and shown in fig. 8.

Using single IDT activations, the rotor rotates with axis of rotation normal to the surface of the substrate. With the 250 μm blind hole configurations and maximum input power of 65 V_p, the maximum rotation speed and torque achieved were ~1000 rpm and ~14 μN.mm respectively. The micro motor was able to operate without performance degradation up to 30 sec.
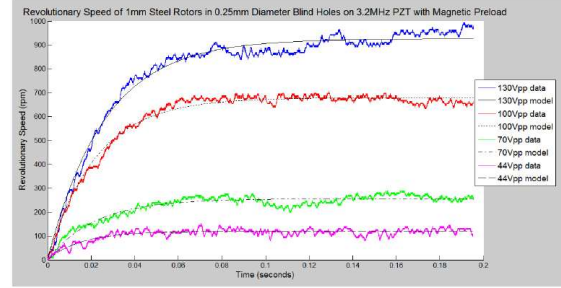
Fig. 7. The transient response of the motor during operation with the magnetic pre-load. The motor start-up speeds were measured using a Laser Tachometer (Canon, S-100Z). The maximum speed achieved was approximately 1000 rpm.
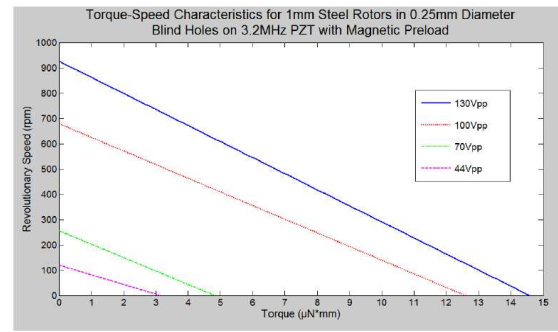
Fig. 8. The torque speed characteristic of the motor during operation with the magnetic pre-load. The torque was calculated using the method proposed by Nakamura et al [5]. The maximum torque achieved was over 14 μN.mm.

We subsequently continued to visualize the SAW actuated by multiple IDTs activation. These are also essential for achieving arbitrary motions. The results can be viewed on fig. 9. The measured area is located in front of two IDTs, whose axes of wave propagation are perpendicular to each other. We followed by demonstrating the rotor capability to rotate in arbitrary directions. The rotational directions of the rotor follow the LDV results closely.
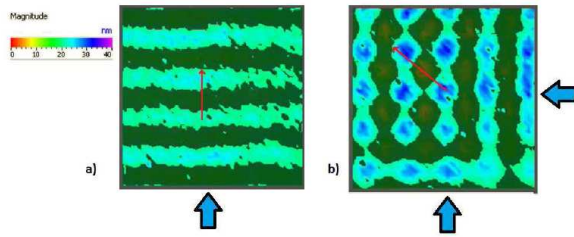
Fig. 9. Laser Doppler Vibrometer (LDV) visualization of SAW generated by multiple IDTs actuations. Fig. 9 (**a**) illustrates the SAW propagation from one IDT (below the image), while fig. 9 (**b**) illustrates the SAW propagation at the intersection from two perpendicularly orientated IDTs. The SAW travelling directions are indicated by the blue arrows and the motion of the peak displacements are indicated by the inset red arrows.

REFERENCES

[1]   M. K. Kurosawa, M. Chiba, and T. Higuchi, "Evaluation of a surface acoustic wave motor with a multi-contact-point slider," Smart Mater. Struc. , pp. 305-311, 1998.

[2]   K. Asai and M. K. Kurosawa, "Performance Estimation of Surface Acoustic Wave Motor Using Simulation Model of Friction Drive," Electronics and Communications in Japan, Part3. Vol. 88, No. 1, 2005.

[3]   K. Sakano, M. K. Kurosawa, and T. Shigematsu, "Driving Characteristic of a Surface Acoustic Wave Motor using a Flat-Plate Slider," Advanced Robotics 24, pp. 1407-1421, 2010.

[4]   Y. Xing, Y. Li, J. Zhang, and G. Gao, "Surface Acoustic Wave Linear Motor for Two-dimensional Optical Positioning System," Proceedings of the 2009 4th IEEE International Conference on Nano/Micro Engineered and Molecular Systems, January 2009.

[5]   K. Nakamura, M. Kurosawa, H. Kurebayashi, and S. Ueha, "An Estimation of Load Characteristics of an Ultrasonics Motor by Measuring Transient Responses" IEEE Transactions on Ultrasonics, Ferroelectrics, and Frequency Control, Vol. 38, No. 5, September 1991.

[6]   M. Kurosawa, M. Takahashi, and T. Higuchi, "Friction Drive Surface Acoustic Wave Motor," Ultrasonics, 34, pp. 243-246, 1996.

[7] M. K. Kurosawa, "State-of-the-art Surface Acoustic Wave Linear Motor and Its Future Applications," Ultrasonics, 38, pp. 15-19, 2000.

[8] M. Takahashi, M. Kurosawa, and T. Higuchi, "Optimum Contact Conditions for Miniaturized Surface Acoustic Wave Linear Motor" Ultrasonics, 38, pp. 51-53, 2000.

Appendix C

ZnO/sapphire based layered surface acoustic wave devices for microfluidic applications

Tjeung, R. T., Maurya, D. K., Yeo, L. Y., Friend, J. R. & Kandasamy, S.

Proceedings of the 2011 6th IEEE International
Conference on Nano/Micro Engineered and Molecular Systems
February 20-23, 2011, Kaohsiung, Taiwan

ZnO/sapphire based layered surface acoustic wave devices for microfluidic applications

Ricky T. Tjeung[1], Devendra K. Maurya[1], Leslie Y. Yeo[1,2], and James R. Friend[1,2]*

1 Micro/Nanophysics Research Laboratory,

Monash University, Clayton 3800, Victoria, Australia

* E-mail: ▮▮▮▮▮▮▮▮▮▮▮

Sasikaran Kandasamy[2],

[2]Melbourne Centre for Nanofabrication,

151 Wellington Road, Clayton 3168, Victoria, Australia

E-mail: ▮▮▮▮▮▮▮▮▮▮▮▮▮▮▮

Abstract- The microfluidic applications of a ZnO/Sapphire based layered surface acoustic wave structure are being investigated. Properties of the ZnO/Sapphire layered SAW device including surface wave velocity and propagation loss were measured and correlated to the fluidic behavior of micro droplets. Acoustic streaming was observed in the form of two vortices. Micro particles were also observed to concentrate in the vortices within 4 seconds of device activations.

I. INTRODUCTION

Surface acoustic wave (SAW) microfluidics has generated considerable interest. SAW technology offers simpler and more compact devices and do not involve moving parts. The fluid-acoustic energy interaction arising from SAW can be harnessed to generate various types of micro to nano liter scale fluid manipulation. Depending on the actuation power, the manipulation could be in form of mixing, transport or even atomization [1-10].

There is also considerable interest in using thin film piezoelectric materials for SAW microfluidics due to several advantages. The foremost would be the possibility of incorporation with controller circuits to achieve an integrated Lab-On-a-Chip (LOC) device.

ZnO is a versatile material for many applications due to its structural, electrical and optical properties [11-12]. Piezoelectric ZnO possesses a high coupling coefficient, which make it attractive for thin films SAW devices. ZnO thin films have been deposited by several techniques, including sol-gel, MOCVD, MBE, PLD and sputtering. Among these techniques, sputtering is the most commonly used deposition method for polycrystalline ZnO, typical for acoustic applications.

SAW microfluidics devices based on thin film ZnO has been recently reported and showed promising results. Du et al [13-15] has developed a SAW device using deposited thin film ZnO on a silicon substrate; and showed the feasibility of utilizing it for microfluidics manipulation.

There is furthermore, an increasing interest in developing surface acoustic wave (SAW) devices operating at high frequencies without fabricating submicron electrode. By depositing a piezoelectric thin film on a high acoustic velocity substrate, the surface velocity can be significantly increased.

Sapphire (Al_2O_3) substrate is widely used for its high acoustic velocity and relatively low loss. ZnO on sapphire devices have been reported [16-20], yet it usage for microfluidics is limited to date. For this reason, in this work, we correlate the ZnO/Sapphire device characteristics with the fluidic manipulation. The fabrication of ZnO/sapphire layered structures is detailed, the SAW frequency response characteristics are measured, and the interaction of the acoustic wave and the coupled fluid is discussed.

II. EXPERIMENTAL

ZnO thin films were deposited on sapphire (0001) substrate by RF magnetron sputtering (Hummer BC-20 DC/RF Sputter system, Anatech USA). The substrate temperature during the deposition process was 150ºC and a sequential post-annealing treatment was carried out at 500ºC for 5 hrs in ambient air. This was done to provide sufficient energy to rearrange the atoms in the crystal sites and also to eliminate the intrinsic stress induced by sputtering. The sputtering rate was approximately 0.25 μm/hour.

TABLE I: ZnO deposition process parameters

Target	ZnO (purity 99.99%)
Target-substrate distance	~12cm
Sputtering gas	60% Ar + 40% O2
Substrate temperature	150ºC
RF power	150W
Sputtering pressure	10mTorr

The crystalline structure of ZnO on sapphire was examined by X-ray diffraction with Cu Kα, λ of 0.1542 nm (Phillips X-ray Diffractometer); and the surface morphologies were observed with atomic force microscopy. The XRD result in Fig. 1 shows the high *2θ* intensity at *34.4º*. This angle, representing (002) diffraction peak, indicates that the ZnO deposited on sapphire is c-axis oriented. The SEM cross-section showed the ZnO grew in a column structure. The AFM scan reveals a surface roughness of ~6nm over a 5x5 µm scan area. The c-axis orientation and smooth surface are critical parameters of a SAW device.
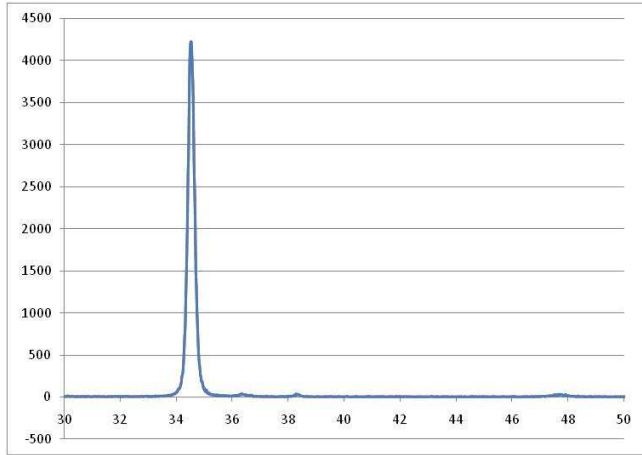

Fig. 1. XRD result of the sputtered ZnO on sapphire substrate. Diffraction peak is observed at *2θ* of *34.4º*, which indicates the (002) crystallographic orientation.

The interdigital transducer (IDT) patterns were transferred on to the ZnO surface using a conventional lift-off process. The IDT consists of an adhesion layer of 10nm Cr and 200nm of Au, which were thermally evaporated. Both the width and the spacing of the IDT patterns were 8µm, which corresponds to a wavelength of 32µm.

The frequency response of the ZnO/Sapphire SAW structure was measured using a network analyzer (Agilent E5062A). A set of experiments were conducted to examine the effects of acoustic streaming in a droplet using the fabricated ZnO/sapphire based layered device. Water droplet with a volume of 1 µL seeded with 4.8 µm size fluorescent polymer microspheres (Duke Scientific Corporation, USA) was placed onto the surface of ZnO, in the propagation pathway of the SAW for flow visualization. The images were captured using a high speed camera (Motion BLITZ, Mikroton GMBH). The input power was provided using a signal generator (Agilent N9310A) coupled with an amplifier (Model 10W 1000C, Amplifier Research). The power input to the IDT was monitored using a power sensor (U2004A, Agilent Technologies).

III. RESULTS AND DISCUSSIONS
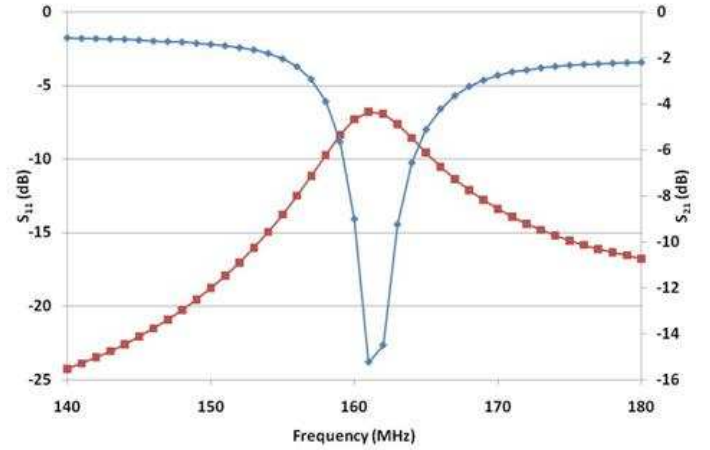
Fig. 2. Frequency Response S_{11} and S_{21} of the ZnO/Sapphire SAW devices

Fig. 2 shows the measured frequency response of the fabricated ZnO/Sapphire device. The SAW device is designed to have a value of λ = 32µm. The thickness (h) of ZnO film is 1 µm (h/λ = 0.03), while the centre frequency is 161MHz. The calculated phase velocity is 5152 m/s from the relation $V_p = F_o.\lambda$. In Fig. 3, the successive images of the SAW streaming inside a 1 µL water droplet seeded with 4.8 µm fluorescent particles is shown. The IDT is located to the right of the droplet. The particles are concentrated in the two vortices within 4 seconds of IDT activations.
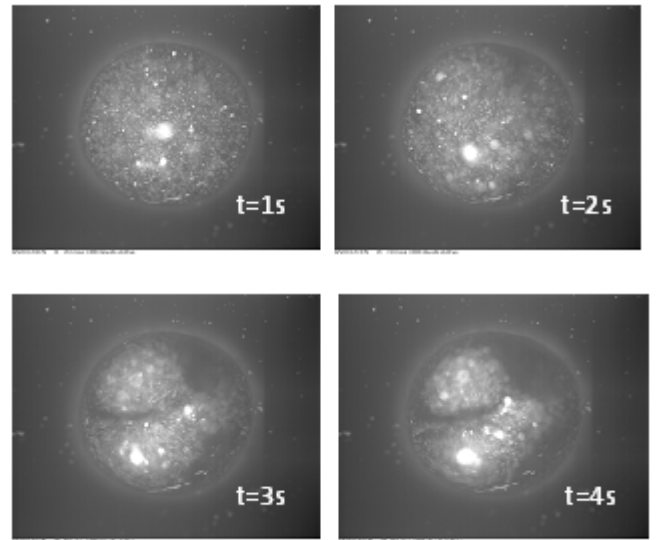
Fig. 3. Successive images of the SAW streaming inside a 1 µL water droplet seeded with 4.8 µm fluorescent particles. The IDT is located to the right of the droplet. The particles are concentrated in the two vortices within 4 seconds of IDT activation.
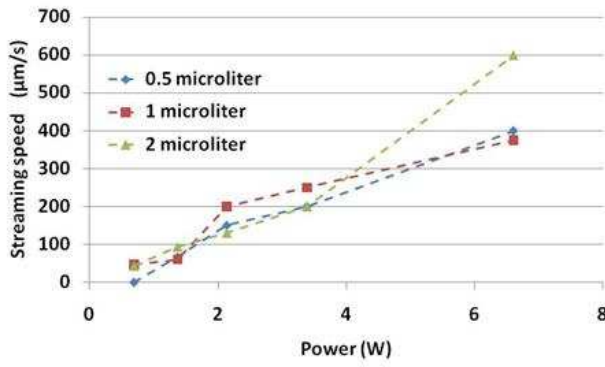
Fig. 4. Acoustic streaming speed of the water droplet resulted from increasing input powers (frequency of 158 MHz)

The streaming speed with respect to increasing input power is shown in Fig. 4. Three different volumes of water droplet were used. A maximum streaming speed of 600μm/s was observed for an input power of 6.61 W at frequency of 158 MHz.

In Fig. 5 the acoustic streaming speeds of droplets with the same volumes (1μL) but with different input frequencies are compared. The device operated at 158MHz showed higher streaming speed than at 161MHz, approximately up to 4 times. This frequency shift could be due to damping caused by the droplet, which is placed in the propagation pathway of the SAW.

Fig. 5. Comparison of the streaming speed for different input frequencies.

One interesting phenomenon that occurs in a thin film SAW device is the occurrence of the higher order harmonic wave. This wave, called the Sezawa wave, appears in addition to more commonly observed Rayleigh wave. The Sezawa wave normally has a higher phase velocity than the Rayleigh wave; this is attributed to the higher resonance frequency of this mode [16-18]. It has been reported that the electromechanical
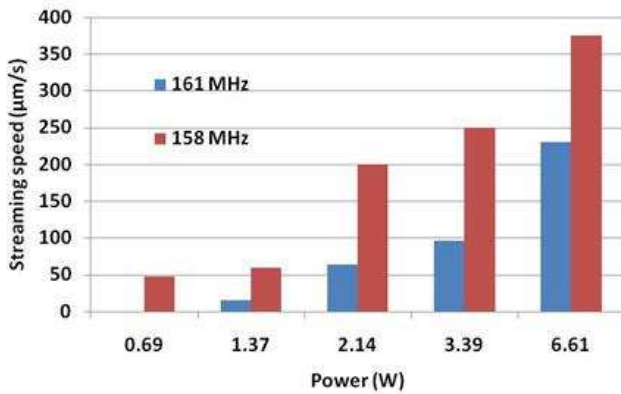
coupling coefficient (K^2) of the Sezawa mode is up to 4 times higher compared to the Rayleigh mode for the same devices [21].

The Sezawa waves appearances nevertheless, are very limited. They only appear in multiple layers substrate; and only if to the acoustic velocity of the surface layer lower than or equal to the acoustic velocity in the lower substrate [16-19]. Not only that the material selection must be satisfied, another essential requirement for the Sezawa wave to appear is that the surface layer thickness and the acoustic wavelength must be over a certain ratio; $h/\lambda \geq 0.15$, in which h and λ are the film thickness and acoustic wavelength, respectively [16-18].

It is within the scope of this work to utilize the Sezawa wave for microfluidics. ZnO film with various thicknesses has been deposited onto sapphire substrates using the same parameters, as given in Table 1. Work on characterizing the Sezawa waves and fluidic coupling are being carried out. By employing the Sezawa waves, more efficient acoustic streaming is expected. Comparison of the acoustic streaming caused by the Rayleigh and Sezawa waves shall be presented.

IV. CONCLUSIONS

The acoustic streaming in droplets has been investigated using a ZnO/sapphire based layered device. Acoustic streaming was observed in the form of two vortices. Micro particles were also observed to concentrate in the vortices within 4 seconds of device activation. A maximum acoustic streaming of ~600μm/s was observed when the device was operated at 158MHz. Furthermore, work on utilizing a higher order harmonic wave, called the Sezawa wave is being conducted. The acoustic steaming result shall be presented.

REFERENCES

[1] L. Y Yeo. and J. R. Friend "Ultrafast microfluidics using surface acoustic waves." Biomicrofluidics 3, 2009.

[2] A. Wixforth, C. Strobl, Ch. Gauer, A. Toegl, J. Scriba and Z.v. Guttenberg, "Acoustic Manipulation of small Droplets." Analytical and Bioanalytical Chemistry 379: 982-991, 2004.

[3] D. Beyssen, L. Le Brizoual, O. Elmazria and P. Alnot, "Microfluidic device based on surface acoustic wave." Sensors and Actuators B: Chemical 118: 380- 385, 2006.

[4] M. Cecchini, S. Girardo, D. Pisignano, R. Cingolani and F. Beltram, "Acoustic-counterflow microfluidics by surface acoustic waves." Applied Physics Letters 92: 104103-3, 2008.

[5] M. K. Tan, J.R. Friend and L.Y. Yeo, "Direct visualization of surface acoustic waves along substrates using smoke particles." Applied Physics Letters 91, 2007.

[6] K. Sritharan, C. J. Strobl, M.F. Schneider, A. Wixforth and Z. Guttenberg, "Acoustic mixing at low Reynold's numbers." Applied Physics Letters 88, 2006.

[7] A. Rathgeber, M. Wassermeier and A. Wixforth, "Acoustic 'distributed source' mixing of smallest fluid volumes." Journal of ASTM International 2: 259-266, 2005.

[8] A. Renaudin, P. Tabourier,V. Zhang, J.C. Camart and C. Druon, "SAW nanopump for handling droplets in view of biological applications." Sensors and Actuators, B: Chemical 113: 389-397, 2006.

[9] A. Qi, J.R. Friend and L.Y. Yeo,"SAW atomization application on inhaled pulmonary drug delivery." Biomedical Applications of Micro- and Nanoengineering IV and Complex Systems, Melbourne, Australia, SPIE, 2008.

[10] M. Kurosawa, T. Watanabe, A. Futami and T. Higuchi, "Surface acoustic wave atomizer." Sensors and Actuators, A: Physical 50(1-2): 69-74, 1995.

[11] Y-J Kim and K-W Kim, "Characteristics of Epitaxial ZnO Films on Sapphire Substrates Deposited using RF-Magnetron Sputtering," *Jpn. J. Appl. Phy.,* vol. 36, pp. 2277-2280, 1997.

[12] M. Kadota and M. Minakata, "Piezoelectric Properties of ZnO Films on a Sapphire Substrate Deposited by an RF-Magnetron-Mode ECR Sputtering System", *Jpn. J. Appl. Phy.,* vol. 37, pp. 2923-2926, 1998.

[13] X.Y. Du, Y.Q. Fu, J.K. Luo, A.J. Flewitt and W.I. Milne, "Microfluidic pumps employing surface acoustic waves generated in ZnO thin films." Journal of Applied Physics 105: 024508-7, 2009.

[14] X.Y. Du, Y.Q. Fu, S.C. Tan, J.K. Luo, A.J. Flewitt, S. Maeng, S. H. Kim, Y.J. Choi, D.S. Lee, N.M. Park, J. Park and W.I. Milne, "ZnO film for application in surface acoustic wave device." Journal of Physics: Conference Series 76: 012035, 2007.

[15] X.Y. Du, Y.Q. Fu, S.C. Tan, J.K. Luo, A.J. Flewitt, W.I. Milne, D.S. Lee, N.M. Park, Y.J. Choi, S.H. Kim and S. Maeng, "ZnO film thickness effect on surface acoustic wave modes and acoustic streaming," *Applied Physics Letters*, 93, 2008.

[16] N. W. Emanetoglu, C. Gorla, Y. Liu, S. Liang and Y. Lu, "Epitaxial ZnO piezoelectric thin Film for SAW Filters", Material Science in Semiconductor Processing, vol. 2, pp. 247-252, 1999.

[17] N. W. Emanetoglu, G. Patounakis, S. Liang, C. Gorla, R. Wittstruck and Y. Lu, "Analysis of SAW Properties of Epitaxial ZnO Films Grown on R-AL$_2$O$_3$ Substrates", IEEE Transactions on Ultrasonics, Ferroelectrics, and Frequency Control, Vol. 48, pp. 1389-1394, 2001.

[18] N. W. Emanetoglu, S. Liang C. Gorla and Y. Lu, "Epitaxial Growth and Characterization of High Quality ZnO Film for Surface Acoustic Wave Applications", IEEE Ultrasonics Symposium, 1997.

[19] T. Mitsuyu, S. Ono and K. Wasa, "Structures and SAW properties of rf-sputtered single-crystal films of ZnO on sapphire," *Journal of Apped. Physics.,* 51, pp. 2464-2470, 1980.

[20] T-T. Wu and W-S. Wang, "An Experimental Study on the ZnO/Sapphire layered surface acoustic wave device", Journal of Applied Physics, vol. 96, pp. 5249-5253, 2004.

[21] A.H. Weber, G. Weiss and S. Hunklinger, "Comparison of Rayleigh and Sezawa Wave Modes in ZnO-SiO$_2$-Si Structures", IEEE Ultrasonics Symposium, 1991.

Appendix D

Patent: Single and multi-axis surface acoustic wave motor

James R. Friend, Leslie Yu-ming Yeo, **Ricky Theodore Tjeung,** Mark St.Clair Hughes

SINGLE AND MULTI-AXIS SURFACE ACOUSTIC WAVE MOTOR

FIELD OF THE INVENTION

The present invention is directed to surface acoustic wave (SAW) actuated motors.

5   ## BACKGROUND TO THE INVENTION

A surface acoustic wave (SAW) motor is a millimetre sized motor actuated by travelling waves. Most SAW motors utilise a Rayleigh wave, a type of acoustic wave which is confined to travel along the surface of piezoelectric material, as the actuating mechanism. The surface acoustic waves are generated by means of

10   an inter digital transducer (IDT) electrode located on the surface of the piezoelectric substrate. Application of a continuous sinusoidal electrical input into the IDT electrode results in a surface acoustic wave being generated along the surface of that piezoelectric substrate.

SAW motors have been developed which utilise surface acoustic waves to

15   drive a slider in a linear motion over the surface of a piezoelectric substrate. For example, US 6,331,747 (Minolta Co., Ltd.,) describes the use of such a linear SAW motor for driving a photographic lens of a camera. US 6,710,511 (Matsushita Electric Industrial Co., Ltd.,) describes the use of a linear SAW motor developed to control the linear motion of a head arm within a computer hard

20   drive.

In the above described applications, the SAW micro motors are limited to linear motion of a slider along a path relative to the surface of the piezoelectric substrate.

It is an object of the present invention to provide a surface acoustic wave

25   motor that can achieve rotational actuation.

It is also a preferred object of the present invention to provide a surface acoustic wave motor which can allow for more than one axes of rotation.

The above discussion of background art is included to explain the context of the present invention. It is not to be taken as an admission that any of the

30   material referred to was published, known or part of the common general knowledge at the priority date of any one of the claims of the specification.

SUMMARY OF THE INVENTION

According to the present invention, there is provided a surface acoustic wave (SAW) actuated motor including:

a piezoelectric substrate having a surface;

5   at least one inter digital transducer (IDT) electrode located on the surface of the piezoelectric substrate;

a signal generator means for applying a sinusoidal electrical input to the IDT electrode;

at least one cavity located in the surface; and

10   a spherical rotor located over the cavity;

wherein actuation of the IDT electrode generates a surface acoustic wave along the surface, the cavity being located in the propagation path of the surface acoustic wave so that rotational motion of the spherical rotor is actuated about an axis of rotation thereof.

15   The cavity may be generally circular in shape and may therefore provide a generally circular peripheral edge in the piezoelectric substrate surface. The spherical rotor may at least partially contract the peripheral edge of the cavity. It has been found that the spherical rotor may rotate about an axis of rotation perpendicular to the SAW propagation path and parallel to the piezoelectric 20   substrate surface if the cavity is positioned in the propagation path of the surface acoustic wave, and the spherical rotor is supported over the cavity.

A magnetic preload be preferably be applied to the spherical rotor by magnetic means when located on the cavity, the preload acting to draw the spherical rotor towards the cavity. It has been found that such a magnetic 25   preload may alter the position of the axis of rotation of the spherical rotor such that the axis of rotation remains perpendicular to the SAW propagation path, the axis of rotation is now normal to the piezoelectric substrate surface. This arrangement therefore allows for the position of the axis of rotation to be varied from being parallel to the piezoelectric substrate surface to normal thereto.

30   Preferably more than one IDT electrode may be located on the piezoelectric substrate, the IDT electrodes being angled relative to each other such that the respective SAW propagation path of each IDT electrode crosses at an angle relative to each other. The cavity may be located such that the cavity is

located within the SAW propagation path of each IDT electrode. It has been found that the use of more than one IDT electrode generating surface acoustic waves may allow the position of the axis of rotation of the spherical rotor to be varied as a function of the direction of the SAW propagation paths of each of IDT

5   electrode.

The piezoelectric substrate may be formed from piezoelectric material having an anisotropic nature. Preferably, lead zirconate titanate which has this nature may be used for this purpose. The use of other anisotropic piezoelectric materials are also envisaged. The anisotropic nature of the piezoelectric material

10   allows for any SAW generated on the surface of the piezoelectric substrate to be similar regardless of the planar direction.

DETAILED DESCRIPTION OF THE INVENTION

It will be convenient to further describe the invention with reference to the accompanying drawings which illustrate a preferred embodiment of the present

15   invention. Other embodiments are possible, and consequently, the particularity of the accompanying drawings is not be understood as superseding the generality of the preceding description of the invention.

In the drawings:

Figure 1 is a schematic top and side view of a SAW motor according to the

20   present invention;

Figure 2 are schematic top and side views of the SAW motor of Figure 1 showing the axis of rotation of the spherical rotor;

Figures 3(a) and 3(b) are respective schematic side views of the SAW motor of Figure 1 showing the change in the position of the axis of rotation of the

25   spherical rotor with the application of a magnetic preload on the rotor;

Figure 4 is a graph showing the transient response of the SAW motor during operation with a magnetic preload;

Figure 5 is a graph showing the torque speed characteristics of the SAW motor during operation with the magnetic preload; and

30   Figures 6(a) and 6(b) are laser doppler vibrometer (LDV) visualisations of the surface acoustic wave respectively generated by a single IDT electrode, and a pair of perpendicularly orientated IDT electrodes.

Referring initially to Figures 1 to 3(a) and 3(b), there is shown the configuration of a preferred embodiment of the SAW motor 1 according to the present invention. The SAW motor 1 includes a piezoelectric substrate 3 having a surface 5 upon which is located an inter digital (IDT) electrode 7. A generally

5   circular cavity 9 having a diameter of about 250 μm is provided in the surface 5 of the piezoelectric substrate 3. The cavity 9 has a generally circular peripheral edge 11 which is at least partially in contact with a spherical rotor 15 sitting on and located over the cavity 9. The spherical motor 11 is made from metal such as steel and has a diameter of about 1 mm. A permanent magnet 16 is located

10   on a side of the piezoelectric substrate 3 on the opposing side to the surface 5 accommodating the cavity 9. The permanent magnet 16 is located in close proximity to the cavity 9 to thereby apply a magnetic preload on the spherical rotor 15. A continuous sinusoidal electrical input can be applied to the IDT electrode 7 by a signal generator 8.

15   The substrate material selected for this purpose was Lead Zirconate Titanate (PZT) rather than the more common 127.68° Y-X cut Lithium Niobate (LiNbO3) due to the anisotropic nature of the material. This helps to ensure that the surface acoustic wave generated on its surface will be similar in any planar direction.

20   SAWs were generated by applying a continuous sinusoidal electrical input into the IDT electrode 7 (Ag 7-finger pair electrode) patterned on a surface of the PZT ceramic substrate surface 5. The devices were designed to work with a 3.2 MHz resonance frequency, which results in a 700 μm wavelength.

A permanent magnet, with strength of 0.088±0.002T was used as the pre-

25   load on the spherical rotor. The cavity 9 was used to confine the rotor 15 from translating during operation.

Experiments conducted on the SAW motor 1 has revealed that the rotor 15 rotates about an axis of rotation 17 perpendicular to the direction of the SAW propagation path as shown by arrow 19. When there is no magnetic preload on

30   the spherical rotor 15, the axis of rotation 17 of the spherical rotor 15 is generally parallel to the substrate surface 5 as shown in Figure 2. Figure 2 also shows the direction of rotation 18 of the spherical rotor 15 which is aligned with the direction of the SAW provocation path 19.

Figures 3(a) and 3(b) show the effect of applying a magnetic preload on the axis of rotation 17 of the spherical rotor 15, with the axis of rotation 17 moving from being parallel to the substrate surface 5 with no magnetic preload as shown in Figure 3A to be normal to the substrate surface 5 when a magnetic preload is

5 applied to the spherical rotor 15 as shown in Figure 3(b) (and also Figure 1). A magnetic preload of 0.08±0.002T was utilised in the experiments. This demonstrates one mechanism for varying the orientation of the axis of rotation 17 of the spherical rotor 15.

Figure 4 shows the measured transient response of the SAW motor 1 were

10 measured using a laser tachometer during operation with the magnetic preload, the input voltage across the IDT electrode 7 being varied to measure the change in transient response. The maximum speed achieved was approximately 1000 rpm when a voltage of 130Vpp applied to the IDT electrode 7.

Figure 5 shows a torque speed characteristic of the SAW motor 1 during

15 operation with the magnetic preload, the input voltage across the IDT electrode 7 being varied to obtain the different torque curves. The torque values were calculated using a method proposed by Nakamura *et al*, "An Estimation of Load Characteristics of an Ultrasonics Motor by Measuring Transient Responses" IEEE Transactions of Ultrasonics, Ferroelectrics, and Frequency Control, Vol. 38,

20 No. 5, September 1991. The maximum torque achieved was over 14 μN.mm.

Experiments were also conducted using multiple IDT electrode actuations. The results can be viewed in Figures 6(a) and 6(b) which are laser doppler vibrometer (LDV) visualisations of the surface acoustic waves generated by a single IDT electrode in Figure 6(a), and two perpendicularly oriented IDT

25 electrodes shown in Figure 6(b). The visualisation shown in Figure 6(a) shows a surface acoustic wave generated by a single IDT electrode, the direction of the SAW propagation path being indicated by arrow 21. The resultant rotational direction of the spherical rotor 15 follows closely the motion of the peak displacement shown by arrow 23. It is noted that the peak displacement is in the

30 same direction as the direction of SAW propagation 21 when a single IDT electrode is used. Figure 6(b) shows the visualisation of the surface acoustic waves generated by two perpendicularly oriented IDT electrodes with the direction of SAW propagation of each IDT electrode being shown by arrows 21.

6

The intersection of the two surface acoustic waves results in the pattern shown in Figure 6(b) and results in a motion of peak displacement as shown by arrow 23 in Figure 6(b). The motion of peak displacement is approximately 45 degrees relative to the respective SAW propagation paths 21 of each IDT electrode.

5   The resultant direction of rotation of a spherical rotor exposed to the intersecting SAW propagations was found to follow closely the motion of the peak displacements. The use of multiple IDT electrodes therefore provides another mechanism for varying the axis of rotation for varying the direction of rotation and therefore the orientation of the axis of rotation of the spherical rotor.

10   The surface acoustic wave motor according to the present invention therefore allows for rotary motion to be generated by a surface acoustic wave actuated motor. In addition, the surface acoustic wave actuated motor according to the present invention may allow for changes to be made in the position of the axis of rotation of the rotating spherical rotor.

15   Modifications as would be deemed obvious to the person skilled in the art are included within the ambit of the present invention as claimed in the appended claims.

CLAIMS:

1.   A surface acoustic wave (SAW) actuated motor including:

a piezoelectric substrate having a surface;

at least one inter digital transducer (IDT) electrode located on the surface

5   of the piezoelectric substrate;

a signal generator means for applying a sinusoidal electrical input to the
IDT electrode;

at least one cavity located in the surface; and

a spherical rotor located over the cavity;

10   wherein actuation of the IDT electrode generates a surface acoustic wave
along the surface, the cavity being located in the propagation path of the surface
acoustic wave so that rotational motion of the spherical rotor is actuated about an
axis of rotation thereof. ·

2.   A surface acoustic wave (SAW) actuated motor according to claim 1
15   further including magnetic means for applying a magnetic preload on the
spherical rotor.

3.   A surface acoustic wave (SAW) actuated motor according to claim 1 or 2,
including a plurality of IDT electrodes located on the piezoelectric substrate
surface, the IDT electrodes being angled relative to each other such that the
20   respective propagation path of the surface acoustic wave generated by each IDT
electrode crosses at an angle relative to each other, the cavity being located
within the surface acoustic wave propagation path of each IDT electrode.

4.   A surface acoustic wave (SAW) actuated motor according to claim 3,
including two perpendicularly orientated said IDT electrodes.

5.   A surface acoustic wave (SAW) actuated motor according to any one of the preceding claims, wherein the piezoelectric substrate is Lead Zirconate Titanate.

MONASH UNIVERSITY
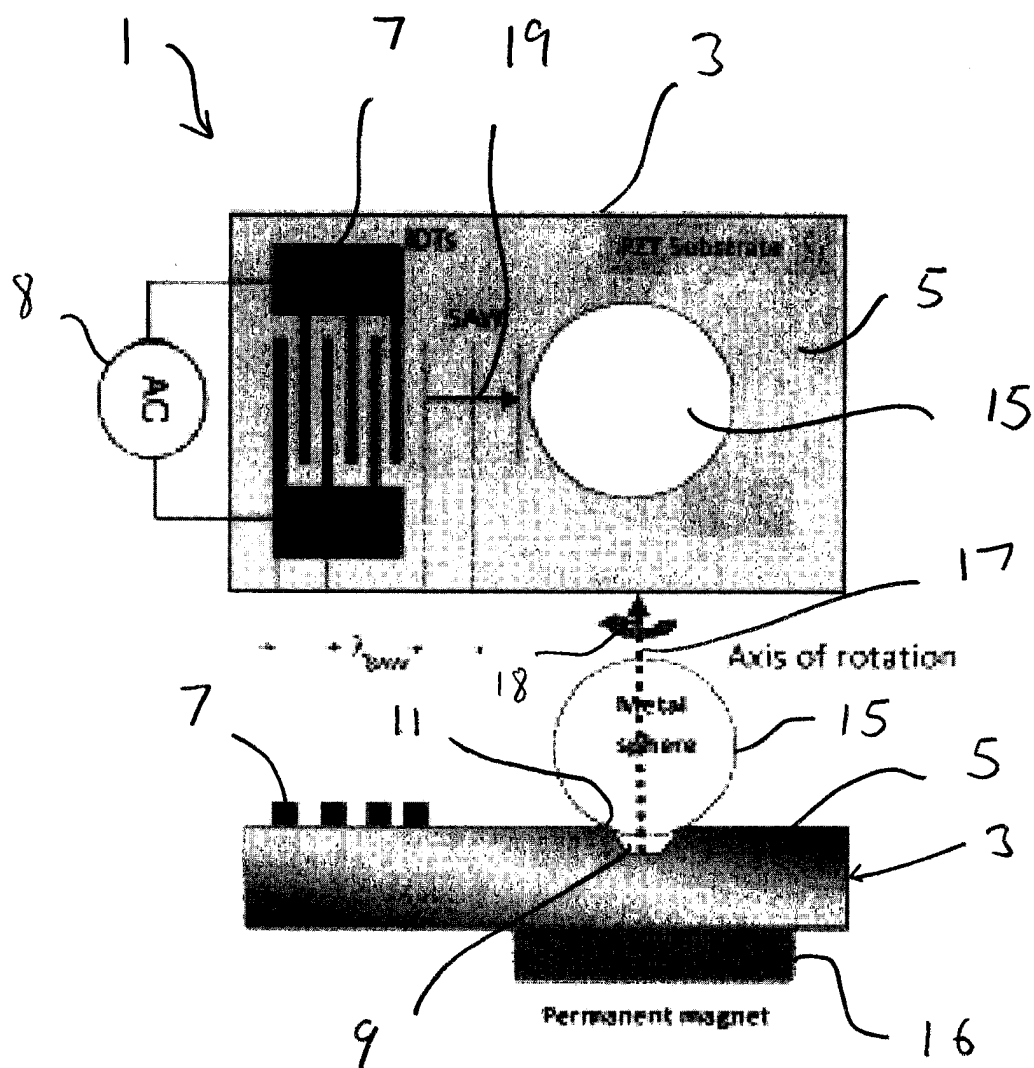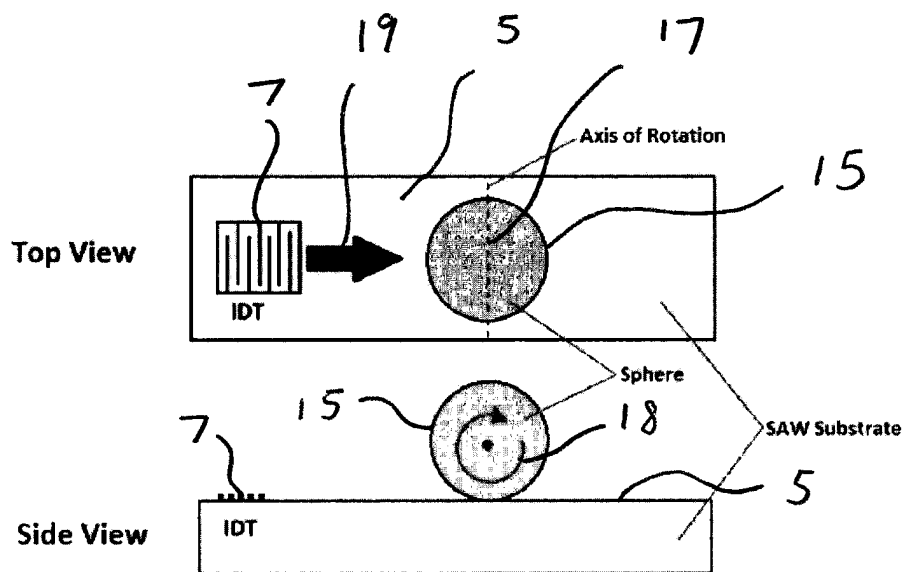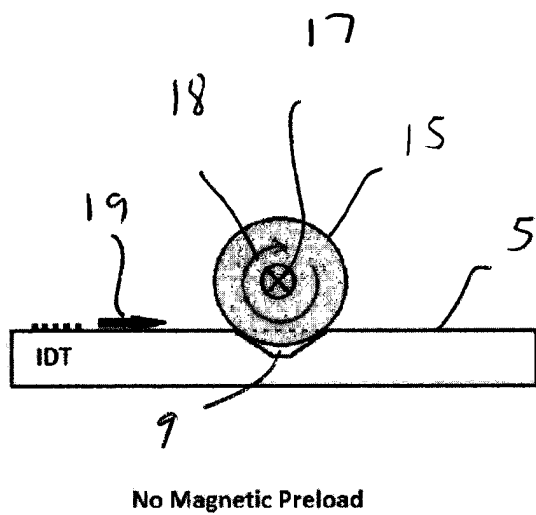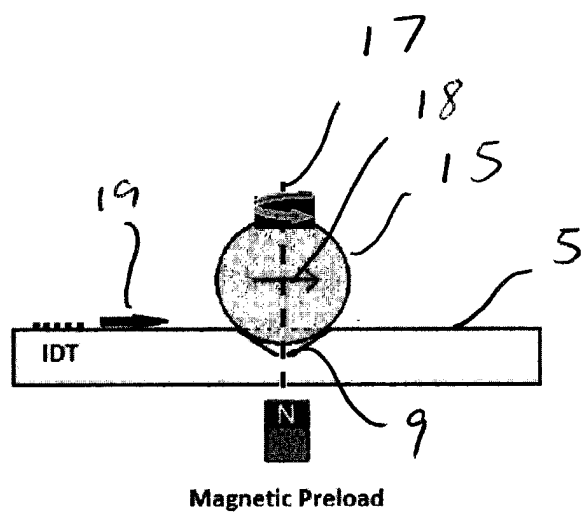
WATERMARK PATENT & TRADE MARK ATTORNEYS

P33891AUP1

Fig. 1

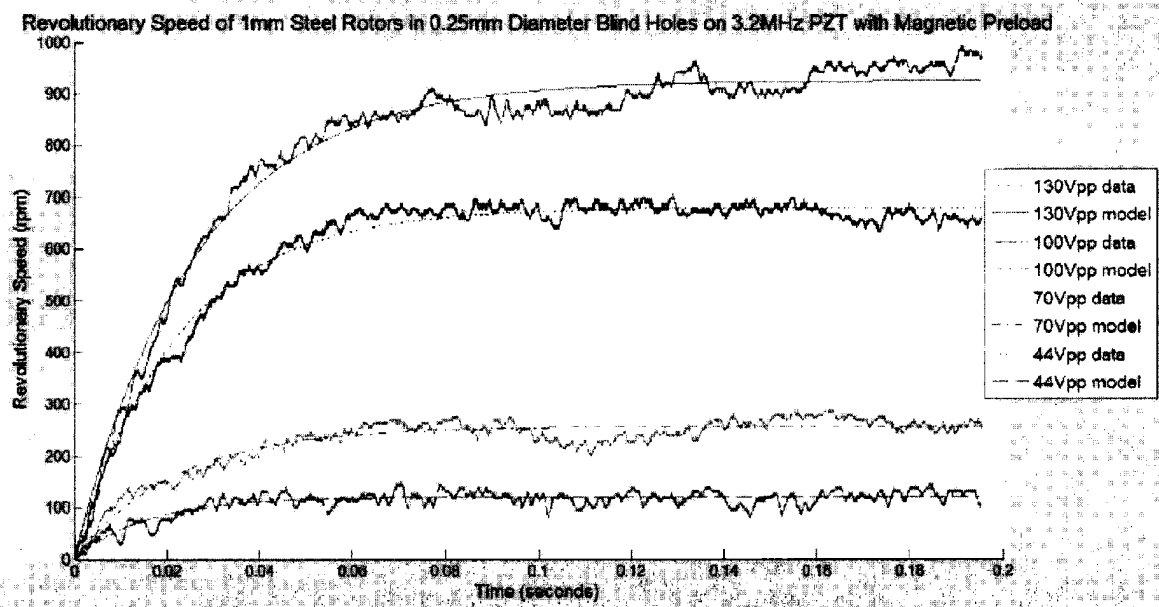**Fig. 2**
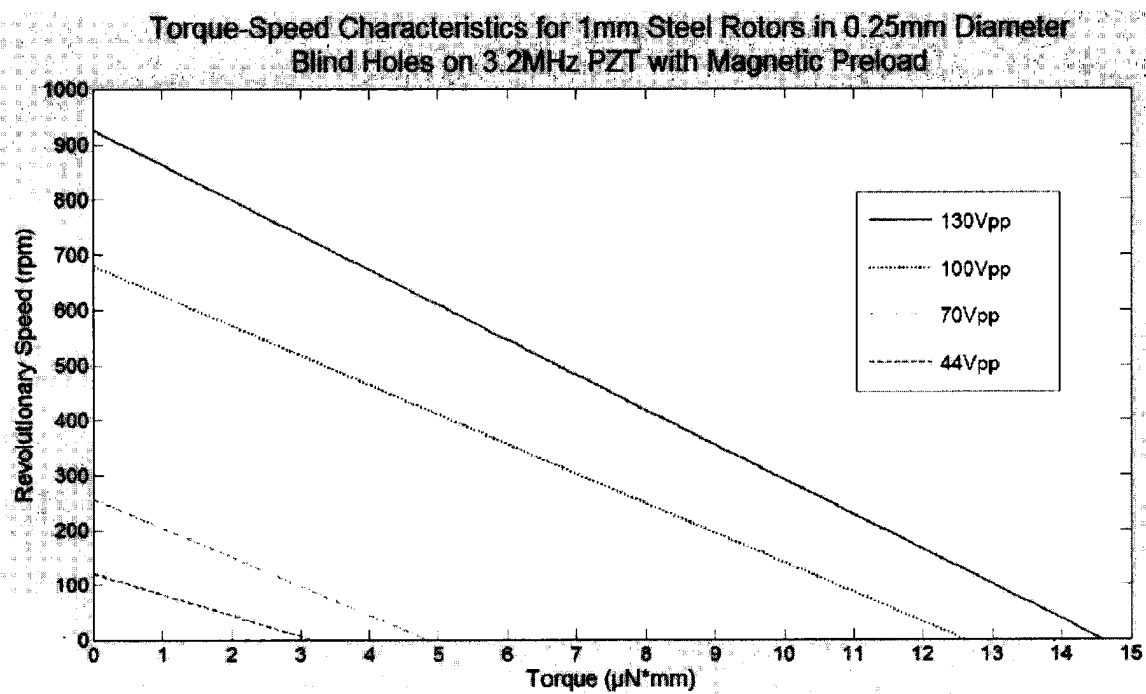

No Magnetic Preload

Magnetic Preload

Fig. 3 (a)

Fig. 3 (b)

Fig. 4

Fig. 5

Fig. 6(a) and 6(b)